

**Effects of brain gyrification on impact-induced strain
measurements with a preliminary study on viable *ex
vivo* porcine brain**

by

Ashley Mazurkiewicz

A thesis submitted to the Faculty of Graduate Studies and Research
in partial fulfilment of the requirements for the degree of

Master of Applied Science

in

Biomedical Engineering

Ottawa-Carleton Institute for Biomedical Engineering
Department of Mechanical and Aerospace Engineering
Carleton University
Ottawa, Ontario, Canada
June 2020

Copyright ©

2020 - Ashley Mazurkiewicz

The undersigned recommend to
the Faculty of Graduate Studies and Research
acceptance of the Thesis

**Effects of brain gyrification on impact-induced strain
measurements with a preliminary study on viable *ex vivo* porcine
brain**

Submitted by **Ashley Mazurkiewicz**
in partial fulfilment of the requirements for the degree of
Master of Applied Science

O.E. Petel, Thesis Supervisor

H. Frei, Thesis Co-Supervisor

S. Rajan, SYSC

X. Wang, MAE

E. Matida, MAE (in place of University of Ottawa)

R. Miller, Department Chair

Carleton University

2020

Abstract

Traumatic brain injuries can be devastating. In post-mortem brains, injury accumulation has been found at surface depressions; a feature in brains with gyrification. A study into the importance of brain gyrification on impact-induced strain measurements was undertaken. Two surrogates, lacking and possessing gyrification, were impacted at multiple heights and orientations. Radiopaque speckle sheets within the surrogates were used to visualize motion at 7,500 fps via high-speed X-ray radiography. Strain responses between select markers were determined using digital image correlation and particle tracking. The surrogate with gyrification mostly displayed larger strain magnitudes and variations in response patterns compared to the smooth surrogate. Differences in gyrification may contribute to the damage incurred, where models representing human level gyrification may reveal unknown injury information. Additionally, a preliminary study was conducted on *ex vivo* porcine brain. Large strain values and variations in responses were observed, a trend experienced by the surrogate with gyrification.

Acknowledgments

Almost three years ago, I began a new adventure. I moved to a new city and started my masters in a new field. This chapter in my life would not have been possible without a few key people.

First and foremost, my thesis would not have been possible without the ideas and support of my supervisor, Professor Oren E. Petel. The opportunities you have provided have made me a better researcher and has opened my eyes to different possibilities. To my co-supervisor, Professor Hanspeter Frei, your constructive, insightful comments and guidance has transformed my thesis into a stronger document. I am sincerely grateful to you both for all you have done.

Coming to a new university and department was a bit of a learning curve. Those who helped me grow were my fellow graduate students. A special thank you to Scott Dutrisac and Anton Lebar for dealing with my persistent questions about Matlab, for providing insight into solving many problems, and for helping me become a better engineering student. I want to give a mini shout-out to Stéphane Magnan for the encouragement you gave in the form of puns and Lord of the Rings memes. To all the current grad students in the Impact Research Lab (Sheng, Jennifer, Hannah, Andrew, Rafaella, and Feng), thank you for your constructive comments in group meetings, and for being friends, not just research colleagues. I would like to give a special thank you to Christian Comtois-Arnaldo. Thank you for being a good neighbour when I moved here, for being a voice of

reason when I needed it, a shoulder to lean on, for sharing in my triumphs, and so much more. This time in my life would not have been the same without you.

My masters would not have been complete without hands-on work. Thank you to Alex Proctor and Kevin Sangster from the machine shop for teaching me how to make my designs a reality. Your patience with me, especially after all the drop-ins swearing "it's only just holes!", has not gone unnoticed and our talks will be missed. I would also like to thank Steve Truttman and Stephan Biljan for their guidance on various technical aspects of research and for the good conversations.

A few more people should also be thanked. Without the help of our undergraduate summer research assistants, Paige Stufko and Cody York, I would probably still be doing data processing. Thank you to Mackenzie Brannen for redesigning a new, sanitary brain slicing matrix. Furthermore, I would like to thank Professor Matthew Holahan and Brendan Hoffe from the Department of Neuroscience for the dimension their research added to the viable *ex vivo* porcine brain tissue study.

To everyone in Ottawa, you made this city feel like a home. To my friends back home and abroad, thank you for being supportive, for checking in, and although we were apart, I knew you were with me in spirit.

To Mama, Dad, and Sarah, I know this time away from home has been quite an adjustment and it was not always easy. Thank you for always being a phone call away when I needed someone to talk to and for those 6-hour car rides to see me "just because." Thank you for also putting Ruby on the phone so we could talk our parrot nonsense. I am so incredibly lucky to have such wonderful parents and a sister who believe in me no matter what. Kocham was najbardziej.

Lastly, this research received financial support from the Department of the Army, U.S. Army Research Office under contract WP911F-17-2-0222.

In the wise words of a famous hobbit, "I think I'm... quite ready for another adventure" [*The Lord of the Rings: The Return of the King*, 2003].

Table of Contents

Abstract	iv
Acknowledgments	v
Table of Contents	vii
List of Tables	x
List of Figures	xiii
Nomenclature	xxxvi
1 Introduction	1
1.1 Motivation	1
1.2 Objectives	2
1.3 Focus of the Present Study	3
2 Traumatic Brain Injuries and Models	4
2.1 Basic Neuroanatomy	4
2.1.1 The Brain	4
2.2 Brain Injuries	6
2.3 Brain Injury Models	11
2.3.1 Specimen models	11

2.3.2	Surrogate models	21
2.3.3	Computational models	22
3	Forms of Particle Analysis	26
3.1	Digital Image Correlation	26
3.1.1	X-ray Digital Image Correlation	34
3.2	Particle Tracking	35
4	Experimental Methods	40
4.1	Design and Specimen Preparation	40
4.1.1	Brain Tissue Surrogates	45
4.1.2	Porcine Brain Tissue Preparation	50
4.2	Injury-Inducing Impact Scenarios	56
4.3	Image Processing and Analysis	61
4.3.1	Digital Image Correlation	62
4.3.2	Particle Tracking	67
5	Results and Discussion	75
5.1	Brain Gyrfication Study	75
5.1.1	Digital Image Correlation Analysis	75
5.1.2	Particle Tracking Analysis	88
5.1.3	A Direct Comparison between Digital Image Correlation and Particle Tracking Data	111
5.1.4	Discussion	117
5.2	Preliminary Viable <i>Ex Vivo</i> Porcine Brain Tissue Study	124
6	Conclusions	136
	List of References	141

Appendix A	Trials and Limitations	154
Appendix B	Standard Operating Procedure	157
B.1	Porcine Tissue Experiment	157
B.1.1	Encasement Preparation	157
B.2	Marker Preparation	158
B.3	Porcine Brain Experiment Day	158
B.4	Brain Surrogate Experiment	162
B.4.1	Surrogate Preparation	162
Appendix C	Supplementary Figures and Data	165
C.1	Analysis Parameters	166
C.2	Digital Image Correlation: Main Orientation Figures and Additional Data	167
C.3	Particle Tracking: Brain Gyrification Facing Downward	178
C.4	Particle Tracking: Brain Gyrification Facing Upward	179
C.5	Particle Tracking: Brain Gyrification Facing Inward	181
C.6	Particle Tracking: Supplementary Orientations	182

List of Tables

1	The average strain values per marker pairing obtained when the smooth surrogate was at rest on the anvil in the downward orientation. Values in brackets represent the standard deviation.	73
2	The average strain values per marker pairing obtained when the complex surrogate was at rest on the anvil in the downward orientation. Values in brackets represent the standard deviation.	74
3	Averaged strain data between Markers 6 and 7 for both surrogates in all orientations analysed with DIC. Markers 6 and 7 are found near the vicinity of the sulcus and at the peak of the gyrus, respectively. Instantaneous maximum strain values were only considered during the first 20 ms of the impact event and may not have occurred concurrently.	86
4	Averaged strain data between Markers 1 and 6 for both surrogates in all orientations analysed with DIC. Markers 1 and 6 are found within the internal capsule and near the vicinity of the sulcus, respectively. Instantaneous maximum strain values were only considered during the first 20 ms of the impact event and may not have occurred concurrently.	87
C.1	Parameters used for the DIC analysis	166

C.2	Parameters and main values used for the Mosaic analysis of the surrogates and <i>ex vivo</i> porcine brain.	166
C.3	Averaged peak volumetric strain between Markers 1 and 6 for both surrogates in all orientations analysed with DIC. As a note, strain values were only considered during the first 20 ms of the impact event.	176
C.4	Averaged peak volumetric strain between Markers 6 and 7 for both surrogates in all orientations analysed with DIC. As a note, strain values were only considered during the first 20 ms of the impact event.	177
C.5	Average peak compressive and tensile strains for each marker pair obtained from three trials at each height for the smooth surrogate when dropped in the downward orientation. Values in brackets represent the standard deviation.	202
C.6	Average peak compressive and tensile strains for each marker pair obtained from three trials at each height for the complex surrogate when dropped in the downward orientation. Values in brackets represent the standard deviation.	203
C.7	Average peak compressive and tensile strains for each marker pair obtained from three trials at each height for the smooth surrogate when dropped in the upward orientation. Values in brackets represent the standard deviation.	204
C.8	Average peak compressive and tensile strains for each marker pair obtained from three trials at each height for the complex surrogate when dropped in the upward orientation. Values in brackets represent the standard deviation.	205

C.9 Averaged peak tensile and compressive strains within the porcine brains measured in regions surrounding the highlighted Markers in each figure in Chapter 5.2. Values in brackets represent the standard deviation. 210

List of Figures

1	Coronal section of a porcine brain.	5
2	The labelled components of a neuron; image licensed under CC BY-SA 3.0.	6
3	DTI scans of a (a) healthy individual and (b) an individual who has a mild TBI. Water diffusion differences are visibly noticeable.	9
4	A depiction of an axon undergoing degradation. After injury, the axon can undergo misalignment (a), which then can lead the axon to swell until it forms an axonal bulb (b). This leads to total axonal disconnection and degradation.	10
5	Reduction in neurite distribution across select neurite orientation after samples were loaded with 0.50 strain at 30s^{-1} strain rate in comparison to sham cultures.	13
6	A smooth cerebral cortex is found in rodent brains.	14
7	Strain fields in the (A) x-direction, (B) y-direction and (C) shear obtained at 2.5ms during testing where the injury scenario occurred from the left side of the specimens. Strain values tended to be greater around the surface of the samples	15
8	Gyrification of the cerebral cortex is found in porcine brains.	17

9	<p>A displacement field superimposed on the porcine tissue section. Increasing displacement values occurred near the surface of the cortex when compared to more central regions within the specimen. The authors indicate that H represented regions of minimal to no tissue displacements.</p>	19
10	<p>A headform filled with a brain simulant with a cavity for the biological specimen.</p>	21
11	<p>Stress map from specimens (a) lacking brain gyrification and (b)-(d) having varying degrees of brain gyrification. High stress concentrations were found at the depths of the valleys in the more complex models. Images reorganized, which are licensed under CC BY-NC 2.0.</p>	23
12	<p>A simplified illustration of a DIC analysis with a focus on subset deformations. (a) The central point, $C(x_0, y_0)$, within the reference subset (red) is defined in the reference image. When the image deforms (b), the subset deforms as well. The new central point, $C'(x'_0, y'_0)$, and remains in the center of the subset even after deformation. The reference and deformed subsets are then matched (c), with the subset's displacement (arrow) being calculated. Figures adapted, licensed under CC by 4.0.</p>	28
13	<p>Three subsets are highlighted (circles) in a reference image (a). Under deformation (b), the subsets deform as well. The correlation coefficient locates the same set of pixels from the reference subset (c) in the deformed subset (d). The images were obtained while using Ncorr, a DIC programme.</p>	29
14	<p>A flowchart on the process of the inverse computational Gauss-Newton method.</p>	31

15	A flowchart on how a DIC programme computes strains from a sequence of images; the DIC programme used in this study was Ncorr.	34
16	An image of the specimen (a) is filtered with a convolution kernel (b). A grayscale dilation is then applied to the image (c), while providing initial estimates of the particles location; this is shown as dark spots in the center of the lightly coloured particles. The final estimates of the particle locations are provided (d).	37
17	Individual markers are highlighted on sample (a) by providing characteristic parameters into the particle tracking programme Mosaic ParticleTracker. Markers can also be selected, and their individual trajectories visualised (b).	39
18	Dimensioned images of each component created for the encasement model; all units are in mm. The base used in the brain gyrification study (a) had an ellipsoidal cavity. Both the top (left) and a translucent side view (right) are provided. The cap (b) was used in both studies to seal the specimens within the base’s cavity. The coronal shaped cavity within the base (c) was used in the preliminary <i>ex vivo</i> porcine brain tissue study. From left to right the internal shape increases corresponding to smaller, middling, and larger brain sections. The dimensions were only provided for the leftmost base as it was the only one used within the preliminary study. Note that the external dimensions provided in (a) are the same for (b) and (c), with the exception of the width being different in (b).	43
19	The final assembled encasement model has the cap (red) fitting into the base (blue). The design creates a cavity (a) where the specimen (b) will be housed.	44

20	The moulding process: (a) a containment field (blue) is made around the specimen, (b) after spraying the interior of the mould and sample with a mould release, a moulding mixture (white) is poured within the bounds of the containment field and is then left to cure, (c) once cured, the inverse mould is removed from the containment field, along with the sample.	44
21	The final assembled encasements with both the smooth (a) and complex (b) surrogates contained within the internal cavity. Material composition is the same for both surrogates.	45
22	Both surrogates were based off of an MRI scan of a coronal porcine brain section visualised with 3D slicer (a). A different <i>ex vivo</i> coronal porcine brain tissue section is provided for comparison (b). The outline (blue) of the smooth gyrification surrogate (c) followed the outline of the MRI scan, but was smoothed to represent a brain that lacked gyrification. The outline (blue) of the complex gyrification surrogate (c) followed the exact outline of the MRI scan. Both final models of the smooth (e) and complex (f) surrogates are shown. . . .	47
23	The speckle patterns incorporated into the smooth (a) and complex (b) surrogates.	48
24	The process of making a surrogate. A thin base layer of the Sylgard mixture (left) is added to the bottom of a surrogate mould. Once partially cured, the radiopaque speckle sheet is added on top of the thin Sylgard layer (middle) and additional Sylgard mixture is added to cover the radiopaque speckle sheet and fill the mould (right). The finished surrogate can be found in Figure 25b	49
25	The smooth (a) and complex (b) surrogates that were used for the study.	50

26	Once removed from the porcine head, the porcine brain is placed in the brain slicing matrix (a). Five blades were used to section the porcine brain into four sections (b), starting from 3 cm from the front (the leftmost and narrowest section of brain in the image).	52
27	Four porcine brain tissue sections cut using the brain slicing matrix; two sections were for control and two were used as treatment tissues. The image was taken after marker insertion while the sections were acclimating in the incubation unit.	53
28	A marker insertion system (a) was created to insert individual radiopaque markers into porcine brain tissue. The individual components are as follows: the cannula, with the acrylic guide, were used to create and place individual markers into the tissue and a plunger was used to push the markers into the tissue. The marker insertion system would produce a marker (b) with dimensions of approximately (1.27 x 1.25) mm.	54
29	A steel melting disc, with an internal depth of 1.25 mm was used to melt the radiopaque mixture. The internal depth also set the length of the markers placed into the porcine brain. Shown are the disc without (a) and with (b) the radiopaque marker mixture.	54
30	(a) Markers were placed into the porcine brain tissue with the marker insertion system. The image shown is of the initial system which did not have an acrylic guide, nor was the tissue on an ice pack; these were implemented to the procedure afterwards. (b) A coronal porcine brain tissue section after marker insertion.	55
31	The drop assembly used in all surrogate and porcine experiments. . .	57

32	A side view of the encasement sandwiched between two acrylic plates. The colours shown in the diagram may not be representative of the objects in real life.	58
33	Orientations of the smooth (left) and complex (right) surrogates with brain gyrification facing (a) downward, (b) upward, and (c) inward.	60
34	X-ray images of the orientations of the smooth (left) and complex (right) surrogates with gyrification facing (a) downward, (b) upward, and (c) inward.	60
35	Smooth (a) and complex (b) surrogates with highlighted markers (blue) with the rectangular ROI (red) used to calculate strain within a region.	66
36	Smooth (a) and complex (b) surrogates with individual markers of interest circled and enumerated.	70
37	The averaged strain response superimposed on the individual trials used to create the average between Markers 1 and 6 of (a) the smooth and (b) the complex surrogates. The strain data is from a 90 cm drop with the surrogates being dropped in the downward orientation. The averaged and median strain history follow near identical paths.	72
38	Strain fields from the smooth surrogate when dropped in the downward orientation from 50 cm from one trial. Each image corresponds to a specific strain field occurring at 4 ms after initial contact with the impact plate: a) ϵ_{xx} , b) ϵ_{yy} , and c) ϵ_{xy}	76
39	Strain fields from the complex surrogate when dropped in the downward orientation from 50 cm from one trial. Each image corresponds to a specific strain field occurring at 4 ms after initial contact with the impact plate: a) ϵ_{xx} , b) ϵ_{yy} , and c) ϵ_{xy}	77

40	A sequence of strain fields denoting ϵ_{yy} strains experienced by the smooth surrogate when dropped in the downward orientation from 50 cm from one trial. The sequence includes frames before contact and initial contact with the anvil. The times labelled correspond to time after initial contact with the anvil.	79
41	A sequence of strain fields denoting ϵ_{yy} strains experienced by the complex surrogate when dropped in the downward orientation from 50 cm from one trial. The sequence includes frames before contact and initial contact with the anvil. The times labelled correspond to time after initial contact with the anvil.	79
42	A sequence of strain fields denoting ϵ_{xx} strains experienced by the smooth surrogate when dropped in the upward orientation from 50 cm from one trial. The sequence includes frames before contact and initial contact with the anvil. The times labelled correspond to time after initial contact with the anvil.	80
43	A sequence of strain fields denoting ϵ_{xx} strains experienced by the complex surrogate when dropped in the upward orientation from 50 cm from one trial. The sequence includes frames before contact and initial contact with the anvil. The times labelled correspond to time after initial contact with the anvil.	80
44	A sequence of strain fields denoting ϵ_{xy} strains experienced by the smooth surrogate when dropped in the inward orientation from 50 cm from one trial. The sequence includes frames before contact and initial contact with the anvil. The times labelled correspond to time after initial contact with the anvil.	81

45	A sequence of strain fields denoting ϵ_{xy} strains experienced by the complex surrogate when dropped in the inward orientation from 50 cm from one trial. The sequence includes frames before contact and initial contact with the anvil. The times labelled correspond to time after initial contact with the anvil.	82
46	Sample data from one trial of the complex surrogate being dropped from 50 cm in the downward orientation. The (a) trajectory path of Marker 7, (b) the x- versus y- displacement, (c) the x-displacement versus time, and (d) the y-displacement versus time. Note that scales may vary across all figures.	89
47	Strain responses between Markers 1 and 2 of the smooth surrogate (a) and the complex surrogate (b) being dropped in the downward orientation. All four averaged responses from different drop heights are shown.	91
48	Strain responses between Markers 1 and 2 of the smooth surrogate (a) and the complex surrogate (b) being dropped in the upward orientation. All four averaged responses from different drop heights are shown.	91
49	The averaged strain response between Markers 1 and 2 of the smooth surrogate (a) and the complex surrogate (b) being dropped in the inward orientation at 50 cm.	92
50	Strain responses between Markers 1 and 3 of the smooth surrogate (a) and the complex surrogate (b) being dropped in the downward orientation. All four averaged responses from different drop heights are shown.	94

51	Strain responses between Markers 1 and 3 of the smooth surrogate (a) and the complex surrogate (b) being dropped in the upward orientation. All four averaged responses from different drop heights are shown.	95
52	The averaged strain responses between Markers 1 and 3 of the smooth surrogate (a) and the complex surrogate (b) being dropped in the inward orientation at 50 cm.	96
53	Strain responses between Markers 1 and 6 of the smooth surrogate (a) and the complex surrogate (b) being dropped in the downward orientation. All four averaged responses from different drop heights are shown.	97
54	Strain responses between Markers 1 and 6 of the smooth surrogate (a) and the complex surrogate (b) being dropped in the upward orientation. All four averaged responses from different drop heights are shown.	98
55	The averaged strain responses between Markers 1 and 6 of the smooth surrogate (a) and the complex surrogate (b) being dropped in the inward orientation at 50 cm.	99
56	Strain responses between Markers 1 and 7 of the smooth surrogate (a) and the complex surrogate (b) being dropped in the downward orientation. All four averaged responses from different drop heights are shown.	101
57	Strain responses between Markers 1 and 7 of the smooth surrogate (a) and the complex surrogate (b) being dropped in the upward orientation. All four averaged responses from different drop heights are shown.	102

58 The averaged strain responses between Markers 1 and 7 of the smooth surrogate (a) and the complex surrogate (b) being dropped in the inward orientation at 50 cm. The x- vs y- displacements of Markers 1 and 7 are shown for both the smooth surrogate (c) and the complex surrogate (d) for one trial. The start point is at the origin. 104

59 Strain responses between Markers 6 and 7 of the smooth surrogate (a) and the complex surrogate (b) being dropped in the downward orientation. All four averaged responses from different drop heights are shown. 107

60 Strain responses between Markers 6 and 7 of the smooth surrogate (a) and the complex surrogate (b) being dropped in the upward orientation. All four averaged responses from different drop heights are shown. The x- vs y- displacements of Markers 6 and 7 are shown for both the smooth surrogate (c) and the complex surrogate (d) at one trial with a drop height of 90 cm. The start point is at the origin. 108

61 The averaged strain responses between Markers 6 and 7 of the smooth surrogate (a) and the complex surrogate (b) being dropped in the inward orientation at 50 cm. 110

62 The relative x- vs y- displacement plots obtained through DIC and particle tracking for Marker 2 for a) the smooth surrogate dropped in the downward orientation at 90 cm and b) the complex surrogate dropped in the inward orientation at 50 cm. Each plot was obtained from the median trial. 112

63	The relative x- vs y- displacement plots obtained through DIC and particle tracking for Marker 7 for a) the smooth surrogate dropped in the inward orientation at 50 cm and b) the complex surrogate dropped in the upward orientation at 90 cm. Each plot was obtained from the median trial.	113
64	A comparison between DIC and particle tracking strain results for marker pairing 1 and 2 for the a) smooth and b) complex surrogates when dropped in the upward orientation (median trial, height of 90 cm).	114
65	A comparison between DIC and particle tracking strain results for marker pairing 1 and 6 for the a) smooth and b) complex surrogates when dropped in the inward orientation (median trial, height of 50 cm).	115
66	A comparison between DIC and particle tracking strain results for marker pairing 1 and 7 for the a) smooth and b) complex surrogates when dropped in the downward orientation (median trial, height of 90 cm)	116
67	A comparison between DIC and particle tracking strain results for marker pairing 6 and 7 for the a) smooth and b) complex surrogates when dropped in the upward orientation (median trial, height of 90 cm).	116
68	One set of porcine brain sections taken from a) May 16, 2019 and b) June 6, 2019.	128

69	Strain data (a) from the marker pairing indicated in the left gyrus (b) of the porcine brain obtained on May 16, 2019. This specimen was in the encasement to the left of the drop apparatus. The image to the right is an overlay of the X-ray image with markers and an optical image of the tissue.	132
70	Strain data (a) from the marker pairing indicated in the right gyrus (b) of the porcine brain obtained on May 16, 2019. This specimen was in the encasement to the left of the drop apparatus. The image to the right is an overlay of the X-ray image with markers and an optical image of the tissue.	132
71	Strain data (a) from the marker pairing indicated in the left gyrus (b) of the porcine brain obtained on May 16, 2019. This specimen was in the encasement to the right of the drop apparatus. The image to the right is an overlay of the X-ray image with markers and an optical image of the tissue.	133
72	Strain data (a) from the marker pairing indicated in the right gyrus (b) of the porcine brain obtained on May 16, 2019. This specimen was in the encasement to the right of the drop apparatus. The image to the right is an overlay of the X-ray image with markers and an optical image of the tissue.	133
73	Strain data (a) from the marker pairing indicated in the left gyrus (b) of the porcine brain obtained on June 6, 2019. This specimen was in the encasement to the left of the drop apparatus. The image to the right is an overlay of the X-ray image with markers and an optical image of the tissue.	134

74	Strain data (a) from the marker pairing indicated in the right gyrus (b) of the porcine brain obtained on June 6, 2019. This specimen was in the encasement to the left of the drop apparatus. The image to the right is an overlay of the X-ray image with markers and an optical image of the tissue.	134
75	Strain data (a) from the marker pairing indicated in the left gyrus (b) of the porcine brain obtained on June 6, 2019. This specimen was in the encasement to the right of the drop apparatus. The image to the right is an overlay of the X-ray image with markers and an optical image of the tissue.	135
76	Strain data (a) from the marker pairing indicated in the right gyrus (b) of the porcine brain obtained on June 6, 2019. This specimen was in the encasement to the right of the drop apparatus. The image to the right is an overlay of the X-ray image with markers and an optical image of the tissue.	135
C.1	A sequence of strain fields denoting ϵ_{xx} strains experienced by the smooth surrogate when dropped in the downward orientation from 50 cm from one trial. The sequence includes frames before contact and initial contact with the anvil. The times labelled correspond to time after initial contact with the anvil.	167
C.2	A sequence of strain fields denoting ϵ_{xx} strains experienced by the complex surrogate when dropped in the downward orientation from 50 cm from one trial. The sequence includes frames before contact and initial contact with the anvil. The times labelled correspond to time after initial contact with the anvil.	168

C.3 A sequence of strain fields denoting ϵ_{xy} strains experienced by the smooth surrogate when dropped in the downward orientation from 50 cm from one trial. The sequence includes frames before contact and initial contact with the anvil. The times labelled correspond to time after initial contact with the anvil. 168

C.4 A sequence of strain fields denoting ϵ_{xy} strains experienced by the complex surrogate when dropped in the downward orientation from 50 cm from one trial. The sequence includes frames before contact and initial contact with the anvil. The times labelled correspond to time after initial contact with the anvil. 169

C.5 A sequence of strain fields denoting ϵ_{xy} strains experienced by the smooth surrogate when dropped in the upward orientation from 50 cm from one trial. The sequence includes frames before contact and initial contact with the anvil. The times labelled correspond to time after initial contact with the anvil. 169

C.6 A sequence of strain fields denoting ϵ_{xy} strains experienced by the complex surrogate when dropped in the upward orientation from 50 cm from one trial. The sequence includes frames before contact and initial contact with the anvil. The times labelled correspond to time after initial contact with the anvil. 170

C.7 A sequence of strain fields denoting ϵ_{yy} strains experienced by the smooth surrogate when dropped in the upward orientation from 50 cm from one trial. The sequence includes frames before contact and initial contact with the anvil. The times labelled correspond to time after initial contact with the anvil. 170

C.8 A sequence of strain fields denoting ϵ_{yy} strains experienced by the complex surrogate when dropped in the upward orientation from 50 cm from one trial. The sequence includes frames before contact and initial contact with the anvil. The times labelled correspond to time after initial contact with the anvil. 171

C.9 A sequence of strain fields denoting ϵ_{xx} strains experienced by the smooth surrogate when dropped in the inward orientation from 50 cm from one trial. The sequence includes frames before contact and initial contact with the anvil. The times labelled correspond to time after initial contact with the anvil. 172

C.10 A sequence of strain fields denoting ϵ_{xx} strains experienced by the complex surrogate when dropped in the inward orientation from 50 cm from one trial. The sequence includes frames before contact and initial contact with the anvil. The times labelled correspond to time after initial contact with the anvil. 173

C.11 A sequence of strain fields denoting ϵ_{yy} strains experienced by the smooth surrogate when dropped in the inward orientation from 50 cm from one trial. The sequence includes frames before contact and initial contact with the anvil. The times labelled correspond to time after initial contact with the anvil. 174

C.12 A sequence of strain fields denoting ϵ_{yy} strains experienced by the complex surrogate when dropped in the inward orientation from 50 cm from one trial. The sequence includes frames before contact and initial contact with the anvil. The times labelled correspond to time after initial contact with the anvil. 175

C.13 Strain responses between Markers 1 and 4 of the smooth surrogate (a) and the complex surrogate (b) being dropped in the downward orientation. All four averaged responses from different drop heights are shown.	178
C.14 Strain responses between Markers 1 and 5 of the smooth surrogate (a) and the complex surrogate (b) being dropped in the downward orientation. All four averaged responses from different drop heights are shown.	178
C.15 Strain responses between Markers 4 and 5 of the smooth surrogate (a) and the complex surrogate (b) being dropped in the downward orientation. All four averaged responses from different drop heights are shown.	179
C.16 Strain responses between Markers 1 and 4 of the smooth surrogate (a) and the complex surrogate (b) being dropped in the upward orientation. All four averaged responses from different drop heights are shown.	179
C.17 Strain responses between Markers 1 and 5 of the smooth surrogate (a) and the complex surrogate (b) being dropped in the upward orientation. All four averaged responses from different drop heights are shown.	180
C.18 Strain responses between Markers 4 and 5 of the smooth surrogate (a) and the complex surrogate (b) being dropped in the upward orientation. All four averaged responses from different drop heights are shown.	180
C.19 The averaged strain responses between Markers 1 and 4 of the smooth surrogate (a) and the complex surrogate (b) being dropped in the inward orientation at 50 cm.	181

C.20	The averaged strain responses between markers 1 and 5 of the smooth surrogate (a) and the complex surrogate (b) being dropped in the inward orientation at 50 cm.	181
C.21	The averaged strain responses between Markers 4 and 5 of the smooth surrogate (a) and the complex surrogate (b) being dropped in the inward orientation at 50 cm.	182
C.22	Orientations of the surrogates with the surrogates (a) facing outwards, (b) in swapped positions, (c) with a 5° tilt inwards, and (d) with a 5° tilt outwards. In subfigures (a), (c), and (d) the smooth surrogate is to the left and the complex surrogate is to the right. . . .	183
C.23	The averaged strain responses between Markers 1 and 2 of the smooth surrogate (a) and the complex surrogate (b) being dropped in the outward orientation at 50 cm.	184
C.24	The averaged strain responses between Markers 1 and 3 of the smooth surrogate (a) and the complex surrogate (b) being dropped in the outward orientation at 50 cm.	184
C.25	The averaged strain responses between Markers 1 and 4 of the smooth surrogate (a) and the complex surrogate (b) being dropped in the outward orientation at 50 cm.	185
C.26	The averaged strain responses between Markers 1 and 5 of the smooth surrogate (a) and the complex surrogate (b) being dropped in the outward orientation at 50 cm.	185
C.27	The averaged strain responses between Markers 1 and 6 of the smooth surrogate (a) and the complex surrogate (b) being dropped in the outward orientation at 50 cm.	186

C.28	The averaged strain responses between Markers 1 and 7 of the smooth surrogate (a) and the complex surrogate (b) being dropped in the outward orientation at 50 cm.	186
C.29	The averaged strain responses between Markers 4 and 5 of the smooth surrogate (a) and the complex surrogate (b) being dropped in the outward orientation at 50 cm.	187
C.30	The averaged strain responses between Markers 6 and 7 of the smooth surrogate (a) and the complex surrogate (b) being dropped in the outward orientation at 50 cm.	187
C.31	The averaged strain responses between Markers 1 and 2 of the smooth surrogate (a) and the complex surrogate (b) being dropped in the inward orientation, but in swapped positions at 50 cm.	188
C.32	The averaged strain responses between Markers 1 and 3 of the smooth surrogate (a) and the complex surrogate (b) being dropped in the inward orientation, but in swapped positions at 50 cm. Note, the complex surrogate had a jitter correction applied to the raw data.	188
C.33	The averaged strain responses between Markers 1 and 4 of the smooth surrogate (a) and the complex surrogate (b) being dropped in the inward orientation, but in swapped positions at 50 cm.	189
C.34	The averaged strain responses between Markers 1 and 5 of the smooth surrogate (a) and the complex surrogate (b) being dropped in the inward orientation, but in swapped positions at 50 cm.	189
C.35	The averaged strain responses between Markers 1 and 6 of the smooth surrogate (a) and the complex surrogate (b) being dropped in the inward orientation, but in swapped positions at 50 cm.	190

C.36	The averaged strain responses between Markers 1 and 7 of the smooth surrogate (a) and the complex surrogate (b) being dropped in the inward orientation, but in swapped positions at 50 cm.	190
C.37	The averaged strain responses between Markers 4 and 5 of the smooth surrogate (a) and the complex surrogate (b) being dropped in the inward orientation, but in swapped positions at 50 cm.	191
C.38	The averaged strain responses between Markers 6 and 7 of the smooth surrogate (a) and the complex surrogate (b) being dropped in the inward orientation, but in swapped positions at 50 cm.	191
C.39	The averaged strain responses between Markers 1 and 2 of the smooth surrogate (a) and the complex surrogate (b) being dropped in the inward orientation with a 5° inwards towards from the center at 50 cm.	192
C.40	The averaged strain responses between Markers 1 and 3 of the smooth surrogate (a) and the complex surrogate (b) being dropped in the inward orientation with a 5° inwards towards from the center at 50 cm.	192
C.41	The averaged strain responses between Markers 1 and 4 of the smooth surrogate (a) and the complex surrogate (b) being dropped in the inward orientation with a 5° tilt inwards towards the center at 50 cm.	193
C.42	The averaged strain responses between Markers 1 and 5 of the smooth surrogate (a) and the complex surrogate (b) being dropped in the inward orientation with a 5° tilt inwards towards the center at 50 cm.	193

C.43 The averaged strain responses between Markers 1 and 6 of the smooth surrogate (a) and the complex surrogate (b) being dropped in the inward orientation with a 5° inwards towards from the center at 50 cm. 194

C.44 The averaged strain responses between Markers 1 and 7 of the smooth surrogate (a) and the complex surrogate (b) being dropped in the inward orientation with a 5° tilt inwards towards the center at 50 cm. 194

C.45 The averaged strain responses between Markers 4 and 5 of the smooth surrogate (a) and the complex surrogate (b) being dropped in the inward orientation with a 5° tilt inwards towards the center at 50 cm. 195

C.46 The averaged strain responses between Markers 6 and 7 of the smooth surrogate (a) and the complex surrogate (b) being dropped in the inward orientation with a 5° tilt inwards towards the center at 50 cm. 195

C.47 The averaged strain responses between Markers 1 and 2 of the smooth surrogate (a) and the complex surrogate (b) being dropped in the inward orientation with a 5° tilt outward from the center at 50 cm. 196

C.48 The averaged strain responses between Markers 1 and 3 of the smooth surrogate (a) and the complex surrogate (b) being dropped in the inward orientation with a 5° tilt outward from the center at 50 cm. 196

C.49	The averaged strain responses between Markers 1 and 4 of the smooth surrogate (a) and the complex surrogate (b) being dropped in the inward orientation with a 5° tilt outward from the center at 50 cm.	197
C.50	The averaged strain responses between Markers 1 and 5 of the smooth surrogate (a) and the complex surrogate (b) being dropped in the inward orientation with a 5° tilt outward from the center at 50 cm.	197
C.51	The averaged strain responses between Markers 1 and 6 of the smooth surrogate (a) and the complex surrogate (b) being dropped in the inward orientation with a 5° tilt outward from the center at 50 cm.	198
C.52	The averaged strain responses between Markers 1 and 7 of the smooth surrogate (a) and the complex surrogate (b) being dropped in the inward orientation with a 5° tilt outward from the center at 50 cm.	198
C.53	The averaged strain responses between Markers 4 and 5 of the smooth surrogate (a) and the complex surrogate (b) being dropped in the inward orientation with a 5° tilt outward from the center at 50 cm.	199
C.54	The averaged strain responses between Markers 6 and 7 of the smooth surrogate (a) and the complex surrogate (b) being dropped in the inward orientation with a 5° tilt outward from the center at 50 cm.	199

C.55 The averaged strain response superimposed on the individual trials used to create the average between Markers 1 and 3 of the smooth sample (a) and the complex sample (b). The strain data is from a 70 cm drop with the surrogates being dropped in the upward orientation. The averaged and median strain responses follow near identical paths. 200

C.56 The averaged strain response superimposed on the individual trials used to create the average between Markers 6 and 7 of the smooth surrogate (a) and the complex surrogate (b). The strain data is from a 50 cm drop with the surrogates being dropped in the inward orientation. The averaged and median strain responses follow similar paths. 201

C.57 The relative x- vs y- displacement plots obtained through DIC and particle tracking for Marker 1 for a) the smooth surrogate dropped in the inward orientation and b) the complex surrogate dropped in the upward orientation. Each displacement plot was obtained from the median trial for that specific surrogate and orientation. 206

C.58 The relative x- vs y- displacement plots obtained through DIC and particle tracking for Marker 6 for a) the smooth surrogate dropped in the upward orientation and b) the complex surrogate dropped in the downward orientation. Each displacement plot was obtained from the median trial for that specific surrogate and orientation. . . . 207

C.59 The direct strain responses taken from the complex surrogate using Markers 6 and 7 at one trial from a height of 50 cm and dropped in the upward orientation. This was from the same trial as the displacement plots in Figure 60d. The influences of sub-pixel jitter are minimal when compared to the corrected strain response that removed jitter. 208

C.60 The direct strain responses taken from the complex surrogate using Markers 1 and 6 at a height of 50 cm. The strain responses are from the same trial (2), when the surrogate was dropped in the swapped position. Both Markers 1 and 6 were corrected for jitter. The influences of sub-pixel jitter are minimal when compared to the corrected strain response, as trends and peak values remained the same. . . . 209

Nomenclature

Latin Characters

Symbol	Description	Units
$A_f^t(x, y)$	Filtered image matrix after restoration at a given time	pixel
C	Location of the subset center	pixel
C'	Location of the subset center after deformation	pixel
i	Initial value	pixel
K^w	Kernel	pixel
n	Current value	pixel
P	Location of a point	pixel
P'	Location of a point after deformation	pixel
R	Distance between two points	pixel
u	x-directional displacement component	pixel
v	y-directional displacement component	pixel
w	Particle radius	pixel

x	x- position value	pixel
x'	x- position value after deformation	pixel
y	y- position value	pixel
y'	y- position value after deformation	pixel

Greek Characters

Symbol	Description	Units
Δ	Variation	-
ϵ	Strain	unitless
η	Displacement mapping function in y-direction	length
ξ	Displacement mapping function in x-direction	length

Subscripts

Symbol	Description
0	Initial value
1	Value of first variable
2	Value of second variable
d	Direct strain
v	Volumetric strain
xx	Normal strain in the x- direction

xy Shear strain

yy Normal strain in the y - direction

List of Abbreviations

Abbreviation	Description
3D	Three Dimensional
BaSO ₄	Barium Sulphate
CT	Computed Tomography
CTE	Chronic Traumatic Encephalopathy
DAI	Diffuse Axonal Injury
DIC	Digital Image Correlation
DTI	Diffusion Tensor Imaging
FEM	Finite Element Model
HSXR	High-Speed X-ray Radiography
IC-GN	Inverse Compositional Gaussian-Newton
MRI	Magnetic Resonance Imaging
NFT	Neurofibrillary Tangle
PMHS	Post-mortem Human Surrogate
RG	Reliability Guided
ROI	Region of Interest
TBI	Traumatic Brain Injury
XDIC	X-ray Digital Image Correlation

Chapter 1

Introduction

1.1 Motivation

Brain trauma affects the lives of millions of individuals worldwide who sustain these injuries as a result of leisure activities, traffic, or occupational accidents. Traumatic brain injuries (TBIs) can have catastrophic physical, emotional, behavioural, and cognitive effects on an individual [1, 2]. Brain injuries are a result of a multitude of factors: the injury event, the motion of the brain within the skull, and the movement of the specific structures in the brain. These factors will determine deformation on the cellular level during a TBI event. Despite advances in diagnosis and treatment, the mechanisms that lead to TBIs are not well understood [3]. A better understanding of the injury mechanisms may lead to better preventative measures and, therefore, reduce injuries. It has been shown during a TBI event that there are alterations in communication pathways that may not be entirely reversible [4]. The most common damage to the axonal pathways is likely through deformation [4]. However, due to the complexity of the brain, it is difficult to link structural injury and mechanisms associated with TBIs to damage at the cellular level.

Most TBI research has focused on models that either use animals or computational models that are not accurate representations of the human brain. Fresh human cadaveric specimens are difficult to obtain and may change properties post-harvest, while human volunteers cannot be ethically subjected to injury on a TBI level. Regardless of the limitations, each model has proven beneficial for advancing TBI research, but there is still more to learn.

There are not many studies that directly investigated the effect of brain gyrification on brain tissue deformation [5,6]. Studies attempt to quantify the differences in brain sizes and degrees of brain gyrification within species and translate the results to humans. Research has shown that specific injury markers accumulate within one geometric region of the brain (the gyri) [7-9], which is typically found within brains that have an increased amount of gyrification. The degree of brain gyrification may influence the damage observed within the brain, something models that lack brain gyrification may not be sensitive enough to pick up.

In this thesis, the importance of using species with similar degrees of brain gyrification to humans in TBI research is analysed first using brain tissue surrogates. The surrogates represent both extremes of brain gyrification (smooth and complex cortices) which are found primarily in rodent and porcine specimens, respectively. The surrogates were matched in size, which allowed for a direct comparison between the extremes of brain gyrifications. This study was used to develop a methodology for measuring strain in biological specimens.

1.2 Objectives

The goal of this thesis is to investigate the influences of brain gyrification on brain deformation and to obtain preliminary data on a porcine *ex vivo* model. This thesis is divided into three parts:

1. Two brain tissue surrogates, one that lacks brain gyrification and the other that has increased cortical gyrification, will be used to determine the influence of brain gyrification on impact-induced strain measurements.
2. Develop a methodology from the brain gyrification study for measuring strain in viable *ex vivo* porcine brain tissue sections.
3. Determine the strain responses experienced by viable *ex vivo* porcine brain tissue sections under impact.

1.3 Focus of the Present Study

The present study includes the following chapters to discuss relevant literature, image analysis methods, experimental methodology, results, discussion, and conclusions:

Chapter 1: Introduction — Motivation of research and objectives.

Chapter 2: Traumatic Brain Injuries and Models — A basic overview of traumatic brain injuries and the models used in TBI research.

Chapter 3: Forms of Particle Analysis — Introduction to image analysis methods.

Chapter 4: Experimental Methods — Details regarding design, sample preparation, the experimental injury-inducing scenario, and analysis of data.

Chapter 5: Results and Discussion — Results from the brain gyrification study and the preliminary viable *ex vivo* porcine tissue study, followed by a discussion of the results.

Chapter 6: Conclusions — Concluding statements on the present study and future recommendations.

Chapter 2

Traumatic Brain Injuries and Models

When a TBI occurs, individual brain cells as well as whole brain tissue regions can be affected as a result of various loading conditions. Classification and medical imaging of TBIs can aid in understanding the outcomes of TBI, but TBI models are required to understand why this injury can be so devastating.

2.1 Basic Neuroanatomy

This chapter provides a brief overview of the relevant neuroanatomy needed to understand the mechanisms of TBI. The human body is a combination of intricate organ systems that work together to make life possible. One of the most complicated systems is the nervous system, which transmits and receives nerve impulses throughout the body [10]. The nervous system consists of the central nervous system and the peripheral nervous system. The central nervous system, consisting of the brain and spinal cord, controls body functions.

2.1.1 The Brain

The most intricate organ within the body is the brain, as it controls all bodily functions. A large amount of research is invested to understand brain function, but

due to its dynamic complexity progress is slow and it remains an active field of research.

Structure and Function

The brain is divided into three structural regions; the brainstem, the cerebellum, and the cerebrum, with the defining structural feature of the cerebrum being the left and right cerebral hemispheres [10]. The outer layer is known as the cerebral cortex, which is composed of grey matter [10]. Surrounded by grey matter are the interior layers of the brain, which is composed of white matter [10]. Within the human brain, the approximate ratio of grey to white matter is 40:60 [11] (Figure 1). Additionally, white matter is mechanically stiffer than grey matter due to the myelination of axons, a component which will be described below [12].

The cerebral hemispheres in humans and higher functioning species are highly convoluted due to gyrification. Gyrification of the brain allows for an increased volume of brain (grey and white) matter to fit into the confined space of the skull, which is made possible by sulci and gyri (see Figure 1) [13].

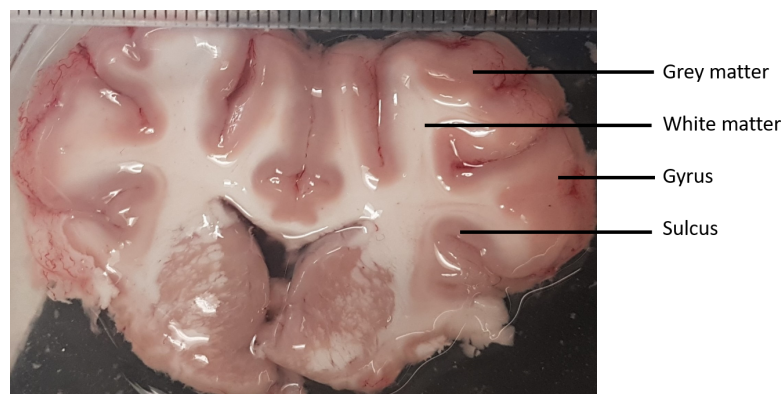


Figure 1: Coronal section of a porcine brain.

The basic unit of the nervous system is the neuron, which carries electrical impulses [10]. Dendrites obtain impulses from other neurons and pass them through

the cell body to the axon, a long slender projection, which then transmits the impulse to other neurons. The dendrites and cell body are found within grey matter. White matter contains axons, which are covered in an insulating myelin sheath (Figure 2) [10]. The normal structure and function of the neuron may change when a brain injury occurs, specifically when it comes to axons [14].

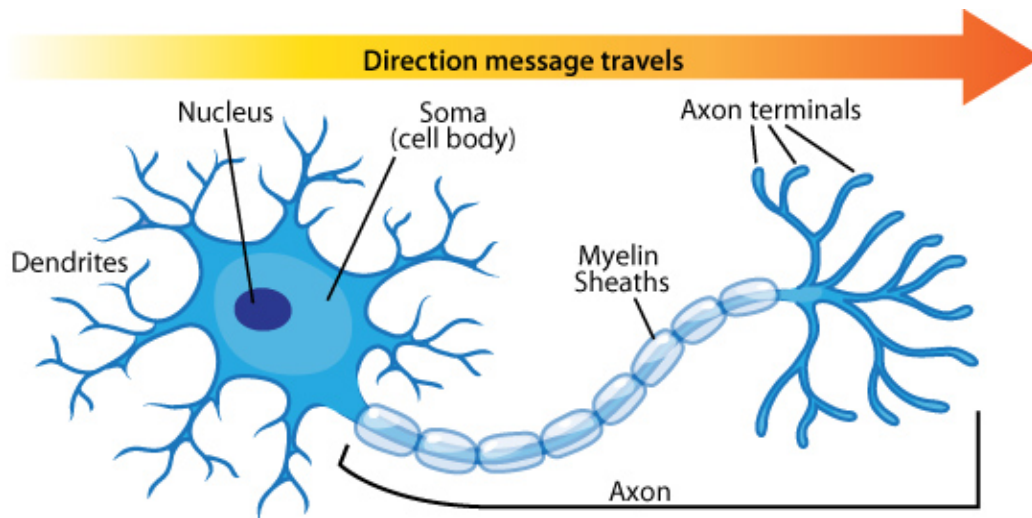


Figure 2: The labelled components of a neuron; image licensed under CC BY-SA 3.0 [15].

2.2 Brain Injuries

According to the Centers for Disease Control and Prevention [16], almost three million TBI-related emergency department visits, hospitalizations, and deaths occurred in the United States in 2014. The most prevalent mechanism for injury were falls, being struck by or against an object, and motor vehicle accidents. The highest age demographics affected by TBIs are seniors, infants, and adolescents. While there are preventative measures to reduce the chances of a TBI, they cannot eliminate all risks.

Brain injuries are not only the result of a single event, but may be due to repetitive injuries where the damage accumulates overtime [17]. Brain injuries can occur due to impact, impulse, and blast overpressure loading [18]. Impact loading occurs when an object strikes the head or vice versa [6, 19]. These injuries are usually associated with vehicular accidents and falls. Direct contact to the head and inertial effects determine the loading condition [19]. During impulse loading, the head is not directly hit, but injury occurs as a result of a bodily region being hit and the subsequent head acceleration which is typically modelled by an impulsive non-impact head rotation [20–22]. The sudden inertial changes cause the brain to move within the skull resulting in damage, i.e. a football player being tackled in the torso region by another player, resulting in head motion. Blast overpressure occurs when a high-strain rate pressure blast wave travels through the brain [23], either as the result of proximity to an explosion or repeated discharges of certain weapons in training [24].

The most prevalent clinical system used for classifying TBIs is the Glasgow Coma Scale [25]. The system uses three categories based on the patient's ability to physically open their eyes, and verbal and motor responses. Each category has numerically ranked results. High scores are associated with individuals that are conscious, can verbally respond to requests, and can perform motor functions [3, 25]. This is known as a mild TBI and is the most common form of TBI [3]. A moderate TBI occurs when individuals are not completely aware of their surroundings and respond to commands with some degree of discomfort [3]. The lowest scoring classification is severe TBI in which severe damage to structures and metabolic functions occur [3]. The individual is likely comatose or has minimal response to commands and is highly susceptible to secondary injuries. The treatment and recovery from a TBI depends on the severity of the injury and the individual [2]. Individuals may recover, but some may suffer from physical, emotional, and/or

cognitive conditions years later [1,2].

Various medical imaging modalities can be used to quantify and visualize brain injuries, alongside the use of qualitative scales to link brain injury level to clinical prognosis. Computed tomography (CT) and magnetic resonance imaging (MRI) scans are the most common imaging methods performed on individuals suspected of having a TBI [3]. However, the issues with these two modalities are that they are not sensitive enough to detect one of the most common forms of TBI, diffuse axonal injury (DAI) [26]. DAI is the microscopic damage to axons associated with swelling or detachment [14].

A different imaging technique must be used to quantify the microscopic changes that occur to axons after injury, as CT and MRI cannot observe these changes. Diffusion tensor imaging (DTI) is a form of MRI that can determine the integrity of white matter tracts by measuring the diffusion and directionality of water molecules [27]. Water diffusion within the brain is anisotropic, as it prefers to diffuse along the length of the white matter tracts [28]; this is seen in healthy individuals (Figure 3a). A healthy human brain has normal structural integrity, which includes intact white matter tracts and axons. Axonal integrity is maintained by the protein tau [8]. This protein stabilises and maintains the structural integrity of axonal microtubules, is used for axonal transport of proteins and organelles, and is required for proper signalling between and within neurons [8].

When a brain injury occurs, axonal integrity may become compromised; the first sign of DAI is misalignment of the axon (Figure 4a) [14,29]. Damage to white matter tracts can lead to disorganization. This results in reduced anisotropy and increased water diffusion, which can be observed with DTI (Figure 3b) [29]. Axons are susceptible to stretch and shear injuries because under high loading conditions they become stiff and brittle, which may be the underlining mechanism for

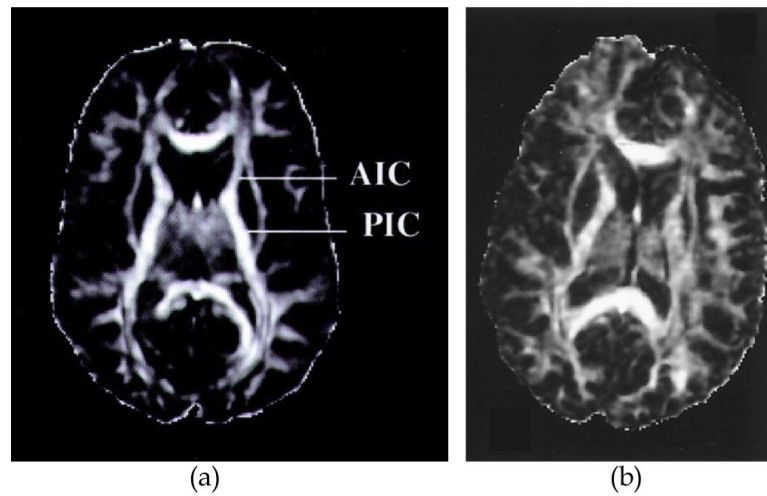


Figure 3: DTI scans of a (a) healthy individual and (b) an individual who has a mild TBI. Water diffusion differences are visibly noticeable. Images reorganized from [29].

DAI [14,27]. The purposed injury thresholds for DAI are estimated to be 5 to 10% strain or greater than 10% for shear strain [30,31]. This can result in a change in the structural integrity of the tau protein, resulting in the protein becoming highly phosphorylated (p-tau) [8]. This modification prevents the tau protein from properly binding to microtubules, causing self-aggregation of the protein. This can lead to the formation of neurofibrillary tangles (NFTs). The subsequent ionic and transport substance imbalance as a result of cellular changes within this region can lead to further axonal damage and disconnection [8,14]. This usually occurs in the form of an axonal bulb, which causes one end of an axon to disconnect, resulting in axon degeneration (Figure 4b). This form of damage can occur in multiple regions along the same axon depending on the loading condition [14].

Post-mortem analyses of brains with suspected impact-induced neurodegeneration (typically caused by repetitive impact events), known as chronic traumatic encephalopathy (CTE), have shown accumulations of insoluble deposits of NFTs

and p-tau protein positive astrocytic tangles, primarily seen around the sulcal regions of brains that have gyrification (see Figure 3 (II.) in [7]) [7–9]. The aforementioned markers target two cells. The first affects the neuron itself. The second are astrocytes, which are supporting cells for neurons [32]. The p-tau protein accumulates within these two cells, resulting in the damages described above. These cadaver brains typically have no supporting background information on loading conditions experienced by humans to cause such injury.

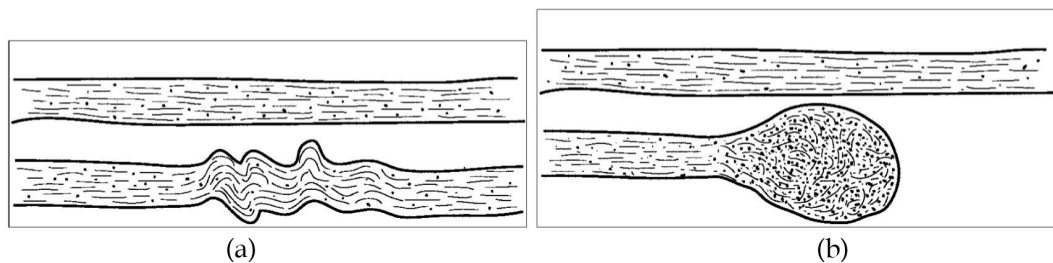


Figure 4: A depiction of an axon undergoing degradation. After injury, the axon can undergo misalignment (a), which then can lead the axon to swell until it forms an axonal bulb (b). This leads to total axonal disconnection and degradation [29].

Summary

TBI-inducing loading conditions may cause axons to stretch, which can lead to axonal degradation. Within living patients, the damage can be observed through DTI, which shows abnormalities along white matter tracts. During brain autopsies, the accumulation of damage is localised to the base of the sulcus, a feature found within brains that possess cortical gyrification.

The following section describes specific brain injury models that are used in TBI research.

2.3 Brain Injury Models

A variety of models have been used in TBI research to provide insight into the mechanics of injury. Models can range from tissue cultures [33, 34] to brain sections [35, 36] to computational simulations [5, 6]. Each model provides specific insights into TBIs, but not one singular model can provide a complete understanding.

2.3.1 Specimen models

Biological models are one of the most prevalent and valuable contributors to the understanding of TBIs. They allow researchers to study injury-inducing events and obtain measurements that could not be ethically conducted on humans. A wide variety of models have been used. The response of specific cells has been investigated and also whole and sectioned brains are used to study TBIs.

In the following subsections, these models are described and their contributions to the understanding of TBI are discussed.

In vitro specimens

Brain injury research can be studied on a cellular level by performing studies outside of the natural biological setting. This is typically done using cell cultures, which are derived from specimens by removing desired brain cells and growing them in a controlled external environment [37]. *In vitro* models are easy to maintain, with some cell cultures having a limited life span of a couple cell divisions, while other, rarer cells, such as those from tumours, can become immortal when using the proper growing medium [38]. The primary focus of these types of studies is not necessarily to determine the mechanical response of the brain and surrounding structures, but to look at how brain injury occurs at the cellular level.

With *in vitro* models, injury on a molecular and cellular level can be observed by focusing on one type of tissue or cell and determining the level of injury related to a specific loading condition [39–42]. Determining the cellular response from an injury-inducing scenario is vital in understanding TBIs. Published cell based *in vitro* studies focus on few main injury-inducing methods such as compression [43], transection (axotomy) [44], stretch (tension) [45], hydrostatic pressure [46], shear strain [33,34], and fluid shear stress [47]. These cell based *in vitro* models typically result in specific damage to one type of cell or tissue with the goal being quantification of molecular and cellular injury markers associated with specific loading conditions.

The shear strain model was used by Bottlang *et al.* [33] to cause cell death in cultured organotypic hippocampal slices from postnatal Wistar rats. To prepare the cultures and preserve the structural organization of the hippocampus (an internal C-shaped structure within the brain associated with learning and memory [48]) and nearby cortical regions were isolated and sectioned to 400 μm thicknesses. The sections were left to stabilize *in vitro* for 12 days post-collection before being placed in a loading module that was used to induce injury. Shear deformations of the specimens at various impact velocities were recorded using a high-speed camera. A stain was then used to quantify cell death. The researchers were able to link impact velocity and sample elongations to cell death, while pinpointing a threshold in which significant levels of cell death occurred.

Another similar study used the shear strain model as well, but with 3D neural cell cultures [34]. Whereas Bottlang *et al.* [33] studied specific regions for injury within cell cultures, LaPlaca *et al.* [34] investigated neuronal cells from rat pups that were cultured in a 3D matrix. In the latter study, specific strain rates of up to 30s^{-1} and strains of 0.25 or 0.50 strain were applied via a linear actuator to the surface of the cultures, which were contained within an elastomer mould. The

setup was mounted to a confocal microscope to obtain 3D images throughout the injury event. Cell death was observed after high shear strain, high strain rates were applied to the cultures. Neuronal cells were stained using fluorescent dye based indicators. Viable cells appeared green, whereas the center of dead cells appeared red. They also determined that the orientation of the cells, specifically neurites (a term given to dendrites and axons [48]), within the cultures influenced the levels of cell death, as certain angles were more detrimental than others (Figure 5). This showed that cell orientation clearly played a role in cell damage and needs to be considered in these models.

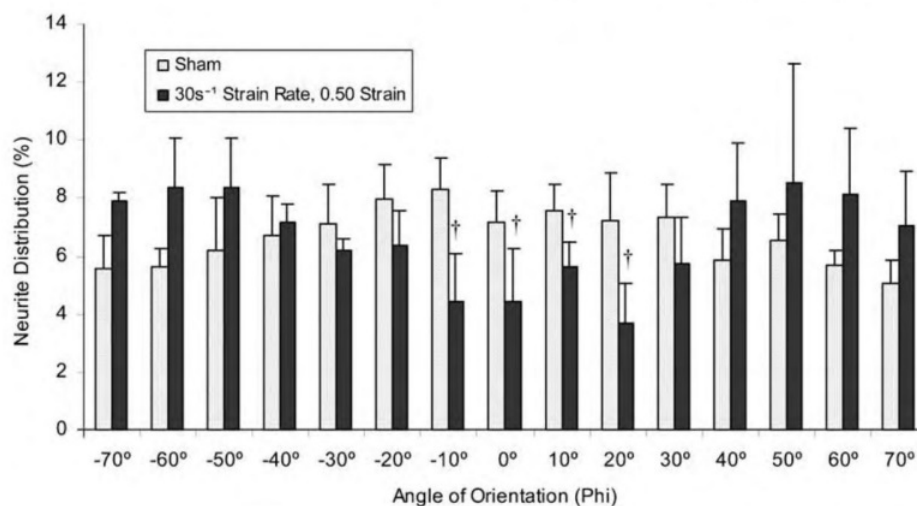


Figure 5: Reduction in neurite distribution across select neurite orientations after samples were loaded with 0.50 strain at 30s^{-1} strain rate in comparison to sham cultures [34].

The cell based models mentioned above can use staining techniques to determine cell death or other injury markers. These selective stains can highlight desired components within the specimen making them visible. While these studies can be highly specific at gaining information on the cellular level, they cannot account for the influences of surrounding structures.

Rodents

One of the most prevalent specimen models used in TBI research has been rodents. Factors such as ease of use, specimen upkeep, and accessibility make them desirable. Rodent brains have many anatomical differences when compared with human brains, as they are significantly smaller in size, lack brain gyrification (lissencephaly, see Figure 6), and have significantly less white matter than humans [11,49,50].

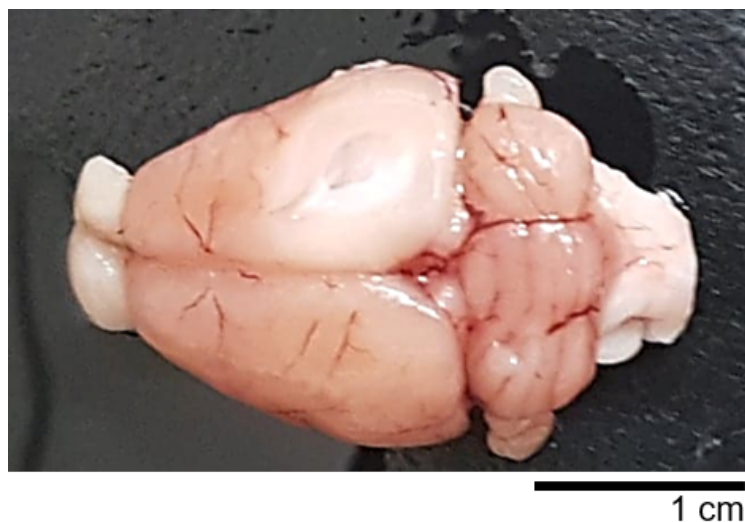


Figure 6: A smooth cerebral cortex is found in rodent brains.

In rodent models, typically three models of injury are used while the animal is usually anaesthetized. Controlled cortical impacts are applied with a pneumatic piston to induce a cortical contusion via hole in the skull [51]. In the fluid percussion model, saline is injected into the brain after a pendulum strikes a saline reservoir, inducing brain deformations [52]. In the last model, a weight is dropped onto the skull to cause injury in the weight-drop model [53]. Similar to the cell based models, injury is quantified through staining techniques, which are sensitive to injury markers or changes within the tissue.

Results from rodent models are difficult to directly relate the mechanical responses to injury found in humans. Although scaling laws can take into account brain matter composition and brain size [49,54,55], rodent brains are able to withstand greater inertial and shear loads when compared to larger brains that have gyrification [56]. Additionally, the brain gyrification found in humans may result in a more complex deformation pattern which cannot be accounted for in a rodent model.

Sarntinoranont *et al.* [35] studied TBIs using rodent brains, which were sectioned between 350-400 μm before inducing injury. High strain rates were applied to the apparatus containing the brain sections, which were embedded in gelatin. The injury event was captured with a high-speed camera and analysed with DIC to determine strain. They found greater tissue strains near the cortex and the base of the lobes, but the researchers attributed this to likely being the result of location, as these regions were closer to the wall boundaries of the apparatus (perpendicular to impact). The strain fields also showed that higher magnitudes of strain were typically found near surface features (see Figure 7). They concluded that the large strain values obtained could potentially correlate to brain injury.

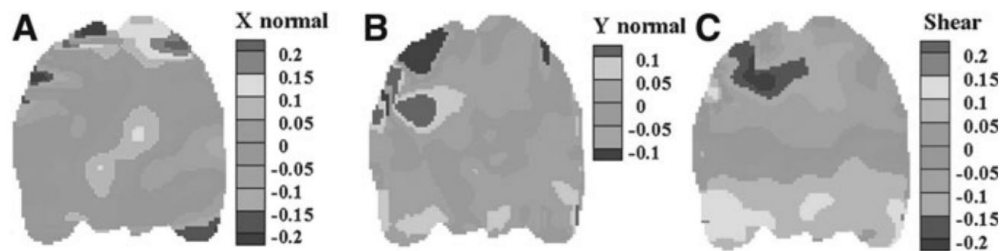


Figure 7: Strain fields in the (A) x-direction, (B) y-direction and (C) shear obtained at 2.5ms during testing [35]. Strain values tended to be greater around the surface of the samples.

The authors did acknowledge that the tissue motion was likely dependent on

the characteristics of the gelatin which the tissue was embedded in, which would influence their results. However, there were other experimental factors to consider. The increased deformation near the surface may be a result of being embedded in gelatin, but may also be a result of sample thickness and lack of brain gyrification. Samples with a sub-millimetre thickness may be more prone to injury due to their delicacy, regardless if it is embedded. A small sample thickness may also not accurately represent the specimen's brain gyrification when impacted. Thicker samples may maintain brain gyrification better, which may affect deformation and injury. As stated above, the lack of brain gyrification found in rodent brains may react to impact incidences differently than the human brain. The smooth cortical surface likely uniformly distributes strain due to the lack of geometric discontinuities.

The authors also stained the brain tissue sections with a fluorescent dye that stained for degenerating neurons within the hippocampus. An increase in neurodegeneration was observed after 4 and 6 hours incubation post-testing when compared to controls. The authors aimed to relate strain history to neurodegeneration, but were unable to do so. They attributed this shortcoming to the dye used as well as mechanical testing.

Figs

Porcine brains have many similarities to human brains. Both have complex and intricate folding patterns due to the presence of sulci and gyri, which are the valleys and peaks found on the brain, respectively (gyrencephaly, see Figure 8). Both specimen brains also have comparable white to grey matter ratios [49]. Due to the similar ratios in white and grey matter, it has been implied that porcine and human brains may experience similar responses to injury [50]. As previously stated, white matter is stiffer than grey matter, which may have implications that overall

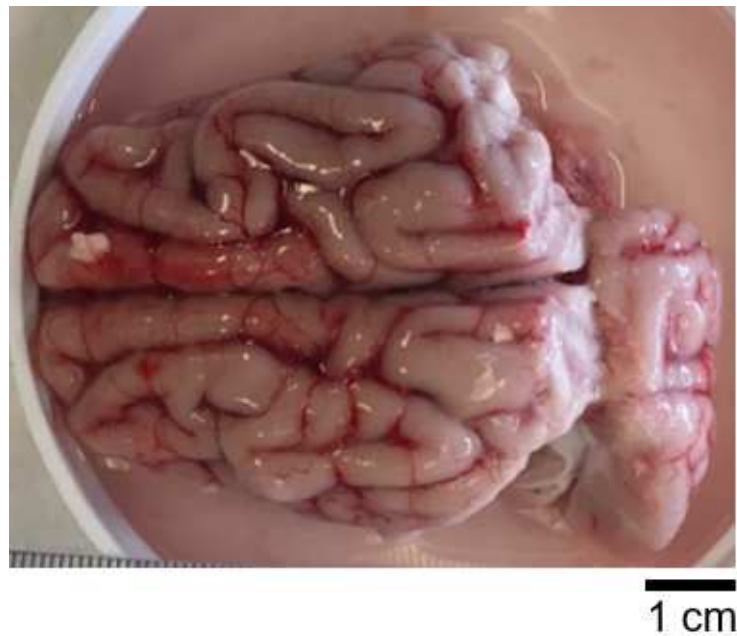


Figure 8: Gyrification of the cerebral cortex is found in porcine brains.

brain stiffness varies across species, as these ratios can vary across species. Also, it was shown that porcine brains deform like human brains and have identical neuropathologies due to TBI, particularly when undergoing rapid, rotational head movements [21]. Not only does stiffness vary between brain matter, but it has also been determined that porcine brain tissue is stiffer *in vivo* than it is *ex vivo* [57].

Many TBI studies have subjected whole pigs to TBI events [21, 58–60]. These studies have therefore maintained the interactions between the brain and the skull. Similar to cell culture and rodent studies, many porcine studies are typically used to study cellular level damage and not specifically brain tissue motion.

Raghupathi *et al.* [59] induced varying amounts of rapid axial rotations to the heads of anesthetized piglets. The brains were then sectioned in the coronal plane and stained for a neurofilament protein associated with traumatic axonal injury. The most axonal damage was observed in the regions within white matter, primarily closest to regions of geometric variations. This suggests that increased brain

gyrification may influence brain deformation and the resulting damage. The convolution of the cortex may lead to strain concentrations at the sulci, which have been quantified using computational models, which will be discussed in a later section [5,6]. These strain concentrations may correspond to axonal damages observed by Raghupathi *et al.* [59], which are common locations of accumulations of injury markers in CTE [7–9].

Using sagittal sections of porcine brains, Lauret *et al.* [36] attempted to replicate crash scenarios by subjecting the samples to acceleration/deceleration forces using an airspring. The same location within the sagittal plane was used across all porcine brains, with the sections being cut 4 mm thick. The experiments were completed within six hours post-mortem to maintain tissue integrity. A high-speed camera was used to track black enamel paint surface markers, which were airbrushed onto the tissue. The samples were contained between two transparent polycarbonate plates. A middle plate, made of polyvinylchloride, was used to create a cavity between the two exterior plates and was contoured to the sagittal shape of the brain section. Injury was introduced to the containment apparatus via an air spring. Increased deformations were observed near the cortex when compared to more central regions within the internal capsule (Figure 9).

The DIC analysis was not able to measure deformations near the boundaries of the tissue section with some regions missing from the final analysis. This issue may likely be a result of the markers used and their application method. Furthermore, sagittal sections do not clearly reveal the gyrification of the brain, and therefore it may be more appropriate to use coronal sections to investigate the effects of brain gyrification.

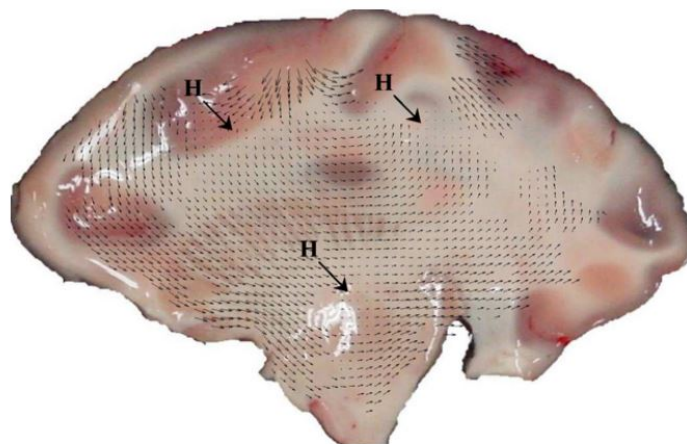


Figure 9: A displacement field superimposed on the porcine tissue section. Increasing displacement values occurred near the surface of the cortex when compared to more central regions within the specimen. The authors indicate that H represented regions of minimal to no tissue displacements [36].

Humans

Since humans cannot be ethically subjected to relevant TBI level injury events for research, some studies have analysed videos of suspected TBI events to look for common characteristics [61, 62]. These studies typically address current sporting regulations and provide suggestions on how to minimize injury in the future. Myer *et al.* [63] investigated how injury can be reduced with a compression neck collar. The collar would apply a slight pressure to jugular vein, which in turn would increase the blood volume in the brain, resulting in less motion being experienced by the brain. That study used MRI and DTI to compare pre- and post-season brain scans of football players who did and did not wear the collar. Overall, the collar did appear to have a marginally positive effect against microstructural changes within the brain.

Brain injury studies that are approved for living human participants focus on understanding the movement of the brain within the head, but not inducing injury [22, 64]. Brain displacements and relative rotation with respect to the skull

have been quantified [64]. The motions were imaged inside an MRI machine, where a frame dropped the participant's head 2 cm onto a stopper. Further investigations using non-invasive tagged MRI showed that applying mild angular accelerations to the head resulted in strain being higher in grey matter than in white matter [22].

Other studies have used post-mortem human surrogates (PMHSs), the results of which are extensively used in validating computational head injury models. Hardy *et al.* [65,66] placed brain tissue matched density markers within the brain of a PMHS to track motion under impact. The motion was captured with high-speed biplanar X-ray imaging. Under impact, the markers moved in a looping motion with peak displacements of around 5 mm [65]. While PMHS studies are the closest TBI models for living humans, the specimens suffer from rapid tissue degradation, which can change the response of the specimen [67].

In human cadaveric studies, the extent of brain injuries are determined via staining techniques; stains use chemicals to enhance the contrast of desired microscopic elements [7,68]. Axonal damage in human cadaver brain sections [7–9] share some similarities to axonal damage found in pigs [59], as injury markers were typically isolated to the sulcal regions.

Other specimen models

Other animals such as cats, dogs, rabbits, lambs, sheep, and non-human primates have been used to model TBI, but on a much smaller scale [50].

Primates were commonly used prior to the 2000s, but have not been a main model for TBI research in recent years because of ethical concerns. In the past, rhesus macaques and baboons have been subjected to impulse loading to the head to assess coma and DAI levels, the results of which may have implications towards human injury [30,31,69].

Sheep and lambs are another less common model. They have gyrencephalic brains, which makes them a comparable model to humans [50]. Lamb heads were subjected to impacts in different regions [70]. The impact and resulting skull injuries caused axonal damage with frontal impacts causing the most damage; skull fractures likely contributed to axonal damage as well.

2.3.2 Surrogate models

Brain surrogates have been extensively used to investigate TBI. The surrogate brains are typically made from gelatin or some form of biofidelic polymer [42, 71, 72]; the properties of which can sometimes be tuned to create a desired material [73]. These models, in general, do not mimic the degree of brain gyrification found in humans and are often compared to cadaveric test data for validation [74].



Figure 10: A headform filled with a brain simulant with a cavity for the biological specimen [42].

Ivarsson *et al.* [71] created a simplified skull and gelatinous brain model with incorporated markers. The impacts were repeated five times, with displacements, shear, and principal strains calculated from marker displacements located near the

front center of the brain. The markers were optically tracked using a high-speed camera. Another model incorporated biological specimens within the brain simulant to determine the biological response on the molecular level to blast overpressure (Figure 10) [42]. Other research simply used a sphere of ballistic gelatin as a head surrogate to look at qualitative damage after a ballistic injury [72].

2.3.3 Computational models

Computational models allow researchers to visualize brain injuries in a unique way. Researchers have direct control over each part, such as anatomical features and their complexity, element size, and boundary conditions [75]. The mechanical properties of the brain and skull are determined through experimental testing and are applied to computational models. Researchers can vary the types of injury methods applied and change the magnitude of forces experienced by the model. Some models may put emphasis on certain components more so than other models depending on the intended purpose. This can be done to reduce computational time, as models with increasingly complex components may take longer to solve.

Computer models allow researchers many liberties that are not possible with specimen models (a few are compared by Dixit and Liu [76]). Most FEM models lack high degrees of brain gyrification, with the brain either having a completely smooth surface or having minimal contours [77,78]. The simplicity of the cortex does not necessarily imply that the simplicity extends to internal brain composition, as many models account for various internal structures as well.

Computational models are typically validated against experimental data. Miller *et al.* [75], validated six different models against five impact orientations

from PMHS data. Even though each model was of the head/brain, each was visually unique from one another, as each model placed emphasis on different features. Each model had different numbers of elements and nodes, brain mass, and brain shearing parameters. The model that performed the best when compared to PMHS data accounted for some degree of brain gyrification. This suggests that brain gyrification is required to accurately simulate brain deformations.

Another FEM analysis focused on four models with varying degrees of geometric variations (Figure 11) [5]. The models with higher degrees of geometric features revealed increased stress values by a factor of 1.3-1.9 when compared to the model with no variations [5]. The authors concluded that a lack of brain gyrification (such as those seen in rodents) uniformly distributes stress near the surface after an impact event. However, brains with higher degrees of brain gyrification (such as those seen in pigs and humans) may have stress concentrations in the depths of the brain at the base of sulci, where stress is observed further away from the surface (Figure 11) [5].

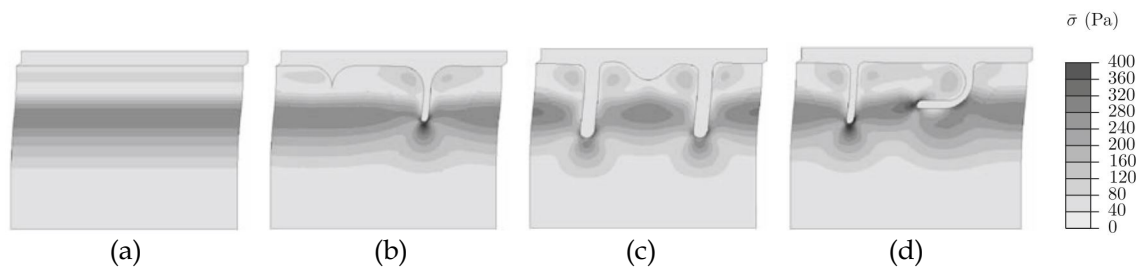


Figure 11: Stress map from specimens (a) lacking brain gyrification and (b)-(d) having varying degrees of brain gyrification. High stress concentrations were found at the depths of the valleys in the more complex models. Images are reorganized from [5], which are licensed under CC BY-NC 2.0.

The importance of geometric variations and its contributions to stress concentrations was validated on a two-dimensional level by Cloots *et al.* [5]. Others have applied similar techniques to a full head model and came to similar conclusions.

Within the Ghajari *et al.* [6] study, a highly biofidelic head model was created from an MRI scan of a healthy 34-year-old male. The model included grey and white matter, along with sulci and gyri. Three different injury scenarios were validated against the model, with all scenarios coming to the same conclusion. Higher strains were found at the depths of the sulci.

The Ghajari study also investigated the sulci by using DTI on healthy subjects and those with known TBIs. Significant changes in white matter integrity were found within the sulci of patients with TBIs. The use of computational modelling and human subjects was able to show a potential link to high strain values (and strain rate) observed in the sulci during an injury event to decreased white matter integrity in the sulci, all of which is indicative of tau pathology commonly seen in CTE.

Summary

Each model mentioned above has provided insights on a biological or mechanical level into TBI mechanisms. The difficulty with most models is the cross-species translation of the results. This has resulted in very few studies directly commenting on the importance of brain gyrification, as this is difficult to do directly using live specimens. The vast differences between the extremes of brain gyrification may lead to different injury mechanisms, which can be more easily observed if both models were on the same scale.

By comparing the results found in literature with the two extremes of brain gyrification, lissencephaly (a smooth cortex) [5, 35] and gyrencephaly (a convoluted cortex) [5, 6, 36, 59], individually it is evident that there are differences in impact-induced measurements, though these are usually obtained using different injury scenarios. These differences can be validated with robust surrogates that are

representative of the extremes of brain gyrification; unlike the Cloots *et al.* computational study, which had simplified, two-dimensional models with varying degrees of brain gyrification. The surrogates in this study can be scaled identically, have the same loading conditions applied, and be subjected to different impact orientations. This kind of comparison is not truly capable with biological specimens, as they have limited viability and would need appropriate scaling to compare the results. The results of this brain gyrification study will highlight the importance of brain gyrification within TBI research using two representative surrogates, which may affect the kind of models used in future TBI studies.

Chapter 3

Forms of Particle Analysis

Quantifying brain motion provides valuable insight into TBIs, allowing researchers to identify different brain regions under high strains. Since the brain is optically hidden, tracking brain motion is challenging. It is outside the scope of this thesis to describe the two common methods of particle analysis in detail, but they will be discussed in brief in the following sections.

3.1 Digital Image Correlation

Digital image correlation (DIC) is a displacement measuring method that analyzes full-field deformations of a specimen by identifying and tracking the motion of a subset of points created by a speckle pattern [79]. In TBI studies, high-speed cameras are used to capture random, high contrast speckle patterns that are applied to brain sections [35,36]. A brief discussion on DIC algorithms is provided below [80,81], with a flowchart showing the process of computing strains from a series of images using a DIC programme (Figure 15).

DIC algorithms require a reference image where no deformation has occurred. As the original images taken by the camera are likely to incorporate a region surrounding the specimen, a region of interest (ROI) is selected in the reference image

that focuses solely on the specimen's speckle pattern. The ROI is divided further into subsets that are used to track smaller areas. The unique patterns within the subsets allows for tracking between the reference image and the deformed images. The subset is based around a central point, $C(x_0, y_0)$, and as the specimen and thus subset deforms, the central point will remain at the center of the subset (Figure 12).

The same conditions apply for points surrounding the central point. When deformation occurs within the specimen, points that surround the central point will remain as surrounding points within the subset. A given nearby point in the reference image, $P(x_i, y_j)$, will change to $P'(x'_i, y'_j)$ under deformation (Figure 12a, b). The change in the x- and y- location of the point is described using the following equations, which includes directional displacement mapping functions, ξ and η [80,82]:

$$x'_i = x_i + \xi(x_i, y_j) \quad (1)$$

$$y'_j = y_j + \eta(x_i, y_j) \quad (2)$$

If the displacement of the given point remains the same after deformation, a zero-order displacement mapping function is applied, though this is uncommon. The first-order displacement mapping function is the most commonly used, as it takes in account translation, rotation, normal, and shear strains. These functions are used to represent the change in motion of the x- and y- coordinates that occur from the reference image to the next image in the analysis. This is defined as [80]:

$$\xi_1(x_i, y_j) = u + u_x \Delta x + u_y \Delta y \quad (3)$$

$$\eta_1(x_i, y_j) = v + v_x \Delta x + v_y \Delta y \quad (4)$$

where u and v are displacements in the x- and y- coordinates of the reference subset

center, $\Delta x = x_i - x_0$ and $\Delta y = y_j - y_0$, and (u_x, u_y, v_x, v_y) are first-order displacement gradients of the reference subset. An additional second-order displacement mapping function can be used to describe large, non-homogeneous deformations, if required.

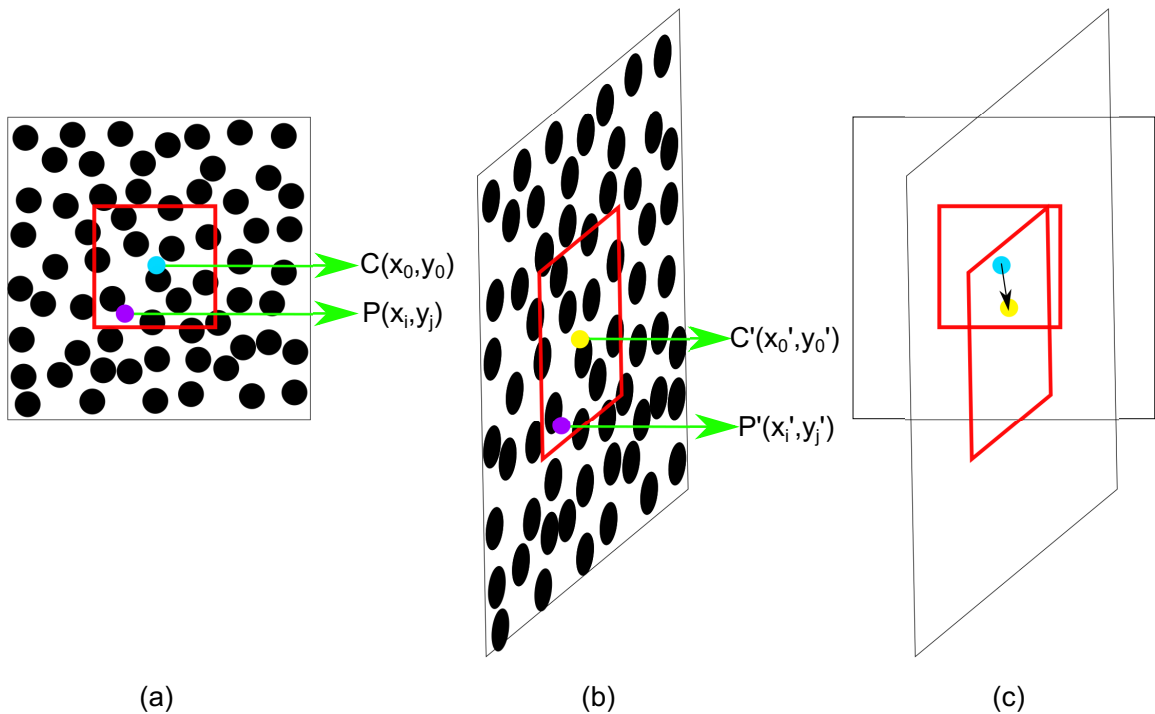


Figure 12: A simplified illustration of a DIC analysis with a focus on subset deformations. (a) The central point, $C(x_0, y_0)$, within the reference subset (red) is defined in the reference image. When the image deforms (b), the subset deforms as well. The new central point, $C'(x'_0, y'_0)$, and remains in the center of the subset even after deformation. The reference and deformed subsets are then matched (c), with the subset's displacement (arrow) being calculated. These figures were adapted from [83], which are licensed under CC BY 4.0.

The relationship between the locations of points in the reference image to where they are located in the deformed images is defined by the equations above. The degree of similarity between the reference and deformed subset is measured by correlation criteria [81]; other correlation criteria that can be used for DIC is summarized

in [80]. These criteria calculate the likelihood of grayscale intensities related to pixels in one frame being the same set of pixels in the next frame. A normalised cross correlation criterion finds the highest correlation coefficient between the reference and deformed subset. This value is the initial integer guess for displacement (Figure 13).

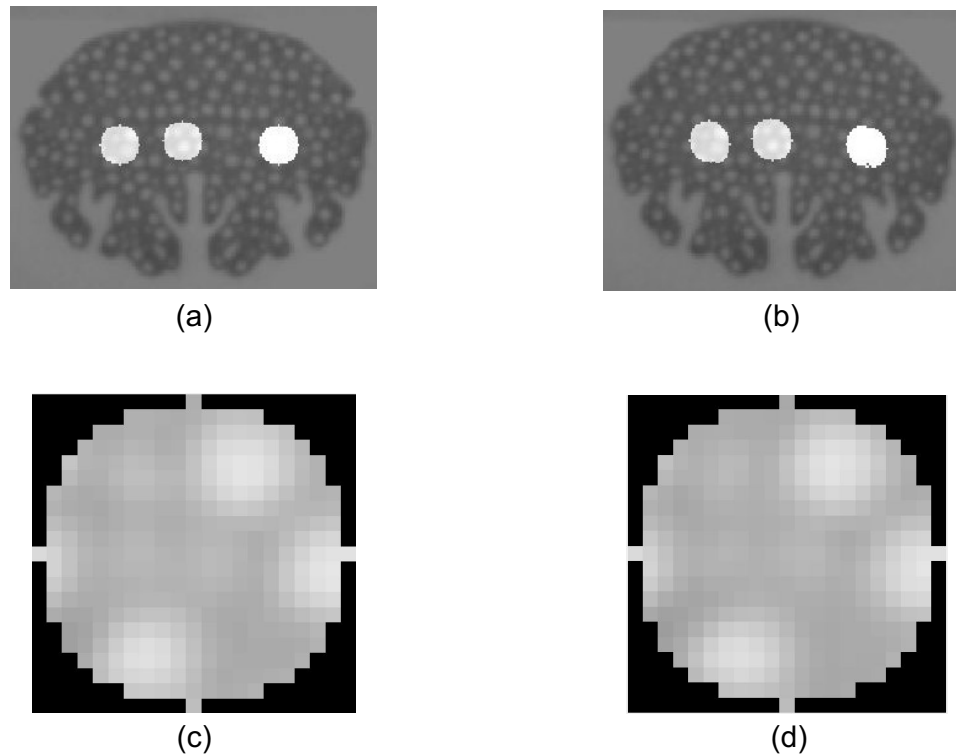


Figure 13: Three subsets are highlighted (circles) in a reference image (a). Under deformation (b), the subsets deform as well. The correlation coefficient locates the same set of pixels from the reference subset (c) in the deformed subset (d). The images were obtained while using Ncorr, a DIC programme [81].

To improve the accuracy of the above calculations, sub-pixel displacements are found using a registration algorithm. This initial guess for the displacement vector is then used by an iterative solver to find an optimum sub-pixel value for the displacement vector [81,84]. As points may move to locations between pixels after

deformation, interpolation is used to find sub-pixel values, with the refined displacement vector being found using the inverse compositional Gaussian-Newton (IC-GN) method [81,84–86]. This method uses a backwards matching strategy to match two subsets. Essentially, this method deforms the reference subset and then compares it to the current deformed subset to obtain displacement parameters for the reference subset. Each iteration produces a new incremental displacement vector, and thus incremental displacement mapping function, which is found when the least-square correlation criterion is minimised [81,84]. The inverse of the incremental displacement mapping function is composed with the current estimate for the displacement mapping function to create a new displacement mapping function for the current subset. The iteration procedure is repeated until convergence is met, and a final displacement vector is found (Figure 14).

The above steps are used in finding a single subset's displacement data. A reliability-guided (RG) method is then implemented to obtain full-field displacement measurements for all subsets [81,87]. The method follows a path of highest reliability from this initial subset to neighbouring subsets. After the initial subset, the neighbouring subset with the highest reliability is analysed first. The displacement data from the initial subset is used as the neighbouring subset's initial guess in the IC-GN method; this ensures that the displacement vector used in each calculation is from a point with high reliability [81,87]. The process of using the previous subset data as the starting point for the neighbouring subset with highest reliability is repeated until all subsets are computed. This ensures that points with low reliability are computed last, thus decreasing their influence on the displacement measurements.

Once full-field displacement measurements are found, strain values can then be calculated [80,81]. As differentiation is susceptible to noise, displacement fields are

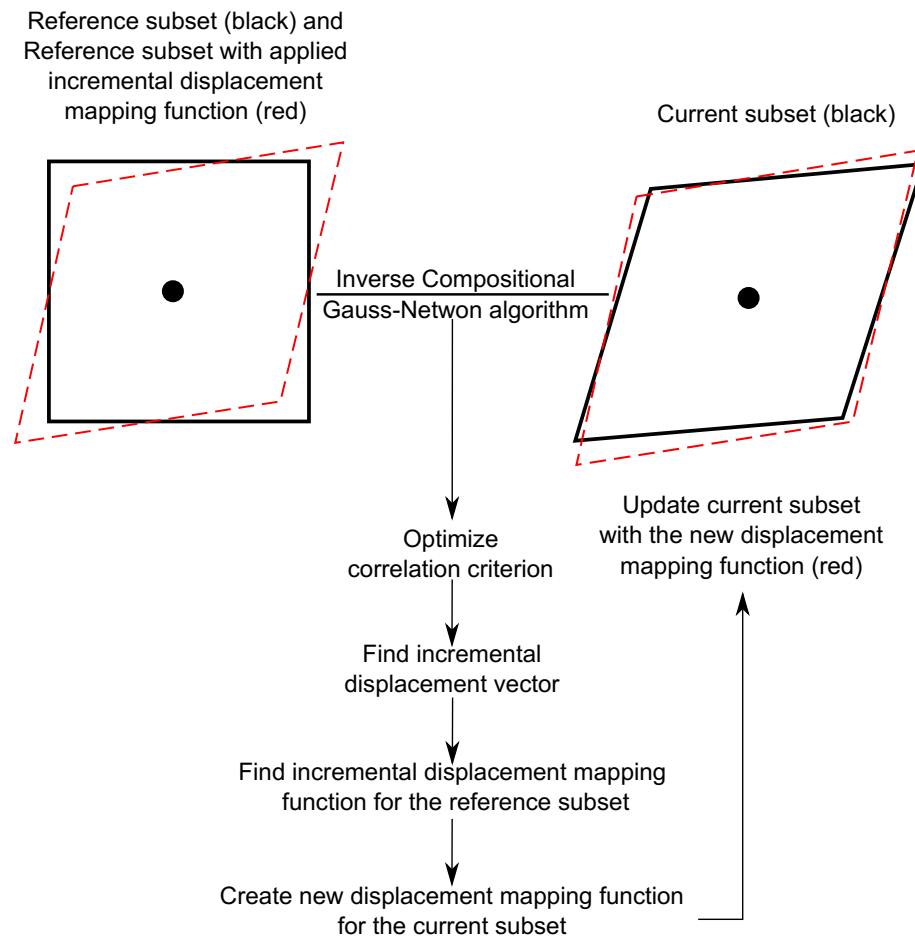


Figure 14: A flowchart on the process of the inverse computational Gauss-Newton method. This figure was adapted from [84].

typically smoothed before calculating strain. Ncorr [81], a DIC programme, uses a strain window algorithm to perform this task, which was proposed by Pan *et al.* [88,89]. The strain window uses a least squares plane, which is fitted to a group of displacement data points to calculate strain values. This process reduces the noise caused by differentiation. At the end of the DIC analysis, full-field displacement and strain fields are displayed (Figure 15).

It should be noted that while DIC can effectively calculate displacements and strains within an ROI, difficulties can arise at the ROI boundary. When the subset is moved to a region near or at the boundary, some pixels will be within the ROI

(valid) and others will be outside the ROI (invalid); there will be fewer valid pixels at boundaries [90]. The deformations at these regions cannot be truly defined using displacement mapping functions [90]. This leads to errors at the boundaries. The RG method, as described above, will scan for valid and invalid pixels within the subset. Within a subset, if the number of valid pixels is greater than the amount of invalid pixels, the algorithm will proceed, though it may produce displacements that are less accurate. Valid points that have high reliability from one frame to the next are then used. This ensures that calculation errors caused by invalid points are minimized. Additionally, some programmes extrapolate the data at the boundaries prior to interpolation in the IC-GN method to obtain values at the boundaries [81]. While this process can aid the DIC analysis, strain calculations at boundaries can still suffer. This is due to interpolation errors, as these regions are more noisy than regions that possess subsets than contain only valid pixels.

DIC parameters

Within the DIC algorithm, a few parameters can be modified by the user. These are used to accurately obtain displacement and strain measurements, and minimize error. Four of the key parameters will be discussed below.

The subset radius is ideally the smallest size that includes unique variations in pixel intensities. The intensity pattern within the subset must also have enough variation that it is distinctive from all other subsets; this allows for proper tracking [80]. Ideally, at least three speckle points should be visible within the subset to provide sufficient variation.

Additionally, not all pixels need to be computed within a subset for sake of

computational time. The subset spacing determines the spacing between the centres of neighbouring subsets [91]. For each step, a displacement value is calculated [91]. It is common practice that the subset spacing value is smaller than the subset radius to allow surrounding subsets to have regions of overlap. While precautions can be taken, DIC is known to have difficulties at boundaries, as the amount of particles or variations in intensities decrease [81]. This leads to iteration errors, which are displayed as increased strain concentrations at the boundaries. Smaller subset spacings are beneficial as they also may obtain data closer to boundaries, thus reducing error.

Along with the subset parameters defined above, the iterative solver includes an iteration cutoff number [92]. A low cutoff number reduces computational time, as fewer iterations are used to determine if an optimum displacement vector can be found. Lastly, the number of iterations the algorithm requires is an indicator of the quality of the analysis. A low value is a good sign that the displacement vector converged properly, the opposite is true if the cutoff value is high.

Another parameter is the strain window size [81]. This smoothing parameter is applied to displacement data; this removes noise within the displacement data, thus reducing noise caused by differentiation. This is done by grouping all data pixels within a defined radius and fitting them to a plane, as described in the previous section. This parameter can change the appearance of the strain fields. Small strain windows may show more noise, as fewer pixels are grouped together. A large strain window may over-smooth the strain fields to a point where deformations may be misinterpreted, as valid variations in strain values may get muted by surrounding values [81]. Therefore care must be taken in selecting parameter values that best represent the data, as these parameters are controlled by the user.

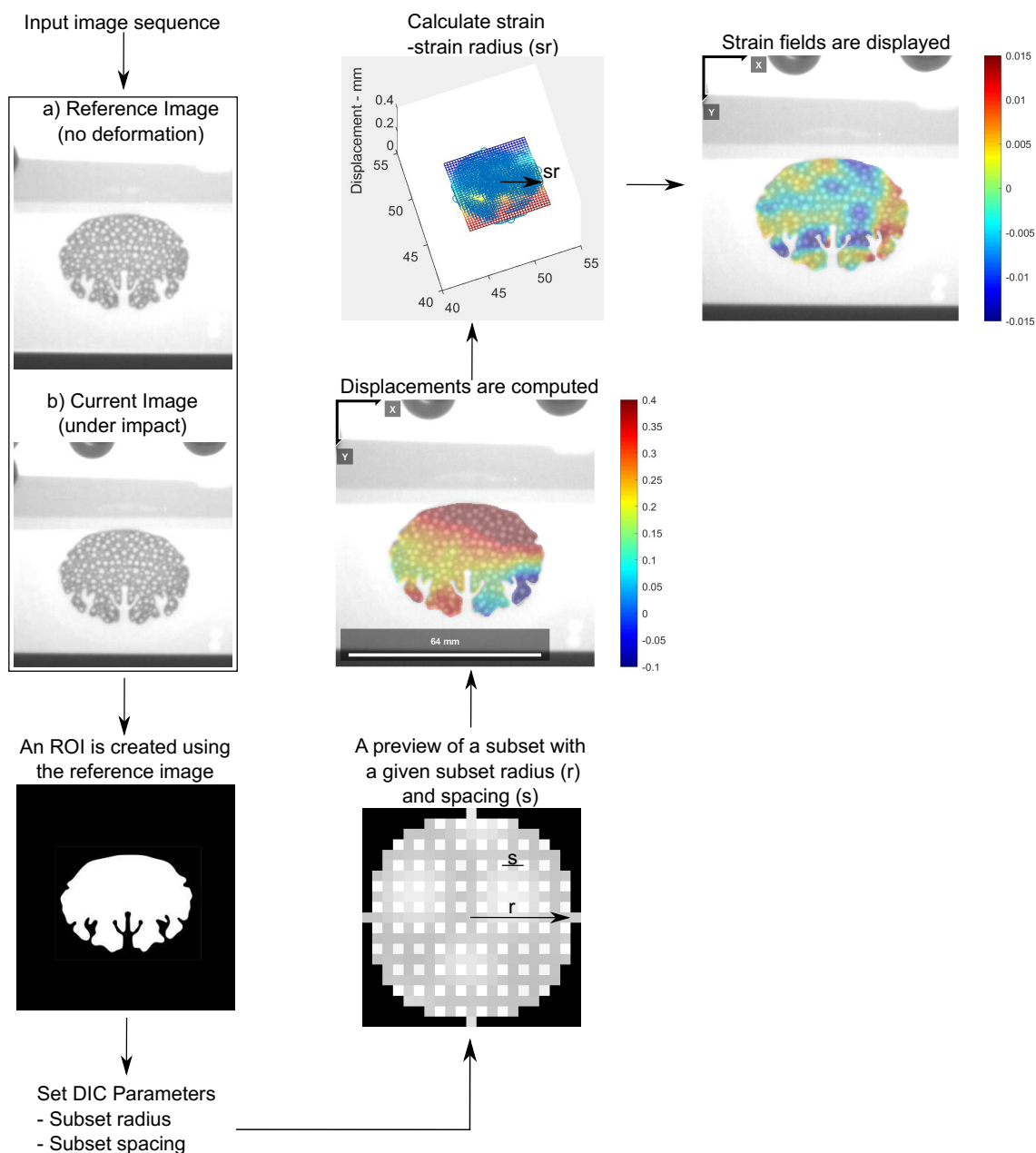


Figure 15: A flowchart on how a DIC programme computes strains from a sequence of images; the DIC programme used in this study was Ncorr [81].

3.1.1 X-ray Digital Image Correlation

The use of X-rays to measure displacements is advantageous for optically hidden specimens such as the brain. The method of tracking and analyzing specimen

deformation remains the same as in DIC when using X-rays. X-ray images can pick up density differences within a material if there is enough contrast. Particularly in brain tissue, the contrast is not sufficient enough to perform DIC.

Unlike the studies discussed above that used surface markers, radiopaque markers must be introduced into the sample in order to be imaged with X-rays; this was done in [65,66] with brain tissue, though XDIC (X-ray digital image correlation) was not used in these studies. The markers must have different attenuation properties than the surrounding material to be distinguishable and traceable with X-rays. Radiopaque materials, such as barium sulphate (BaSO_4), have a high attenuation coefficient due to their high density, meaning they absorb radiation [93], which results in a darker appearance on X-ray. Applying a radiopaque contrast agent to perform deformation measurements has been used in [94,95].

3.2 Particle Tracking

Individual particle tracking, unlike DIC, follows the motion of individual particles within a medium. This can be particularly useful in TBI studies. X-ray cinematography and particle tracking has already been successful in measuring brain deformations [65,66]. Whereas DIC uses subsets to determine deformations in all proceeding images, particle trackers use particle characteristics to track individual particles. Particle tracking methods include particle image velocimetry [96], particle tracking velocimetry [97], and single-particle tracking [98].

The focus of this section will be on a particle tracker published by Sbalzarini and Koumoutsakos [99]; the initial feature point detection steps of this algorithm are based on the work by Crocker and Grier (see Figure 16) [100]. This method uses a feature point tracking algorithm to calculate trajectory data for each particle. The algorithm essentially finds the center of each particle based on brightness

in filtered images. If the bright regions are within the user defined radius, the algorithm then provides pixel coordinates of the particle's trajectory.

Initially, the deformation of a specimen with notable particles is captured with a camera (Figure 16a). Within feature point detection, the images are analyzed by the algorithm, which normalizes the intensities across the full data set such that each frame is considered a matrix of pixel intensity values. A process called image restoration is used to correct image flaws, such as uneven illumination and discretization noise, created or captured by the camera [99, 100]. The calculations used in this step incorporates the particle radius parameter, w , which must encompass the particle, but be small enough to not include nearby particles [99, 101].

The combination of background and noise corrections leads to the final restored image represented as a convolution of the normalized matrix of the image, A^t , and a kernel, K^w (Figure 16b) [99]:

$$A_f^t(x, y) = \sum_{i=-w}^w \sum_{j=-w}^w A^t(x - i, y - j) K^w(i, j) \quad (5)$$

Once the image corrections have been applied to the complete data set, the next step is to estimate the particle's location. This is done using local intensity maximums from the filtered images to find particle coordinates. A grayscale dilation is applied to the image set, with a comparison between pixels from before and after the dilation being completed [99, 100]. This morphological operator adds pixels to objects within an image to make the object appear larger and more visible (Figure 16c) [102]. The algorithm considers a pixel to be a part of a particle if a) the pixel intensity is the same before and after dilation, b) if its intensity is of the upper percentile in brightness, and c) if there are no other brighter pixels within a given distance of w (Figure 17a) [99]. The central location of the particle is assumed to be

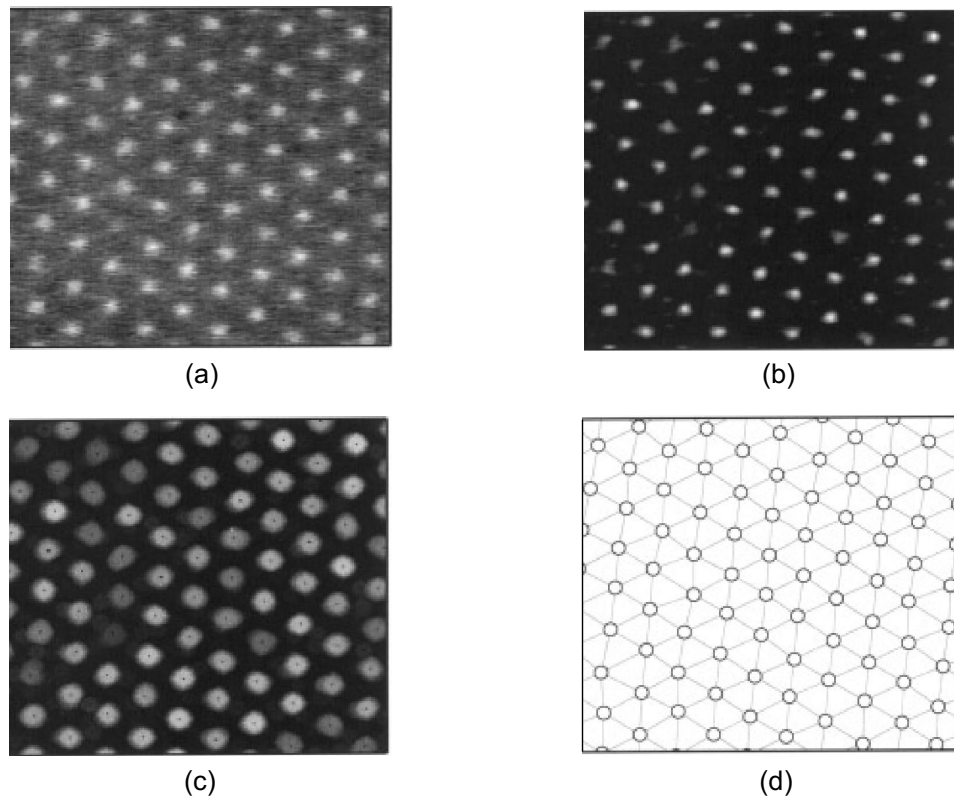


Figure 16: An image of the specimen (a) is filtered with a convolution kernel (b). A grayscale dilation is then applied to the image (c), while providing initial estimates of the particles location; this is shown as dark spots in the center of the lightly coloured particles. The final estimates of the particle locations are provided (d). Images are reorganized from [100].

at the brightest point within the given radius size (Figure 16c).

This position can undergo further refinement. This is done by calculating an offset from the brightest pixel (assumed to be near the true geometric center of the particle) to the brightness-weighted centroid of the particle [99, 100]. Finding the center is susceptible to noise, which positioning error is reduced by image filtering. The particle position can undergo further refinement by shifting the central location by one pixel if the offset is greater than 0.5 pixels.

The detection of particles based on intensity values are controlled by the user [99, 101]. As illegitimate particles may be detected by the algorithm alongside true particles, adjusting the percentile parameter can limit this issue. A higher

percentile value will allow for more particles to be detected, as a larger range of intensity values are included in the search [101]; this includes illegitimate particles. A lower percentile value would be more selective in particle detection, but may not include all desired particles.

As the above step can include illegitimate particles, a refinement of the results must be completed. Therefore the next step in the algorithm is non-particle discrimination [99, 100]. This step tries to differentiate between particles, with the goal of eliminating illegitimate particles. This takes into account the total intensity of a particle and the intensity of the surrounding features. True particles will have similar intensities and sizes, whereas illegitimate particles will have different values. A larger value used in the user defined parameter Cutoff leads to fewer particles being detected, as the algorithm is more likely to think the particle is illegitimate [101]. Given the provided cutoff value, scores are calculated and given to each particle to determine if it is a true particle [99]. If the score value is greater than the given parameter value, then the particle is considered a true particle.

Once the particle's coordinates have been found in each frame (Figure 16d), the algorithm then links their trajectories via an initialization and optimization process [99]; the following stages within this algorithm are based on previous work by [103–105]. These steps take the detected particles and their coordinates, as well as their type of motion, and links them from one frame to the next to create a continuous particle trajectory. A particle in one frame is initially linked to a particle in a nearby location in the next frame, as long as it is not associated with any other particle (initialization). Optimization refines the particle linking to ensure accurate linking of the particle's position from one frame to the next. A minimized cost functional is used, with the cost typically being defined by the particle's position and characteristics. It takes into account the number of pixels a particle is expected

to travel between frames. This is known as the Displacement parameter and provides further constraints on the particles and can limit non-particles [99,101]. Additionally, a frame count, known as Link Range, is selected when linking trajectories [99,101]. It tells the algorithm the number of frames that should be searched to ensure that the particle is the same particle in subsequent frames. Furthermore, a parameter, known as Dynamics, is used to define the motion of the particles [101]. Once this stage is complete, the final trajectory data of the particle is provided (Figure 17b). From the original trajectory data, displacement and strain values can be calculated using other software.

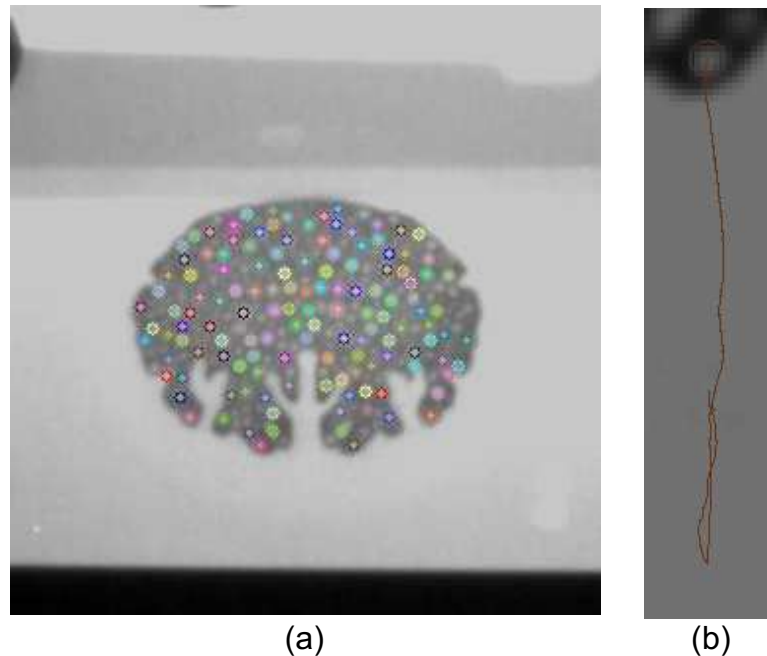


Figure 17: Individual markers are highlighted on sample (a) by providing characteristic parameters into the particle tracking programme Mosaic Particle-Tracker [99]. Markers can also be selected, and their individual trajectories visualised (b).

Chapter 4

Experimental Methods

The following chapter outlines specimen preparation and experimental designs that were used in the brain gyrification study and the preliminary viable *ex vivo* porcine brain tissue study. To evaluate the effects of brain gyrification and tissue motion, a series of drop impact experiments were conducted. A high-speed X-ray radiography (HSXR) system was used to capture the deformations of the specimens. This imaging modality was used over optical methods to avoid the possibility of optical distortion as well as to prepare for potential future applications with optically hidden samples. As this was a non-optical method and the specimens did not have inherent contrast, radiopaque markers had to be implemented in order to image specimen motion.

4.1 Design and Specimen Preparation

Encasement

An encasement system was created with many aspects in mind. The encasement had to house a specimen, have some degree of flexibility, be fluidized without leaking, and withstand repeated impacts.

Design

An encasement model was made in two parts using computer assisted design software (Onshape, a PTC Business, Boston, USA). For the brain gyrification study, an ellipsoidal cavity (5 mm deep) was placed within the base of the encasement model to house the surrogates (Figure 18a). This generic shape was used for both surrogates because it provided adequate spacing around the surrogates. This ensured that they did not interact with the internal walls of the cavity under impact. The external shape of the base and encasement model was rectangular, which provided a flat surface for impact. This ensured that, when under impact, the entire encasement was subjected to a one-dimensional loading profile.

A similar approach as to the one stated above was used when creating the base model for the preliminary viable *ex vivo* porcine brain tissue study. The cavity (4 mm deep) within the base was shaped after brain tissue sections, which were sectioned in the coronal plane (Figure 18c); this is similar to what was done in the Lauret *et al.* study [36]. The cavity was slightly smaller than the thickness of the tissue as to provide a slight compression on the tissue. Three different cavity sizes were produced in case there were size variations across specimens. Initially, porcine brains were collected to get familiarized with fresh brain characteristics. It was noted that brain sizes varied between collection sources and sexes, therefore measurements were taken from *ex vivo* brain tissue specimens that were initially collected. Within this study, the small cavity was used (see Figure 18c, leftmost encasement).

A cap model was created to seal the surrogate and porcine tissues within the cavity (Figure 18b). The interior sizing of the cap model was slightly larger in size than the internal spacing of the base of the encasement model. This was done to

ensure a tight fit between the cap and base to minimize leaking of water or biological fluids. When combined, the cavity between the cap and base caused slight compression of the specimens to hold them in place and to reduce any slipping that may occur; a final assembled model can be found in Figure 19. The final designs of the cap and base models were then 3D printed using a Dimension SST1200ES 3D printer (Stratasys Ltd., Eden Prairie, USA).

Inverse moulds were then created using Mold Max 10T Silicone (Smooth On, Macungie, USA), with all moulds being created using the same following steps. A containment field was created using a moulding clay that surrounded the 3D printed part (Figure 20a). The containment field ensured that the moulding material did not escape while in a liquid state; once cured, the silicone material became solid. The 3D printed part was placed face-up into the mould and Ease Release 200 mould release agent (Mann Release Technologies, Inc., Macungie, USA) was sprayed within the containment field to prevent the silicone mould from sticking to the surrounding parts. The degassed two part mixture was then poured over top the 3D printed part and was left to cure for at least 48 hours at room temperature on a level surface (Figure 20b); the final product is shown in Figure 20c.

Encasement Preparation

The encasement material was chosen based on its properties, as the material would need to maintain its shape, but also be flexible; these were common features in surrogate studies. Two forms of Sylgard, a thermoset polydimethylsiloxane, were used. The first is Sylgard 184, a silicone elastomer, which has a tensile strength of 6.7 MPa [106]. This firm elastomer is commonly used in electrical applications. The second polymer is Sylgard 527, a dielectric gel, which has a gel hardness of

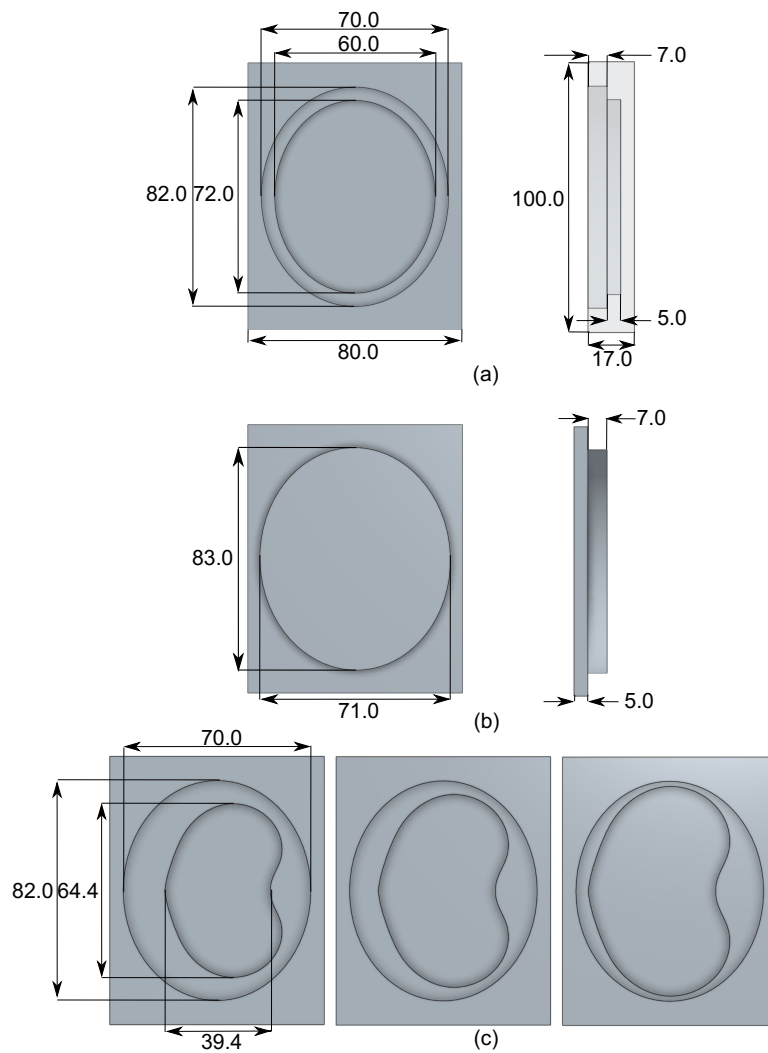


Figure 18: Dimensioned images of each component created for the encasement model; all units are in mm. The base used in the brain gyrification study (a) had an ellipsoidal cavity. Both the top (left) and a translucent side view (right) are provided. The cap (b) was used in both studies to seal the specimens within the base's cavity. The coronal shaped cavity within the base (c) was used in the preliminary *ex vivo* porcine brain tissue study. From left to right the internal shape increases corresponding to smaller, middling, and larger brain sections. The dimensions were only provided for the leftmost base as it was the only one used within the preliminary study. Note that the external dimensions provided in (a) are the same for (b) and (c), with the exception of the width being different in (b).

113 grams [107]. This soft, tacky gel is commonly used in printed circuit board applications. Individually, these two Sylgards had undesirable properties for this

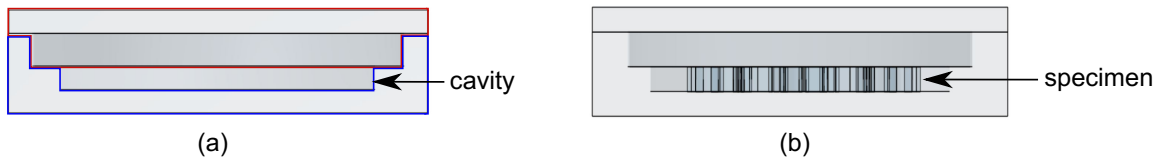


Figure 19: The final assembled encasement model has the cap (red) fitting into the base (blue). The design creates a cavity (a) where the specimen (b) will be housed.

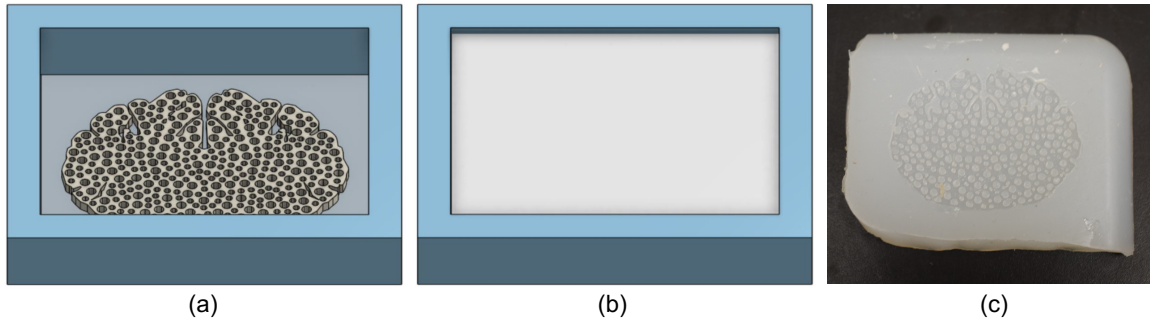


Figure 20: The moulding process: (a) a containment field (blue) is made around the specimen, (b) after spraying the interior of the mould and sample with a mould release, a moulding mixture (white) is poured within the bounds of the containment field and is then left to cure, (c) once cured, the inverse mould is removed from the containment field, along with the sample.

study, but when combined produced desirable characteristics. A mixture of Sylgard 527 and 184 (Dow Silicones Corporation, Midland, USA) were mixed in a 5:1 ratio as per [73]. This ratio of elastomer allowed for the cap and base of the encasement system to adhere and form a light seal. The cured mixture has an approximate elastic modulus of 1.34MPa [73] and resembled a soft rubber material, with a slight surface tack.

When creating the physical encasement, a thin layer of vaseline was used as a mould release agent. Once the mould was filled with the Sylgard mixture (527:184 in a 5:1 ratio), it was left to cure at room temperature for at least 48 hours before being removed from the mould. Once assembled, the encasements would house

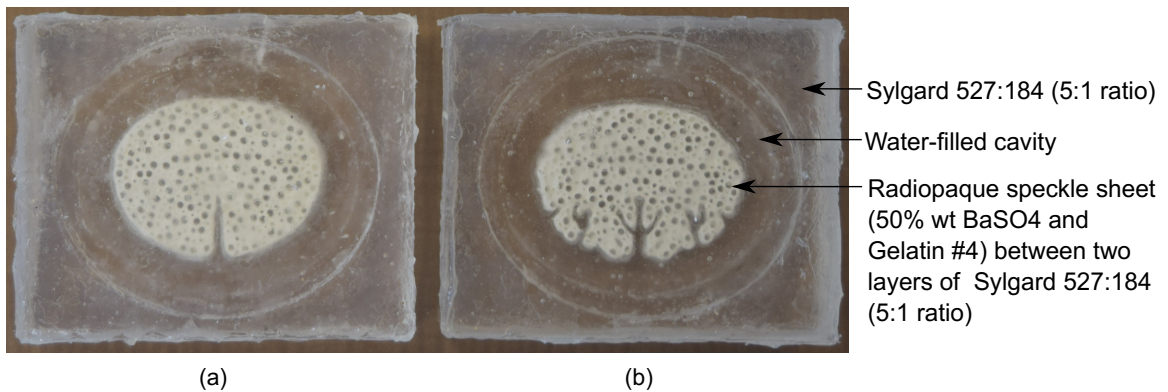


Figure 21: The final assembled encasements with both the smooth (a) and complex (b) surrogates contained within the internal cavity. Material composition is the same for both surrogates.

the specimens within the internal cavity; the final external dimensions of the encasement was (100 x 80 x 22) mm (Figure 21).

4.1.1 Brain Tissue Surrogates

Two brain tissue surrogates were created based on a coronal section of a porcine brain. An open source MRI scan of a domestic pig (*Sus scrofa domesticus*) brain [108–110] was imported into an image visualization programme, 3D Slicer [111–113]. The scan was saved in a file format that created a grayscale version, then the most visually complex coronal section was selected to create both surrogates (Figure 22a). As a point for comparison, an *ex vivo* porcine coronal brain section is provided (Figure 22b).

The image of the MRI brain section was imported into a computer-assisted design software (Onshape) where both surrogates were created. The outline of the MRI brain section was used to create the surrogate with complex cortical gyri-fication (from now on called “complex surrogate”, Figure 22d). The outline of the central gyri within the complex surrogate was simplified from those observed within the MRI scan. There were originally four small gyri in the MRI that were

combined to make two larger gyri in the complex surrogate. This was done as it allowed for the placement of a greater amount of radiopaque markers within this region, which was ideal for image analysis. The second model was a smoothed cortex version of the same coronal section (from now on called "smooth surrogate"). It did not include any complex cortical gyrification, just the distinction between both hemispheres (Figure 22c). The two surrogate models (Figures 22e and 22f) were then 3D printed using a Stratasys Dimension SST1200ES 3D printer and inverse moulds were then created using Mold Max 30 Silicone (Smooth On, Macungie, USA) from the 3D printed surrogates.

In order to image the impact event with X-rays, a radiopaque agent was added to the surrogates in the form of a speckle sheet (Figure 23). A speckle pattern was created within the outline of the surrogates using a vector graphics editor (Inkscape). Circles of two sizes (diameters of 1.25 mm and 2.5 mm) were randomly filled within one of the surrogate's outline. The small circle sizes were chosen, as a large amount could be integrated within the surrogate shape; this is ideal for DIC. The circle sizes were large enough to create a 3D printed part, mould, and speckle pattern with ease, as anything smaller would be difficult to produce, i.e. resolution issues could occur during the 3D printing process and the moulded regions of the circles could have torn out while removing the 3D printed part from the mould. Additionally, the sizes were ideal because they were clearly defined when imaging with X-rays. For these reasons, the pattern was ideal as it created a random, distinct pattern; this is ideal for DIC (see Chapter 3.1). This pattern was then copied over to the other surrogate, with additional circles being added to areas that were void of circles. A key factor in the design of the radiopaque speckle sheet was that the pattern was near identical between surrogates, except for in a few regions of gyrification. This allowed for direct marker to marker comparison

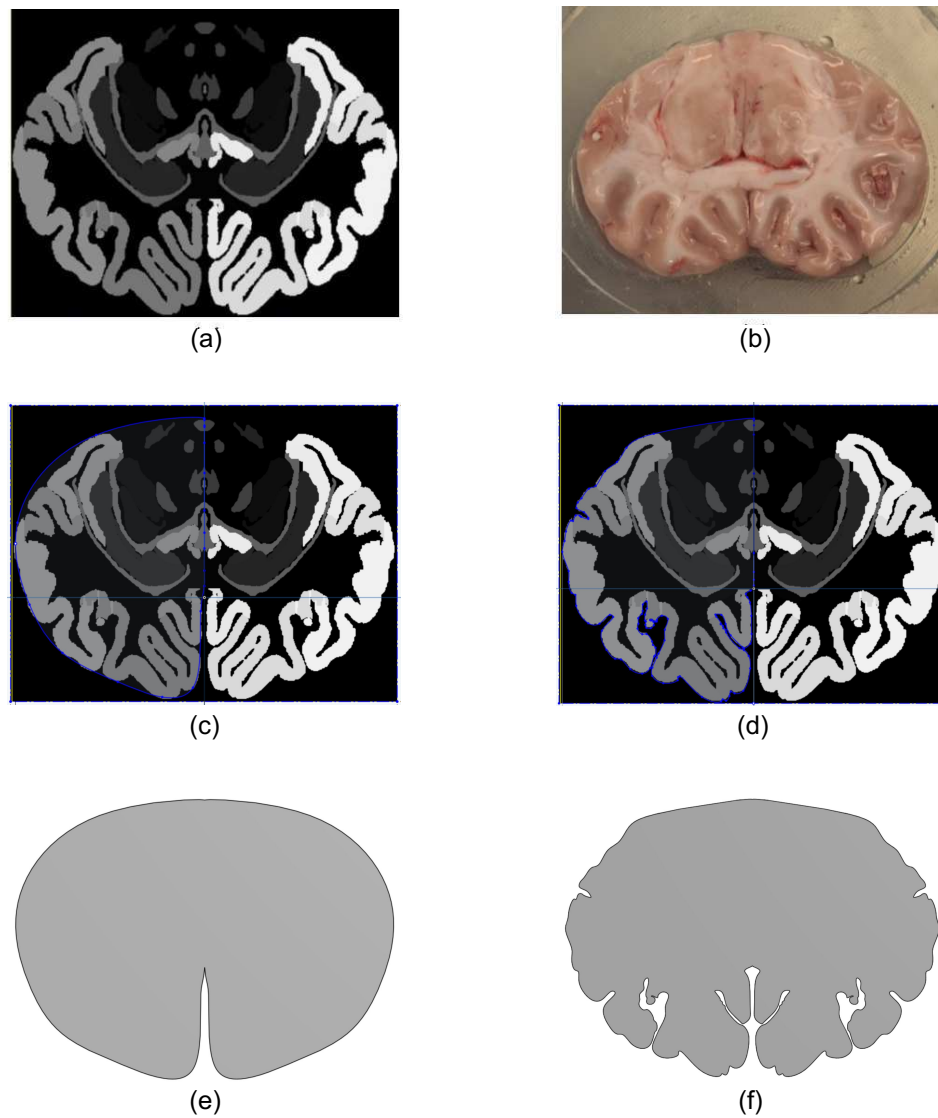


Figure 22: Both surrogates were based off of an MRI scan of a coronal porcine brain section [108–110] visualised with 3D slicer (a) [111–113]. A different *ex vivo* coronal porcine brain tissue section is provided for comparison (b). The outline (blue) of the smooth gyrfication surrogate (c) followed the outline of the MRI scan, but was smoothed to represent a brain that lacked gyrfication. The outline (blue) of the complex gyrfication surrogate (c) followed the exact outline of the MRI scan. Both final models of the smooth (e) and complex (f) surrogates are shown.

across both surrogates.

Once finalized, the speckle sheet patterns were 3D printed to a thickness of

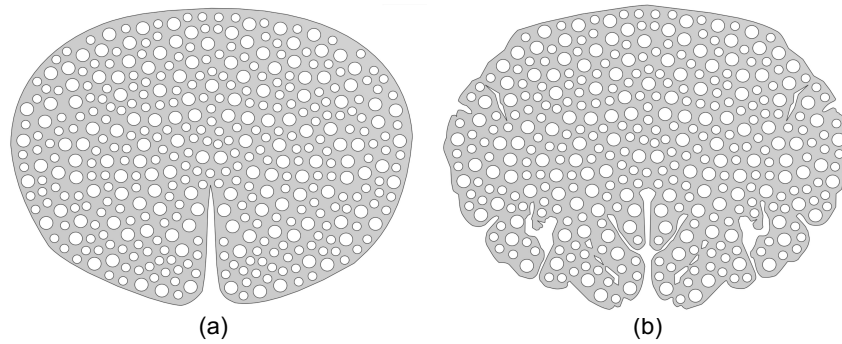


Figure 23: The speckle patterns incorporated into the smooth (a) and complex (b) surrogates.

2.5 mm and moulds were created afterwards. Speckle sheets were created in the speckle pattern moulds, which were then integrated into the surrogates. The speckle sheet material was made from two parts. A mixture of 50% by weight BaSO_4 (Alfa Aesar, Heysham, England) and a thermoplastic gel (Gelatin #4, Humimic Medical, Greenville, USA) were mixed thoroughly together in a heated pan and poured into the speckle pattern moulds in a liquid state. BaSO_4 (density of $4.5\text{g}/\text{cm}^3$) added the necessary contrast to image surrogate deformations under HSXR, while the gel (density of $0.8\text{g}/\text{cm}^3$) was flexible and was easy to incorporate the BaSO_4 . Once set, the sheet was removed and the assembly process for the surrogates began.

Each surrogate was created in three steps; for visualization purposes the complex surrogate will be used to explain the process. The first step used a thin layer of vaseline on the moulds, and then the surrogate moulds were filled with a thin layer of the aforementioned Sylgard mixture (527:184 in a 5:1 ratio, see Figure 24a). The layer of Sylgard was left to partially cure in the oven at 120°C for about 10 minutes or until it was tacky to the touch. The radiopaque speckle sheet was then introduced into the mould (Figure 24b). The mould was then filled to the top with the Sylgard mixture, filling the holes within the speckle sheet in the process (Figure 24c). The surrogate was left to cure in the oven for about 45 minutes at 120°C .

The final surrogates are shown in Figure 25.

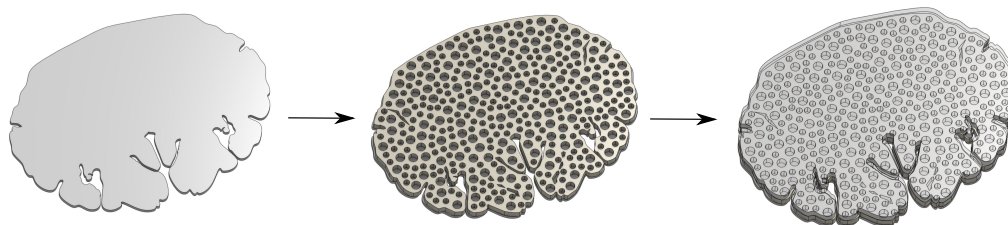


Figure 24: The process of making a surrogate. A thin base layer of the Sylgard mixture (left) is added to the bottom of a surrogate mould. Once partially cured, the radiopaque speckle sheet is added on top of the thin Sylgard layer (middle) and additional Sylgard mixture is added to cover the radiopaque speckle sheet and fill the mould (right). The finished surrogate can be found in Figure 25b

The procedure of introducing the speckle sheet was created based on previous unsuccessful attempts. One trial had the entire surrogate cure at room temperature. Upon inspection hours later, the speckle sheet shrunk significantly within the mould. This was the reason as to why the surrogates were cured in the oven. The oven temperature was also selected based on the melting and curing points of each material. The Gelatin #4 has a low melting point, therefore the curing temperature was selected to reflect this property. The final temperature selected was high enough to cure the surrogates relatively quickly, while not high enough to melt the speckle sheet; this also helped reduce any potential shrinking.

The Sylgard mixture was chosen for its ability to maintain the external geometry of the surrogates, while remaining flexible. This allowed for repeated impacts of the same surrogates for the duration of the study. The surrogates did not take into account grey and white matter and spacing between gyri. Viable *ex vivo* brain tissue sections are soft and fatty, resulting in the gyri moulding into neighbouring tissue. Another, more biofidelic material was tested, but produced less agreeable results, as the material was unable to hold its geometric shape for extended periods

of time.

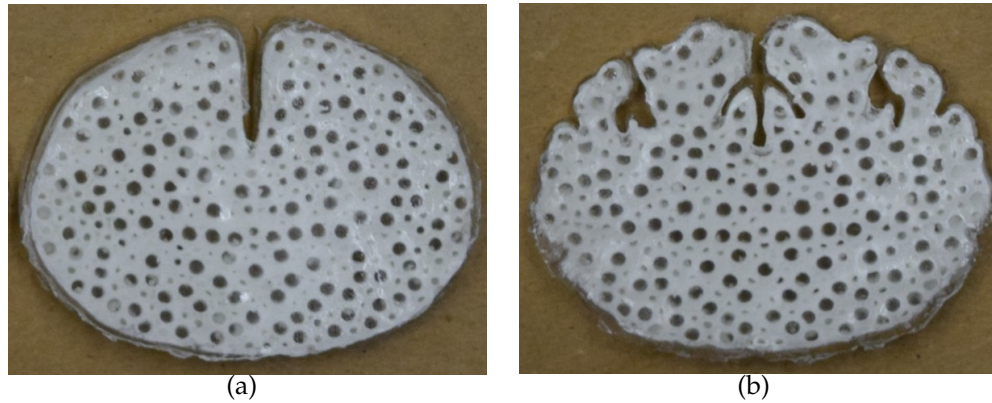


Figure 25: The smooth (a) and complex (b) surrogates that were used for the study.

4.1.2 Porcine Brain Tissue Preparation

A fresh porcine head was obtained from a local abattoir (Tom Henderson's Meats and Abbatoir Inc., Chesterville, ON) and brought back to Carleton University; data collection occurred on May 16, 2019 and June 6, 2019 for this study. The brain was extracted using a combination of a Dremel, and a hammer and chisel. Once extracted, the whole brain was left to firm in cold artificial cerebrospinal fluid (aCSF) for an hour prior to sectioning. This buffer solution provided the extracted brain conditions experienced at physiological levels. The above steps were performed by our collaborators in the Neuroscience Department. The full experimental procedure can be found in Appendix B.

Once the brain was extracted, a method of inserting radiopaque markers was introduced. Initially, the porcine brain sections were immediately injected with markers once the brain was removed and sectioned in prior experimentation. This proved difficult for the marker insertion process, as the tissue was very soft. This caused the tissue to push most markers towards the surface of the tissue. A test

was done on a brain that was placed in cold aCSF for four hours. The markers were easier to place into the firmer brain tissue, but the additional four hours exceeded the time that was determined for the brain to remain viable; other studies were completed within 6 hours post-slaughter [36]. It was then decided that leaving the brain in cold aCSF for an hour would firm the tissue sufficiently for marker insertion; the process is described below.

Afterwards, the brain was sectioned in the coronal plane starting from 3 cm from the frontal lobe into approximately 5 mm sections. This was done using a slicing matrix that was designed and manufactured in-house (Figure 26). The four coronal brain sections were placed in an incubation unit that consisted of aCSF and an air bubbling unit (Figure 27; this was created by colleagues in the Neuroscience Department with additional design input given, as needed). The tissues were left to rest after sectioning for 10 minutes and again after the radiopaque markers were placed into the tissues.

Marker Insertion System

Most studies that used a speckle pattern typically applied it to the surface of the sample using an airbrush [36]. A potential issue with surface markers in this study may be that the interface between the specimen and encasement may influence marker motion. Therefore, using sub-surface markers would most likely avoid this issue, as the motion of the markers would be the result of tissue motion.

A new system was created to introduce markers into the sub-surface level of the tissue (Figure 28). Cannulas with a gauge size of 17 (1.27 mm) were cut to 19 mm in length. Initial testing used two different cannula sizes with two different marker concentrations to distinguish brain matter, but was later abandoned as experimentation progressed, as the visual differences were minimal; this method

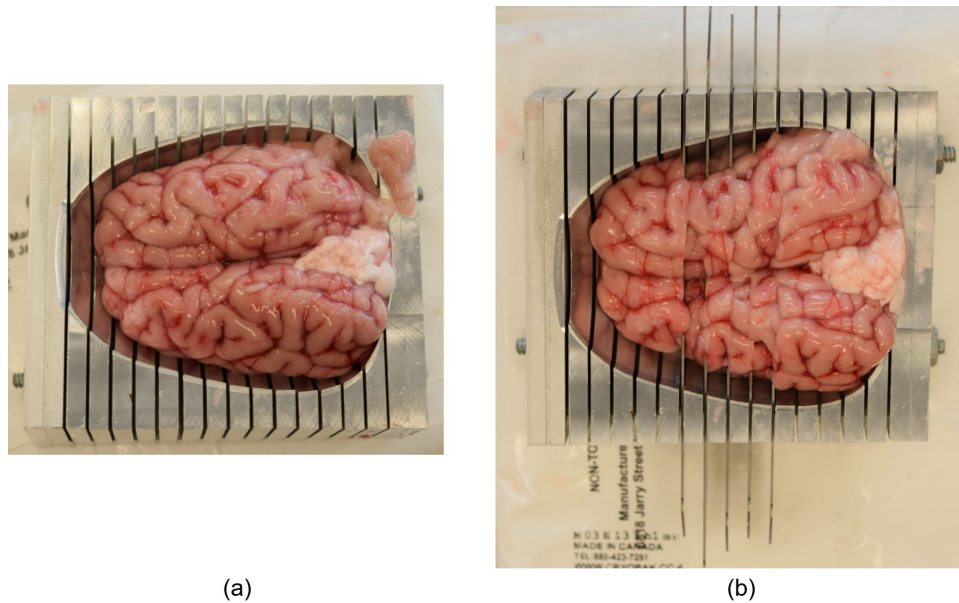


Figure 26: Once removed from the porcine head, the porcine brain is placed in the brain slicing matrix (a). Five blades were used to section the porcine brain into four sections (b), starting from 3 cm from the front (the leftmost and narrowest section of brain in the image).

was used within the May 16th brain.

To prevent inserting markers too far into the tissue, a guide was created. The cannulas were slotted into a simple (10 x 10 x 3) mm square of acrylic and was attached 2.25 mm away from one end of the cannula. This distance was chosen as it would place one marker end near the center of the tissue. Next, a plunger was made out of wire that was bent to 90° at one end; this prevented the markers from passing through the specimen. The plunger was used to then push out the marker from the cannula and into the brain tissue.

Due to the small interior diameter of the cannula, pre-made markers were unable to be placed inside the cannula. This resulted in the markers being made individually before being placed into the tissue. This was done using a melting disc made from steel. A cavity with a depth of 1.25 mm was created within the center. This depth also set the length of the markers, as the marker material was



Figure 27: Four porcine brain tissue sections cut using the brain slicing matrix; two sections were for control and two were used as treatment tissues. The image was taken after marker insertion while the sections were acclimating in the incubation unit.

melted within the cavity (Figure 29). This marker length would ideally place the markers below the surface of the tissue.

The markers were created using a mixture of 60% by weight BaSO_4 to Gelatin #4. This mixture was added to the disc and left to melt. It was determined that setting the hotplate temperature to the melting temperature of Gelatin #4 was too high. This resulted in a mixture with low viscosity that caused the mixture to fill the cannula past the desired 1.25 mm length. Therefore, the mixture was heated to 120°C , which created a more viscous mixture that maintained the desired length.

Once the cannula was dipped into the liquid marker mixture, it was left to cool for a few seconds before removing any excess mixture from the outside of the cannula. Next, the cannula was placed into the tissue using the guide, and the plunger

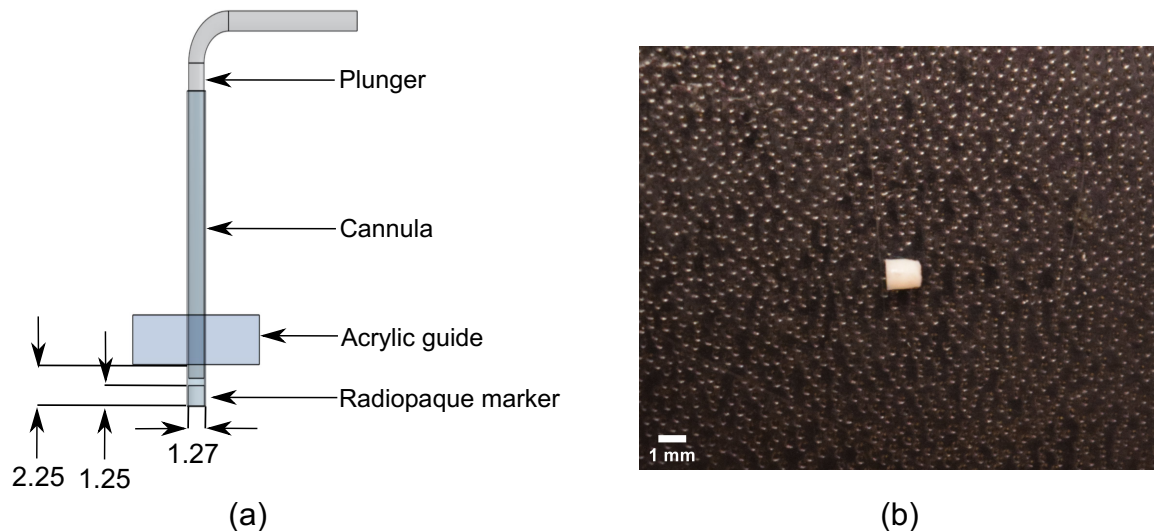


Figure 28: A marker insertion system (a) was created to insert individual radiopaque markers into porcine brain tissue. The individual components are as follows: the cannula, with the acrylic guide, were used to create and place individual markers into the tissue and a plunger was used to push the markers into the tissue. The marker insertion system would produce a marker (b) with dimensions of approximately (1.27 x 1.25) mm.



Figure 29: A steel melting disc, with an internal depth of 1.25 mm was used to melt the radiopaque mixture. The internal depth also set the length of the markers placed into the porcine brain. Shown are the disc without (a) and with (b) the radiopaque marker mixture.

then pushed the marker into the tissue (Figure 30a). This process was repeated numerous times until all desired locations were marked (Figure 30b). During this entire process, the tissues were kept in a petri dish filled with aCSF that sat on an

ice pack to keep the tissue firm.

This technique proved to be the most successful in terms of applying a radiopaque agent and visualizing the markers under X-ray; other techniques and marker materials tested, but not used within this study are described in Appendix A. This technique allowed for markers to be placed into specific locations that were of interest in the tissue; this is not necessarily the case with sprayed on speckle patterns. This method was not entirely perfect as some markers surfaced. This was solved by taking a plunger or tweezers and pushing the markers back into the tissue before being encased.

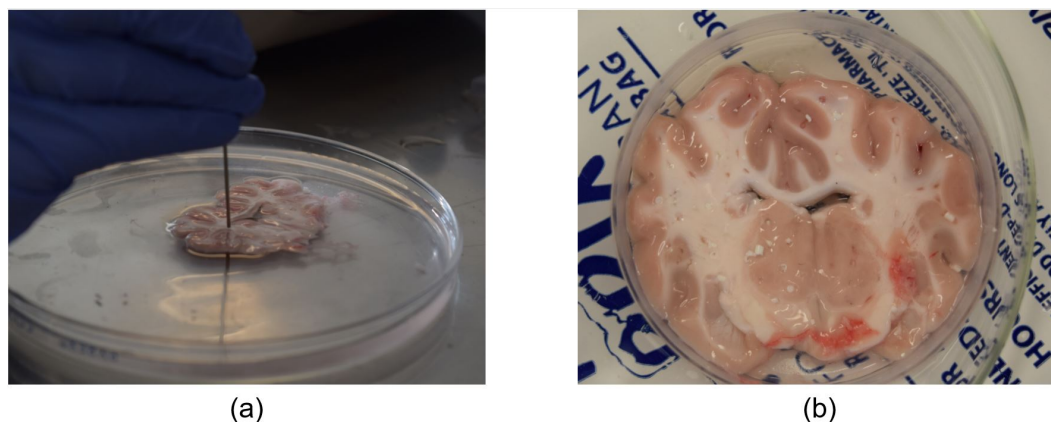


Figure 30: (a) Markers were placed into the porcine brain tissue with the marker insertion system. The image shown is of the initial system which did not have an acrylic guide, nor was the tissue on an ice pack; these were implemented to the procedure afterwards. (b) A coronal porcine brain tissue section after marker insertion.

Attempts were made to place radiopaque markers along key identifying features such that an X-ray image could be compared back to an optical image. With this method, challenges occurred as tissues may have shifted when compressed and when placed within the drop apparatus, which would result in differences between optical and X-ray images. While this issue may be minimized if optical methods were used, the reason for using X-ray techniques over optical techniques

were for potential future applications where X-rays would prove beneficial.

4.2 Injury-Inducing Impact Scenarios

A custom drop tower made out of 80/20 rails (80/20 Inc., Columbia City, USA) was used to drop the specimens as shown in Figure 31. In both studies, the specimens (within the encasements) were placed between two parallel acrylic plates with the encasement bottoms being placed flush with the acrylic. The plates on either side of the encasements were joined by screws, ensuring that the external distance between the parallel plates were the same, which was verified with callipers (Figure 32). Afterwards, the acrylic plates and encasement systems were then attached to two more acrylic plates, which were connected to the two carriages that slid along the 80/20 rails. It should be noted that during the brain gyrification study the elastomer encasements were sealed with a thin layer of Supreme 100% Silicone caulking (General Electric Company, Momentive Performance Materials Inc., Huntersville, USA). This provide an additional seal to prevent water from leaking for the long durations of the experiment.

Three main orientations were tested in the brain gyrification study. This included brain gyrification facing downward, upward, and inward (Figure 33). Different orientations were tested, as it has been shown that impact orientations may cause unique responses, with some orientations being more susceptible to injury [34] and different loading conditions (orientations) creating different responses to injury [6]. Sample X-ray images of the three main orientations are shown in Figure 34. The downward and upward orientations were dropped from four heights (30, 50, 70, 90) cm corresponding to impact velocities between 2 to 4 m/s. The impact durations, calculated from the median trials of the downward

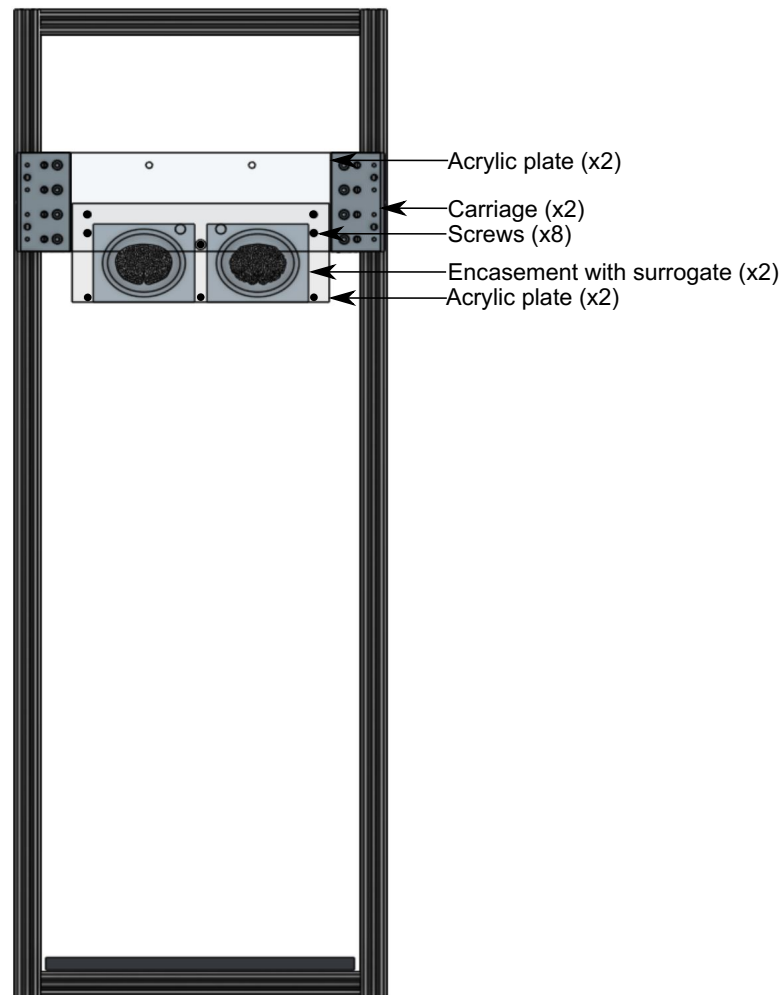


Figure 31: The drop assembly used in all surrogate and porcine experiments.

orientation for the 30 cm, 50 cm, 70 cm, and 90 cm drops, were approximately 20 ms, 14 ms, 13 ms, and 11 ms, respectively; these values were calculated by analysing the X-ray impact images, and as a result the values may vary slightly due to the nature of the images. The inward and supplementary (outward facing gyrification, swapping the positions of the surrogates while in the inward orientation, and applying a 5° tilt inwards and outwards to the surrogates) orientations were only dropped from 50 cm. These orientations showed drastic surrogate motion at higher heights, as gyrification was parallel to the anvil. The supplementary orientations were used to provide additional information on loading conditions

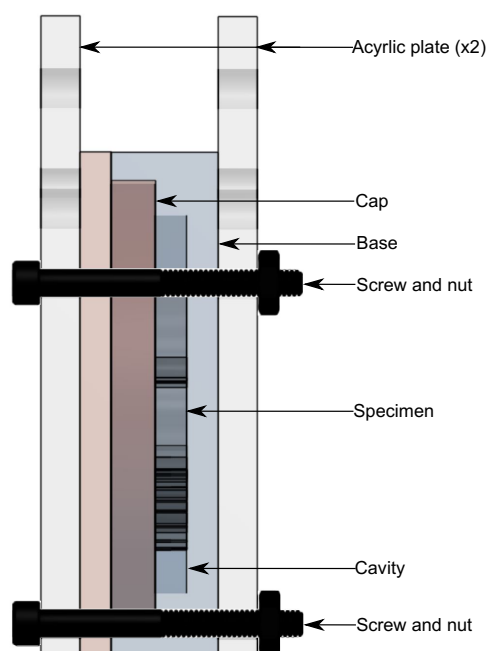


Figure 32: A side view of the encasement sandwiched between two acrylic plates. The colours shown in the diagram may not be representative of the objects in real life.

based surrogate location within the drop apparatus, as well as the influence of surrogate placement if the surrogates were angled within the encasements. Therefore, additional drop heights were not required to support these ideas. At each impact height, three trials were performed for reproducibility. The viable *ex vivo* porcine brain tissue sections were dropped once with the brain gyration facing downward from a drop height of 90 cm.

While in the encasements, boundary conditions were placed on the lateral sides of the specimens in each study (see Figure 32). Each specimen was placed evenly within the center of the cavity. Measurements were taken from each side of the surrogate to the outer edges of the encasement to ensure that the distances were the same for each side to ensure central placement. Acrylic plates were used to evenly compress the specimens at the same time, as each encasement was evenly spaced between the screws used to attach the acrylic plates (see Figures 33 and 34). The

screw pattern varied depending on the orientation of encasements. This resulted in two additional screws being required for drops in the inward and supplementary orientations; this amounted to a 2% weight increase in the drop system (see Figure 34 for screw pattern). Preliminary tests showed, that if no interior screws were used, excessive surrogate motions were observed during impact. Additionally, the same Sylgard mixture was used for both the encasements and surrogates. While motion within the regions of the brain may move on their own or coupled to the encasement, the whole surrogate construct did not slip during the test. As all other conditions were identical, the only contributing factor to differences in the strain response must be from the differences in brain gyrification.

A HSXR system was used to capture the impact events at 7,500 frames per second. This frame rate was chosen as it provided sufficient pixel resolution; increasing the frame rate tends to decrease pixel resolution, thus reducing detail. The specimens from the surrogate and porcine brain tissue studies were respectively dropped within the same apparatus, which ensured equal loading conditions and equal timestamps (for comparison purposes) being applied across specimens, while reducing experimental time. The combination of X-ray imaging and radiopaque markers allowed for motion tracking in the specimens to minimize optical distortion.

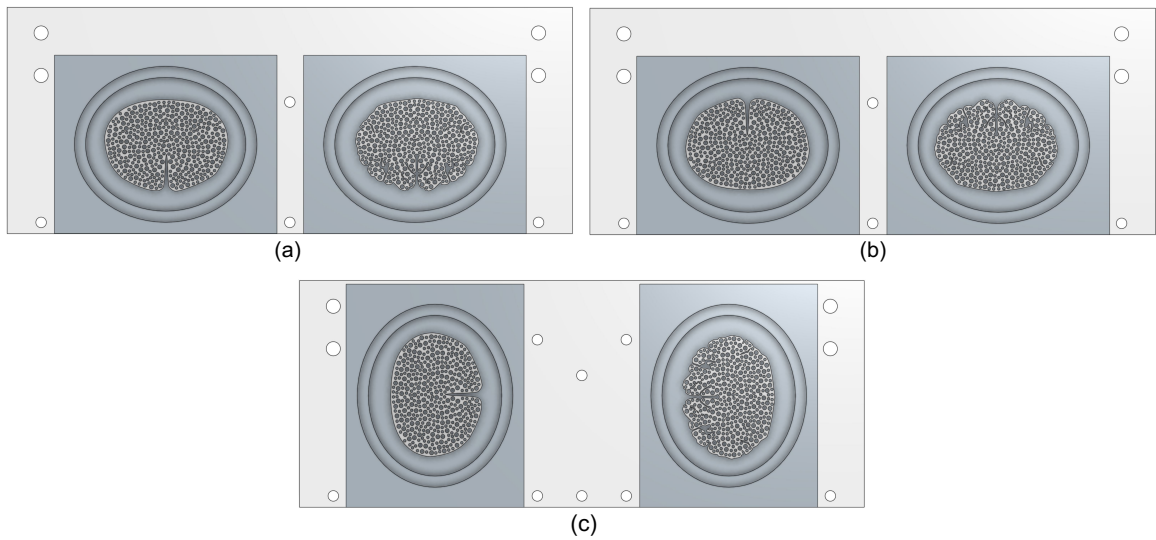


Figure 33: Orientations of the smooth (left) and complex (right) surrogates with brain gyration facing (a) downward, (b) upward, and (c) inward.

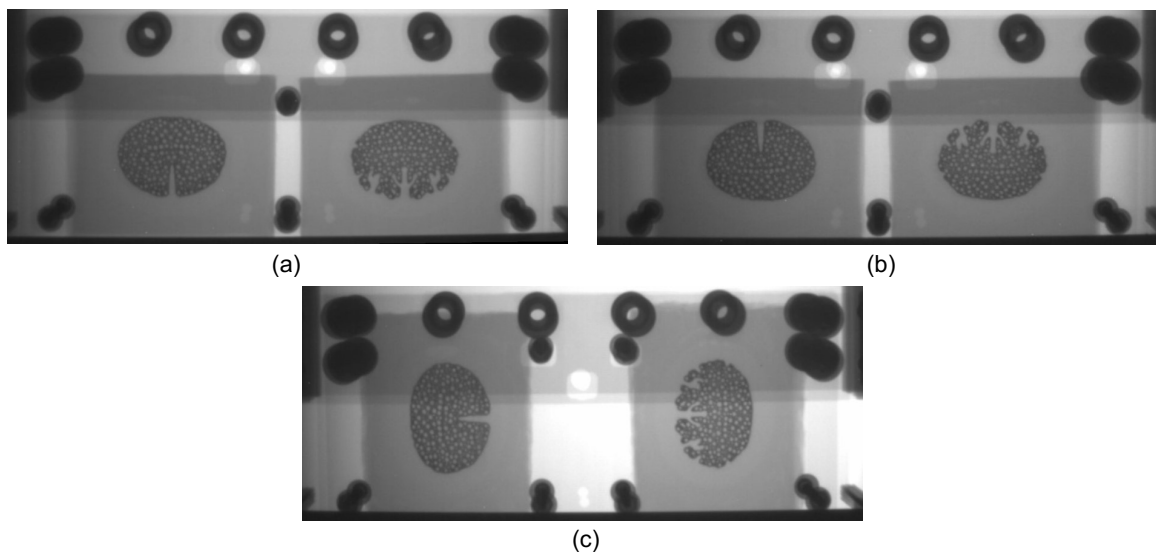


Figure 34: X-ray images of the orientations of the smooth (left) and complex (right) surrogates with gyration facing (a) downward, (b) upward, and (c) inward.

4.3 Image Processing and Analysis

Images from the impact event were saved as 8-bit monochromatic tiff files; Matlab (R2017b; The MathWorks, Inc., Natick, USA) was used for the initial image processing. The frames were cropped down in size to focus on each specimen. For the brain gyrification study, the complex surrogate images were mirrored to match the smooth surrogate images. This allowed for comparable regions to be more easily compared. For the downward and upward orientations, this meant that regions closest to the center of the impact plane were overlaid. For the inward and supplementary orientations this allowed for the regions of gyrification to be overlaid on top of each other. The reference image occurred moments before impact when the specimen was undeformed. Approximately eight frames prior to impact were included within the analysis to ensure that the reference image had no deformation, as well as create a baseline for zero deformation. The image data set consisted of approximately 248 frames or 33 ms, which was used for the entire analysis; after 20 ms, most samples did not experience any large motions. Additional post-processing contrast was applied to enhance the appearance of the specimens.

The pixel resolution of the system was determined after obtaining the X-ray images. This is done by dividing a known object measurement by the pixel value of the object measurement. Various objects with known dimensions were compared to the pixel dimensions obtained from the X-ray image; object measurements were taken from various locations across each image. The experimental pixel resolution was around 0.285 millimetre per pixel for most drop orientations; the standard ratio is 0.264 millimetre per pixel. As a note, the ratio value varied slightly for different experimentation days. Since the impact occurred within the same plane and the experimental setup remained consistent across impacts, the pixel resolution

was the within comparable values throughout the data sets.

In the following subsections, the two forms of image analysis will be discussed. In the DIC analysis, full-field strain measurements were obtained, as well as regions between markers of interest areas were analysed. It should be noted that DIC was only used in the brain gyrification study. Another method was able to select multiple individual markers of interest, many of which corresponded to regions of brain gyrification, and direct strains were calculated. This was done through individual particle tracking.

4.3.1 Digital Image Correlation

XDIC was used as the first method to measure strain within the brain tissue surrogates. This was done using the Matlab add-on script, Ncorr [81]. This DIC programme was verified and validated with several different data sets, which were provided through the Society for Experimental Mechanics' DIC Challenge [81,114].

Within the brain gyrification study, the reference image and deformed images were uploaded into the programme with every other frame being used; this aided in reducing computational time. A single DIC analysis using every frame was compared to that using every other frame. It was confirmed that displacement and strain values obtained in odd frame numbers were consistent with those in even frames; variations were on order of a thousandths. The transition from one frame to the next, i.e., the path of the surrogate, is reasonably smooth, and is not subject to discontinuities; this would be evident otherwise.

A domain boundary, known as the ROI, was created using the outline of each surrogate; Ncorr requires that the ROI be white and the background of the image to be black [92]. The ROI was superimposed directly on the respective surrogate in the reference image. This ensured that a valid ROI boundary was established.

The next steps involved user defined parameters as defined in Chapter 3.1 (see Appendix C, Table C.1 for parameter values).

DIC parameters were chosen by the user in the next step. A preview window with the surrogate's image was used to guide parameter selection. A subset radius of 10 pixels was chosen as it included a minimum of three markers within the subset and did produce largely noisy displacement data; this is a requirement for Ncorr [92]. Additionally, as the speckle pattern was highly contrasted in comparison to other encasement features and only every other frame was used, a subset spacing of 0 was used. This signifies that at every pixel, a subset was used to collect DIC data; in other words, if a subset spacing of 1 was used, a subset would be tracked at every other pixel. Lower subset spacing values can increase computational time, but they provide an overlap in DIC data. This can be beneficial at geometric discontinuities, as higher resolution results would be provided by the small subset spacing. The next parameter was the iteration number cutoff. This was set to 50, which was the maximum amount of times the solver will process the frames, if needed, to ensure the region was solved correctly; the algorithm notifies the user of the amount of iterations used. Ideally, a low number of iterations to convergence (well below the cutoff value) would be required to solve the region properly. If the algorithm required the maximum number of iterations, seed placement should be reconsidered (described below).

Once these parameters were selected, the initial setup for DIC analysis could begin. Seeds were evenly placed within the ROI to allow for parallel computation and acted as initial guesses for the algorithm. A preview window showed seed placement in the reference image and all subsequent images. Proper seed placement resulted in the seeds being in the exact same locations in each frame, which would result in a low correlation coefficient. If the seeds were placed poorly, they would appear in different locations from the initial locations within the reference

image. After proper seed placement was obtained, the programme performed the DIC analysis.

Once the frames were solved, the displacements were calculated by setting a line over an object with a known distance within the reference image and providing the known measurement value. The algorithm then computes the pixel resolution and applies it to the displacement data; the pixel resolution obtained by Ncorr was comparable to those stated above (Chapter 4.3). Finally, strain values were calculated from the displacement data. This was done using a strain radius of 15 pixels and was selected based on previous experimentation. The strain radius, as previously stated, groups data points within the radius and fits them to a plane; this can be visually seen in the preview window and is meant to aid the user. Smaller strain radii resulted in large amounts of noisy strain data. This occurred because fewer points were fitted to the plane, which allowed for more strain variations to be included in the calculation. Larger strain radii produced strain fields that seemed largely uniform because large amounts of data were fitted to the plane, losing any strain variations in the process. Therefore, the selected value was the middle of both extremes. The value was small enough to remove noisy strain data, but not large enough to remove meaningful strain data.

The complete DIC analysis can be visualised and saved in many formats. Displacement (u and v) and strain (ϵ_{xx} , ϵ_{yy} and ϵ_{xy}) plots can be modified in the DIC programme. The main two parameters that can be changed are the axis values and the transparency of the plot on the specimen. Images or .gif files can then be saved for visualization purposes. In the Matlab terminal, the raw displacement and strain data, along with parameter and information pertaining to both, can be obtained. Data for displacements and strains with respect to the reference image or current image can also be obtained.

A sensitivity test was not performed on the parameters used in the DIC analysis. The basis for parameter selection was mainly obtained from a publication [81] by the DIC programme developers and the provided instructional manual [92], as well as other DIC-based literature and educational materials. The outlined requirements and issues to be aware of were considered and followed when choosing the appropriate parameter values. These values were varied when becoming familiar with the programme, prior to usage in this study, to acknowledge the extent at which the programme can analyse data.

As DIC provides full field data, it was of interest to obtain approximate strain values between two regions corresponding to Markers 1 and 6 and Markers 6 and 7 (Figure 35). These regions were of particular interest to observe the influences that the internal capsule and the gyrus has on the sulcus. Rectangular ROIs were created in Matlab to obtain strain data between marker pairings from the outputted full field data (Figure 35). The strain data obtained from within the rectangular ROI was then averaged, producing a singular strain value per frame for the given region between the markers. The size of the new rectangular ROI was reflective of the distance between the markers. Strain in the x- and y- directions, and shear were provided by the algorithm. From these values, peak maximum principal strains (MPS) were calculated using equation 6:

$$\epsilon_{1,2} = \frac{\epsilon_{xx} + \epsilon_{yy}}{2} \pm \sqrt{\left(\frac{\epsilon_{xx} - \epsilon_{yy}}{2}\right)^2 + \left(\frac{\epsilon_{xy}}{2}\right)^2} \quad (6)$$

where ϵ_1 and ϵ_2 are the maximum and minimum principal strains, ϵ_{xx} is strain in the x- direction, ϵ_{yy} is strain in the y- direction, and ϵ_{xy} is shear strain in the tensor form. Additionally, two-dimensional volumetric strain, the change in volume over the initial volume, also defined as the sum of strains in all directions, was also

calculated:

$$\epsilon_v = \frac{\Delta V}{V} = \epsilon_{xx} + \epsilon_{yy} \quad (7)$$

where ϵ_v is volumetric strain, ΔV is the change in volume, V is the volume, ϵ_{xx} is strain in the x- direction, and ϵ_{yy} is strain in the y- direction. The volumetric strain values can be found in Appendix 3.1, Tables C.3 and C.4.

The method of obtaining averaged strain values between marker pairings was not exact due to a combination of Matlab and user capabilities. When averaging the Ncorr data between markers, a new rectangular ROI was selected that was within the region of the marker pairings, but was not a direct path between the markers (Figure 35). For example, two markers that had a direct path that was diagonal would have a vertical rectangular ROI that was slightly to the right of one marker and to the left of the other marker; the rectangular ROI could not be rotated on an angle to average strain values. This may have influenced the results marginally.

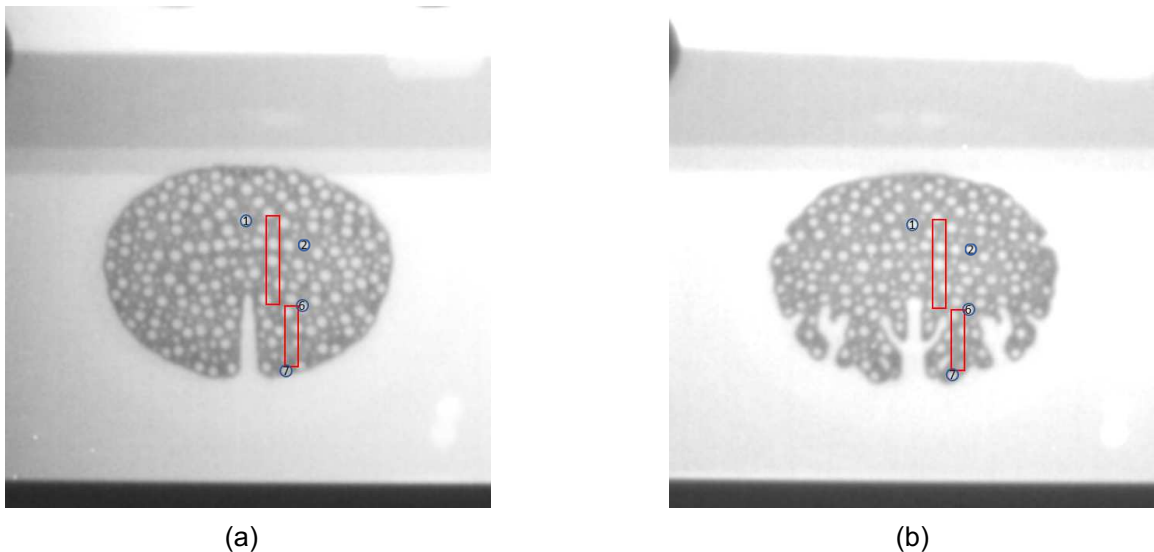


Figure 35: Smooth (a) and complex (b) surrogates with highlighted markers (blue) with the rectangular ROI (red) used to calculate strain within a region.

A direct comparison between DIC and individual particle tracking was also desired. This was done using a similar methods as described above, but on a few selected markers (circled in Figure 35) and only on the three main orientations. The center pixel coordinates of each marker was then used to extract displacement data via a Matlab script. The DIC displacement data was first compared to displacements found through individual particle tracking. A Matlab script was then used to calculate direct strains between two markers:

$$\epsilon_d = \frac{R - R_0}{R_0} \quad (8)$$

and

$$R = \sqrt{(x_2 - x_1)^2 + (y_2 - y_1)^2} \quad (9)$$

where R_0 is the original distance between both markers, R is the current distance between both markers, and x_1 , x_2 , y_1 , and y_2 are the coordinates of two markers within a pairing.

4.3.2 Particle Tracking

The Mosaic ParticleTracker [99] was used to detect particle features, which allowed for the motion of individual markers to be tracked; every frame was analysed (See Appendix C, Table C.2 for parameter values). The parameters described below have been defined in Chapter 3.2.

The image sequence was uploaded into an open-source add-on to Fiji [115], a distribution of ImageJ [116], an image processing programme. Next, the Mosaic ParticleTracker app was launched and initially provided a list of parameters, along with a preview window. A particle radius of 3 was used to create a region

of interest around the marker. This smaller value allowed for continuous tracking of every marker within the surrogate, but was susceptible to jitter. This was mainly observed in markers within the internal capsule. A radius of 4 was also tested, but it led to additional issues. That radius had increased failed tracking attempts for markers throughout the surrogate. That radius was more susceptible to jumping from the originally detected marker to neighbouring markers. Attempts were made to correct this issue using information provided in the particle tracker's manual [101], but it proved unsuccessful. Trajectories that could be obtained were identical to those obtained when using a radius of 3, but had fewer instances of sub-pixel jitter. A radius of 4 would lead to cleaner strain responses, but as using that parameter value was difficult to successfully and continuously use, the smaller radius of 3 was chosen instead.

The other parameters were also based on marker characteristics, as described in Chapter 3.2. Within the algorithm, non-particle discrimination aimed to differentiate between particles (markers) and non-particles. This parameter, known as the cutoff, was based on brightness intensities scores. A value of 0 was used for maximum detection, meaning that the algorithm detected all bright pixel values within each image. As the speckle patterns within the surrogates were highly contrasted, this parameter value ensured that all markers within the surrogate were detected. In combination with the cutoff value, a percentile value of 2 was used. This parameter determines what brightness pixels must have to be considered a marker. A percentile value of 2, being on the larger range for the parameter, allowed for more markers to be detected within the surrogates, as more intensities were included in the detection. The low cutoff value and high percentile value meant that other high contrast regions (i.e., around the screws and anvil) had false markers detected. Although regions outside of the speckle pattern were detected, only desired markers from within the surrogates were selected and saved individually.

As the previous parameters were used to detect the markers, additional parameters were used to link markers throughout the entire data set. The link range and displacement parameters were kept small, as the markers were well defined, were easily tracked, and did not move far from frame to frame. A link range of 2 was used and meant that the algorithm took into account two subsequent frames when matching a marker in one frame to the next. A displacement value of 6 pixels was used, meaning that the algorithm limited particle motion to 6 pixels between each frame. The markers did not have significant motion between each frame, therefore keeping this value small limited the algorithm's ability to incorrectly match particles. Additionally, three options for dynamics were available: Brownian, constant velocity, and straight line motion. Brownian motion was chosen because the shift in pixels within each marker moved rapidly between frames due and it provided continuous tracking of the markers. A test was performed to determine if the type of dynamics selected changed the x - and y - coordinates of the markers. Marker 7 from the complex surrogate (conditions: one trial, 50 cm, downward orientation) was tracked three times, keeping all parameters consistent, except for the dynamics. The outputted x - and y - coordinates were identical across all dynamic types.

To determine the capabilities of the Mosaic ParticleTracker algorithm, a series of tests were performed. Initially, 10 identical images were used to track a single marker three times. The outputted pixel coordinate values were the same. The same was true when analysing 10 moving images. Additional tests were performed with known displacements to determine the accuracy of the tracking algorithm. This was done by determining the number of frames crossed by an object with a known size. Afterwards, a marker was tracked for the same amount of frames to obtain coordinate data. Next, the experimental pixel to millimetre ratio was applied. Within the y - direction, the resulting differences in displacement values were found to be minimal (approximately 1% error). Additionally, when

moving an artificial marker in only the y-direction by 0.1 mm for a total of 1 mm, the algorithm outputted y- values that deviated by 0.09 ± 0.04 mm when selecting a particle radius that was slightly smaller than the marker radius. The x- values, which were consistent in the images and therefore should be at the same y- position, produced relative displacement values of 0.00 ± 0.05 mm. When using a particle radius that was slightly larger than the marker radius, the y- values varied by 0.10 ± 0.00 mm and the x- values varied by 0.00 ± 0.00 mm; the values were quite small, and therefore accurate. As a note, very small values for standard deviations were calculated when using a large particle radius, but were reported as 0.00 mm due to significant figures.

Mosaic ParticleTracker allowed for individual markers to be tracked, unlike Ncorr. Seven, near identical regions were selected across both surrogates within the brain gyrification study (Figure 36). These regions were based on areas within the complex surrogate, as its gyrification had the most variation. These locations included: the internal capsule, the main fissure, the sulcus, and the gyrus.

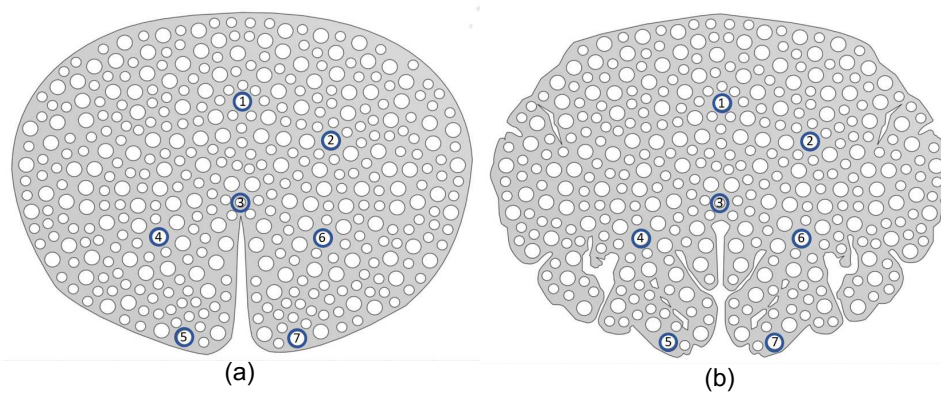


Figure 36: Smooth (a) and complex (b) surrogates with individual markers of interest circled and enumerated.

Individual markers that were situated in different regions were mainly compared to a single marker that was within the internal capsule. An additional set of

marker comparisons were made between markers in the gyrus and near the sulcus. The ability to select and track individual markers provides a unique insight, especially when a full field analysis cannot be used; this method removed the uncertainties caused by boundary iteration errors.

The pixel coordinates of each marker were exported as a CSV file. An alignment correction was then applied to each trial to ensure that surrogate location relative to the number of frames to impact was consistent across trials. This was done by removing initial data coordinates within the raw CSV files, if required. This step aided in aligning each trial's strain history with the other trials.

Additional post-Mosaic analysis was done using Matlab scripts, which took the marker data and calculated displacements. Direct strain values were also calculated using Equations 8 and 9. All three trials were averaged to create one plot, with the final plot having all four averaged strain responses across each drop height, if applicable. Averaging the data to create one averaged strain response was proven to be an adequate representation of the individual trials; the average and median trial were near identical (Figure 37). Additional supporting figures can be found within Appendix C, Figures C.55 and C.56. Furthermore, for each surrogate, the average and standard deviations for peak compressive and tensile strains across all four averaged drop heights per main marker pairing were calculated and can be found within Chapter 5.1.2; for the inward orientation this was done using the three trials. The average and standard deviation for peak compressive and tensile strains across the three trials per drop height for the downward and upward orientations were also calculated for each surrogate. This was only completed for Markers 1 and 2, 1 and 6, and 6 and 7, and can be found within Appendix C, Tables C.5 to C.8. The average and standard deviations for peak strains were calculated using strain data that occurred prior to 20 ms, as after this time the strain

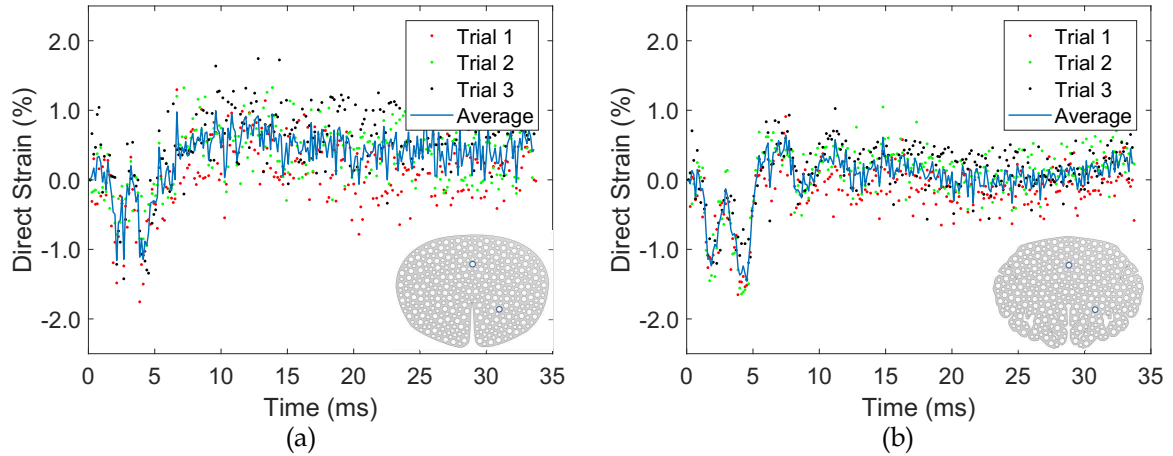


Figure 37: The averaged strain response superimposed on the individual trials used to create the average between Markers 1 and 6 of (a) the smooth and (b) the complex surrogates. The strain data is from a 90 cm drop with the surrogates being dropped in the downward orientation. The averaged and median strain history follow near identical paths.

responses showed minimal to no variations; values tended to return to $\sim 0\%$ strain.

Previously, tests were performed on the particle tracker to determine the capabilities of the tracking algorithm. Once the marker pairings were defined, the resulting uncertainty in the strain measurements was determined. This was done using post-impact images from one trial when the surrogates and apparatus were at rest on the anvil some time after impact. Ideally, the strain between marker pairings should have been zero at this time, as the specimens should not be deforming, nor the drop apparatus moving. The markers were tracked using the same parameter values defined above and strains were then computed. The average strain values and standard deviations can be found in Tables 1 and 2.

Once strain calculations were completed, strain rate was also computed from the averaged strain responses for the surrogates when they were dropped from a height of 90 cm for the downward and upward orientations and from a height of

Table 1: The average strain values per marker pairing obtained when the smooth surrogate was at rest on the anvil in the downward orientation. Values in brackets represent the standard deviation.

Marker Pairing	Average strain value (%)
1 and 2	0.2 (0.5)
1 and 3	0.0 (0.1)
1 and 4	0.1 (0.1)
1 and 5	0.0 (0.0)
1 and 6	0.0 (0.1)
1 and 7	0.0 (0.0)
4 and 5	-0.2 (0.4)
6 and 7	0.0 (0.1)

50 cm for the inward orientation. This calculation was only completed for Markers 1 and 6 (internal capsule to sulcus) and Markers 6 and 7 (sulcus to gyrus); these two marker pairings included a marker in the sulcus, which has been previously discussed as a location of interest within brain injury research. A Savitzky-Golay filter with a window of 15 was used to smooth the data. This provided a smoothed version of the unfiltered average strain response without losing the main trends of the original data.

The above direct strain calculations were also performed on the viable *ex vivo* porcine brain tissue sections. Markers within regions of gyrification were selected and compared. Within the regions of the sulci and gyri, tissue discontinuities are possible. The markers chosen for comparison were therefore carefully selected to minimize the possibility of their being a material discontinuity between the two chosen markers, as this could affect the strain results. For example, if neighbouring gyri separated during impact, there would not be continuous tissue material between both markers, there would only be a void caused by the separation. The

Table 2: The average strain values per marker pairing obtained when the complex surrogate was at rest on the anvil in the downward orientation. Values in brackets represent the standard deviation.

Marker Pairing	Average strain value (%)
1 and 2	-0.5 (0.2)
1 and 3	-0.1 (0.1)
1 and 4	-0.1 (0.0)
1 and 5	-0.1 (0.0)
1 and 6	0.0 (0.1)
1 and 7	0.0 (0.0)
4 and 5	-0.2 (0.1)
6 and 7	0.0 (0.1)

strain experienced between markers would then be reflective of that separation; it would not be a valid strain caused within the tissue material. To ensure that marker pairings would always have tissue between them, optical and X-ray images were compared.

Chapter 5

Results and Discussion

5.1 Brain Gyrification Study

The design of the brain tissue surrogates allowed for direct comparisons to be made between both extremes of brain gyrification, as the speckle pattern was near identical between both surrogates. Additionally, as the two surrogates were dropped in unison with the same constraints, they experienced the same loading conditions. The following sections will review and discuss the results from the brain gyrification study.

5.1.1 Digital Image Correlation Analysis

All main orientations were analysed using DIC via Ncorr, a Matlab-based software [81]. Ncorr outputs strain in three ways: normal to the impact plane, lateral, and shear. A sample set of strain responses showing the three kinds of strain are provided for both surrogates in the downward facing orientation (Figures 38 and 39). The sample data sets are of strain fields at 4 ms after initial contact with the anvil from one trial with a drop height of 50 cm.

Under the same loading conditions, both surrogates exhibited differences in

strain, particularly within regions of gyrification. The lateral strain field of the surrogate with a smooth cortex showed a single, low level compressive strain concentration at the fissure (Figure 38a). The compression may have been the result of the two hemispheres moving towards each other during impact. At 4 ms after initial impact, the strain field normal to the impact plane (Figure 38b) and in shear (Figure 38c) remained muted with only minor strain concentrations. The lateral tensile strain may correspond to the surrogate being compressed from impact causing the surrogate to stretch outwards. Additionally, the surrogate did not experience large amounts of shear strain at this point, which was likely due to a combination of orientation and lack of brain gyrification.

The lack of gyrification in the smooth surrogate appeared to not allow for large movements of the two hemispheres. The strain caused by the impact did not create a large localized response. Instead, the strain appears to be distributed uniformly through the regions that lacks gyrification, closest to the region of impact. The strain within the surrogates were relatively negligible, with the majority of peak strains occurring at boundaries, which may be the result of boundary errors.

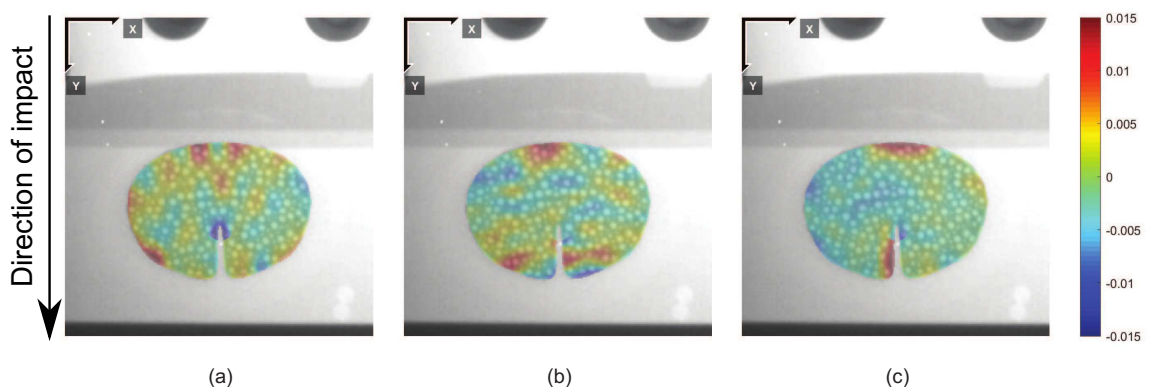


Figure 38: Strain fields from the smooth surrogate when dropped in the downward orientation from 50 cm from one trial. Each image corresponds to a specific strain field occurring at 4 ms after initial contact with the impact plate: a) ϵ_{xx} , b) ϵ_{yy} , and c) ϵ_{xy} .

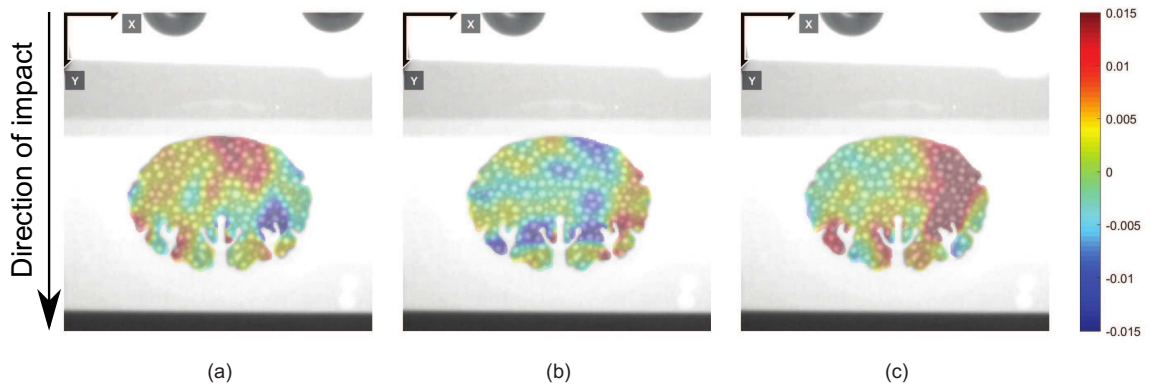


Figure 39: Strain fields from the complex surrogate when dropped in the downward orientation from 50 cm from one trial. Each image corresponds to a specific strain field occurring at 4 ms after initial contact with the impact plate: a) ϵ_{xx} , b) ϵ_{yy} , and c) ϵ_{xy} .

While keeping the range of strain values consistent across both surrogates, it was observed that the complex surrogate experienced greater strain concentrations than the smooth surrogate. A direct comparison between both sets of strain data can be made as the images are from the same drop event. An increase in strain was primarily seen throughout the cortical region with a focus within the gyri and near the sulci (Figure 39). After initial contact, the lateral strain field showed large tensile strains within the internal capsule, which dissipated towards the regions of gyrification. Isolated concentrations of tensile and compressive strains were observed in the regions of gyrification (Figure 39a). Within the strain field normal to the impact plane, large concentrations of compressive strain were observed mainly within the regions of gyrification, a likely combination of gyrification and orientation of impact (Figure 39b). Additionally, large positive shear strains were observed in the surrogate as well (Figure 39c). This was mainly observed on the right side of the surrogate, the likely result of its positioning in the drop apparatus; a slight increase in motion was observed in regions of both surrogates that were closer to the center of the drop apparatus.

The strain fields of the complex surrogate showed large strain values, especially within regions of gyrification. Each gyrus was independent from neighbouring gyri, and were relatively thin with a smaller area compared to the two larger hemispheres on the smooth surrogate. The thinner regions may be more susceptible to external forces and strain concentrations than the two larger, uniform regions of the other surrogate. The variations in gyrification may have caused the strain response to be seen further away from the surface, moving the strain effects inward towards the center of the surrogate, surrounding the sulci. The differences in strain responses between surrogates implies that a specimen with increased gyrification contributes to strain within those regions, while those with minimal to no gyrification may not.

The above strain fields showed clear differences between each surrogate at a given time and orientation. A focus on time-lapsed images of a given strain component (i.e., ϵ_{xx} , ϵ_{xy} , and ϵ_{yy}) for each orientation and surrogate is provided below. Beginning with the downward orientation and looking at the strain component ϵ_{yy} showed distinct trends; additional figures with strain components ϵ_{xx} and ϵ_{xy} can be found in Appendix C, Figures C.1 to C.4. The smooth surrogate did not experience large variations in strain, especially within the central region (away from boundaries) as the values appeared to remain mostly near $\sim 0 \pm 0.4\%$ strain (Figure 40). Only localised, concentrated strain values of around -2% and $+2\%$ strain were observed around the boundaries. This could be the contributing effect of iteration errors, which DIC programmes are known to have near boundaries.

Under the same loading conditions, the complex surrogate experienced much larger strain variations throughout the surrogate as the impact event progressed

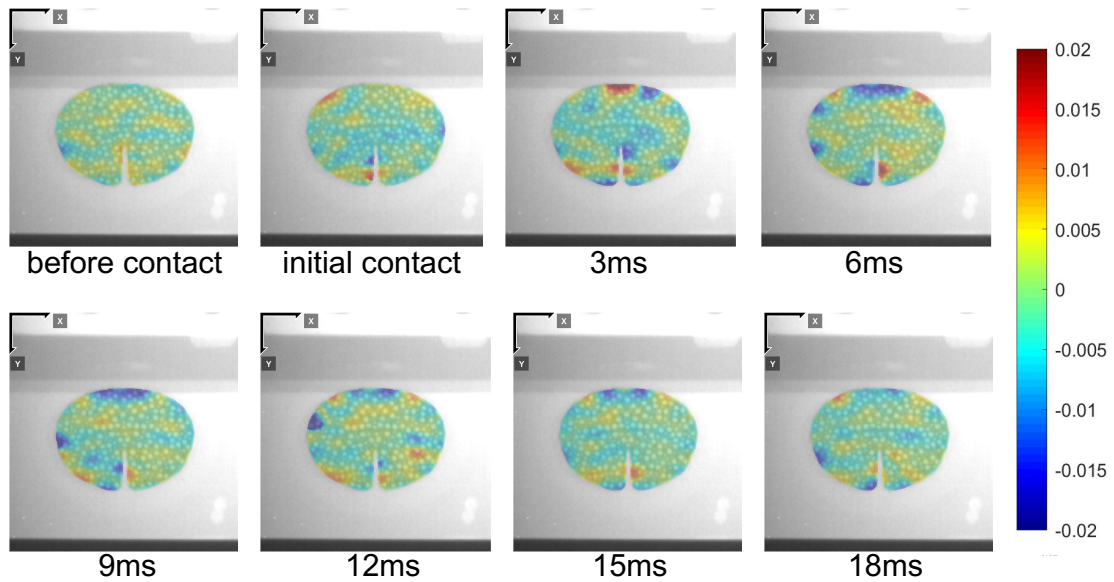


Figure 40: A sequence of strain fields denoting ϵ_{yy} strains experienced by the smooth surrogate when dropped in the downward orientation from 50 cm from one trial. The sequence includes frames before contact and initial contact with the anvil. The times labelled correspond to time after initial contact with the anvil.

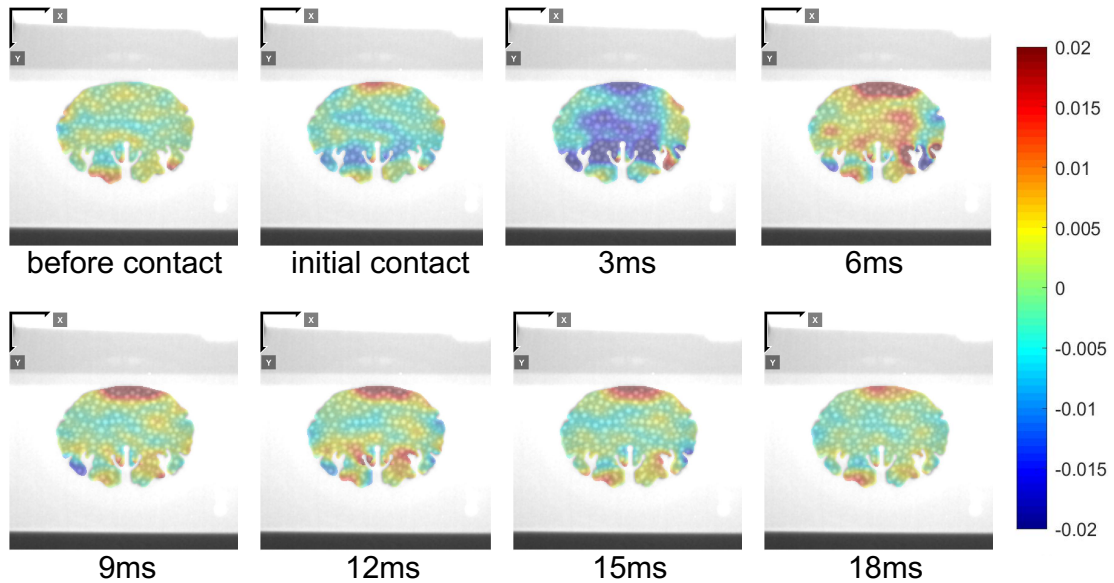


Figure 41: A sequence of strain fields denoting ϵ_{yy} strains experienced by the complex surrogate when dropped in the downward orientation from 50 cm from one trial. The sequence includes frames before contact and initial contact with the anvil. The times labelled correspond to time after initial contact with the anvil.

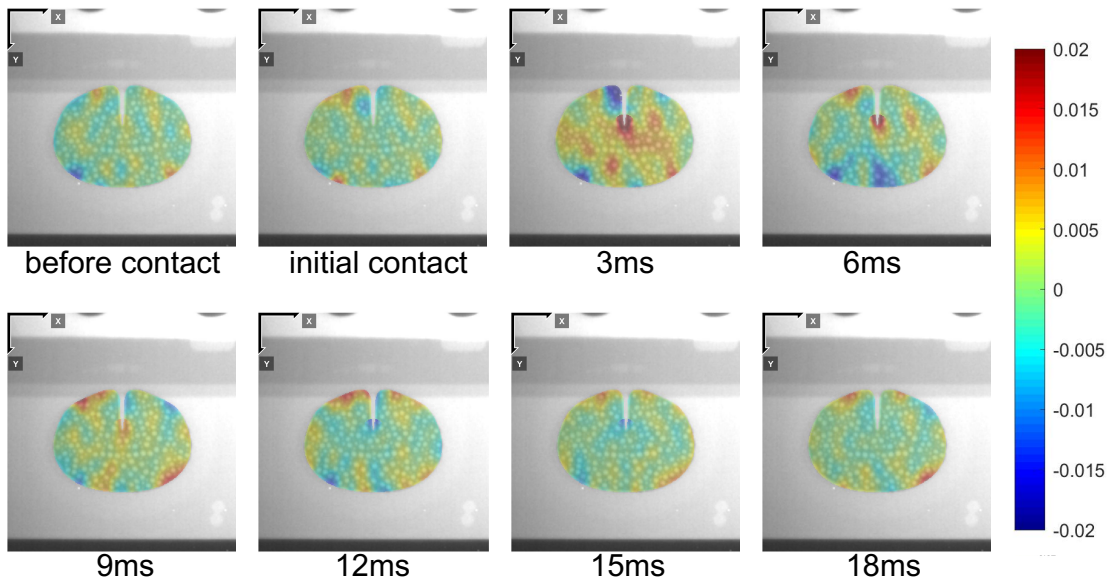


Figure 42: A sequence of strain fields denoting ϵ_{xx} strains experienced by the smooth surrogate when dropped in the upward orientation from 50 cm from one trial. The sequence includes frames before contact and initial contact with the anvil. The times labelled correspond to time after initial contact with the anvil.

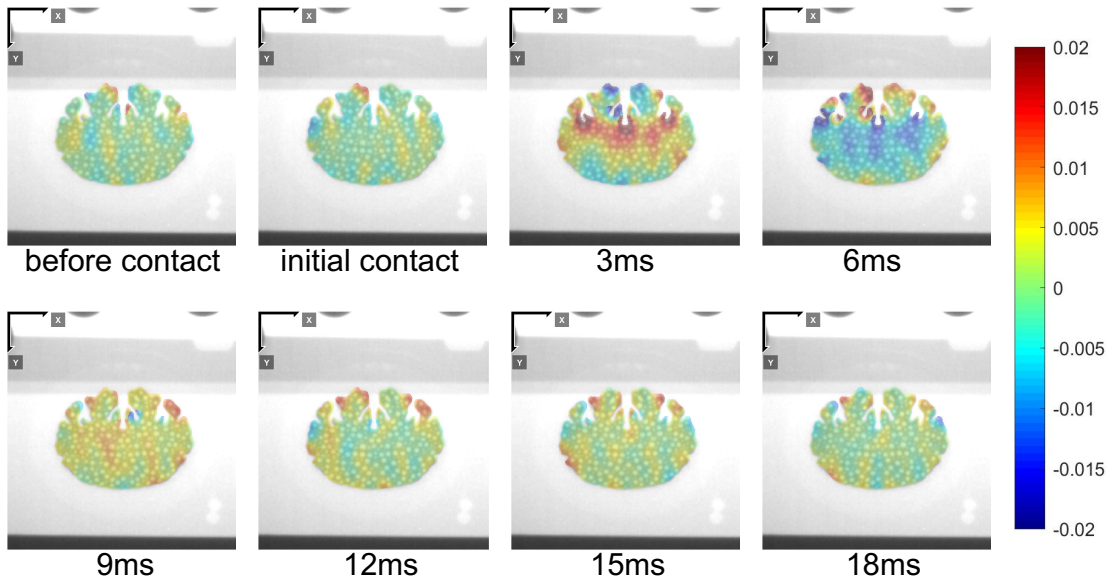


Figure 43: A sequence of strain fields denoting ϵ_{xx} strains experienced by the complex surrogate when dropped in the upward orientation from 50 cm from one trial. The sequence includes frames before contact and initial contact with the anvil. The times labelled correspond to time after initial contact with the anvil.

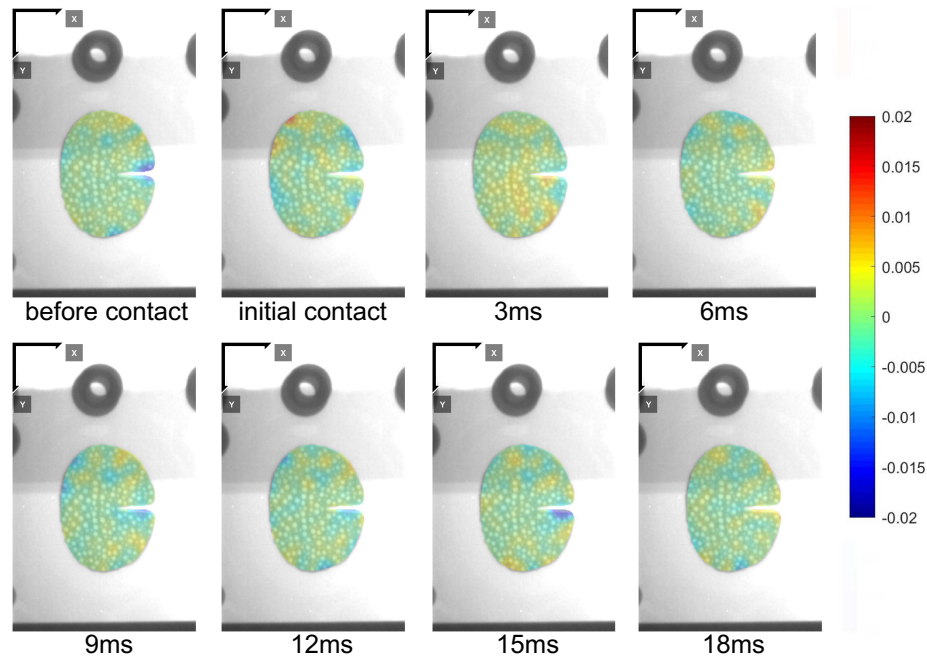


Figure 44: A sequence of strain fields denoting ϵ_{xy} strains experienced by the smooth surrogate when dropped in the inward orientation from 50 cm from one trial. The sequence includes frames before contact and initial contact with the anvil. The times labelled correspond to time after initial contact with the anvil.

(Figure 41). At approximately 3 ms after initial contact with the anvil, large compressive strains ($\sim 2\%$) appeared within regions of gyrification, which extended into the central regions of the surrogate. This was expected, as the surrogate was impacted moments before near the cortex. Following this time, the surrogate experienced tension before returning to near zero strain ($\sim 0 \pm 0.3\%$ strain).

Both surrogates had different responses, especially at the 3 ms mark. The smooth surrogate did not experience large compressive strains, unlike the complex surrogate. These differences are a likely result of gyrification. The bulkier, more uniform regions possessed by the smooth surrogate may distribute strain better, whereas the complex surrogate, which has gyri and sulci, may be more susceptible to such impacts. This region in the complex surrogate has geometric

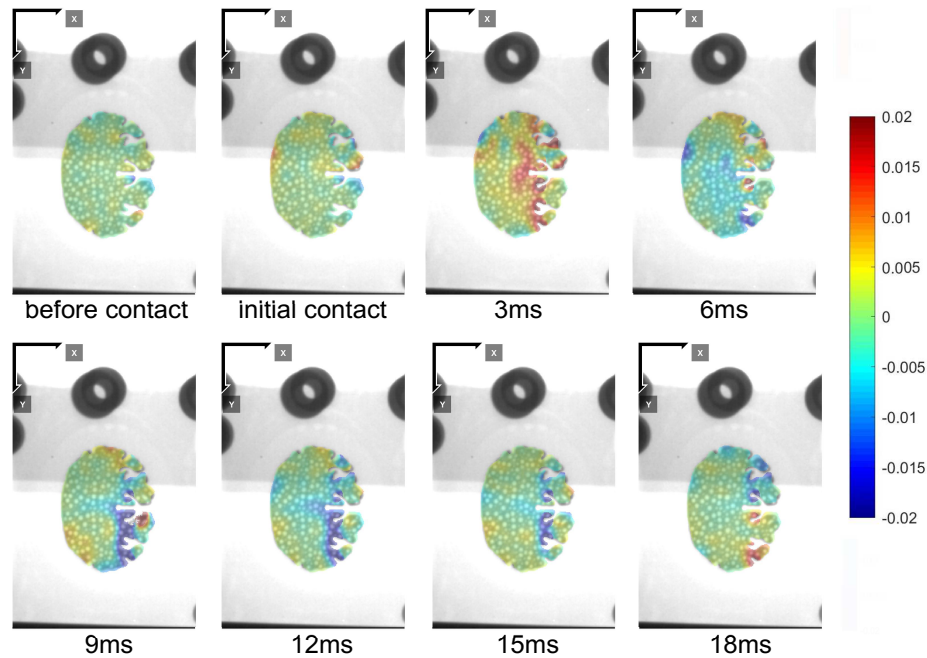


Figure 45: A sequence of strain fields denoting ϵ_{xy} strains experienced by the complex surrogate when dropped in the inward orientation from 50 cm from one trial. The sequence includes frames before contact and initial contact with the anvil. The times labelled correspond to time after initial contact with the anvil.

discontinuities, which can lead to strain concentrations.

Similar trends were observed in the surrogates when dropped in the upward orientation and measuring ϵ_{xx} strains (Figures 42 and 43); additional figures with strain components ϵ_{xy} and ϵ_{yy} can be found in Appendix C, Figures C.5 to C.8. Both surrogates experienced minimal strain prior to impact and after 12 ms. At 3 ms, the smooth surrogate experienced tensile strains (between 0.5% to 1.5%), which was mostly isolated to the interior region; at this same time it should be noted that the smooth surrogate experienced large compressive strains ($\sim 1.8\%$) in the y-direction (ϵ_{yy}), but the effects did not last long. A tensile strain concentration of $\sim 2\%$ strain was observed at the location of hemispheric distinction (the fissure) at this time as well. This was followed by a slight shift to compressive strains (of

around 1%) at 6 ms (as the surrogate is leaving the anvil), before returning to near zero strains.

The complex surrogate, under the same conditions, experienced similar trends as the smooth surrogate, but with larger magnitudes of strain. Tensile strains between 1% to 2% strain were observed at 3 ms. These strains were observed within a larger region than that of the smooth surrogate. Within the complex surrogate, tensile strains were experienced across the entire region below the sulci and gyri. This is likely an effect of gyrification, where strain concentrations occur around regions of geometric discontinuity. Additionally, as a result of the impact, the surrogate experienced motion within the regions of gyrification that likely caused the regions that underwent tension to extend outwards. At the 6 ms mark, the surrogate underwent compression (between 0.8% to 2%) within the same region, the result of this region coming together during the rebound from the anvil. Afterwards, the surrogate experienced near zero strains, as it returned to its initial placement configuration.

The trend of the complex surrogate experiencing increased strain values over the smooth surrogate regardless of orientation and strain component continued with the inward orientation and shear strains. This was also true for strain components ϵ_{xx} and ϵ_{yy} when the surrogates were dropped in the inward orientation (Appendix C, Figures C.9 to C.12). Overall, the smooth surrogate appeared to not experience any notable shear strains, although minimal shear strains of around 0.6% was observed at 3 ms (Figure 44). In this orientation, minimal motion observed in the surrogate is a likely explanation.

Under the same conditions, large quantities of shear strain were observed near regions of gyrification in the complex surrogate (Figure 45). Positive shear strains (between 0.5% to 2%) were first observed at 3 ms, followed by negative shear

strains of the same magnitude for almost the remainder of time. The smaller regions (gyri and sulci) within gyrification were likely more susceptible to motion, causing the observed response.

A Comparison of Select Regions within Each Surrogate Using DIC

Two pairs of markers that were of particular interest within the brain gyrification study were analysed using DIC. This included Markers 1 and 6, corresponding to the internal capsule and the base of the sulcus, and Markers 6 and 7, which corresponded to the base of the sulcus and the peak of the gyrus. Within Tables 3 and 4 are the strain data sets for both surrogates; volumetric strain values can be found in Appendix C, Tables C.3 and C.4. As Ncorr may be susceptible to iteration errors, only the markers of interest were studied to see how the results compare to those obtained through individual particle tracking.

Within the tables, all strain values were of the greatest value calculated within the initial 20 ms of data recording. Only data prior to 20 ms was analysed in this section, although Ncorr data was obtained for the entire time frame, as most strain values returned to near zero after this time. The values within the tables may have occurred at different timestamps than all other values. The peak MPS and volumetric strain values were calculated from the raw data output and were calculated independently from the strain values shown in the tables. As Ncorr exported strain values per pixel within the ROI, pixel values were averaged within the ROI first and then averaged across three trials. The size of the ROI varied for each marker pairing, as the ROI expanded the distance between markers; the ROI region for Markers 1 and 6 was 432 pixels and for Markers 6 and 7 the value was 288 pixels. For each surrogate, across all orientations and trials, the individual strain values used to calculate the averaged strain value were comparable; typically a standard

deviation of less than 0.2% in strain values amongst trials.

The differences in responses may have implications that increased brain gyration may influence strain fields. These conclusions are supported in Tables 3 and 4. Per marker pair, strain values tended to increase with drop height, and were location and orientation dependent. The peak MPS was always greater for the complex surrogate when comparing Markers 6 and 7; this was also true for volumetric strain. These trends were expected as the variations in gyration are likely to influence strain, which was also supported by the strain fields images showed previously.

While strain values were greatly influenced by gyration (observed between Markers 6 and 7), Markers 1 and 6 showed similar trends, but with minor variations. The values within Table 4 showed instances where the smooth surrogate experienced higher peak MPS than the complex surrogate; this was also observed within the volumetric strain values. This was mainly isolated to the upward orientation, which was the least realistic loading orientation. The other two orientations saw the complex surrogate having higher peak MPS values, which was also observed in marker pairing 6 and 7. Additionally, many peak MPS values were higher in marker pairing 1 and 6 than in marker pairing 6 and 7. It is known from previous literature that injury markers accumulate in regions of the sulci [7–9] and this area corresponds most closely to Marker 6. The higher strain values could indicate, to some degree, that the strain experienced within the surrogates after impact may contribute to the overall magnitude in the strain response. This can imply that gyration may influence the internal strains and not only those observed at the cortex.

The DIC results showed that the complex surrogate had increased strain values over that of the smooth surrogate. This was especially observed in the regions

Table 3: Averaged strain data between Markers 6 and 7 for both surrogates in all orientations analysed with DIC. Markers 6 and 7 are found near the vicinity of the sulcus and at the peak of the gyrus, respectively. Instantaneous maximum strain values were only considered during the first 20 ms of the impact event and may not have occurred concurrently.

Gyrification	Orientation	Height (cm)	Peak Tensile Strain (%)		Peak Compressive Strain (%)		Peak Shear Strain (%)	Maximum Principal Strain (%)	
			ϵ_{xx}	ϵ_{yy}	ϵ_{xx}	ϵ_{yy}	ϵ_{xy}	ϵ_1	ϵ_2
			Smooth	Downward	30	0.1	0.2	0.2	0.3
Complex			0.3	0.3	0.3	1.0	0.5	0.4	-1.0
Smooth		50	0.1	0.4	0.2	0.3	0.2	0.4	-0.3
Complex			0.7	0.7	0.4	1.2	0.9	0.9	-1.3
Smooth		70	0.3	0.3	0.2	0.4	0.2	0.3	-0.4
Complex			0.8	0.7	0.3	1.5	0.7	0.9	-1.5
Smooth		90	0.3	0.3	0.2	0.5	0.3	0.4	-0.5
Complex			1.0	0.7	0.5	1.6	0.5	1.1	-1.6
Smooth	Upward	30	0.2	0.2	0.2	0.3	0.2	0.3	-0.3
Complex			0.4	0.5	0.3	1.4	0.4	0.5	-1.4
Smooth		50	0.5	0.2	0.1	0.7	0.4	0.5	-0.7
Complex			0.5	1.0	0.3	1.5	0.5	1.0	-1.5
Smooth		70	0.7	0.1	0.1	1.0	0.5	0.7	-1.0
Complex			0.6	1.2	0.3	1.8	0.5	1.2	-1.8
Smooth		90	0.5	0.4	0.0	0.3	0.4	0.6	-0.3
Complex			0.5	0.9	0.3	1.5	0.5	0.9	-1.6
Smooth	Inward	50	0.3	0.1	0.1	0.4	0.2	0.3	-0.4
Complex			1.5	0.3	0.6	0.4	1.0	1.5	-0.8

Table 4: Averaged strain data between Markers 1 and 6 for both surrogates in all orientations analysed with DIC. Markers 1 and 6 are found within the internal capsule and near the vicinity of the sulcus, respectively. Instantaneous maximum strain values were only considered during the first 20 ms of the impact event and may not have occurred concurrently.

Gyrification	Orientation	Height (cm)	Peak Tensile Strain (%)		Peak Compressive Strain (%)		Peak Shear Strain (%)	Maximum Principal Strain (%)	
			ϵ_{xx}	ϵ_{yy}	ϵ_{xx}	ϵ_{yy}	ϵ_{xy}	ϵ_1	ϵ_2
			Smooth	Downward	30	0.4	0.2	0.4	0.4
Complex			0.7	0.5	0.3	1.0	0.5	0.8	-1.0
Smooth		50	0.4	0.2	0.5	0.6	0.4	0.4	-0.7
Complex			0.8	0.7	0.4	1.2	0.5	0.8	-1.2
Smooth		70	0.6	0.4	0.6	0.9	0.5	0.6	-0.9
Complex			0.9	0.8	0.5	1.7	0.4	1.0	-1.7
Smooth		90	1.0	0.5	0.5	1.3	0.5	1.0	-1.3
Complex			1.0	0.8	0.5	1.8	0.3	1.0	-1.8
Smooth	Upward	30	0.5	0.4	0.2	0.8	0.4	0.5	-0.9
Complex			0.7	0.5	0.5	1.2	0.3	0.8	-1.2
Smooth		50	1.0	0.5	0.2	1.4	0.7	1.0	-1.5
Complex			0.9	0.9	0.7	1.6	0.3	0.9	-1.6
Smooth		70	1.6	0.5	0.0	1.9	0.8	1.7	-2.0
Complex			0.9	1.0	0.9	1.9	0.5	1.0	-1.9
Smooth		90	1.2	0.5	0.1	1.6	0.6	1.2	-1.6
Complex			1.1	1.1	0.6	2.0	0.5	1.1	-2.0
Smooth	Inward	50	0.4	0.0	0.1	0.7	0.4	0.4	-0.7
Complex			0.6	0.0	0.3	0.7	0.7	0.7	-0.8

of the sulci and gyri. It is well documented that DIC algorithms like Ncorr, may produce computational errors around the boundaries of the ROI, which appear as high strain concentrations at the boundaries and can be magnified by smoothing parameters. This was of particular concern around the regions of increased gyrification, where some, though not all, of the strain differences observed between the surrogates may have been the result of computational errors.

To be certain that the differences in strain were in fact a result of gyrification, a second image analysis approach was used. This removed our uncertainties at boundary locations and allowed for selection of specific markers in regions of interest to be analysed. Using a different form of image analysis verified whether the high strain concentrations within regions of gyrification were valid.

5.1.2 Particle Tracking Analysis

The Mosaic ParticleTracker [99] was used to selectively track individual markers at specific locations. The output from Mosaic included x- and y- pixel trajectory coordinates according to frame number and trajectory number. Figure 46a is a portrayal of a selected marker's trajectory that Mosaic can output.

Another form of data interpretation was to convert the x- and y- pixel coordinates to displacement values using Matlab. Displacement data for the markers can also be presented as x-t, y-t, or x-y plots (Figure 46b, 46c, and 46d). While displacement plots are valid, more meaningful results can be obtained such as estimates of direct strain between two markers; strain is commonly used to quantify brain injuries.

As described in Chapter 4.3.2, a total of seven markers were selected from the entire data set based on regions with increased gyrification. As the brain tissue surrogates are symmetrical about the mid-sagittal plane, only one set of markers

will be displayed. The markers within the main text are the pairs that were closest to the center of the impact plane. The other marker pairings, which are mirrors of the markers shown in the main text, came to the similar conclusion as their comparable markers did. The other marker pairings, as well as the supplementary orientations, can be found in Appendix C.

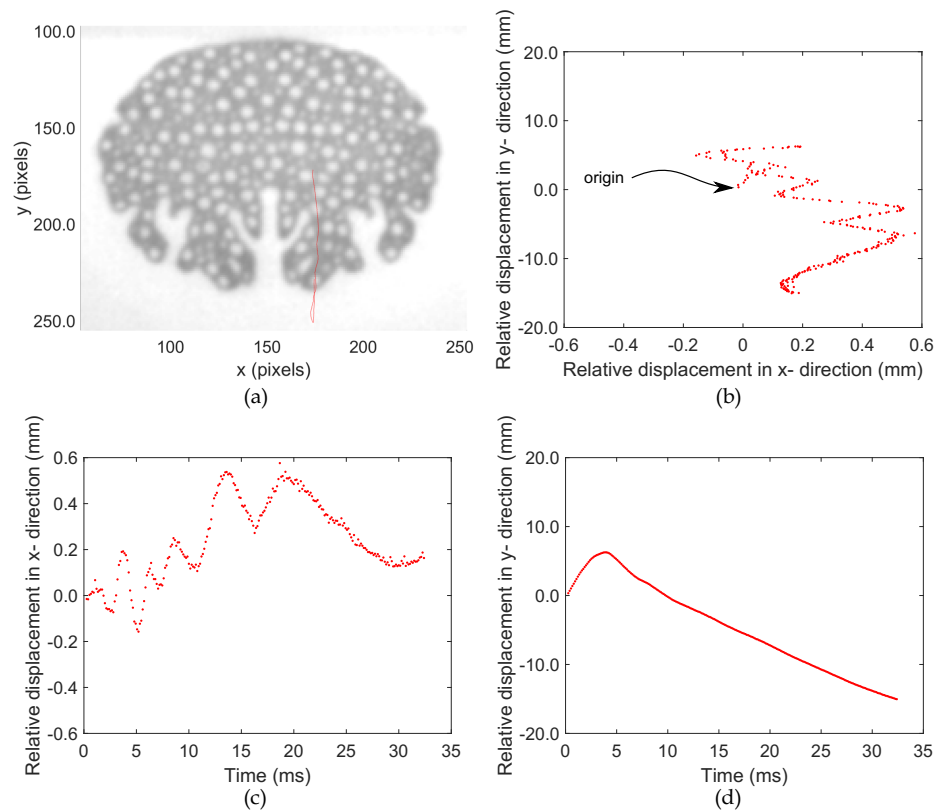


Figure 46: Sample data from one trial of the complex surrogate being dropped from 50 cm in the downward orientation. The (a) trajectory path of Marker 7, (b) the x- versus y- displacement, (c) the x-displacement versus time, and (d) the y-displacement versus time. Note that scales may vary across all figures.

Markers within the internal capsule

Both surrogates shared a common region, the internal capsule. Markers were selected from this region as a baseline for all other comparisons due to their similarities and their distance away from cortical gyrification. The two markers that were selected were completely surrounded by other markers and elastomer material.

Within the internal capsule, marker pairing 1 and 2 showed similar trends in strain values across all orientations and surrogates. In the downward orientation, the strain values remained within a range of $\sim \pm 1\%$ strain for the smooth surrogate (Figure 47a); peak compressive and tensile strains across all four averaged drop heights were $-0.6 \pm 0.2\%$ and $0.8 \pm 0.2\%$, respectively. The strain range experienced by the complex surrogate did exhibit minor strain variations, but within a similar range of strain values as the smooth surrogate; peak compressive and tensile strains across all four averaged drop heights were $-1.1 \pm 0.2\%$ and $1.3 \pm 0.3\%$, respectively. The strain response experienced two minor compressive peaks and one tensile peak. This was the likely result of orientation, where gyrification may be influencing the strain at a distance (Figure 47b), hence a noticeable effect on trends with a muted effect on magnitude.

The upward orientation also showed minimal strain variations between both surrogates (Figure 48). The strain responses were approximately 0% strain, with only minor compressive or tensile peak strains which all remained around $\sim \pm 1.2\%$. For the smooth surrogate, peak compressive and tensile strains across the four drop heights were $-0.9 \pm 0.3\%$ and $0.9 \pm 0.2\%$, respectively, whereas peak compressive and tensile strains for the complex surrogate were $-0.9 \pm 0.3\%$ and $0.5 \pm 0.2\%$, respectively. This response was reflective of marker location and orientation. These markers were further away from the influences of gyrification, as

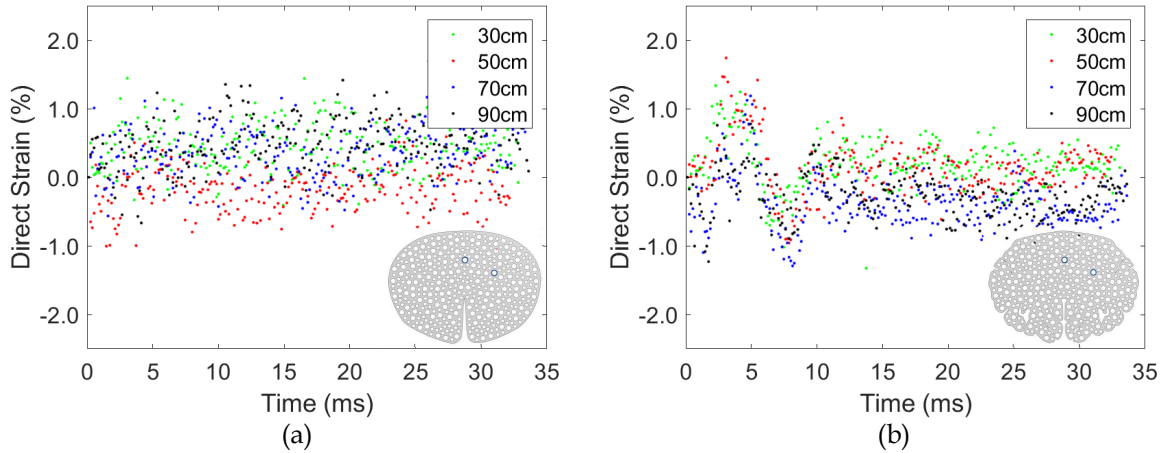


Figure 47: Strain responses between Markers 1 and 2 of the smooth surrogate (a) and the complex surrogate (b) being dropped in the downward orientation. All four averaged responses from different drop heights are shown.

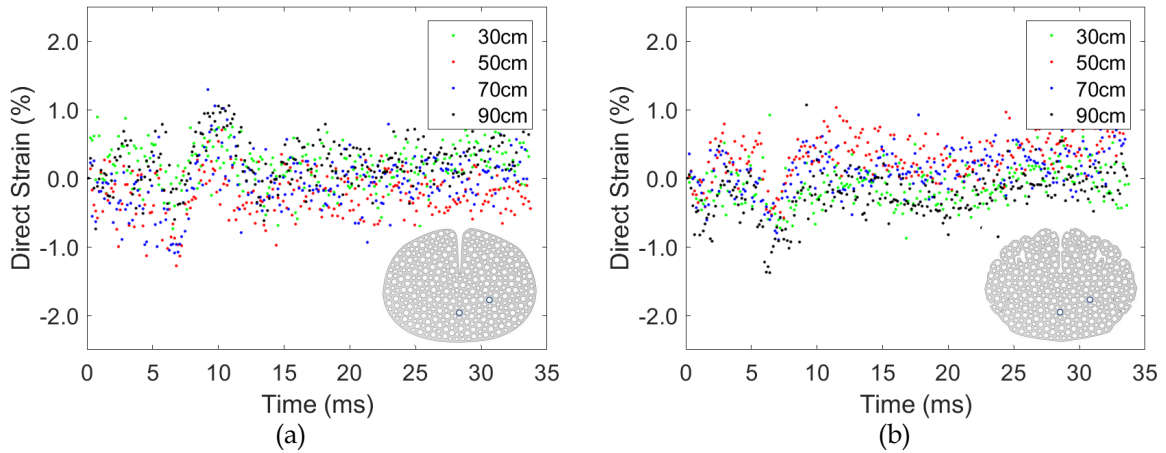


Figure 48: Strain responses between Markers 1 and 2 of the smooth surrogate (a) and the complex surrogate (b) being dropped in the upward orientation. All four averaged responses from different drop heights are shown.

they were closer to the impact anvil.

For both surrogates facing inwards, the direct strain responses were approximately 0% strain throughout the impact event (Figure 49). The range for peak compressive and tensile strains between trials for the smooth surrogate was large, $-0.4 \pm 0.9\%$ and $1.1 \pm 0.7\%$, respectively. The peak compressive and tensile strains

for the complex surrogate were $-0.6 \pm 0.2\%$ and $0.7 \pm 0.1\%$, respectively. The strain responses were most similar to one another when compared to the other two orientations. This was likely an effect of orientation. If one were to place an imaginary vertical line separating the regions of gyrification and the internal capsule, both markers are in regions that are not near gyrification. This may reduce some of the influences of gyrification due to orientation, which may explain the similar strain responses that were observed by both surrogates. Within the other two orientations, Marker 2 was either directly above or below a region with gyrification, which may have marginally influenced the strain response.

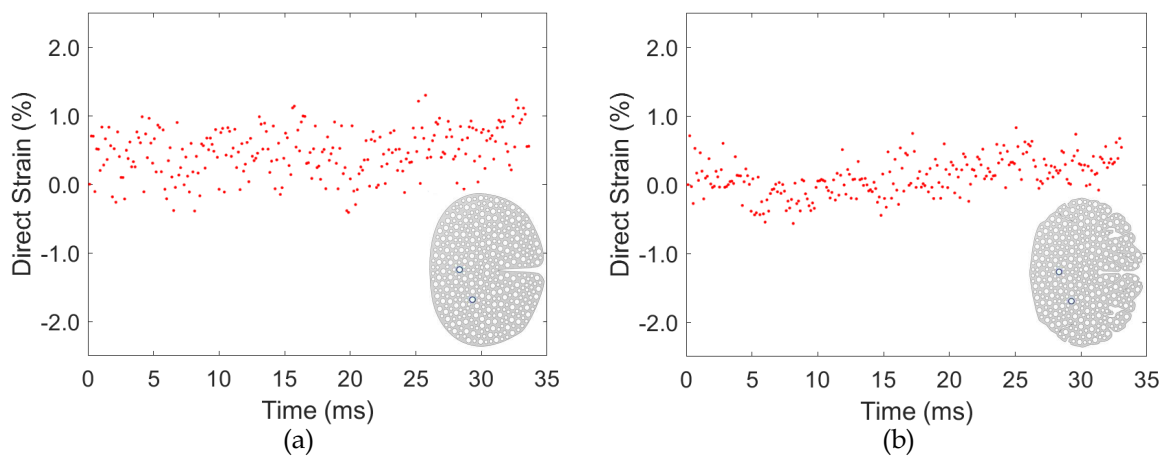


Figure 49: The averaged strain response between Markers 1 and 2 of the smooth surrogate (a) and the complex surrogate (b) being dropped in the inward orientation at 50 cm.

Markers within the internal capsule produced strain responses that had little variation, which was likely due to the coupling of markers within the internal capsule, the stiffness of the material, and the lack of motion observed within this region. Additionally, this specific marker pairing had the largest deviations within the strain responses from when the surrogates were at rest (see Tables 1 and 2); this can introduce a small degree of uncertainty within this specific marker pairing.

This, along with typically large standard deviations amongst peak strains (across averaged responses and trials), likely contributed to deviations observed within the strain responses responses. As this region also appeared to not be greatly influenced by gyrification, additional marker pairings were analysed that were closer to regions of gyrification.

Markers at the base of the fissure

The fissure, in an anatomical sense, signifies hemispheric distinction within the brain. The location of Marker 3 was at a transition point between the internal capsule and the region with gyrification. This point was also one of the few markers analysed that was in a geometric region that was identical across both surrogates. This region was selected as it was of interest to see if the sulci and gyri influenced an area that was not directly within the regions of gyrification.

When dropped in the downward orientation, the overall strain response was similar across both surrogates, yet there were specific differences. The smooth surrogate had a strain response that varied minimally. The surrogate underwent compression followed by tension, which occurred before 15 ms (Figure 50a). The averaged peak compressive and tensile strains were $-1.0 \pm 0.3\%$ and $0.9 \pm 0.2\%$, respectively. While the complex surrogate experienced similar general trends, the trends were more defined (Figure 50b). Two compressive peaks were experienced before 5 ms at heights greater than 30 cm; the compressive strain values were almost twice as large as those in the smooth surrogate. The surrogate then experienced tension before returning to zero strain, which occurred sooner than the smooth surrogate. For the complex surrogate, the averaged peak compressive and tensile strains were $-1.8 \pm 0.6\%$ and $0.7 \pm 0.1\%$, respectively. The transition between compression to tension within the surrogates' strain responses corresponded to the surrogates coming into contact with the anvil (compression) and then moving into

tension after leaving the anvil. The strain responses were also likely influenced by the impact durations; this was more clearly seen in the complex surrogate. At a drop height of 30 cm, the impact duration was the longest and the strain response was did not have many variations i.e. the complex surrogate did not have two peak compressive strains. At the larger drop heights, the impact durations were quite similar, which likely contributed to the similar strain responses.

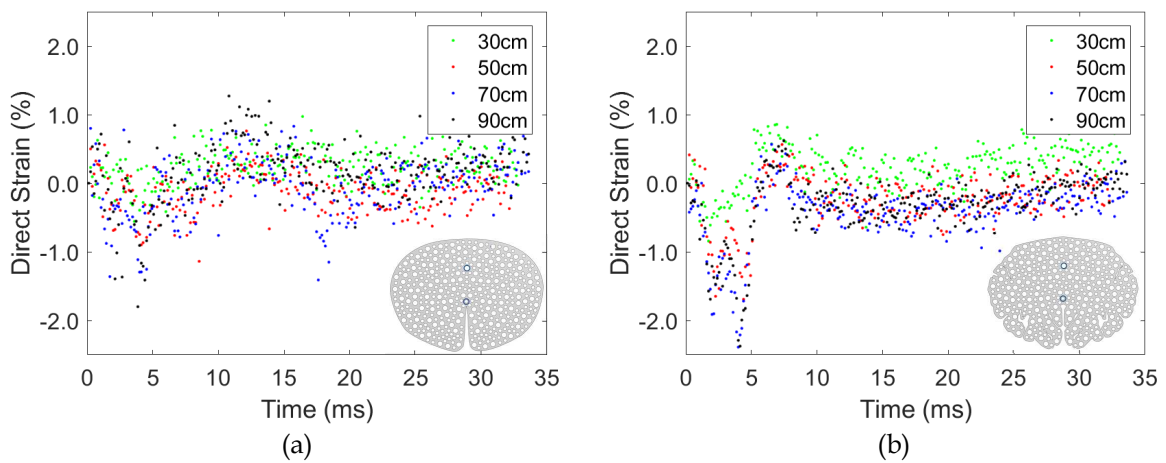


Figure 50: Strain responses between Markers 1 and 3 of the smooth surrogate (a) and the complex surrogate (b) being dropped in the downward orientation. All four averaged responses from different drop heights are shown.

Similar trends were observed when the surrogates were dropped in the upward orientation. Both surrogates underwent compression followed by tension. The major difference was the degree of deviation amongst data within the averaged strain responses for the smooth and complex surrogates, particularly after 10 ms; the spread was larger for the smooth surrogate (Figure 51). Regardless, similar peak strain values were obtained from both surrogates. The peak compressive and tensile strains across the four averaged drop heights were $-1.4 \pm 0.2\%$ and $1.1 \pm 0.4\%$ for the smooth surrogate and $-1.6 \pm 0.4\%$ and $1.1 \pm 0.2\%$ for the complex surrogate.

The strain response of the complex surrogate showed two peak compressive

strain events and had similar trends as those seen in the downward orientation for the same surrogate. The differences between both orientations was that the first peak compressive strain was larger than the second in the upward orientation. Additionally, the peak tensile strain was $\sim 0.5\%$ larger when dropped in the upward orientation (Figure 51b).

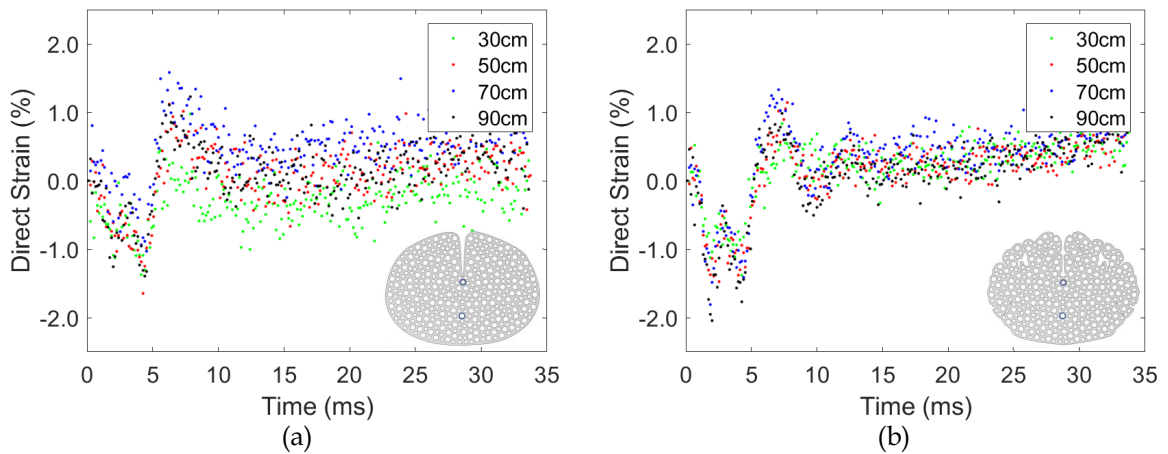


Figure 51: Strain responses between Markers 1 and 3 of the smooth surrogate (a) and the complex surrogate (b) being dropped in the upward orientation. All four averaged responses from different drop heights are shown.

Both surrogates when dropped in the inward orientation had strain responses that had minimal variation within the response (Figure 52). The peak compressive and tensile strains, obtained from the three trials, for the smooth and complex surrogates were $-0.3 \pm 0.1\%$ and $0.8 \pm 0.2\%$, and $-0.7 \pm 0.7\%$ and $0.4 \pm 0.3\%$, respectively. These low values could be orientation related such that gyrification has minimal influence on this region. This marker pairing was not within a region of gyrification nor would its movement have much influence over this region due to orientation.

Across all orientations, both sets of surrogates had minor variations when compared to one another. The strain responses were typically more defined in the

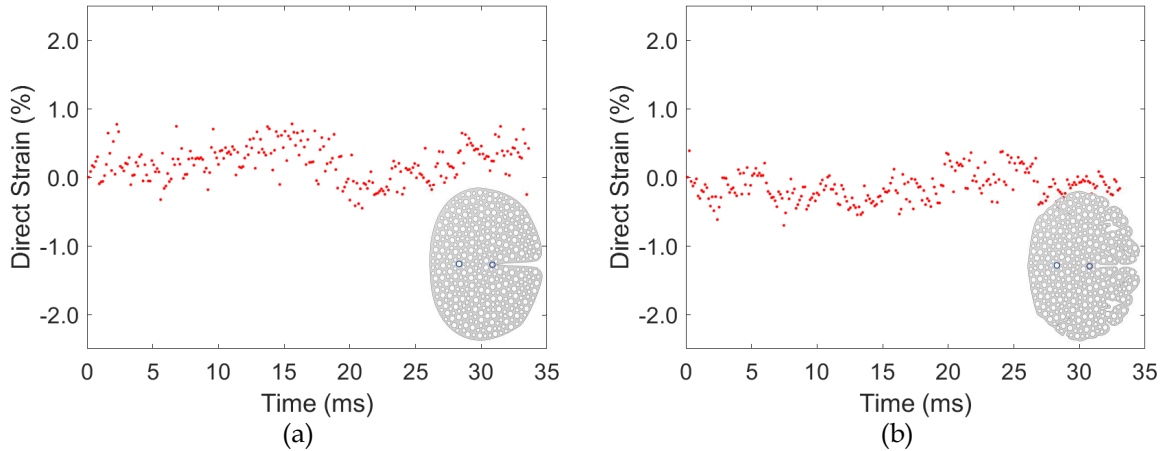


Figure 52: The averaged strain responses between Markers 1 and 3 of the smooth surrogate (a) and the complex surrogate (b) being dropped in the inward orientation at 50 cm.

complex surrogate, as the variations in motion between both markers were more pronounced than the smooth surrogate; a likely effect of gyrification. As similar peak strains were experienced by both surrogates, gyrification may not have had a large influence in this region as other marker pairings within regions with gyrification may have.

Markers in the vicinity of the sulcus

Marker 1 (within the internal capsule) and Marker 6 (in the vicinity of the sulcus) were compared next. In previous literature, an accumulation of brain injury markers were found after injury around the sulcus [7–9], which may be the result of high strain concentrations at this location [5, 6]. Therefore, a marker was selected in this area, where material discontinuities may occur, to determine if higher strain values were observed in this region.

Within the vicinity of the sulcus, the surrogates had similar variations within

the strain responses, but with different magnitudes when dropped in the downward orientation (Figure 53). Specifically, the averaged peak compressive and tensile strains of the four drops heights were $-0.8\pm 0.2\%$ and $0.7\pm 0.3\%$ for the smooth surrogate and $-1.3\pm 0.4\%$ and $0.5\pm 0.2\%$ for the complex surrogate. Overall, the strain response for the complex surrogate was cleaner than that of the smooth surrogate and had two peak compressive incidences. This was not as clearly observed in the smooth surrogate, which had larger deviations between data points in the strain response, resulting in peak compressive strains that were not clear. Additionally, the peak strain rates when dropped from a height of 90 cm for the smooth and complex surrogates were $9.3s^{-1}$ and $12.1s^{-1}$, respectively. As a note, the downward orientation followed similar trends (variations within the strain response, influences of impact duration, and the transition from compression to tension) seen in the fissure under the same loading conditions.

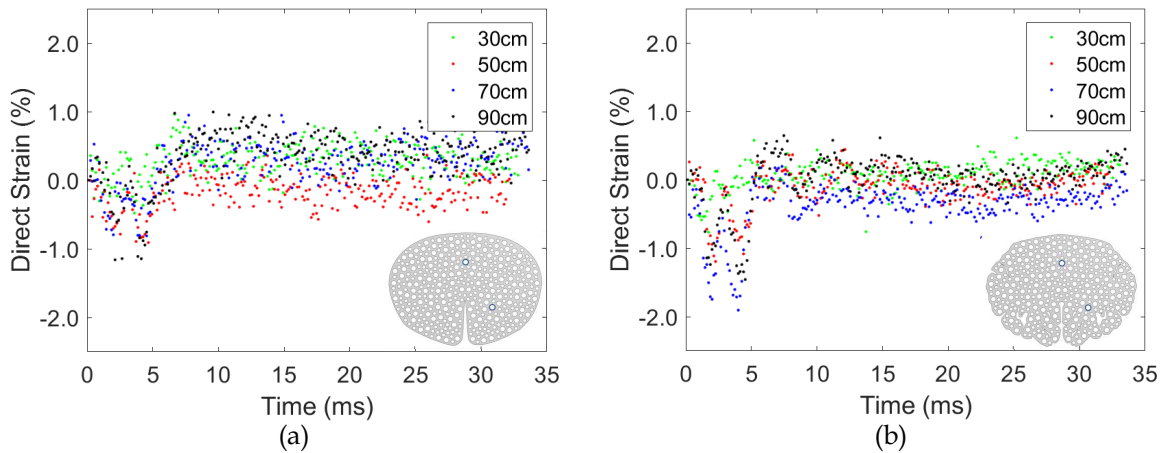


Figure 53: Strain responses between Markers 1 and 6 of the smooth surrogate (a) and the complex surrogate (b) being dropped in the downward orientation. All four averaged responses from different drop heights are shown.

The surrogates observed two unique responses when dropped in the upward orientation. The magnitudes of strain experienced by the smooth surrogate were

slightly larger than that of the complex surrogate (Figure 54). This difference was also observed using DIC (see Table 4). While the peak strains may have been larger, the strain response itself did not have many variations. The smooth surrogate only experienced one compressive ($-1.8 \pm 0.3\%$ strain) and tensile ($1.0 \pm 0.4\%$ strain) peak strain over the averaged drop heights. The strain response of the complex surrogate had more variations, with two compressive peaks (the larger being $-1.5 \pm 0.4\%$ strain) and one tensile peak ($0.9 \pm 0.2\%$ strain). The peak strain rate from the 90 cm drop for the smooth surrogate was smaller than the peak strain rate obtained from the complex surrogate ($8.3s^{-1}$ and $16.5s^{-1}$, respectively). These trends were likely due to orientation, which was also the least realistic of all loading conditions, and gyrification.

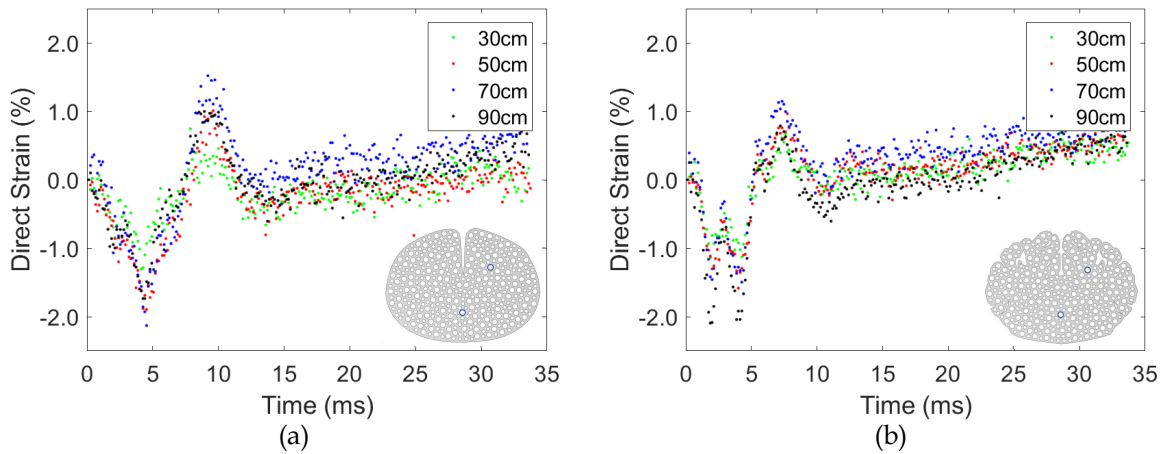


Figure 54: Strain responses between Markers 1 and 6 of the smooth surrogate (a) and the complex surrogate (b) being dropped in the upward orientation. All four averaged responses from different drop heights are shown.

While the two aforementioned orientations had notable trends and strain values, the strain values from the surrogates facing the inward orientation remained minimal in comparison. When comparing the internal capsule to the sulcus, some

variations were observed. The smooth surrogate had a strain response of approximately 0% strain with minor variations within the response; peak compressive and tensile strains between trials were $-0.3 \pm 0.4\%$ and $0.6 \pm 0.2\%$. This trend was not experienced by the complex surrogate. The strain response varied between $\pm 0.5\%$ until about 10 ms before returning to near zero strain; peak compressive and tensile strains between the three trials were $-0.5 \pm 0.2\%$ and $0.6 \pm 0.2\%$. Additionally, the peak strain rates for the smooth and complex surrogates were $4.1s^{-1}$ and $7.4s^{-1}$, respectively. While the strain range remained smaller than the two other orientations, the differences between both surrogates were notable (Figure 55). This was the first instance within the inward orientation where there were differences in trends although it was minimal.

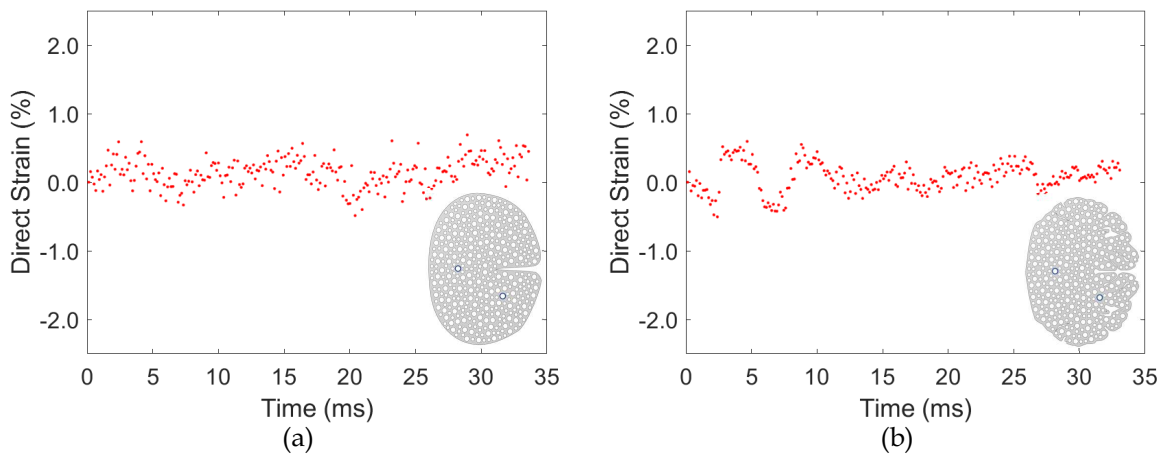


Figure 55: The averaged strain responses between Markers 1 and 6 of the smooth surrogate (a) and the complex surrogate (b) being dropped in the inward orientation at 50 cm.

The complementary marker pairing for the inward orientation (see Appendix C Figure C.19) had a different response due to orientation and marker location; this was only the case for the complex surrogate. While marker pairing 1 and 6 had small variations within the strain response, the complementary pair experienced

a more muted response of approximately 0% strain. A small compressive strain of $\sim 0.5\%$ was observed at 5 ms, before experiencing minimal tensile strain. This marker pairing was further away from the anvil than the other main marker pairing, a possible explanation of the muted response.

Overall, within this marker comparison, markers were closer to the cortex, with markers in the complex surrogate being directly adjacent to geometric variations. In almost all comparisons, the complex surrogate had larger strain values, with more complicated strain variations than those produced by the smooth surrogate. The influence of impact duration was also observed in this marker pairing, as well as the common trend of the surrogates undergoing compression, followed by tension. As a result, the influences of increased gyrification became more pronounced in the vicinity of the sulcus.

Markers in the gyrus

Markers within the gyrus corresponded to the area of gyrification that was closest to the surface of the cortex, which was also where the largest geometric variations occurred between surrogates. The smooth surrogate had two large, uniform hemispheres, whereas the complex surrogate had multiple, small gyri. Based on previous literature, the motion of the gyrus may influence the damage seen at the base of the sulcus. It was then postulated that this region would be influenced by the impact more than any other region of the surrogate. It should be noted that a material discontinuity existed between Markers 1 and 7 (and Markers 1 and 5) in the complex surrogate, which would influence the strain response.

Beginning with the downward orientation, both surrogates had similar strain responses, but with different magnitudes of compressive strain (Figure 56). The averaged peak compressive strain experienced by the complex surrogate ($-1.5 \pm 0.4\%$ strain) was approximately double the value of averaged peak compressive strain

obtained from the smooth surrogate ($-0.8\pm 0.3\%$ strain). The complex surrogate observed many variations within the strain response, which varied between tensile (peak averaged strain of $0.5\pm 0.1\%$) and compressive strains, before returning to near zero strain at ~ 15 ms. Similar trends were observed in the smooth surrogate, but after undergoing compression the strain response returned to near zero strain shortly after 7.5 ms; the averaged peak tensile strain was $0.5\pm 0.1\%$.

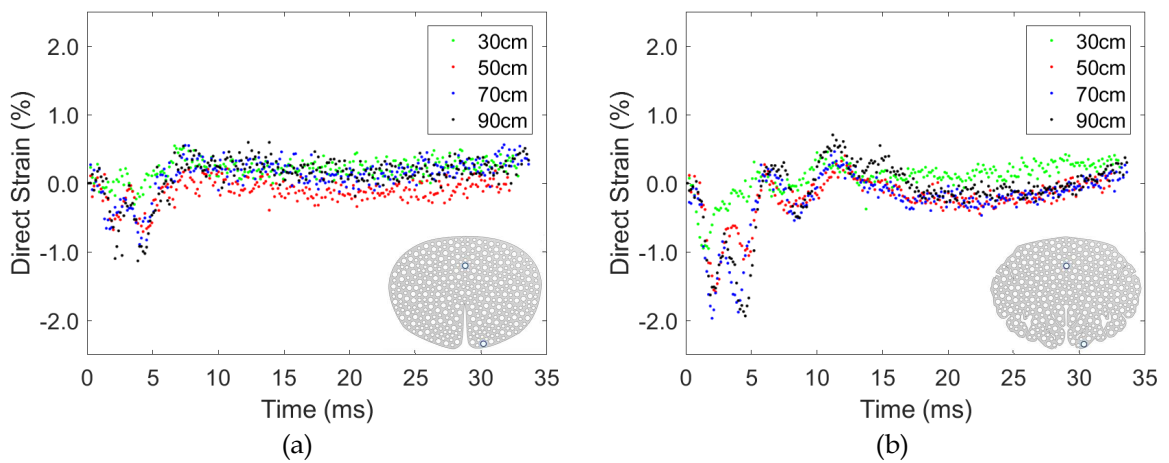


Figure 56: Strain responses between Markers 1 and 7 of the smooth surrogate (a) and the complex surrogate (b) being dropped in the downward orientation. All four averaged responses from different drop heights are shown.

Within the upward orientation, similar general trends were observed within both surrogates, but there were differences in strain magnitudes and peak strains (Figure 57). The averaged peak strain values experienced by the smooth surrogate ($-1.2\pm 0.1\%$ strain and $0.9\pm 0.2\%$ strain) were less than the averaged peak strain values experienced by the complex surrogate ($-1.9\pm 0.3\%$ strain and $1.1\pm 0.4\%$ strain). Peak strains could again be the result of the degree of gyrification and orientation, as shown in other pairings. Another notable difference occurred in the tensile phase of the strain response. The complex surrogate experienced one large tensile

strain peak over a short duration (5 ms), whereas the smooth surrogate experienced a smaller tensile strain over a longer duration (10 ms); potentially the result of marker location and gyrification. Additionally, the complex surrogate experienced two larger compressive peaks than that of the smooth surrogate, another possible indication that the presence of complex cortical gyrification may be more susceptible to impact events.

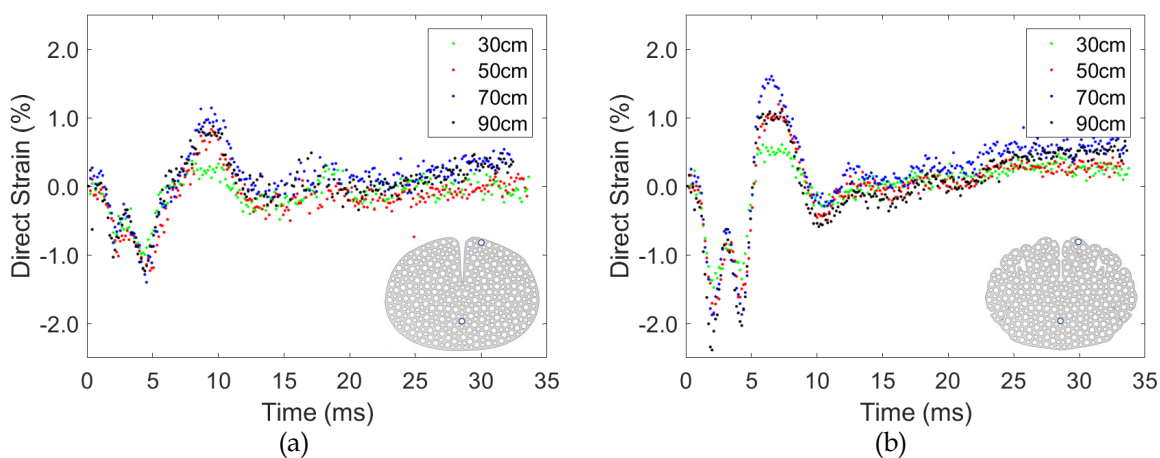


Figure 57: Strain responses between Markers 1 and 7 of the smooth surrogate (a) and the complex surrogate (b) being dropped in the upward orientation. All four averaged responses from different drop heights are shown.

Similarities with minor differences in trends can be seen between the upward and downward orientations. The strain responses of both surrogates resembled one another, but with different magnitudes. Both the upward and downward orientations had peak compressive strains of similar magnitudes when comparing the same surrogates across orientations. The main difference was the response in the tensile phase and the strain duration between these two orientations. In the upward orientation, the magnitude of the tensile and compressive strains were near identical and there was only one peak tensile strain; unlike the downward orientation. The duration of the strain response was also shorter for the complex

surrogate when dropped in the upward orientation; the opposite was true for the smooth surrogate. Additionally, the influences of drop height and impact duration were also observed, as the strain responses from the 30 cm drop were different than those obtained from the higher drop heights.

Additional comparisons can be noted within the upward orientation across marker pairings. Comparing the marker within the gyrus (Marker 7) to the marker within the sulcus (Marker 6) showed opposite trends. Marker pairing 1 and 6 saw the smooth surrogate having marginally greater tensile strain magnitudes than that of the complex surrogate (Figure 54). The larger strain values within the smooth surrogate may be the result of marking positioning, as it was marginally closer to the rightmost edge of the surrogate and more likely susceptible to motion. The opposite trend was observed between Markers 1 and 7, where the complex surrogate had larger tensile and compressive strains than the smooth surrogate (Figure 57). The gyrus of the complex surrogate may have been influenced more by the impact, resulting in greater strain at the gyrus than near the sulcus.

The most interesting of comparisons occurred within the inward orientation (Figure 58). The smooth surrogate had a strain responses of approximately 0% strain (averaged peak compressive and tensile strain were $-0.1 \pm 0.2\%$ and $0.5 \pm 0.3\%$, respectively), whereas the strain response of the complex surrogate had larger variations. A large peak tensile strain ($2.3 \pm 0.2\%$) was experienced during impact, followed by a peak compressive strain of $-2.4 \pm 0.4\%$ within the region. This could represent the motion of the gyrus, as this region had more freedom to move during the impact due to orientation. The strain response returned to $\sim 0\%$ at 20 ms.

The relative displacement plots at 50 cm for one trial for both surrogates showed supporting trends (Figure 58c and 58d). The motion of both markers followed similar paths for the smooth surrogate; the trajectory data was limited in

the x-direction for both markers (Figure 58c). Within the displacement plot for the complex surrogate, similar paths were found near the beginning and end of the impact event (Figure 58d). Within the impact time frame, both markers followed different paths and with higher displacements; the trajectory data had more deviations in the x-direction. The differences noted above resulted in the increased strain values and variations obtained between 5 and 20 ms.

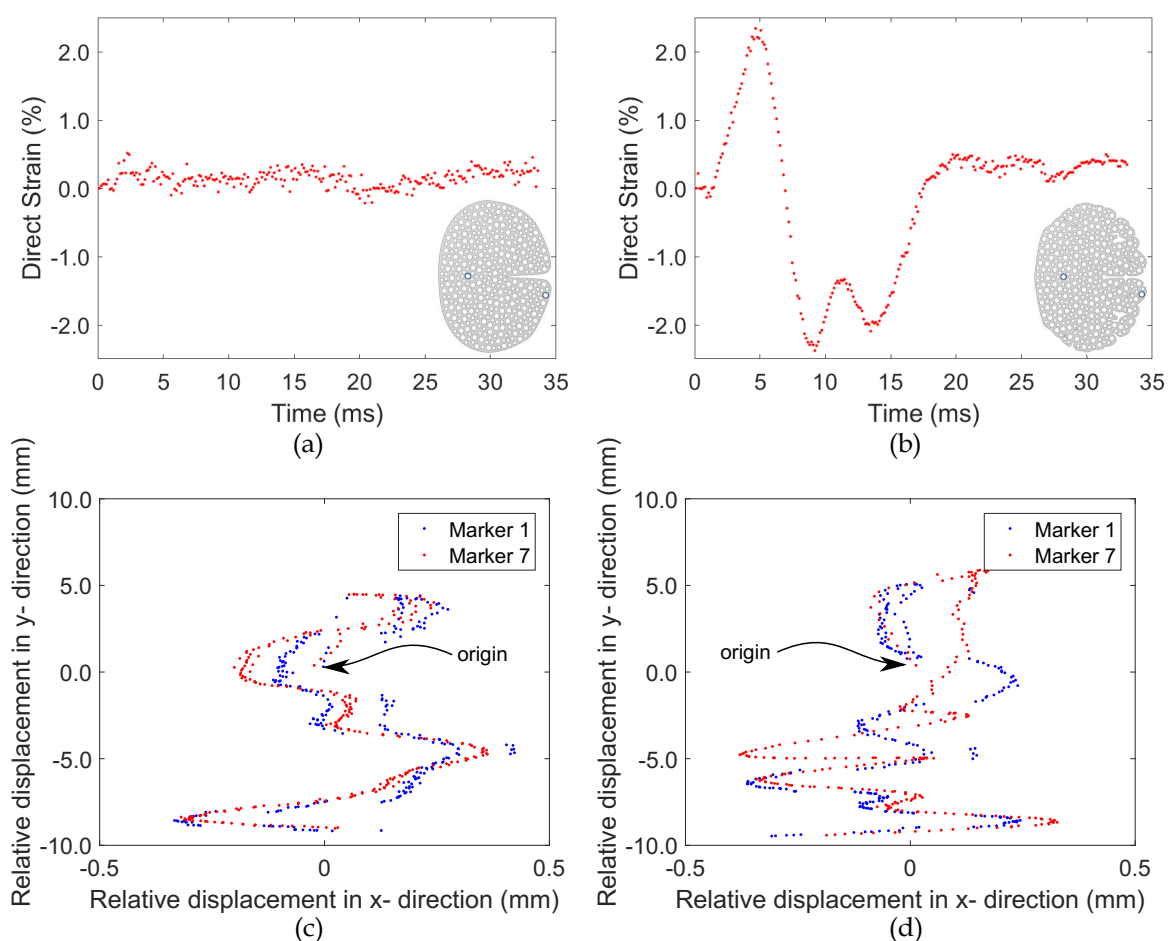


Figure 58: The averaged strain responses between Markers 1 and 7 of the smooth surrogate (a) and the complex surrogate (b) being dropped in the inward orientation at 50 cm. The x- vs y- displacements of Markers 1 and 7 are shown for both the smooth surrogate (c) and the complex surrogate (d) for one trial. The start point is at the origin.

The complementary marker pairing for the complex surrogate when dropped in inward (see Appendix C, Figure C.20b) had a different response for the same reasons as discussed in the previous marker comparison. The complex surrogate was mainly in tension (1% strain for ~ 12 ms) before returning to near zero strain. At 5 ms, marker pairing 1 and 5 experienced their highest peak compressive strain. At the same time, marker pairing 1 and 7 experienced their highest peak tensile strain. The strain range of marker pairing 1 and 5 (between -1.3% to 1.2% strain) was much lower than that of marker pairing 1 and 7, a possible reason being marker location.

In conclusion, every surrogate comparison showed the same supporting trends, many of which were observed in previous marker pairings. The strain response for the smooth surrogate became more diminished in this marker pairing, likely an influence of the lack of gyrification. The complex surrogate had higher strain values and more variations within the strain response, a result of the gyrus, but as it was noted previously this pairing had a material discontinuity. The higher strain values observed within the gyrus may contribute to the strain observed within the sulcus, as this region had the largest degree of gyrification. Further analysis on the direct influence of the gyrus on the sulcus will be discussed next.

Markers at the apex of the gyrus and base of the sulcus

The influence of the gyri on the sulci will be compared next as this region corresponded to pure cortical gyrification, which may contribute to the strain observed within the sulci [6]. This cortical region has the greatest geometric variations between the two brain classifications. This specific comparison will show how different degrees of cortical gyrification may influence impact-induced measurements, which can have implications towards future models used in TBI research.

When dropped in the downward orientation, the surrogates had gyrification perpendicular and closest to the anvil when impacted. Starting with the smooth

surrogate, the range in strain values remained between $0\pm 0.8\%$ (Figure 59a). The surrogate appears to have experienced minimal compression (averaged peak strain across four drop heights of $-0.6\pm 0.2\%$ strain) and tension (averaged peak strain across four drop heights of $0.4\pm 0.1\%$), as most strain values remained around zero. The peak strain rate obtained from the 90 cm drop strain response for this surrogate was $4.0s^{-1}$. Across all four drop heights, the direct strain values did not vary notably. This marker pairing is the second occurrence where there appears to be minimal to no variations within the strain response; the first being markers within the internal capsule.

Unlike the aforementioned surrogate, the complex surrogate had a more intricate strain response (Figure 59b). There was one large compressive peak strain, the average from the four drop heights was $-1.2\pm 0.4\%$ strain, which occurred at ~ 5 ms; this corresponded to when the drop apparatus began to rebound from the anvil. As the apparatus left the anvil, two peak tensile strains of approximately $\sim 1\%$ strain (the larger averaged peak tensile strain being $0.9\pm 0.3\%$ strain) are seen after ~ 7.5 ms. Not only did the complex surrogate experience higher strains and increased variations in the strain response, the effects of the impact lasted longer than it did for the smooth surrogate. The effects of impact duration were also clearly seen between drop heights; a trend previously discussed. Additionally, the peak strain rate obtained from the 90 cm drop strain response was $9.7s^{-1}$; a value twice as large as the strain rate obtained from the smooth surrogate. It appeared that gyrification played a role in strain variations, magnitudes, and durations when dropped in the downward orientation, which all may lead to the brain experiencing more injurious effects.

In the upward orientation, the brain gyrification was perpendicular to the anvil, with the internal capsule lying between the regions of gyrification and the anvil.

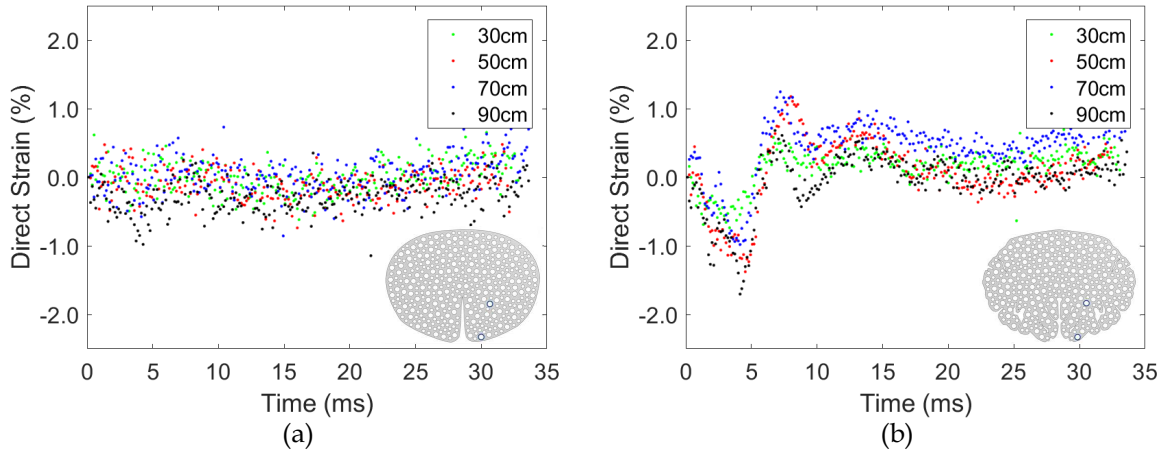


Figure 59: Strain responses between Markers 6 and 7 of the smooth surrogate (a) and the complex surrogate (b) being dropped in the downward orientation. All four averaged responses from different drop heights are shown.

The strain responses of both surrogates in both the upward and downward orientations showed similar trends, with minor differences. Within the upward orientation, the smooth surrogate experienced no major strain variations, similar to when it was dropped in the downward orientation. The range in strain was between $0 \pm 0.8\%$, with minimal compressive (averaged peak strain of $-0.6 \pm 0.2\%$) and tensile (averaged peak strain of $0.6 \pm 0.2\%$) responses from the impact event (Figure 60a). The peak strain rate obtained from this surrogate when dropped from a height of 90 cm was $8.7s^{-1}$. These trends were more muted than those seen in the complex surrogate, a likely effect of the lack of gyrification.

Comparing the behaviour of the complex surrogate in the upward orientation to that of the downward showed comparable peak strain magnitudes as well as trends between drop heights, but there were differences in the response. The peak compressive strain obtained using all four averaged drop heights in the upward orientation was $-1.6 \pm 0.2\%$ strain, with peak tensile strains of $1.0 \pm 0.4\%$ (Figure 60b). The strain rate for when the complex surrogate was dropped from a height of 90 cm in the upward orientation was $13.3s^{-1}$. The upward orientation

saw more compressive and tensile peaks than when it was dropped in the downward orientation. This could indicate that orientation of the markers and gyrfication may contribute to the unique responses observed.

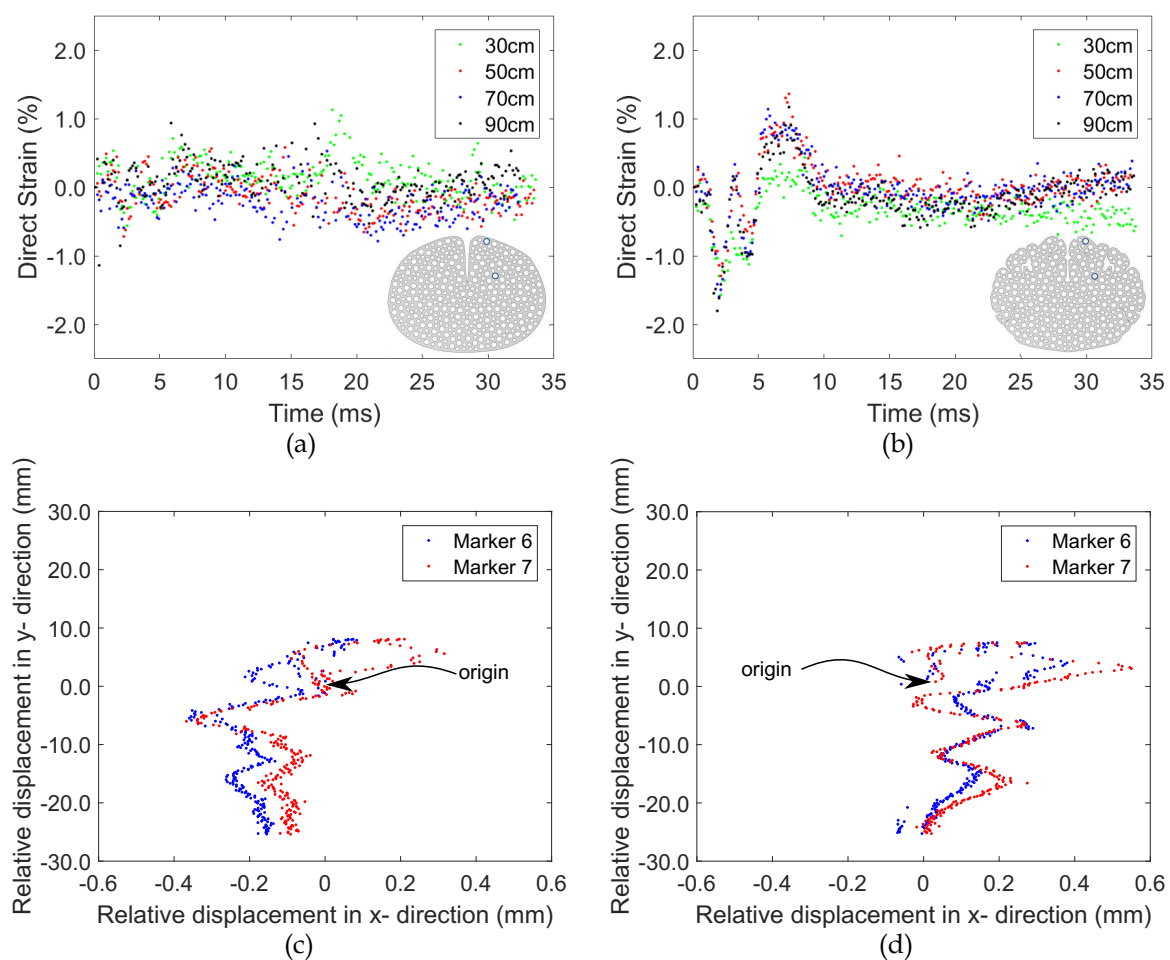


Figure 60: Strain responses between Markers 6 and 7 of the smooth surrogate (a) and the complex surrogate (b) being dropped in the upward orientation. All four averaged responses from different drop heights are shown. The x- vs y-displacements of Markers 6 and 7 are shown for both the smooth surrogate (c) and the complex surrogate (d) at one trial with a drop height of 90 cm. The start point is at the origin.

Displacement plots for both surrogates when dropped in the upward orientation are shown in Figures 60c and 60d. The markers in the smooth surrogate did

not travel far from the origin, with only minor excursions at the beginning. The trajectory of Marker 6 was fairly limited in the x - direction, while Marker 7 had slightly more motion in the x - direction. The same marker pairing in the complex surrogate had extreme displacements in one direction for both markers, which was likely due to the movement of the gyrus; the trajectories of each marker had large deviations in the x -direction. Near the origin, the x - displacement values of both markers positively increase, then decrease, before increasing once more. A small looping pattern occurred, which likely contributed to the strain response within the first few milliseconds. It should be noted as well that the scale on the x -axis is different than the y -axis within the plots. The displacements of the markers are minimal in the x -direction, although they appear quite large in the current figures. There also appears to be minimal sub-pixel jitter of less than 0.1 mm within the x -displacement measurements.

The inward orientation produced unique strain responses for this marker pairing as well. In this orientation, brain gyrification was parallel to the anvil. This implied that when the surrogates were impacted, a uniform impacting force was not equally distributed across all regions of gyrification. Starting with the smooth surrogate, the strain response had minimal variations (Figure 61a); the values for peak compressive and tensile strains were $-0.5 \pm 0.2\%$ and $0.5 \pm 0.3\%$, respectively. Additionally, the peak strain rate was $3.9s^{-1}$. This may be the result of the position of the markers with respect to the anvil, along with gyrification, which had two large, uniform regions surrounding the markers.

The complex surrogate had a different strain response (Figure 61b). Minor compression (peak strain of $-0.7 \pm 0.1\%$), followed by a longer period of tension (peak strain of $1.1 \pm 0.3\%$) was observed. A peak strain rate of $3.9s^{-1}$, was also obtained. The complementary pairing (see Appendix C, Figure C.21b), remained near zero strain but produced two small tensile peak strain values ($\sim 0.5\%$). As previously

stated when comparing the complementary marker pairings, positioning is likely the contributing factor to differences in strain response.

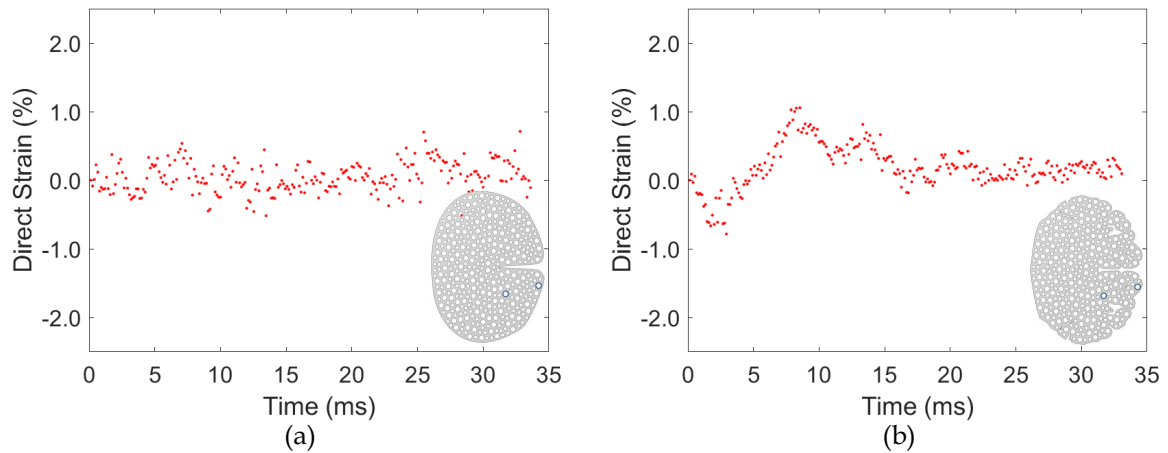


Figure 61: The averaged strain responses between Markers 6 and 7 of the smooth surrogate (a) and the complex surrogate (b) being dropped in the inward orientation at 50 cm.

The trends obtained through both image analysis methods were comparable (i.e., DIC and particle tracking). The complex surrogate had, with a few exceptions, larger strain values than those of the smooth surrogate. The strain values across larger drop heights were similar, with each orientation having unique strain responses. The common trends can imply that both image analysis methods can be used as complementary methods, with each providing a unique visual insight into surrogate movement.

Overall, it appears that increased brain gyrification had the greatest influence over strain. The smaller size of the gyri made the region with gyrification more susceptible to impacts. The range of motion that could be observed in the complex surrogate was not the same for the smooth surrogate. The two large hemispheres

in the smooth surrogate covered more area surrounding the two markers of interest. This region appears to have experienced less strain than the smaller, heterogeneous regions in the complex surrogate, which had geometric discontinuities within the region surrounding the markers.

5.1.3 A Direct Comparison between Digital Image Correlation and Particle Tracking Data

As described in Chapter 3, DIC and particle tracking are two unique image analysis methods. DIC calculates displacement and strain data using a subset of pixels. Unlike DIC, particle trackers can track the motion of individual particles and output trajectory coordinate data. This can then be used to calculate displacements of individual particles and strains between two particles. In the sections above it was clear that both methods produced trends with comparable results. The outputted form of data from each method provided unique visual representations of data as well. It was of interest to determine for future studies, if using one method of analysis would be better suited than the other. This was of particular interest when it came to the preliminary viable *ex vivo* porcine brain tissue study.

A comparison using displacement and strain plots was done to determine if both image analysis methods would produce similar results from the same data set. The four markers that were chosen for this comparison were found within the internal capsule (Markers 1 and 2) and within regions of gyrification (Markers 6 and 7); comparisons for Markers 1 and 6 can be found in Appendix C, Figures C.57 and C.58. Overall, DIC and particle tracking were able to produce similar results specific to each marker, surrogate, and orientation. Comparisons between displacements plots will be shown first. The common feature in each figure is the marker compared, but each subfigure is data from one surrogate and a different

orientation. A comparison between strain data will be compared afterwards.

The displacement plots from the markers within the internal capsule produced the most variation between image analysis methods. The main differences occurred in the x-direction, where some x-displacement values obtained through particle tracking were marginally offset from those obtained through DIC (Figure 62); the largest offset in Figure 62b was 0.1 mm. This could be the result of the different way each image analysis method obtains data. Additionally, the particle tracker is sensitive to sub-pixel jitter, which can contribute to the occasional sub-millimetre jumps observed in the displacement plots; this is more notable in regions that do not experience a great deal of motion. This issue was not observed in the displacement plots obtained through DIC, which were smoother and continuous.

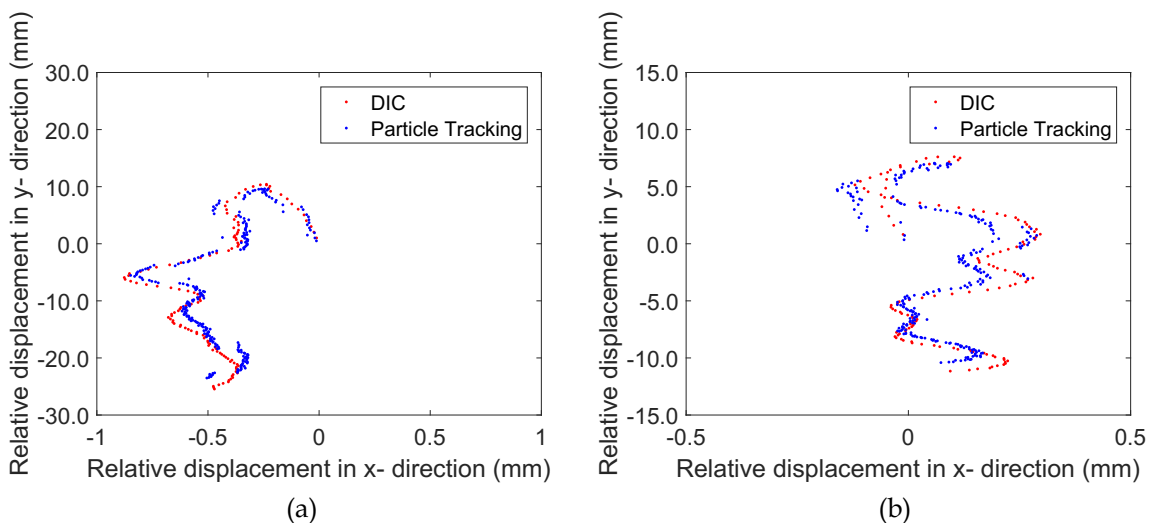


Figure 62: The relative x- vs y- displacement plots obtained through DIC and particle tracking for Marker 2 for a) the smooth surrogate dropped in the downward orientation at 90 cm and b) the complex surrogate dropped in the inward orientation at 50 cm. Each plot was obtained from the median trial.

While minor variations were observed in markers within the internal capsule, the displacement plots from markers within regions of gyrification showed even less variation in displacement values. Both displacement plots in Figure 63 showed

an increasing amount of data overlap, which occurred less within the internal capsule. Minimal offsets were also observed within this comparison, with both image analysis methods producing smooth plots with similar trends.

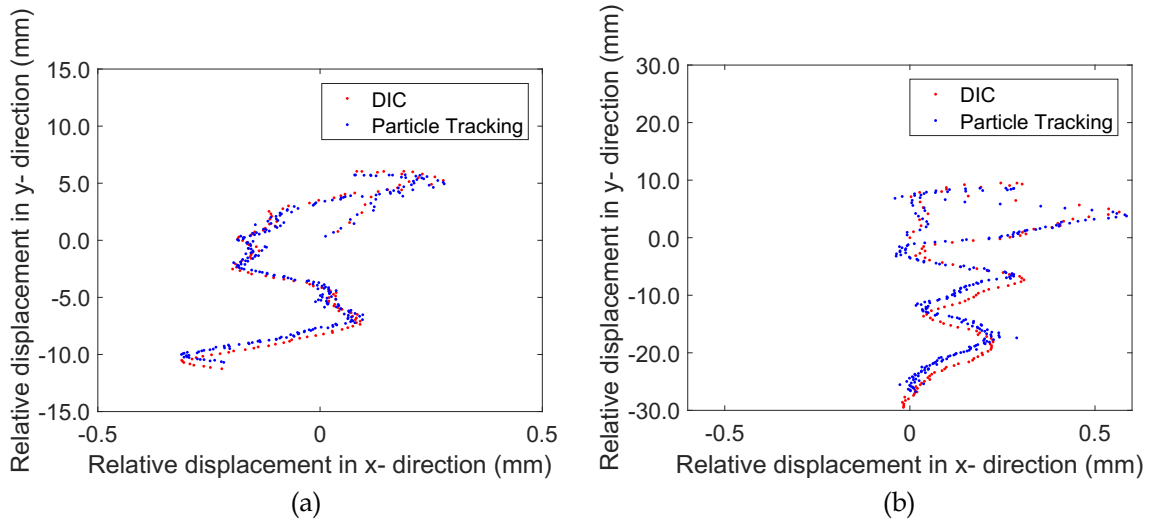


Figure 63: The relative x- vs y- displacement plots obtained through DIC and particle tracking for Marker 7 for a) the smooth surrogate dropped in the inward orientation at 50 cm and b) the complex surrogate dropped in the upward orientation at 90 cm. Each plot was obtained from the median trial.

The similarity in data between both image analysis methods is expected, as both used the same data sets. Next, a comparison was made between direct strains using DIC and particle tracking data. A focus will be placed on the internal capsule, the sulci, and the gyri using both surrogates and different orientations.

Within the internal capsule, similar overall trends were observed between both image analysis methods, with the difference being in the level of deviation between data points within the strain response produced by each method (Figure 64). DIC was able to produce a smooth strain response, with minimal deviations occurring between data points. This is likely the result of the algorithm using a set of pixels within a subset to calculate displacements at a given pixel. The strain data was unlike those produced by the particle tracker. While the particle tracker produced

strain data that followed a similar path as DIC, the strain data had larger deviations between neighbouring points. This produced a strain response that was not as clear as the strain response obtained through DIC. This method, as previously stated, uses particle characteristics to obtain trajectory data from the center of the particle. It is therefore likely to be more susceptible to small variations within the particle's trajectory (minimal motion occurred within the internal capsule), which can propagate when calculating strain.

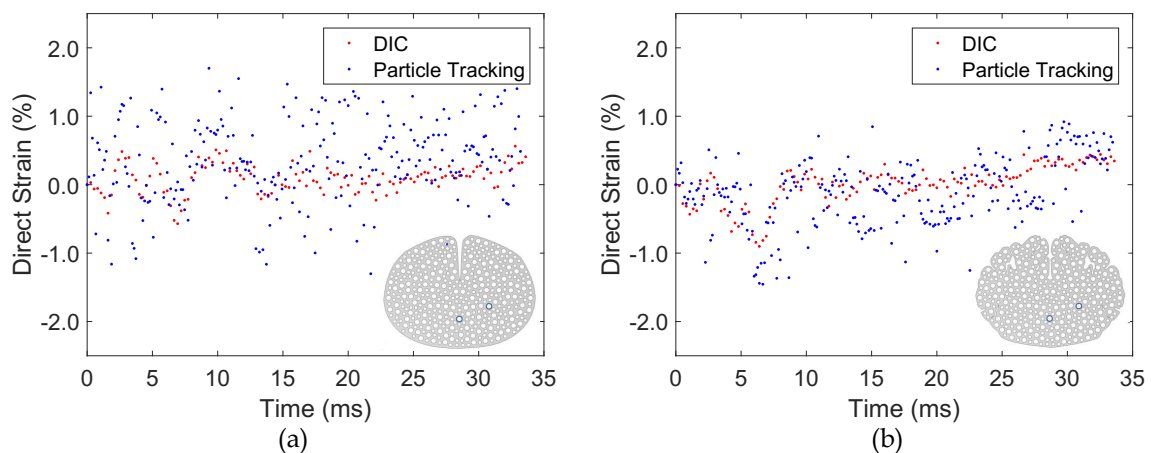


Figure 64: A comparison between DIC and particle tracking strain results for marker pairing 1 and 2 for the a) smooth and b) complex surrogates when dropped in the upward orientation (median trial, height of 90 cm).

Common with the internal markers, the DIC strain data obtained at the sulci was smooth, with minimal deviations between data points. The strain response of the smooth surrogate was consistently near 0% strain. The particle tracking strain data had more deviations between neighbouring points, but it followed the general trends seen in the DIC data (Figure 65a). Specifically within the complex surrogate, the peak tensile and compressive strains occurred at approximately the same time, though the strain values were slightly shifted (Figure 65b). This was likely due to the increased motion observed by Marker 6. More defined motion resulting from

larger movements in a region between frames likely created less jitter within the particle tracker, resulting in the smoother strain response.

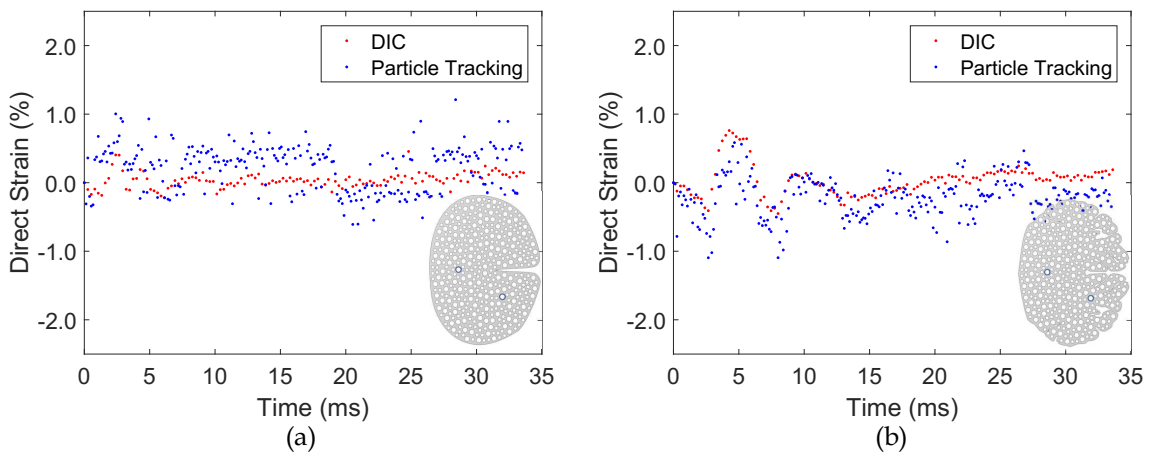


Figure 65: A comparison between DIC and particle tracking strain results for marker pairing 1 and 6 for the a) smooth and b) complex surrogates when dropped in the inward orientation (median trial, height of 50 cm).

The above two comparisons between markers more central within the surrogates showed a few differences between image analysis methods, primarily relating to the degree of deviation between strain data points. A shift to markers within the regions of gyrification showed increasing similarities between DIC and particle tracking. Starting with a comparison between Markers 1 (internal capsule) and 7 (gyrus) showed near identical strain responses, especially from the complex surrogate (Figure 66). Both methods produced strain responses had minimal deviations between data points, resulting in the smooth appearance of the response. For the particle tracking data, this could be the result of the increased deformations observed within this region as well as the markers being more vertical, as opposed to lateral, to one another; unlike internal regions which have minimal motion and are more laterally positioned. The strain data from both methods had peak strains occurring at the same time and produced similar magnitudes of strain as well.

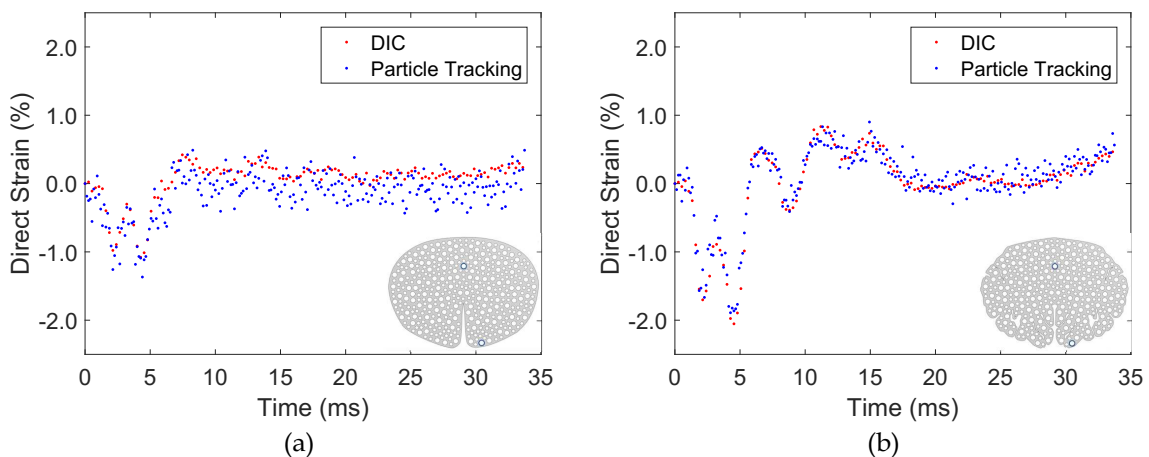


Figure 66: A comparison between DIC and particle tracking strain results for marker pairing 1 and 7 for the a) smooth and b) complex surrogates when dropped in the downward orientation (median trial, height of 90 cm)

DIC and particle tracking also showed similar results when looking at markers within regions of gyrfication (Figure 67). Common with the other comparisons, the DIC data was smooth, while the particle tracking data had some larger deviations between data points. The peak strain values occurred at similar times, while strain magnitudes remained within a comparable range.

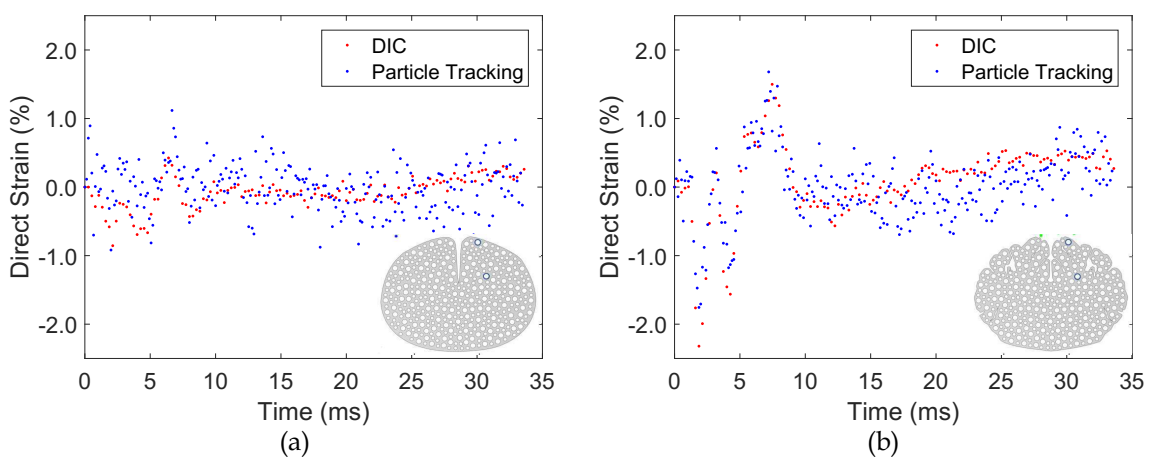


Figure 67: A comparison between DIC and particle tracking strain results for marker pairing 6 and 7 for the a) smooth and b) complex surrogates when dropped in the upward orientation (median trial, height of 90 cm).

5.1.4 Discussion

The surrogates within this study were extreme versions of their *ex vivo* counterparts. The purpose of the surrogates was to show how brain gyrification played an important role in tissue deformation. Orientation was also used to highlight the effects of loading conditions on strain measurements. Overall, there were distinct variations between surrogates, orientations, and marker locations.

The analysis of the surrogate data used two approaches, as each method had its benefits and drawbacks. DIC provided full-field strain data, but can be susceptible to boundary iteration errors. The strain field plots overall were a visually impressive representation of the data, as it was overlaid on top of the entire ROI. When using DIC and examining full-field measurements, the complex surrogate showed increased strain concentrations in regions of gyrification across each orientation, the effects of which typically lasted longer than those within the smooth surrogate. This was likely due to the degree of brain gyrification. The smooth surrogate generally produced low-level strains across each comparison throughout the entire surrogate, implying that under the same loading conditions a specimen with little to no gyrification may not experience the same strain response as a specimen with a high degree of gyrification would. Some, though not all, strain values may have had some contributions from boundary iteration errors, therefore a second approach was used as a complementary method in calculating strain.

Individual particle tracking was used to eliminate uncertainties surrounding boundary errors, which can occur using DIC. This method allowed for individual markers to be tracked, which could later be compared to other markers of interest. While boundary errors may not be an issue in single particle tracking, this approach was susceptible to sub-pixel jitter, which was mainly seen at low-level strain responses and markers within the internal capsule; the jitter appeared

to only influence the x-direction coordinates. While strain is a derivative of displacements, the jitter did not appear to greatly influence the results, specifically for markers within regions of gyrification, which was proven in Appendix C, Figures C.59 and C.60. After applying the correction to those sets of data, the trends and peak values remained similar between the original and corrected strain responses. Only one strain response from all the data sets had the jitter correction applied; this was done for a supplementary orientation for the comparison between the marker within the internal capsule and the fissure (Appendix C, Figure C.34b). Additionally, it was determined that the uncertainty in the strain calculation (obtained from when the surrogates were at rest on the anvil) was higher for markers in the internal capsule than it was for other marker pairings, which were separated by a greater distance and were located more vertically to one another. This likely contributed to the larger deviations observed between neighbouring data points within the strain responses of markers within the internal capsule.

Each marker comparison was carefully selected to highlight regions with large degrees of brain gyrification. Although the selected markers are in near identical locations, if the surrogates were overlaid on top of one another, the regions of the cerebral cortex appeared vastly different. Markers within the internal capsule were selected, as the area was common between both surrogates. Looking at the complex surrogate, markers in the gyri and near the sulci were selected and compared because they corresponded to pure cortical gyrification in the complex surrogate. This region was where the two surrogates strain data varied remarkably.

While both image analysis methods compute data in different ways, the results supported similar conclusions. Of the two different degrees of gyrification, the greatest strain variation and magnitudes of strain were primarily exhibited by the complex surrogate; the variations within the strain response typically lasted longer for this surrogate as well. These differences were clearly noted in the comparisons

between the gyrus and the sulcus. These trends were also seen in two supplementary orientations where the surrogates were dropped with gyrification facing outward and with the placement of the surrogates in swapped positions; these were analysed with the particle tracker (see Appendix C, Figures C.23 to C.38).

Of all the marker pairings analysed, the most interesting strain variations occurred between the markers near the sulcus and at the peak of the gyrus. The strain responses were the most dynamic and typically had the highest magnitudes, which was observed within the complex surrogate. This can imply that the presence of the gyrus influenced strain seen at the sulcus. The increased strain values within this region demonstrates that there was a localisation of strain within the cortex.

Many trends, which were mentioned above, were observed when analysing the surrogates and marker pairings. It was also determined that the impact durations, which were largest for the 30 cm drop height and comparable for the remaining drop heights, showed similar trends, particularly in the complex surrogate, throughout the marker pairings; this was clearly observed in the marker pairings analysed with the particle tracker. This likely contributed to the similar strain responses observed in each surrogate at larger drop heights, whereas the strain responses from the 30 cm drops had fewer variations and smaller magnitudes. It was also observed throughout most marker pairings that the surrogates typically underwent compression, followed by tension during the impact event. This is was the likely result of the impact, followed by the rebound from the anvil.

The purpose of using two different image analysis methods was to determine if both could produce reliable strain data. The individual marker data obtained through DIC was clean across data sets, unlike those obtained through particle tracking. In the particle tracking method, marker pairings that were more lateral to one another observed more deviations between points that is then amplified

when calculating strain; possible contributing factors included the effect of jitter, the possible lack of motion in this region, particle radius, and surrogate stiffness. Regions within and near the internal capsule of the surrogates benefited from DIC as a result. Although there were differences, both generally produced similar strain data, as peak strains occurred at similar times and their magnitudes were comparable. The DIC and particle tracking data were highly comparable in regions of with gyrification. This was a good indicator that boundary errors had minimal influence on the DIC data as well.

The knowledge gained from understanding the capabilities of both methods can be applied to other TBI studies, as not all specimens can be analysed using both methods. DIC requires a high contrast, randomized speckle pattern for the algorithm to work optimally. In studies where a randomized speckle pattern can be applied to the entire specimen, DIC should be the method of choice, as the strain data was clean and smooth. If marker placement is sparse, resulting in an unsuccessful DIC analysis, then particle tracking should be used. This method performs best when specimens contain individual, uniform markers. Since both methods produced comparable results within this study, this indicated that either method can be used reliably. A few factors to consider when selecting a method are the marker type, spacing, and quantity of markers within the specimen.

The resulting differences between each surrogate, specifically within regions of gyrification, draw interesting parallels to literature. Reviewing previous literature on brain injury, a sign of brain trauma is an accumulation of damage, such as NFTs, primarily at the sulcus [7–9], which may occur due to strain concentrations [5, 6]. This suggests that the motion of the gyri and the resulting effect at the base of the sulci by the impact event would likely contribute to cellular and tissue damage. Therefore, it appears that increased brain gyrification may contribute to the high strain values experienced at the sulci, as minimal strains were observed within the

smooth surrogate at this location. This can also imply that certain models that do not have the appropriate degree of brain gyrification may not undergo the same mechanisms of injury as species with gyrencephalic brains would. This leads to complications of cross-species translation of results. It is then important to select a model that is representative of humans when conducting such research.

Studies that have used models with similar degrees of brain gyrification as humans shared some similarities with the complex surrogate in this study. In the Raghupathi *et al.* [59] study, an increased density of injured axons were found in white matter, primarily in the regions of the sulci and gyri. This could be the result of strain concentrations, which will be discussed later. The complex surrogate experienced higher strain values within this region, which may indicate that increased gyrification is a likely contributor to injury. The same injury mechanisms may not be seen in specimens that lack gyrification. This was a point of validation towards using a specimen with a similar degree of gyrification in future studies.

While the Raghupathi *et al.* [59] study did not link strain values to axonal damage, others have determined that axonal injuries occur between 5% to 10% strain [30]. Although the complex surrogate did not experience strain values that high, they did however have larger strain values than the smooth surrogate and had more variations within the strain responses in the regions of the gyri and sulci. This was likely due to the strain values being linked to material stiffness. Given that the elastomer used was stiffer than brain tissue, lower strains were measured.

Further factors that influenced strain measurements were the impact loading conditions. Each injury scenario in the Ghajari *et al* [6] study saw unique strain responses within the models, with some scenarios showing increased strain values in different areas of the brain. This was likely due to the loading conditions within each injury scenario. Comparable to that study, the brain surrogates saw unique strain responses based on orientation of impact in this study. The common

factor within that study and this study was the high strain values experienced in the regions of the sulci, as observed in the complex surrogate. While the strain values observed in the complex surrogate were not on axonal damage level [30], the results suggest that strain concentrations within regions of increased gyrification may be a likely mechanism leading to tau pathology and the accumulation of NFTs at the sulci.

There were also notable differences between regions of gyrification and the internal capsule. The ratio of peak strain near the gyri was found to be 2-3 times the strain in the internal capsule. Between the sulcus and gyrus of the complex surrogate, the surrogate not only had large magnitudes of strain following the impact, but the strain response itself had a complicated path that experienced compression and tension for tens of milliseconds before returning to near zero strain. This was unlike the internal capsule within both surrogates, which largely remained around 0% strain. These conclusions are comparable to the Ghajari *et al* study as well, where larger strains were found near the sulci and lower strains were found within the internal capsule [6].

Of the three major orientations analysed in this study, the inward orientation had the most unique differences in strain between both surrogates and marker pairings. This was likely due to the orientation of cortical gyrification with respect to the anvil, which was most susceptible to motion. The influences of surrogate tilt beyond that of zero were analysed for the inward orientation (see Appendix C Figures C.39 to C.54). As there was spacing between each gyri, the gyrus could be influenced more when in the inward orientation. In the case of the downward and upward orientations where the gyri and sulci were perpendicular to the anvil, the spacing between the gyri was a less dominant factor in initiating motion, which was reflective in the common strain responses.

In this present study, it was proven that brain tissue surrogates with two different degrees of brain gyrification (smooth and complex) had differences in strain responses. The differences seen in this study are comparable to those by Cloots *et al.* [5]. In that study, two-dimensional computational models were used to represent differences in degrees of gyrification. They also observed increased strains in regions that had material discontinuities, particularly at the base of the their "sulcus". Within their model that lacked geometry, uniform stress along the surface was experienced under loading. While the region of the smooth surrogate in this study was not linear as in that study, the simplicity of the gyrification produced comparable results, as minimal strain was experienced in this region across all orientations. Therefore it appears that gyrification does contribute to strain concentrations, particularly at the base of the sulci.

The brain gyrification study was not meant to recreate injury scenarios that corresponded to specific impacts that may lead to TBIs. This study aimed to keep many experimental parameters consistent to focus purely on the influence of brain gyrification on impact-induced strain measurements. This is something which cannot be truly done using biological specimens. This study has showed that strain values were geometry dependent, thus having implications that not all animal models are equal. Under the same loading conditions and when in different orientations, the two surrogates responded differently. The complex surrogate experienced large strain values and complicated strain responses in regions of the gyri and sulci, a common location of injury markers, whereas the smooth surrogate did not. The differences in measured responses appeared to be influenced by the degree of brain gyrification, which could lead to mechanisms relevant to TBI-level injury being unresolved because of the choice of animal model or degree of brain gyrification used in the model.

The unique contributions of this study, in summary, was the ability to directly

compare two identically scaled surrogates, each possessing the extremes of brain gyrification. The ability to compare two unique brain surrogates showcased the regions where the strain responses differ within specific regions. These differences were specifically pronounced near the cortex where the degree of gyrification was vastly different between surrogates. Along with determining the influences of gyrification, the influences of impact orientation were also observed, which were unique across orientations. Additionally, as two different image analysis methods were used to analyse marker motion, it was determined that either method can be used reliably, but factors, with respect to marker amount, type, and spacing between markers should be taken into consideration; this aided in the development of a methodology for measuring strain in biological tissue.

5.2 Preliminary Viable *Ex Vivo* Porcine Brain Tissue Study

The brain gyrification study was conducted as a precursor to viable *ex vivo* porcine brain tissue testing. From the first study, it was determined that the degree of brain gyrification contributed to the strain responses experienced by the surrogates. The complex surrogate, which had a high degree of brain gyrification, had larger strain values and more intricate strain responses than that of the smooth surrogate, which lacked brain gyrification. These trends were primarily observed in the regions where sulci and gyri were present, a common location of brain injury markers. The distinct variations observed between both degrees of gyrification reaffirmed the choice of using the porcine brain as an *ex vivo* brain model. Additionally, the brain gyrification study aided in developing a methodology for measuring strain

in *ex vivo* porcine brain. Since a surface speckle pattern was not desirable or applicable, this resulted in the creation of individual markers that were placed within the tissue. As individual markers were placed within the brain, the individual particle tracking method was used to track particle motion and the resulting strain.

A previous study using optical DIC used surface markers on their porcine brain specimens [36]. An issue that may arise with this method involves the containment of the specimen. Surface markers may interact with the containment interface, which may result in external factors influencing marker motion. The sub-surface markers used within this study allowed for measurements to be obtained from within the tissue, such that any particle motion could be contributed to tissue motion. This method was beneficial, but also inhibited marker visualization. This proved difficult in further marker placement, where markers were required to be discernible from one another for particle tracking. This also led to fewer markers being placed within the tissue as a result.

Additional knowledge gained from the brain gyrification study was understanding the capabilities of each image analysis method, DIC and individual particle tracking. Applying a radiopaque speckle pattern to the porcine brain tissue was not possible and was also not desired, as stated above. This resulted in the application of individual markers that were placed throughout the tissue, focusing on regions of cortical gyrification. Although approximately 80 markers were placed in each tissue, the markers were placed too sparsely to use DIC successfully. Particle tracking was used instead and was able to successfully track individual markers and produce direct strain data.

Both brain gyrification and viable *ex vivo* porcine brain studies shared some similarities when it came to experimental techniques and analyses. Similar encasements with modified cavities were used, as well as the same drop apparatus.

A new radiopaque marker method was developed for this study using similar concepts as the previous study. Additionally, some of the same image processing and particle tracking methods were used.

During both experiment days, every porcine brain provided two treatment tissues and two control tissues, resulting in a total of four treatment tissues being dropped from 90 cm. The design of the experiment allowed for two specimens to be dropped in unison. This decreased experimental testing time, while also applying the same loading conditions to each tissue.

While markers were placed in various regions within the tissue, the focus of this section will be placed on markers in the regions near and within the gyri. Each strain response was unique between marker pairings. Within the same tissue, markers in different regions produced different strain responses. Generally, each marker pair produced at least one peak compressive or tensile strain, but each response was largely unique. This could imply that each unique brain gyrification responded differently under impact; while all porcine brains are gyrencephalic, each brain had unique folding patterns.

The strain data from each brain produced distinct differences; these will be discussed below. The May 16th brain sections from the left side of the drop apparatus had similar trends. The marker pairing in Figure 69 had peak strains of -3.6% and 12.7% strain. Within the same tissue, the other marker pairing had peak strains of -1.8% and 9.4% strain (Figure 70). The brain section dropped on the right side of the drop apparatus had more variations in the results. The marker pairing in Figure 71 had peak strains of -14.5% and 8.5%. The other marker pairing had peak strains of -22.7% and 5.6% (Figure 72).

The June 6th brain, which appeared visually different than the previous brain, mainly produced smaller magnitudes of strain. The brain sections dropped on the left side of the apparatus had notable variations within the strain response. The

first marker pairing had peak strains of -4.7% and 3.8% strain (Figure 73). The other marker pairing had peak strains of -11.0% and 5.7% strain (Figure 74). The brain section dropped on the right side of the drop apparatus had fewer strain variations compared to the other tissue section. The marker pairing in Figure 75 had peak strains of -6.0% and 2.1%, whereas the second marker pair had peak strains of -22.6% and 8.9% (Figure 76).

There were three factors that likely contributed to the differences in strain response. This included brain gyrification, white and grey matter content, and marker positioning. Although age, sex, and brain size were relatively consistent, each tissue appeared visually different. The brain section from June 6th had more gyri and sulci that were relatively thin compared to the brain section from May 16th (Figure 68). The resulting strain responses from the June 6th brain appeared to have more variations that included both tensile and compressive peak strains than those observed from the May 16th brain, which primarily were in either tension or compression. The smaller, but greater amount of gyri found within the brain sections from June 6th may have created more movement within those regions, resulting in the slight increase in variations within the strain responses.

The level of brain gyrification varied from specimen to specimen regardless that both were from the same species and brain classification. These differences caused notable changes in the way that the white and grey matter were organized, which may have contributed to the strain response. As previously stated, white matter is stiffer than grey matter. The May 16th brain sections appeared to have large regions of white matter. The resulting strain responses were subdued, with fewer variations within the response, but the strain magnitudes were still quite large. The June 6th brain sections had white matter well distributed across the sample. The resulting strain responses had more variations, but had lower magnitudes of

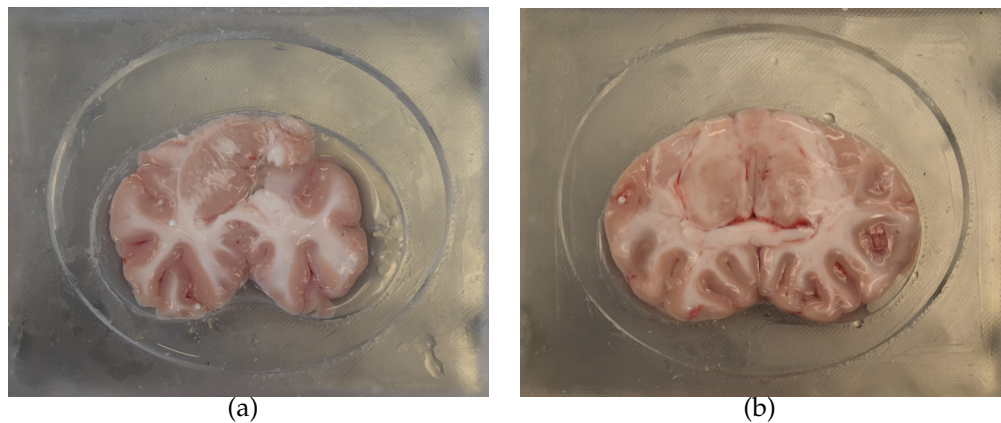


Figure 68: One set of porcine brain sections taken from a) May 16, 2019 and b) June 6, 2019.

strain.

Another factor that may have influenced the response was the distance between two selected markers. Markers that were closer together produced strain responses that did not have extreme variations within the response. There was one marker pairing that produced noticeably different trends (Figure 73). This marking pairing had variations in the strain response until the end of the analysis, while all other pairs had strain responses that were approximately 0% strain after 15 to 20 ms. This likely occurred because the marker pairing was further apart than all other pairings. Markers that were further apart may have experienced larger ranges of motion after impact than markers that were closer together. These closely paired markers had similar trajectories, resulting in fewer variations within the strain responses.

The location of each marker in a pair relative to one another influenced the strain response as well. Markers that had similar x- coordinates generally experienced larger magnitudes of compressive strains over tensile strains when impacted (Figures 71 to 76). This is a likely result of marker placement, which due to the similarities mentioned above, may experience the compressive effects of the impact

to a larger degree. This trend was not seen in markers that were more lateral to one another. These markers tended to experience tension after impact (Figures 69 and 70). This is a likely effect of this marker placement, where the impact likely caused the markers in this configuration to move away from one another. The variability of strain values and responses taken from regions where sulci and gyri are present is indicative that a complex range of motions occurs at locations of geometric variations.

Similarities between the brain gyrification and the viable *ex vivo* porcine brain tissue studies were found, as most strain responses returned to approximately 0% strain before 20 ms. While the strain values were approximately 0% after this time point, not all values returned to near zero strain as was seen in the previous study. This could be the result of the tissue's final position being different than its initial position. The tissues were soft and did not maintain their shape very well. After the initial impact, the tissues may have slid inside the encasements (final strain values in compression) or may have overextended (final strain values in tension); attempts were made to reduce this issue. Although the specimens were slightly compressed laterally, they were not overly compressed. This would have potentially caused additional stress upon the brain tissue sections, influencing the strain data, as well as the staining process that was applied to the brain tissue sections post-impact by collaborators in the Department of Neuroscience. Therefore the initial peak strains may be a good indicator of strains experienced in the tissues, although all are taken into account.

Markers within the region near the fissure produced direct strain values that varied in magnitude (Figures 69 to 76). Many of the peak strain values within the figures were within the range of strain values that is expected to produce DAI [30]. On average, when looking at other marker pairings surrounding the markers highlighted within the figures, the strain values were within the expected DAI range,

with many being on the lower end of the range (see Appendix C, Table C.9).

Studies have observed axonal injury in porcine brains. The Raghupathi *et al.* [59] study saw an increased accumulation of axonal damage in white matter in porcine brains, specifically in regions present with sulci and gyri, after rotational loading. While the loading conditions were different, the link between strain thresholds and regions of axonal injury accumulation are of interest. This may imply that the loading conditions of the porcine tissue sections within this study may have also caused injury.

Markers in the gyrus of the porcine brain tissue had large variations within each strain response, which was commonly seen in the gyrus and sulcus in the complex surrogate. While the magnitudes and degrees of variations within the strain responses were different between both studies, the response between the porcine brain section (see Figure 71) and the complex surrogate (see Figure 59) were broadly similar, but with different magnitudes. This could be another point of validation for using more compatible specimens for TBI research.

Generally, the brain surrogates never experienced strains greater than 2.5%, whereas the porcine tissue sections produced larger strain values. This was likely the result of the surrogate material. The surrogates were firmer than brain tissue, which allowed them to maintain their distinct gyrification pattern and to be repeatedly impacted. These properties are not found within the viable *ex vivo* porcine brain tissue sections, which were soft with slight adhesion to one another due to aCSF and the brain matter itself. Each individual gyrus crept into neighbouring gyri, unlike the surrogates. The matter composition of the brain tissue would likely be more susceptible to motion, which may have contributed to the increased amount of variations within the strain responses, as well as strain magnitudes.

The main contributions from this study, in summary, were the ability to measure strain in viable *ex vivo* porcine brain tissue sections after developing a methodology for strain measurement in the brain gyrification study, and creating new techniques for marker integration into biological tissue. Experimental components from the brain gyrification study were integrated into this study, with similar particle analysis techniques being used to obtain strain values. The porcine model for brain injury showed promising results, which makes it an ideal translation model for TBIs.

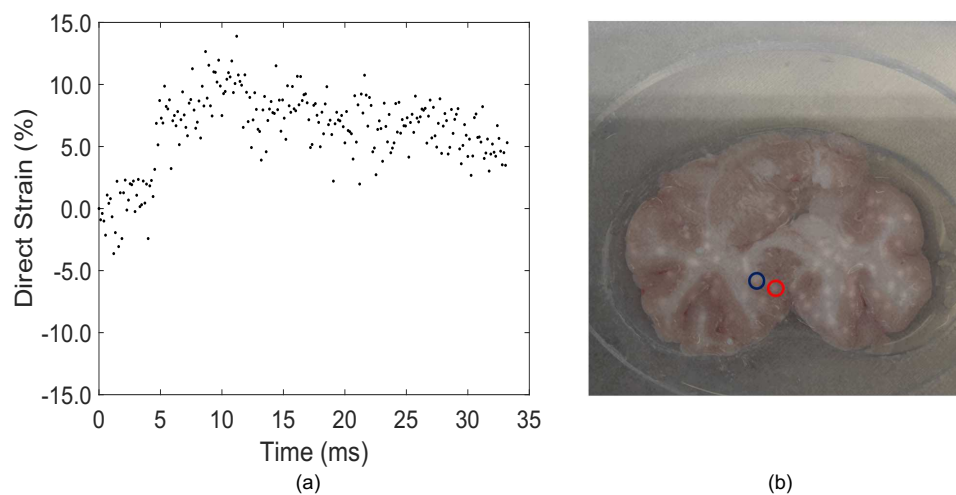


Figure 69: Strain data (a) from the marker pairing indicated in the left gyrus (b) of the porcine brain obtained on May 16, 2019. This specimen was in the encasement to the left of the drop apparatus. The image to the right is an overlay of the X-ray image with markers and an optical image of the tissue.

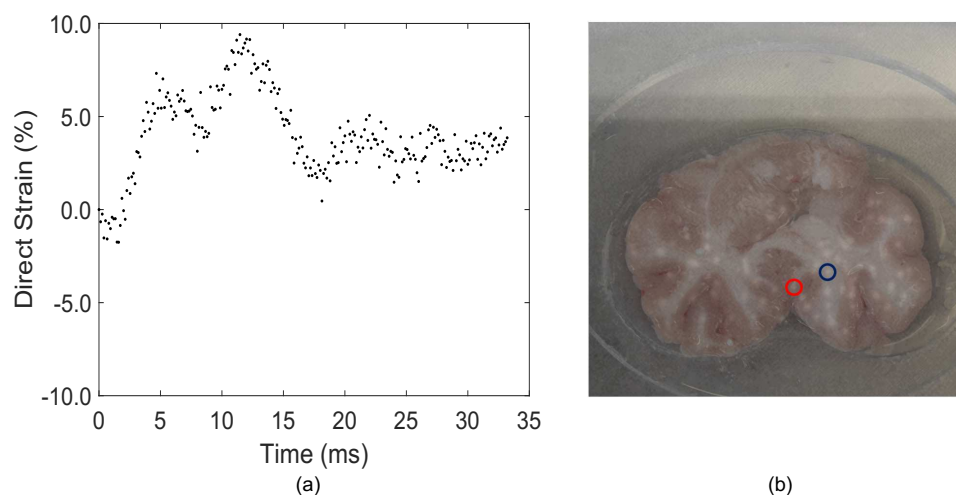


Figure 70: Strain data (a) from the marker pairing indicated in the right gyrus (b) of the porcine brain obtained on May 16, 2019. This specimen was in the encasement to the left of the drop apparatus. The image to the right is an overlay of the X-ray image with markers and an optical image of the tissue.

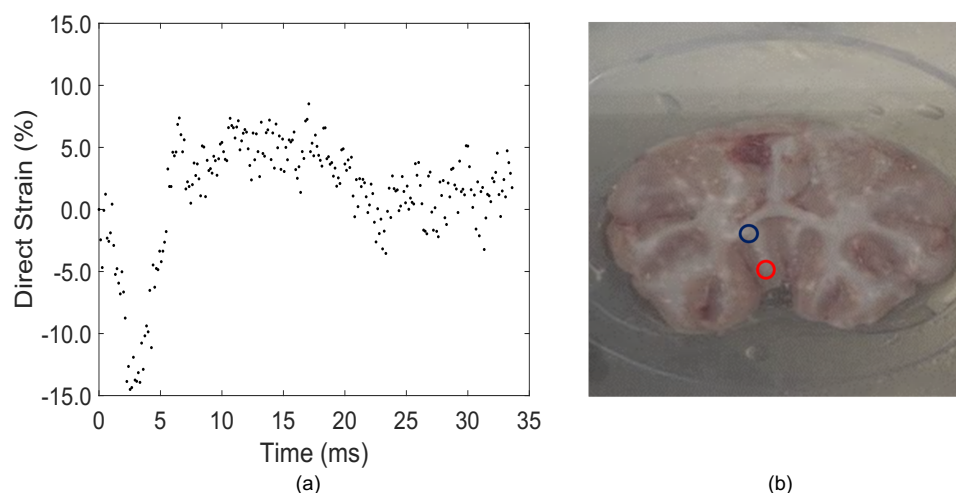


Figure 71: Strain data (a) from the marker pairing indicated in the left gyrus (b) of the porcine brain obtained on May 16, 2019. This specimen was in the encasement to the right of the drop apparatus. The image to the right is an overlay of the X-ray image with markers and an optical image of the tissue.

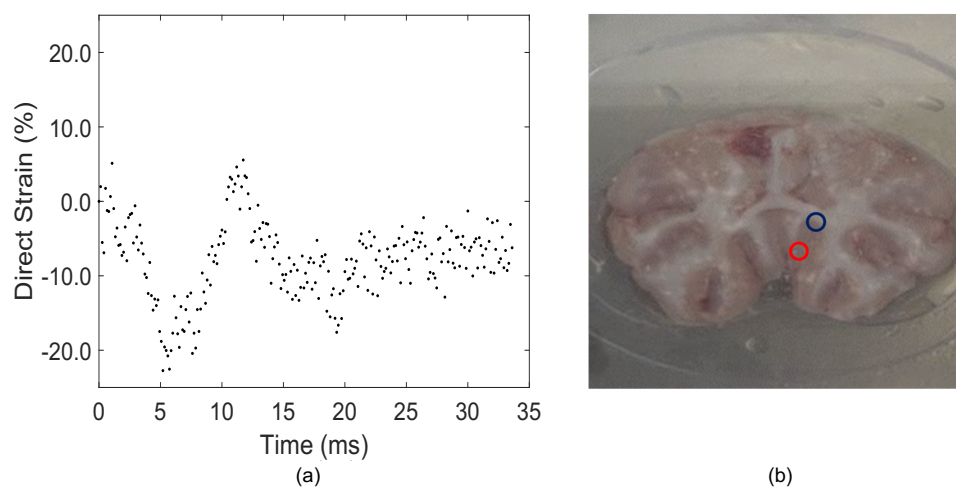


Figure 72: Strain data (a) from the marker pairing indicated in the right gyrus (b) of the porcine brain obtained on May 16, 2019. This specimen was in the encasement to the right of the drop apparatus. The image to the right is an overlay of the X-ray image with markers and an optical image of the tissue.

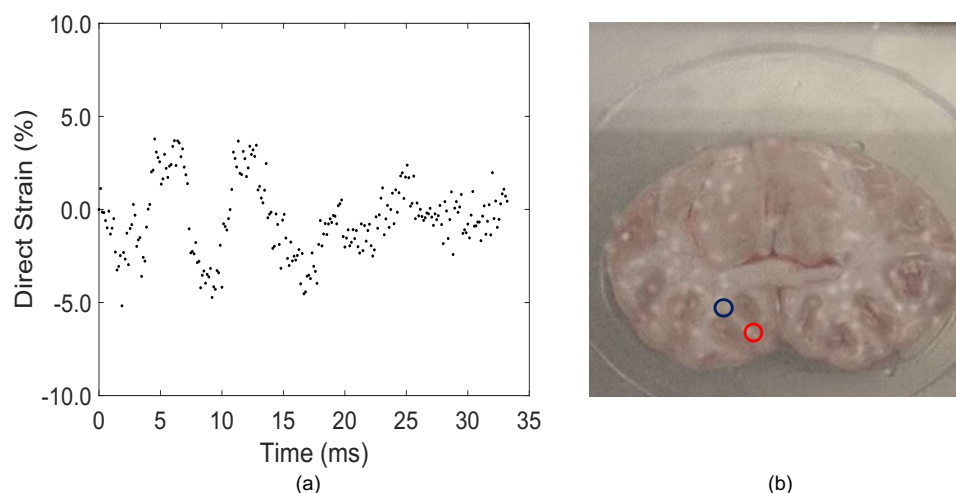


Figure 73: Strain data (a) from the marker pairing indicated in the left gyrus (b) of the porcine brain obtained on June 6, 2019. This specimen was in the encasement to the left of the drop apparatus. The image to the right is an overlay of the X-ray image with markers and an optical image of the tissue.

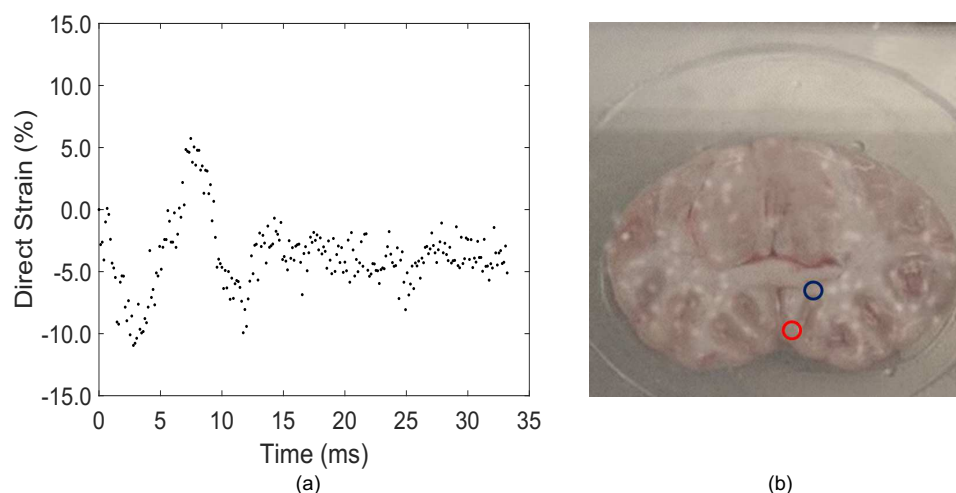


Figure 74: Strain data (a) from the marker pairing indicated in the right gyrus (b) of the porcine brain obtained on June 6, 2019. This specimen was in the encasement to the left of the drop apparatus. The image to the right is an overlay of the X-ray image with markers and an optical image of the tissue.

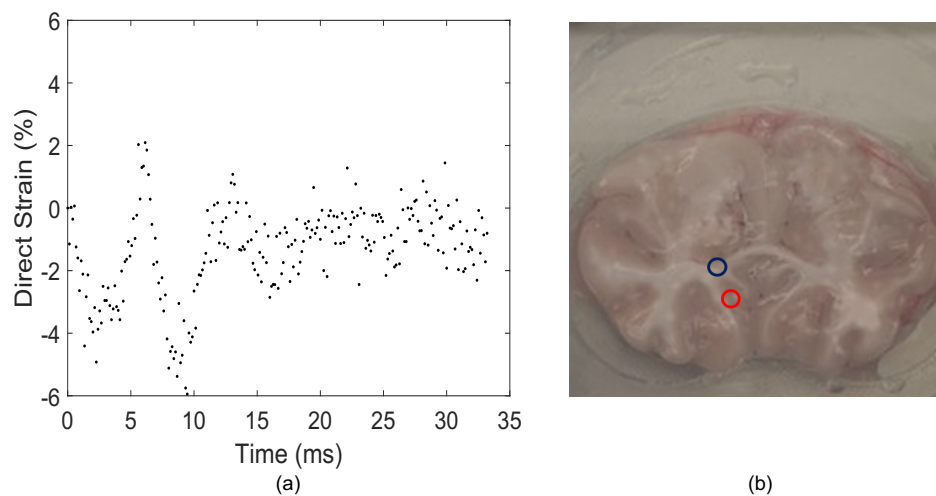


Figure 75: Strain data (a) from the marker pairing indicated in the left gyrus (b) of the porcine brain obtained on June 6, 2019. This specimen was in the encasement to the right of the drop apparatus. The image to the right is an overlay of the X-ray image with markers and an optical image of the tissue.

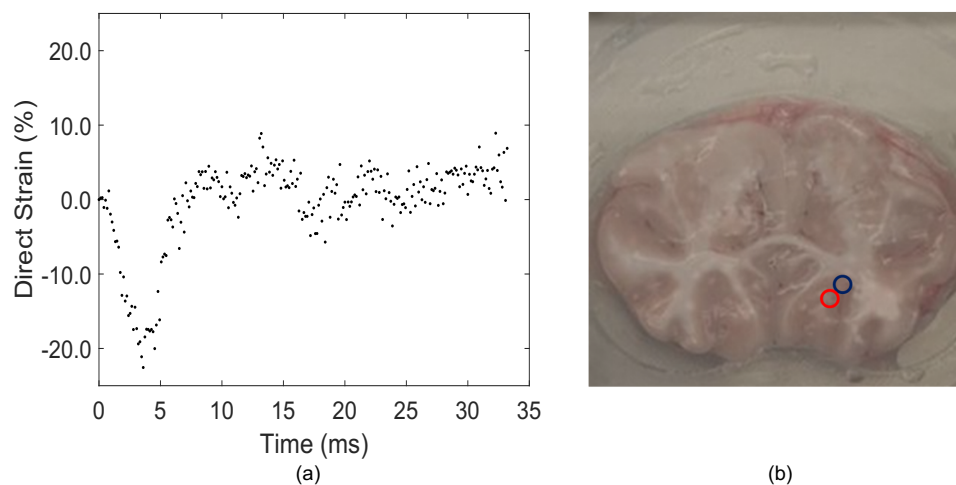


Figure 76: Strain data (a) from the marker pairing indicated in the right gyrus (b) of the porcine brain obtained on June 6, 2019. This specimen was in the encasement to the right of the drop apparatus. The image to the right is an overlay of the X-ray image with markers and an optical image of the tissue.

Chapter 6

Conclusions

Each study within this work has provided unique contributions to this area of research, not only with the individual models used, but for the use of high-speed X-ray radiography as well. The brain gyrification study focused on two brain tissue surrogates that were representative of the extremes of brain gyrification. The first represented specimens with a smooth cortex, such as rodents, and the second was comparable to a brain with gyrification, as seen in porcine and human brains. Both surrogates were impacted at varying heights and in different orientations, with their resulting strain responses being measured. The main objective of this study was to then determine the differences in strain responses observed in both surrogates. This study was also able to test what most animal models cannot. Using surrogates as our model, the direct differences in strain responses caused by both extremes of brain gyrification were compared.

Two different image analysis methods were used to calculate strain: DIC and particle tracking. DIC uses subsets to calculate displacements within a speckle pattern and individual particle trackers use particle characteristics. While both produced similar results, the strain responses obtained through DIC were smooth, whereas this was only true in some scenarios for the strain responses obtained through particle tracking. When choosing an image analysis method, the type of

pattern applied to the specimens should be considered, as not every method can be used successfully.

Within this study, the strain values and variations in strain response varied between all marker locations. The strain responses had minimal variations within the internal capsule for both surrogates. As the analysed markers became closer to regions of gyrification, distinct differences were observed across the surrogates. The regions of gyrification were of particular interest, as these were found to be locations of brain injury markers. The complex surrogate experienced high strain variations and magnitudes, with peak strains between 1 and 2%, across all orientations within these regions. This was not observed in the smooth surrogate, which experienced minimal variations in the strain response and low strain values.

The variations in results observed between surrogates suggest that both extremes of gyrification have different mechanical responses under impact. Not only does increased brain gyrification influence strain, but the orientation of impact also contributes to the variations. These results may suggest that certain mechanisms are missing in animal models that do not possess the same degree of brain gyrification that is possessed by humans. While these models do provide useful insight into some aspects of TBI, likely injury pathways and mechanisms may be biased by the choice of animal model. A shift towards more representative animal models that have brain gyrification resembling that in humans should be taken into consideration in TBI research that involves impact testing.

This study was conducted in preparation for the preliminary study on viable *ex vivo* porcine brain tissue sections, where a methodology was developed to calculate strain; this was the second objective of this thesis. From the previous study, the designs of the drop apparatus and encasements were made such that they could also be applied to the porcine brain tissue sections with minimal to no modifications needed. The radiopaque speckle sheet that was easily incorporated into the

surrogates could not be applied to the porcine brain tissue, therefore a new technique was created to insert markers individually into the tissue at the time of the experiment. This individual marker insertion technique can also be applied if a speckle pattern cannot be applied to the surface of the tissue. From the brain gyrification study, it was determined that both DIC and individual particle tracking produced results that agreed with one another in most scenarios, with DIC producing the cleanest strain responses. When tracking radiopaque markers within the *ex vivo* porcine brain tissue sections, individual particle tracking was selected, as DIC could not be performed successfully, and the same direct strain calculations were performed as the surrogate study.

Within the preliminary viable *ex vivo* porcine brain tissue study, strain responses were obtained from the specimens; this was the third objective of this thesis. It was determined that the strain responses were likely influenced by marker location and gyrification. The two porcine brains used in the study produced brain tissue sections that were visually different, even though they were from the same species. After impacting the specimens at the same height and orientation, many of the peak strains obtained within this study were within the range of DAI-inducing strains. This study provided further evidence that species with similar degrees of brain gyrification to humans are an ideal animal model for TBI research.

Future Recommendations

A few suggestions on improvements can be made for future studies based on image analysis method used. When capturing specimen deformation with a camera, uneven illumination may occur. While image illumination was relatively even in this study, slight variations in pixel intensities caused by uneven illumination may influence the results. This can be corrected by applying an image filter and would

aid in the analysis process of each method. Additionally, in DIC, boundary errors were reduced by using the appropriate parameters. Creating a specimen that is large enough, such that its boundaries are located further away from regions of interest, may reduce boundary error contributions.

Continuing with improvements, a few suggestions can be made for specimens that use the Mosaic ParticleTracker. The surrogate speckle sheet provided a full field of markers. The particle tracker can sometimes have difficulties tracking markers, as the algorithm may sometimes confuse a marker with neighbouring markers; parameters can be changed to minimize this, though it is not always feasible. A possible solution is to only place markers in regions of interest, such that there are no other markers surrounding the area. This can limit the possibility of marker confusion, which can lead to more successful particle tracking; the markers would be more distinguishable from the surrounding material. Additionally, marker location was determined based on brightness. The markers need to appear as bright as possible (white) and the background needs to be as dark as possible without compromising the image. Image processing can be applied to images to perform such enhancements; this was performed to some degree on all data sets within reason. If a hard boundary between the markers and surrounding areas can be created, in which all markers are one intensity value and the boundary is another intensity value, then the marker trajectory values may be more precise.

There are a few additional studies that can be derived from the aforementioned studies. The brain gyrification study can be evolved into a 3D study. The same techniques can be applied with minimal to no modifications. Radiopaque speckle sheets can be introduced into 3D models that possess and lack brain gyrification. These studies would have more realistic boundary conditions, which could be comparable to real-life scenarios. Instead of determining the influence of gyrification in one section, the influence of the whole brain can be measured.

The difficulties associated with marker integration (placement, visualization, quantity) in the preliminary viable *ex vivo* porcine brain tissue study can be rectified in future studies. The purpose of the sub-surface markers was to measure pure tissue motion. Radiopaque markers can be used in future studies if the tissue sections were to remain optically hidden. To continue using this marker technique would require refinement, possibly using a different radiopaque material, which would ideally increase the amount of markers within the tissue, as well as the certainty of marker placement when comparing optical and X-ray images.

Another route this study could take is to move to optical DIC and particle tracking. This would require surface markers. This would allow for markers to be visualized in their exact tissue locations, such that strain measurements can be clearly linked back to regions with gyrification. This may introduce marker adhesion to the interface, but could be resolved using a releasing agent or not completely encasing the tissues. Surface markers would benefit immunohistochemical staining techniques, as surface markers would guarantee tissue integrity within regions that are stained.

List of References

- [1] Centers for Disease Control and Prevention, "Report to Congress on Traumatic Brain Injury in the United States: Epidemiology and Rehabilitation." National Center for Injury Prevention and Control; Division of Unintentional Injury Prevention, Atlanta, GA, USA, 2015.
- [2] Institute of Neurological Disorders and Stroke. National Institutes of Health, "Traumatic Brain Injury : Hope Through Research." Institute of Neurological Disorders and Stroke. National Institutes of Health. Bethesda, MD, USA, 2013.
- [3] F. Zollman, ed., *Manual of Traumatic Brain Injuries*. New York, NY: Demos Medical Publishing, 2011. [E-book]. Available: ProQuest Ebook Central.
- [4] A. C. McKee and M. E. Robinson, "Military-related traumatic brain injury and neurodegeneration," *Alzheimer's and Dementia*, vol. 10, no. 3 Suppl., pp. S242–S253, 2014.
- [5] R. J. Cloots, H. M. Gervaise, J. A. Van Dommelen, and M. G. Geers, "Biomechanics of traumatic brain injury: Influences of the morphologic heterogeneities of the cerebral cortex," *Annals of Biomedical Engineering*, vol. 36, no. 7, pp. 1203–1215, 2008.
- [6] M. Ghajari, P. J. Hellyer, and D. J. Sharp, "Computational modelling of traumatic brain injury predicts the location of chronic traumatic encephalopathy pathology," *Brain*, vol. 140, no. 2, pp. 333–343, 2017.
- [7] A. C. McKee, T. D. Stein, C. J. Nowinski, R. A. Stern, D. H. Daneshvar, V. E. Alvarez, H.-S. Lee, G. Hall, S. M. Wojtowicz, C. M. Baugh, D. O. Riley, C. A. Kubilus, K. A. Cormier, M. A. Jacobs, B. R. Martin, C. R. Abraham, T. Ikezu, R. R. Reichard, B. L. Wolozin, A. E. Budson, L. E. Goldstein, N. W. Kowall, and R. C. Cantu, "The spectrum of disease in chronic traumatic encephalopathy," *Brain*, vol. 136, pp. 43–64, 2013.

- [8] T. Guo, W. Noble, and D. P. Hanger, "Roles of tau protein in health and disease," *Acta Neuropathologica*, vol. 133, no. 5, pp. 665–704, 2017.
- [9] M. F. Horstemeyer, P. R. Berthelson, J. Moore, A. K. Persons, A. Dobbins, and R. K. Prabhu, "A Mechanical Brain Damage Framework Used to Model Abnormal Brain Tau Protein Accumulations of National Football League Players," *Annals of Biomedical Engineering*, vol. 47, no. 9, pp. 1873–1888, 2019.
- [10] R. Sugerman, "Psychobiologic bases of behavior," in *Psychiatric Nursing* (N. Keltner, C. Bostrom, and T. McGuinness, eds.), pp. 44–59, St. Louis: Elsevier Mosby, 6th ed., 2013.
- [11] P. R. Krafft, E. L. Bailey, T. Lekic, W. B. Rolland, O. Altay, J. Tang, J. M. Wardlaw, J. H. Zhang, and C. L. Sudlow, "Etiology of stroke and choice of models," *International Journal of Stroke*, vol. 7, no. 5, pp. 398–406, 2012.
- [12] J. Weickenmeier, R. de Rooij, S. Budday, P. Steinmann, T. C. Ovaert, and E. Kuhl, "Brain stiffness increases with myelin content," *Acta Biomaterialia*, vol. 42, pp. 265–272, 2016.
- [13] V. Fernández, C. Llinares-Benadero, and V. Borrell, "Cerebral cortex expansion and folding: what have we learned?," *The EMBO Journal*, vol. 35, no. 10, pp. 1021–1044, 2016.
- [14] D. H. Smith and D. F. Meaney, "Axonal damage in traumatic brain injury," *Neuroscientist*, vol. 6, no. 6, pp. 483–495, 2000.
- [15] B. Szymik, "Neuron Anatomy." *ASU - Ask a Biologist*, May 3, 2011. [Online]. Available: <https://askabiologist.asu.edu/neuron-anatomy>, 2011. [Accessed: Mar. 2, 2020].
- [16] Centers for Disease Control and Prevention, "Surveillance Report of Traumatic Brain Injury-related Emergency Department Visits, Hospitalizations, and Deaths—United States, 2014." Centers for Disease Control and Prevention. U.S. Department of Health and Human Services, Atlanta, GA, USA, 2019.
- [17] R. A. Stern, D. O. Riley, D. H. Daneshvar, C. J. Nowinski, R. C. Cantu, and A. C. McKee, "Long-term Consequences of Repetitive Brain Trauma: Chronic Traumatic Encephalopathy," *PM and R*, vol. 3, no. 10 Suppl. 2, pp. S460–S467, 2011.

- [18] D. F. Meaney, B. Morrison, and C. D. Bass, "The mechanics of traumatic brain injury: A review of what we know and what we need to know for reducing its societal burden," *Journal of Biomechanical Engineering*, vol. 136, no. 2, pp. 021008–1 – 021008–14, 2014.
- [19] D. F. Meaney and D. H. Smith, "Biomechanics of Concussion," *Clinics in Sports Medicine*, vol. 30, no. 1, pp. 1–12, 2011.
- [20] M. P. Poirier, "Concussions: Assessment, management, and recommendations for return to activity," *Clinical Pediatric Emergency Medicine*, vol. 4, no. 3, pp. 179–185, 2003.
- [21] D. K. Cullen, J. P. Harris, K. D. Browne, J. A. Wolf, J. E. Duda, D. F. Meaney, S. S. Margulies, and D. H. Smith, "A Porcine Model of Traumatic Brain Injury via Head Rotational Acceleration," *Methods in Molecular Biology*, vol. 1462, pp. 289–324, 2016.
- [22] D. D. Chan, A. K. Knutsen, Y. C. Lu, S. H. Yang, E. Magrath, W. T. Wang, P. V. Bayly, J. A. Butman, and D. L. Pham, "Statistical Characterization of Human Brain Deformation during Mild Angular Acceleration Measured in Vivo by Tagged Magnetic Resonance Imaging," *Journal of Biomechanical Engineering*, vol. 140, no. 10, pp. 101005–1–101005–13, 2018.
- [23] S. Ouellet and O. E. Petel, "On the prospective contributions of the shock physics community to outstanding issues concerning blast-induced traumatic brain injury," *Shock Waves*, vol. 27, pp. 821–827, 2017.
- [24] S. Wiri, A. C. Ritter, J. M. Bailie, C. Needham, and J. L. Duckworth, "Computational modeling of blast exposure associated with recoilless weapons combat training," *Shock Waves*, vol. 27, pp. 849–862, 2017.
- [25] G. Teasdale and B. Jennett, "Assessment of coma and impaired consciousness. A practical scale," *The Lancet*, vol. 2, no. 7872, pp. 81–84, 1974.
- [26] M. E. Shenton, H. M. Hamoda, J. S. Schneiderman, S. Bouix, O. Pasternak, Y. Rathi, M. A. Vu, M. P. Purohit, K. Helmer, I. Koerte, A. P. Lin, C. F. Westin, R. Kikinis, M. Kubicki, R. A. Stern, and R. Zafonte, "A review of magnetic resonance imaging and diffusion tensor imaging findings in mild traumatic brain injury," *Brain Imaging and Behavior*, vol. 6, no. 2, pp. 137–192, 2012.
- [27] D. Laskowitz and G. Grant, eds., *Translational Research in Traumatic Brain Injury*. Boca Raton: CRC Press/Taylor and Francis Group, 2016. [E-book]. Available: NCBI Bookshelf.

- [28] S. Mori and J. Zhang, "Principles of Diffusion Tensor Imaging and Its Applications to Basic Neuroscience Research," *Neuron*, vol. 51, no. 5, pp. 527–539, 2006.
- [29] K. Arfanakis, V. M. Haughton, J. D. Carew, B. P. Rogers, R. J. Dempsey, and M. E. Meyerand, "Diffusion tensor MR imaging in diffuse axonal injury," *American Journal of Neuroradiology*, vol. 23, no. 5, pp. 794–802, 2002.
- [30] S. S. Margulies and L. E. Thibault, "A proposed tolerance criterion for diffuse axonal injury in man," *Journal of Biomechanics*, vol. 25, no. 8, pp. 917–923, 1992.
- [31] S. S. Margulies, L. E. Thibault, and T. A. Gennarelli, "Physical model simulations of brain injury in the primate," *Journal of Biomechanics*, vol. 23, no. 8, pp. 823–836, 1990.
- [32] M. V. Sofroniew and H. V. Vinters, "Astrocytes: Biology and pathology," *Acta Neuropathologica*, vol. 119, no. 1, pp. 7–35, 2010.
- [33] M. Bottlang, M. B. Sommers, T. A. Lusardi, J. J. Miesch, R. P. Simon, and Z. G. Xiong, "Modeling neural injury in organotypic cultures by application of inertia-driven shear strain," *Journal of Neurotrauma*, vol. 24, no. 6, pp. 1068–1077, 2007.
- [34] M. C. LaPlaca, D. K. Cullen, J. J. McLoughlin, and R. S. Cargill, "High rate shear strain of three-dimensional neural cell cultures: A new in vitro traumatic brain injury model," *Journal of Biomechanics*, vol. 38, no. 5, pp. 1093–1105, 2005.
- [35] M. Sarntinoranont, S. J. Lee, Y. Hong, M. A. King, G. Subhash, J. Kwon, and D. F. Moore, "High-strain-rate brain injury model using submerged acute rat brain tissue slices," *Journal of Neurotrauma*, vol. 29, no. 2, pp. 418–429, 2012.
- [36] C. Lauret, M. Hrapko, J. A. van Dommelen, G. W. Peters, and J. S. Wismans, "Optical characterization of acceleration-induced strain fields in inhomogeneous brain slices," *Medical Engineering and Physics*, vol. 31, no. 3, pp. 392–399, 2009.
- [37] Thermo Fisher Scientific - US, "Introduction to Cell Culture." [Online]. Available: <http://www.invitrogen.com/site/us/en/home/References/gibco-cell-culture-basics/introduction-to-cell-culture.html>. [Accessed: Jun. 6, 2019].

- [38] H. Lodish, A. Berk, S. Zipursky, P. Matsudaira, D. Baltimore, and J. Darnell, *Molecular Cell Biology*. New York, NY: W.H. Freeman, 4th ed., 2000. [E-book]. Available: NCBI Bookshelf.
- [39] T. W. Sawyer, D. V. Ritzel, Y. Wang, T. Josey, M. Villanueva, P. Nelson, Y. Song, Y. Shei, G. Hennes, C. Vair, S. Parks, C. Fan, and L. McLaws, "Primary Blast Causes Delayed Effects without Cell Death in Shell-Encased Brain Cell Aggregates," *Journal of Neurotrauma*, vol. 34, pp. 174–186, 2018.
- [40] T. W. Sawyer, T. Josey, Y. Wang, M. Villanueva, D. V. Ritzel, P. Nelson, and J. J. Lee, "Investigations of primary blast-induced traumatic brain injury," *Shock Waves*, vol. 28, pp. 85–99, 2018.
- [41] T. Piehler, R. Banton, N. Zander, J. Duckworth, R. Benjamin, and R. Sparks, "High-speed imaging and small-scale explosive characterization techniques to understand effects of primary blast-induced injury on nerve cell structure and function," *Shock Waves*, vol. 28, pp. 37–50, 2018.
- [42] P. Thielen, T. Mehoke, J. Gleason, A. Iwaskiw, J. Paulson, A. Merkle, B. Wester, and J. Dymond, "Exploration of the molecular basis of blast injury in a biofidelic model of traumatic brain injury," *Shock Waves*, vol. 28, pp. 115–126, 2018.
- [43] E. Bar-Kochba, M. T. Scimone, J. B. Estrada, and C. Franck, "Strain and rate-dependent neuronal injury in a 3D in vitro compression model of traumatic brain injury," *Scientific Reports*, vol. 6, pp. 1–11, 2016.
- [44] J. A. Chuckowree and J. C. Vickers, "Cytoskeletal and morphological alterations underlying axonal sprouting after localized transection of cortical neuron axons in vitro," *Journal of Neuroscience*, vol. 23, no. 9, pp. 3715–3725, 2003.
- [45] S. A. Sherman, J. K. Phillips, J. T. Costa, F. S. Cho, S. R. Oungoulian, and J. D. Finan, "Stretch Injury of Human Induced Pluripotent Stem Cell Derived Neurons in a 96 Well Format," *Scientific Reports*, vol. 6, pp. 1–12, 2016.
- [46] E. J. Murphy and L. A. Horrocks, "A Model for Compression Trauma: Pressure-Induced Injury in Cell Cultures," *Journal of Neurotrauma*, vol. 10, no. 4, pp. 431–444, 1993.
- [47] M. C. LaPlaca and L. E. Thibault, "Dynamic mechanical deformation of neurons triggers an acute calcium response and cell injury involving the

- N-methyl-D-Aspartate glutamate receptor," *Journal of Neuroscience Research*, vol. 52, no. 2, pp. 220–229, 1998.
- [48] M. Patestas and L. Gartner, *A Textbook of Neuroanatomy*. Malden, MA: Blackwell Publishing, 2006.
- [49] K. Zhang and T. J. Sejnowski, "A universal scaling law between gray matter and white matter of cerebral cortex," *Proceedings of the National Academy of Sciences of the United States of America*, vol. 97, no. 10, pp. 5621–5626, 2000.
- [50] R. Vink, "Large animal models of traumatic brain injury," *Journal of Neuroscience Research*, vol. 96, no. 4, pp. 527–535, 2018.
- [51] E. D. Hall, Y. D. Bryant, W. Cho, and P. G. Sullivan, "Evolution of Post-Traumatic Neurodegeneration after Controlled Cortical Impact Traumatic Brain Injury in Mice and Rats as Assessed by the De Olmos Silver and Fluorochrome Staining Methods," *Journal of Neurotrauma*, vol. 25, no. 3, pp. 235–247, 2008.
- [52] C. E. Dixon, B. G. Lyeth, J. T. Povlishock, R. L. Findling, R. J. Hamm, A. Marmarou, H. F. Young, and R. L. Hayes, "A fluid percussion model of experimental brain injury in the rat," *Journal of Neurosurgery*, vol. 67, no. 1, pp. 110–119, 1987.
- [53] A. Marmarou, M. A. Abd-Elfattah Foda, W. Van den Brink, J. Campbell, H. Kita, and K. Demetriadou, "A new model of diffuse brain injury in rats. Part I: Pathophysiology and biomechanics," *Journal of Neurosurgery*, vol. 80, no. 2, pp. 291–300, 1994.
- [54] A. K. Ommaya, P. Yarnell, A. E. Hirsch, and E. H. Harris, "Scaling of Experimental Data on Cerebral Concussion in Sub-Human Primates to Concussion Threshold for Man," tech. rep., Naval Ship Research and Development Center, 1967.
- [55] A. Jean, M. K. Nyein, J. Q. Zheng, D. F. Moore, J. D. Joannopoulos, and R. Radovitzky, "An animal-to-human scaling law for blast-induced traumatic brain injury risk assessment," *Proceedings of the National Academy of Sciences of the United States of America*, vol. 111, no. 43, pp. 15310–15315, 2014.
- [56] J. W. Finnie, "Animal models of traumatic brain injury: a review," *Australian Veterinary Journal*, vol. 79, no. 9, pp. 628–633, 2001.

- [57] C. A. Guertler, R. J. Okamoto, J. L. Schmidt, A. A. Badachhape, C. L. Johnson, and P. V. Bayly, "Mechanical properties of porcine brain tissue in vivo and ex vivo estimated by MR elastography," *Journal of Biomechanics*, vol. 69, no. 12, pp. 10–18, 2018.
- [58] D. H. Smith, X.-H. Chen, M. Nonaka, J. Q. Trojanowski, V.-Y. Lee, K. E. Saatman, M. J. Leoni, B.-N. Xu, J. A. Wolf, and D. F. Meaney, "Accumulation of Amyloid β and Tau and the Formation of Neurofilament Inclusions Following Diffuse Brain Injury in the Pig," *Journal of Neuropathology & Experimental Neurology*, vol. 58, no. 9, pp. 982–992, 1999.
- [59] R. Raghupathi, M. F. Mehr, M. A. Helfaer, and S. S. Margulies, "Traumatic Axonal Injury is Exacerbated following Repetitive Closed Head Injury in the Neonatal Pig," *Journal of Neurotrauma*, vol. 21, no. 3, pp. 307–316, 2004.
- [60] E. M. Fievisohn, V. S. S. Sajja, P. J. Vandevord, and W. N. Hardy, "Evaluation of Impact-Induced Traumatic Brain Injury in the Göttingen Minipig Using Two Input Modes," *Traffic Injury Prevention*, vol. 15, no. February 2015, pp. S81–S87, 2014.
- [61] C. Withnall, N. Shewchenko, R. Gittens, and J. Dvorak, "Biomechanical investigation of head impacts in football," *British Journal of Sports Medicine*, vol. 39, no. Suppl. 1, pp. 49–57, 2005.
- [62] K. Kindschi, M. Higgins, A. Hillman, G. Penczek, and A. Lincoln, "Video analysis of high-magnitude head impacts in men's collegiate lacrosse," *BMJ Open Sport and Exercise Medicine*, vol. 3, no. 1, pp. 1–6, 2017.
- [63] G. D. Myer, W. Yuan, K. D. Barber Foss, S. Thomas, D. Smith, J. Leach, A. W. Kiefer, C. Dicesare, J. Adams, P. J. Gubanich, K. Kitchen, D. K. Schneider, D. Braswell, D. Krueger, and M. Altaye, "Analysis of head impact exposure and brain microstructure response in a season-long application of a jugular vein compression collar: A prospective, neuroimaging investigation in American football," *British Journal of Sports Medicine*, vol. 50, no. 20, pp. 1276–1285, 2016.
- [64] Y. Feng, T. M. Abney, R. J. Okamoto, R. B. Pless, G. M. Genin, and P. V. Bayly, "Relative brain displacement and deformation during constrained mild frontal head impact," *Journal of the Royal Society Interface*, vol. 7, no. 53, pp. 1677–1688, 2010.

- [65] W. N. Hardy, C. D. Foster, M. J. Mason, K. H. Yang, A. I. King, and S. Tashman, "Investigation of Head Injury Mechanisms Using Neutral Density Technology and High-Speed Biplanar X-ray," *Stapp car crash journal*, vol. 45, pp. 337–368, 2001.
- [66] W. N. Hardy, M. J. Mason, C. D. Foster, C. S. Shah, J. M. Kopacz, K. H. Yang, A. I. King, J. Bishop, M. Bey, W. Anderst, and S. Tashman, "A study of the response of the human cadaver head to impact.," *Stapp car crash journal*, vol. 51, pp. 17–80, 2007.
- [67] L. E. Bilston, "Brain Tissue Mechanical Properties," in *Biomechanics of the Brain* (K. Miller, ed.), ch. 4, pp. 69–89, New York, NY: Springer New York, 1st ed., 2011. [E-book]. Available: Scholar Portal Books.
- [68] D. H. Smith, X.-h. Chen, A. Iwata, and D. I. Graham, "Amyloid β accumulation in axons after traumatic brain injury in humans," *Journal of Neurosurgery*, vol. 98, no. 5, pp. 1072–1077, 2003.
- [69] T. A. Gennarelli, L. E. Thibault, J. H. Adams, D. I. Graham, C. J. Thompson, and R. P. Marcincin, "Diffuse axonal injury and traumatic coma in the primate," *Annals of Neurology*, vol. 12, no. 6, pp. 564–574, 1982.
- [70] J. W. Finnie, C. Van Den Heuvel, V. Gebiski, J. Manavis, G. E. Summersides, and P. C. Blumbergs, "Effect of impact on different regions of the head of lambs," *Journal of Comparative Pathology*, vol. 124, no. 2-3, pp. 159–164, 2001.
- [71] J. Ivarsson, D. C. Viano, and P. Lövsund, "Influence of the lateral ventricles and irregular skull base on brain kinematics due to sagittal plane head rotation," *Journal of Biomechanical Engineering*, vol. 124, no. 4, pp. 422–431, 2002.
- [72] M. J. Thali, B. P. Kneubuehl, U. Zollinger, and R. Dirnhofer, "The 'Skin-skull-brain model': A new instrument for the study of gunshot effects," *Forensic Science International*, vol. 125, no. 2-3, pp. 178–189, 2002.
- [73] R. N. Palchesko, L. Zhang, Y. Sun, and A. W. Feinberg, "Development of Polydimethylsiloxane Substrates with Tunable Elastic Modulus to Study Cell Mechanobiology in Muscle and Nerve," *PLoS ONE*, vol. 7, no. 12, 2012.
- [74] S. Ouellet and M. Philippens, "The multi-modal responses of a physical head model subjected to various blast exposure conditions," *Shock Waves*, vol. 28, pp. 19–36, 2018.

- [75] L. E. Miller, J. E. Urban, and J. D. Stitzel, "Validation performance comparison for finite element models of the human brain," *Computer Methods in Biomechanics and Biomedical Engineering*, vol. 20, no. 12, pp. 1273–1288, 2017.
- [76] P. Dixit and G. R. Liu, "A Review on Recent Development of Finite Element Models for Head Injury Simulations," *Archives of Computational Methods in Engineering*, vol. 24, no. 4, pp. 979–1031, 2017.
- [77] E. G. Takhounts, S. A. Ridella, V. Hasija, R. E. Tannous, J. Q. Campbell, D. Malone, K. Danelson, J. Stitzel, S. Rowson, and S. Duma, "Investigation of traumatic brain injuries using the next generation of simulated injury monitor (SIMon) finite element head model.," *Stapp car crash journal*, vol. 52, pp. 1–31, 2008.
- [78] H. Mao, L. Zhang, B. Jiang, V. V. Genthikatti, X. Jin, F. Zhu, R. Makwana, A. Gill, G. Jandir, A. Singh, and K. H. Yang, "Development of a finite element human head model partially validated with thirty five experimental cases," *Journal of Biomechanical Engineering*, vol. 135, no. 11, pp. 111002–1 – 111002–15, 2013.
- [79] G. Lionello and L. Cristofolini, "A practical approach to optimizing the preparation of speckle patterns for digital-image correlation," *Measurement Science and Technology*, vol. 25, no. 10, 2014.
- [80] B. Pan, K. Qian, H. Xie, and A. Asundi, "Two-dimensional digital image correlation for in-plane displacement and strain measurement: A review," *Measurement Science and Technology*, vol. 20, no. 6, 2009.
- [81] J. Blaber, B. Adair, and A. Antoniou, "Ncorr: Open-Source 2D Digital Image Correlation Matlab Software," *Experimental Mechanics*, vol. 55, no. 6, pp. 1105–1122, 2015.
- [82] H. A. Bruck, S. R. McNeill, M. A. Sutton, and W. H. Peters, "Digital image correlation using Newton-Raphson method of partial differential correction," *Experimental Mechanics*, vol. 29, no. 3, pp. 261–267, 1989.
- [83] W. LePage, "digitalimagecorrelation.org." <https://digitalimagecorrelation.org/>. [Website]. Available: <https://digitalimagecorrelation.org/>. [Accessed: Mar. 7, 2020].
- [84] B. Pan, K. Li, and W. Tong, "Fast, Robust and Accurate Digital Image Correlation Calculation Without Redundant Computations," *Experimental Mechanics*, vol. 53, no. 7, pp. 1277–1289, 2013.

- [85] S. Baker and I. Matthews, "Equivalence and efficiency of image alignment algorithms," *Proceedings of the IEEE Computer Society Conference on Computer Vision and Pattern Recognition. CVPR, 2001*. Kauai, HI, USA, 2001.
- [86] S. Baker and I. Matthews, "Lucas-Kanade 20 Years On: An Unifying Framework," *International Journal of Computer Vision*, vol. 56, no. 3, pp. 221–255, 2004.
- [87] B. Pan, "Reliability-guided digital image correlation for image deformation measurement," *Applied Optics*, vol. 48, no. 8, pp. 1535–1542, 2009.
- [88] B. Pan, "Full-field strain measurement using a two-dimensional Savitzky-Golay digital differentiator in digital image correlation," *Optical Engineering*, vol. 46, no. 3, pp. 033601–1 – 033601–10, 2007.
- [89] B. Pan, A. Asundi, H. Xie, and J. Gao, "Digital image correlation using iterative least squares and pointwise least squares for displacement field and strain field measurements," *Optics and Lasers in Engineering*, vol. 47, no. 7-8, pp. 865–874, 2009.
- [90] B. Pan, Z. Wang, and Z. Lu, "Genuine full-field deformation measurement of an object with complex shape using reliability-guided digital image correlation," *Optics Express*, vol. 18, no. 2, pp. 1011–1023, 2010.
- [91] International Digital Image Correlation Society, Jones, E.M.C. and Iadicola, M.A., ed., *A Good Practices Guide for Digital Image Correlation Standardization*. 2018.
- [92] J. Blaber and A. Antoniou, "Ncorr - Instruction Manual Version 1.2.2." [Online]. Available: <http://www.ncorr.com/index.php/downloads>, 2017. [Accessed: Jun. 20, 2018].
- [93] National Center for Biotechnology Information, "Barium sulfate." [Online]. Available: <https://pubchem.ncbi.nlm.nih.gov/compound/Barium-sulfate>. [Accessed: Nov. 8, 2019].
- [94] S. S. Russell and M. A. Sutton, "Strain-field analysis acquired through correlation of X-ray radiographs of a fiber-reinforced composite laminate," *Experimental Mechanics*, vol. 29, no. 2, pp. 237–240, 1989.
- [95] P. Synnergren, H. T. Goldrein, and W. G. Proud, "Application of digital speckle photography to flash x-ray studies of internal deformation fields in impact experiments," *Applied Optics*, vol. 38, no. 19, pp. 4030–4036, 1999.

- [96] T. Yagi, A. Sato, M. Shinke, S. Takahashi, Y. Tobe, H. Takao, Y. Murayama, and M. Umezu, "Experimental insights into flow impingement in cerebral aneurysm by stereoscopic particle image velocimetry: Transition from a laminar regime," *Journal of the Royal Society Interface*, vol. 10, no. 82, pp. 1–14, 2013.
- [97] H. Mestre, J. Tithof, T. Du, W. Song, W. Peng, A. M. Sweeney, G. Olveda, J. H. Thomas, M. Nedergaard, and D. H. Kelley, "Flow of cerebrospinal fluid is driven by arterial pulsations and is reduced in hypertension," *Nature communications*, vol. 9, pp. 1–9, 2018.
- [98] S. Sokoll, Y. Prokazov, M. Hanses, B. Biermann, K. Tönnies, and M. Heine, "Fast three-dimensional single-particle tracking in natural brain tissue," *Biophysical Journal*, vol. 109, no. 7, pp. 1463–1471, 2015.
- [99] I. F. Sbalzarini and P. Koumoutsakos, "Feature point tracking and trajectory analysis for video imaging in cell biology," *Journal of Structural Biology*, vol. 151, no. 2, pp. 182–195, 2005.
- [100] J. C. Crocker and D. G. Grier, "Methods of digital video microscopy for colloidal studies," *Journal of Colloid and Interface Science*, vol. 179, no. 1, pp. 298–310, 1996.
- [101] The MOSAIC Group, "ParticleTracker." [Online]. Available: <http://mosaic.mpi-cbg.de/MosaicToolboxSuite/ParticleTracker.html>. Accessed: Feb. 2, 2019.
- [102] C. Solomon and T. Breckon, "8.4 Dilation and erosion," in *Fundamentals of digital image processing a practical approach with examples in Matlab*, ch. 8, pp. 200–201, John Wiley & Sons, Incorporated, 2 ed., 2011. [E-book]. Available: ProQuest Ebook Central.
- [103] F. L. Hitchcock, "The Distribution of a Product from Several Sources to Numerous Localities," *Journal of Mathematics and Physics*, vol. 20, pp. 224–230, apr 1941.
- [104] S. B. Dalziel, "Decay of rotating turbulence: some particle tracking experiments," *Applied Scientific Research*, vol. 49, no. 3, pp. 217–244, 1992.
- [105] S. B. Dalziel, "Rayleigh-Taylor instability: experiments with image analysis," *Dynamics of Atmospheres and Oceans*, vol. 20, no. 1-2, pp. 127–153, 1993.

- [106] The Dow Chemical Company, "SYLGARD™ 184 Silicone Elastomer." Form No. 11-3184-01 C, 2017.
- [107] The Dow Chemical Company, "SYLGARD™ 527 Silicone Dielectric Gel." Form No. 11-3136-01 D, 2017.
- [108] S. Saikali, P. Meurice, P. Sauleau, P. A. Eliat, P. Bellaud, G. Randuineau, M. Vérin, and C. H. Malbert, "A three-dimensional digital segmented and deformable brain atlas of the domestic pig," *Journal of Neuroscience Methods*, vol. 192, no. 1, pp. 102–109, 2010.
- [109] "Pig Brain Atlas." *Institut National de la Recherche Agronomique. University of Rennes*. [Online]. Available: https://www6.rennes.inra.fr/adnc_eng/. [Accessed: Nov. 22, 2017].
- [110] "Anatomical Pig Brain Atlas." *Internet Archive*, 2011. [Online]. Available: http://web.archive.org/web/20110810120753/http://w3.rennes.inra.fr/senah/brain_atlas/atlas.html. [Accessed: Jun. 2, 2020].
- [111] "3D Slicer." *3D Slicer*. [Website]. Available: <https://www.slicer.org/>. [Accessed: Oct. 18, 2017].
- [112] A. Fedorov, R. Beichel, J. Kalpathy-Cramer, J. Finet, J. C. Fillion-Robin, S. Pujol, C. Bauer, D. Jennings, F. Fennessy, M. Sonka, J. Buatti, S. Aylward, J. V. Miller, S. Pieper, and R. Kikinis, "3D Slicer as an image computing platform for the Quantitative Imaging Network," *Magnetic Resonance Imaging*, vol. 30, no. 9, pp. 1323–1341, 2012.
- [113] R. Kikinis, S. D. Pieper, and K. G. Vosburgh, "3D Slicer: A Platform for Subject-Specific Image Analysis, Visualization, and Clinical Support," in *Intraoperative Imaging and Image-Guided Therapy* (F. A. Jolesz, ed.), pp. 277–289, New York, NY: Springer New York, 2014. [E-book]. Available: SpringerLink.
- [114] Society for Experimental Mechanics, "DIC Challenge." *Society for Experimental Mechanics*. [Online]. Available: <https://sem.org/dicchallenge>. [Accessed: May. 29, 2020].
- [115] J. Schindelin, I. Arganda-Carreras, E. Frise, V. Kaynig, M. Longair, T. Pietzsch, S. Preibisch, C. Rueden, S. Saalfeld, B. Schmid, J.-Y. Tinevez, D. J. White, V. Hartenstein, K. Eliceiri, P. Tomancak, and A. Cardona, "Fiji: an open-source platform for biological-image analysis," *Nature Methods*, vol. 9, no. 7, pp. 676–682, 2012.

- [116] C. Schneider, W. Rasband, and K. Eliceiri, "NIH Image to ImageJ: 25 years of image analysis," *Nature Methods*, vol. 9, no. 7, pp. 671–675, 2012.
- [117] T. Tallinen, J. Y. Chung, J. S. Biggins, and L. Mahadevan, "Gyrification from constrained cortical expansion," *Proceedings of the National Academy of Sciences of the United States of America*, vol. 111, no. 35, pp. 12667–12672, 2014.

Appendix A

Trials and Limitations

The initial brain gyrification study used different techniques for sample preparation and method of impact. The surrogates contained individually placed radiopaque markers. The process of creating individual markers included: creating the radiopaque markers within a grid, cutting the markers into smaller sections, individually placing the markers into the bottom of sample moulds, filling the mould with a Sylgard mixture (527:184 in a 5:1 ratio), rearranging any displaced markers that may have shifted when the Sylgard mixture was poured, and letting the surrogate cure. Under X-ray, it was difficult to determine the boundaries of the surrogates, as there was no distinct boundary. The radiopaque speckle sheet allowed for the ability to see the direct outline of the surrogates. A distinct boundary was desirable for DIC, which required a ROI to be drawn around the sample.

The surrogates were initially impacted individually with a pneumatic linear impactor at various low-end velocities. The issue with the experimental setup was that the mount the samples were attached to recoiled backwards in an arc during initial contact with the impactor head, before returning to a vertical position and proceeding to move out of frame. As the samples were individually impacted, it was difficult to match the impact velocity, as well as match the sample trajectories. This proved difficult for the analysis, as it required surrogates to be overlayed to

determine differences in strain responses.

Multiple impacting methods and conditions were also tested. Initially, specimens were impacted one at a time with a pneumatic linear impactor. While this method had some success, the loading condition of a linear drop system provided more desirable impact conditions. A linear drop tower was then created for the impacts, in which surrogates were dropped one at a time. The limitations to this method, as well as the pneumatic linear impactor, was when it came to comparing specimens directly. Although drop velocities may have been within a reasonable range, it was difficult to line up the surrogates for the analysis. By dropping two specimens at once, this issue was eliminated. Not only did this aid in the analysis, it also decreased time spent collecting data.

As future work for the surrogate study may include inserting the elastomer surrogate into a 3D brain, preliminary experimentation was conducted. The experiment followed the procedure outlined in [117]. That study was able to create a unique, self-convoluting 3D elastomer brain. While an ideal brain sample was created, the inability for the sample to remain convoluted was a factor in not pursuing this further. The idea was to take the brain sphere and create a mould, then create a brain surrogate that would possess convolutions and the surrogate slice.

Multiple marker application techniques and marker types were experimented with to determine an appropriate marker for the viable *ex vivo* porcine brain tissue. Powdered BaSO₄ was sprinkled, sieved, and placed through large hole patterns to create individual marker spots on the surface. The issues with these trials was that the ratio of BaSO₄ concentration to contrast on X-ray were low; large amounts of powdered BaSO₄ appeared faint on X-ray. Another potential marker used was lead solder which produced high contrast under X-ray, but the motion of the solder was not reflective of the tissue. A unique method attempted was tattooing a BaSO₄-water mixture into the tissue. When trying on pork, this method

proved to work, although it appeared faint under X-ray. When applying the same depth, pressure, and time to create a marker on pork, these same conditions proved unsuccessful on brain; most markers were invisible.

A large, 60+ cannula marker insertion system was initially created and worked to some degree. This method would allow for tens of markers to be placed at once, but it lost the ability to be selective and target specific areas. This method did not work in its entirety, as some markers would insert into the tissue and not others; this was likely due to the surface tension on the tissue.

The result of the previous trials lead to the choice of individual marker insertion, which allowed for the selective placement of markers in desired locations. A combination of a Gelatin #4 and BaSO₄, produced the ideal marker. This mixture was able to be inserted into the tissue with minimal issues. An attempt was made to visualise the two different matters within *ex vivo* brain sections. This was done using two different marker concentrations: 40% and 60% by weight BaSO₄ to Gelatin #4. Additionally, two different cannula sizes (ID of 1.07 mm and 1.27 mm) were tested. After imaging the tissue with X-rays, minor differences were noticed in marker concentration, but not in size. As the differences were not significant enough to distinguish matter boundaries, further experimentation only used one marker concentration and one cannula size.

The aforementioned techniques were developed over the course of a few months. When trying new methods on readily available store bought pork, some techniques worked well, but once it was applied to porcine brain, the techniques were unsuccessful. Brain tissue has a consistency and texture like no other tissue commonly available; grey matter is minimally firm and easy to work with, but white matter is fatty and was not easy to integrate markers into. Therefore, a great effort was placed into preliminary marker testing on porcine brain before securing a final marker insertion design.

Appendix B

Standard Operating Procedure

B.1 Porcine Tissue Experiment

B.1.1 Encasement Preparation

- Thermo Lab
 - Obtain moulds for both parts of encasement
 - Add in total volume for both parts into Excel Sylgard mixture spreadsheet
 - * Spreadsheet separates total volume into 5:1 ratio of Sylgard 527:184 and then into respective individual ratios (following mixture instructions)
 - Mix Sylgard 527 and 184 parts A and B individually then combine both Sylgards and mix thoroughly
 - Degas mixture in dessicator until most of the air bubbles are gone
 - Apply a thin layer of Vaseline Original Petroleum Jelly to moulds (acts as a mould release)
 - Air cure on a level surface for at least 24 hours

- Remove elastomer encasement from mould and expose section that was confined in the mould to the air until encasement is needed

B.2 Marker Preparation

- Weigh Humimic #4 with an electronic scale
- Calculate the percent ratio needed for BaSO₄
- Melt Humimic and sieve in BaSO₄
- Mix thoroughly and turn off hotplate
- Let cool until bearable and hand mix marker mixture
- Reheat mixture
- Let cool
- Place mixture in bag once cooled and label bag

B.3 Porcine Brain Experiment Day

Wednesday Before Brain Removal Item Checklist Engineering Component

- Tissue Lab Items:
 - * Cannula systems
 - * Melting plates
 - * 60% wt BaSO₄ and Humimic
 - * Hot plate
 - * Acrylic plates with screws
 - * Elastomer encasements (base and cap)

- * Matrix with blades
- * Tweezers
- Cleaning supplies:
 - * Accel wipes
 - * Paper towels
 - * Soap
 - * Gloves (M)
- HSXR Room:
 - * Set up drop tower (switch cables)
- Thermo Lab:
 - * Put aCSF in fridge

Neuroscience Component

- Items for incubation unit:
 - * Plastic container
 - * Air filter
 - * Air tube
 - * Plastic grate
 - * Plastic Wells x6
- Marker for labeling
- Ice pack
- Make sure 4% PFA is prepared and put in fridge for cooling
- Prepare aCSF solution from stock and put in fridge. Should be done as late as possible

- Get dry ice and put in -80 freezer and set aside some ethanol in container
- Items for removal kit (Tissue Lab):
 - * Dremel and saw heads
 - * Surgery kit
 - * Hammer and chisel
 - * Garbage bags

Thursday- Collection and Impact Day

- Approx. 7am- 9am
 - * Bring large cooler filled with ice
 - * Bring spare letterhead
 - * Leave for Henderson's (7am)
 - * Arrive at Henderson's (8am)
 - * Collect porcine head
 - * Leave for Carleton University
- Approx. 8:30-9am
 - * Warm up X-ray system
 - * Line up drop apparatus
 - * Practice test drop (do three (3) times)
- 9am in Tissue Lab:
 - * Remove brain with dremel and hammer and chisel
 - * Wait one (1) hour for brain to firm in a beaker of cold aCSF
 - * Slice four (4) sections of brain (two (2) treatment, two (2) control)
 - * Label them with corresponding control/treatment numbers

- * Let tissues acclimate in incubation unit for ten (10) minutes post sectioning
 - * Warm up marker sheet in melting plate at 120°C
 - * Tissue is placed in a petri dish with aCSF and is on a freezer pack
 - * Dip cannula into melted marker, remove excess, and implant marker into white or gray matter in treatment and control tissues
 - * Repeat above step until tissue is filled with markers
 - * Let slices rest for ten (10) minutes in incubation unit.
 - * Pack porcine head and ready for freezer storage in HSB
 - * Place marked treatment tissues into encasement
 - * Marker side facing bottom of encasement cavity
 - * Seal encasement between acrylic plates
 - External spacing between both acrylic plates is 34.6 +/-0.2 mm
 - * Bring samples to HSXR Room
- In HSXR Room:
- * Screw encasement/acrylic assembly into drop tower plate with base of encasement facing away from individual
- In HSXR Control Room:
- * Take still image of encasement
- In HSXR Room:
- * Set drop height and latch assembly into dropping position
- In HSXR Control Room:
- * Prime X-ray and press impact button

- * The assembly falls and the drop is recorded
- * Save original data file as well as tiff conversion
- In HSXR Room:
 - * Remove assembly from the drop tower
- In Tissue Lab:
 - * Bring assembly back to tissue room
 - * Remove treatment tissues
 - * Place impacted tissue into incubation unit for one (1) hour
- End of experiment (Approx. 12:30pm):
 - Clean all surfaces and instruments with soap and water and then Accel wipes
 - Place tissue into PFA after one (1) hour (Tissue Lab)
 - Transfer tissue back to HSB for sectioning and staining

B.4 Brain Surrogate Experiment

B.4.1 Surrogate Preparation

Marker sheets

- Obtain both radiopaque marker sheet moulds
- Heat up radiopaque marker sheet moulds in approximately 120°C oven
- Melt pre-made Humimic/BaSO₄ marker mixture on a hotplate
- Pour marker mixture into marker moulds

- Take tongue depressor and smooth out mixture into mould
- Reheat mould and mixture
- Remove from heat and let cool

Surrogate Preparation

- Mould release surrogate moulds
- Fill mould with approximately 1 mm of Sylgard 527:184 mixture and partially cure (tacky to touch)
- Place in radiopaque speckle sheet and fill to the top with the remainder Sylgard 527:184 mixture
- Remove air bubbles with dental picks
- Place sample in 120°C oven for approximately 45 minutes or until cured
- Remove sample from mould and store until needed

Experimentation Day

- Place samples into the cavity of the ellipsoidal encasement bottom, measuring distances from sample to edge of encasements to keep spacing consistent between complex and smooth surrogates
- Seal the encasements with silicone caulking and wait until cured
- Fluidise encasements with water via syringe
- Weigh the encasements
- Place encasements in desired orientation on one of the acrylic plates
- Situate encasements evenly between hole pattern
- Use the second acrylic plate to line up encasements with edge of first acrylic plate

- Tighten screws such that 34.6 ± 0.2 mm is the external spacing between acrylic plates.
- Take encasement/acrylic system and attach to acrylic plates connected to carriages.
- Set drop height on drop tower, starting at lowest height
- Do three trials per height
- Reset height and image again until all heights are completed
- For each new orientation, rotate samples to desired position and repeat process above
- Save files and shutdown lab

Appendix C

Supplementary Figures and Data

Within this appendix, additional figures and data are included that provide supporting information on the surrogate data, as well as the *ex vivo* porcine brain tissue sections. Throughout the main text, select figures were chosen to reinforce the importance of brain gyrification for the downward, upward, and inward orientations. Additional strain fields obtained using DIC are provided below for each surrogate for the same conditions as described within the main text figures. For the particle tracker, as the specimens were symmetric about the mid-sagittal plane, the marker pairings that were furthest away from the center of the anvil were placed within the appendix. These remaining figures, although interesting, were placed in the appendix as supplementary figures that still support the validity of the importance of gyrification. The supplementary figures are divided by orientation. The figures for the supplementary orientations proceed the main orientations.

It should be noted that the complementary marker pairings from the upward orientation tended to remain in a tensile phase after impact. The slightly increased constraint of the 80/20 rails, along with gyrification not being directly impacted may have delayed the return of the surrogates to near zero strain.

C.1 Analysis Parameters

The following are tables of parameters used in DIC and the Mosaic ParticleTracker.

Table C.1: Parameters used for the DIC analysis

Parameter name	Parameter value
Step size	0 pixels
Subset radius	10 pixels
Iteration number cutoff	50
Strain radius	15 pixels

Table C.2: Parameters and main values used for the Mosaic analysis of the surrogates and *ex vivo* porcine brain.

Parameter name	Parameter value
Radius	3 pixels
Cutoff	0
Percentile	2 %
Link range	2 frames
Displacement	6 pixels
Dynamics	Brownian

C.2 Digital Image Correlation: Main Orientation Figures and Additional Data

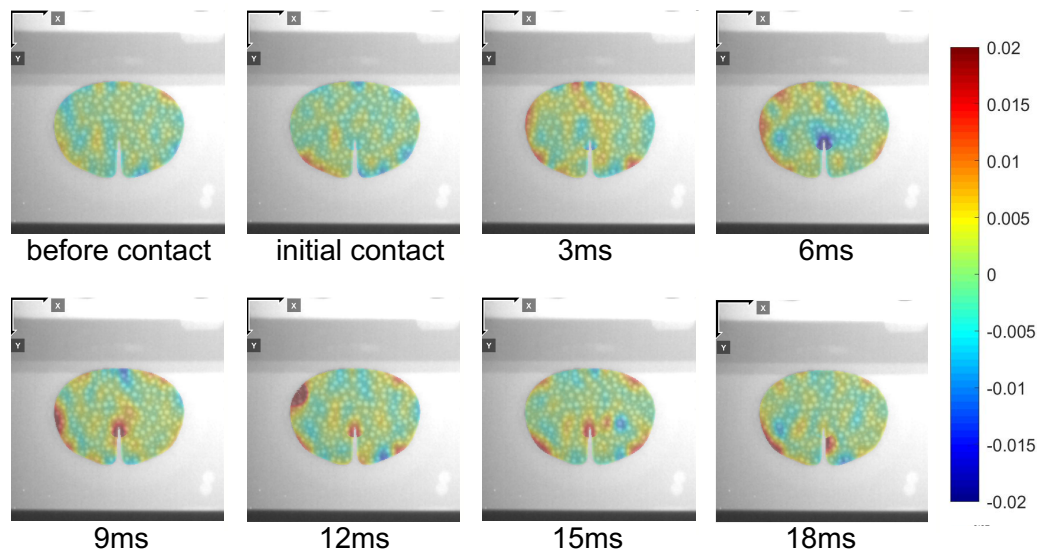


Figure C.1: A sequence of strain fields denoting ϵ_{xx} strains experienced by the smooth surrogate when dropped in the downward orientation from 50 cm from one trial. The sequence includes frames before contact and initial contact with the anvil. The times labelled correspond to time after initial contact with the anvil.

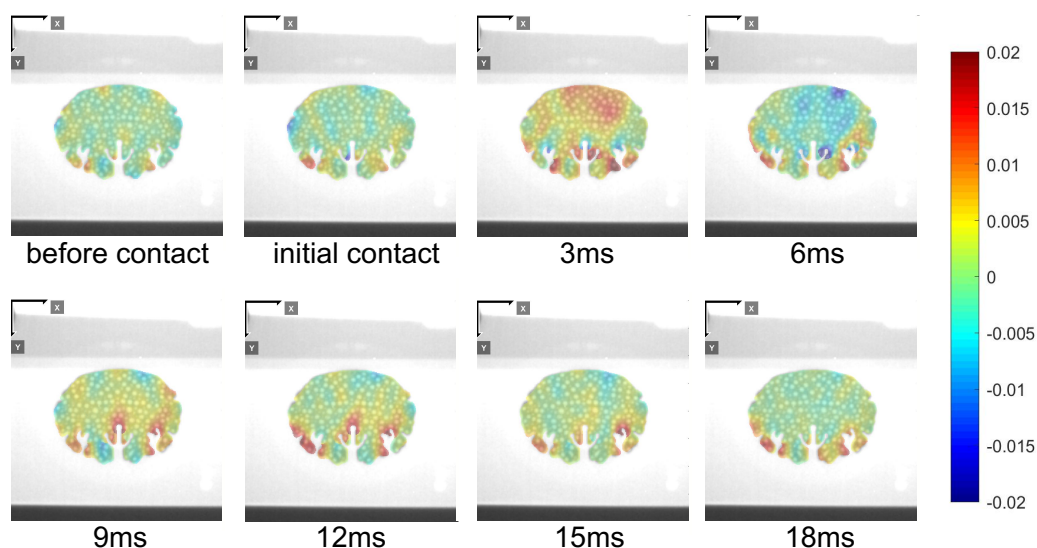


Figure C.2: A sequence of strain fields denoting ϵ_{xx} strains experienced by the complex surrogate when dropped in the downward orientation from 50 cm from one trial. The sequence includes frames before contact and initial contact with the anvil. The times labelled correspond to time after initial contact with the anvil.

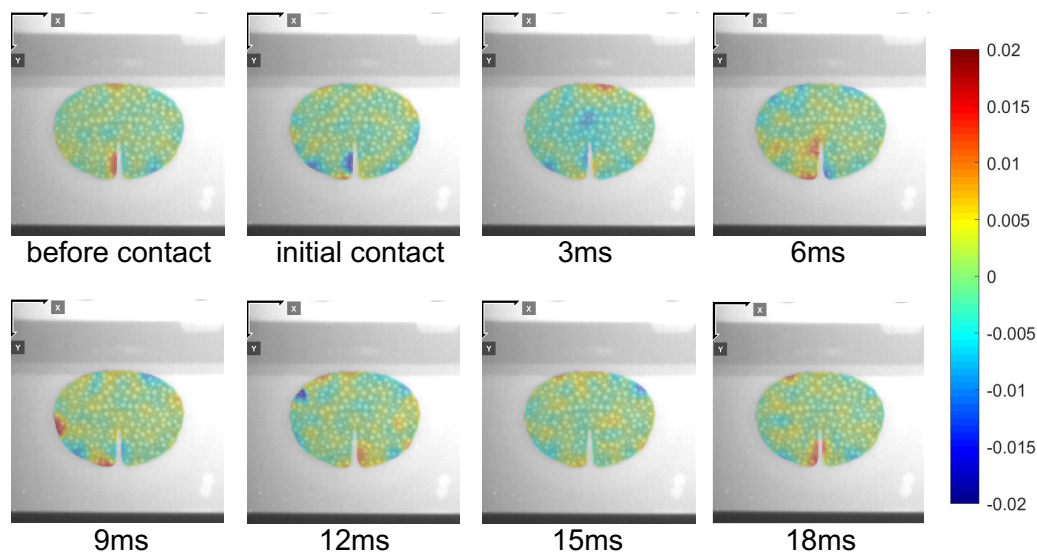


Figure C.3: A sequence of strain fields denoting ϵ_{xy} strains experienced by the smooth surrogate when dropped in the downward orientation from 50 cm from one trial. The sequence includes frames before contact and initial contact with the anvil. The times labelled correspond to time after initial contact with the anvil.

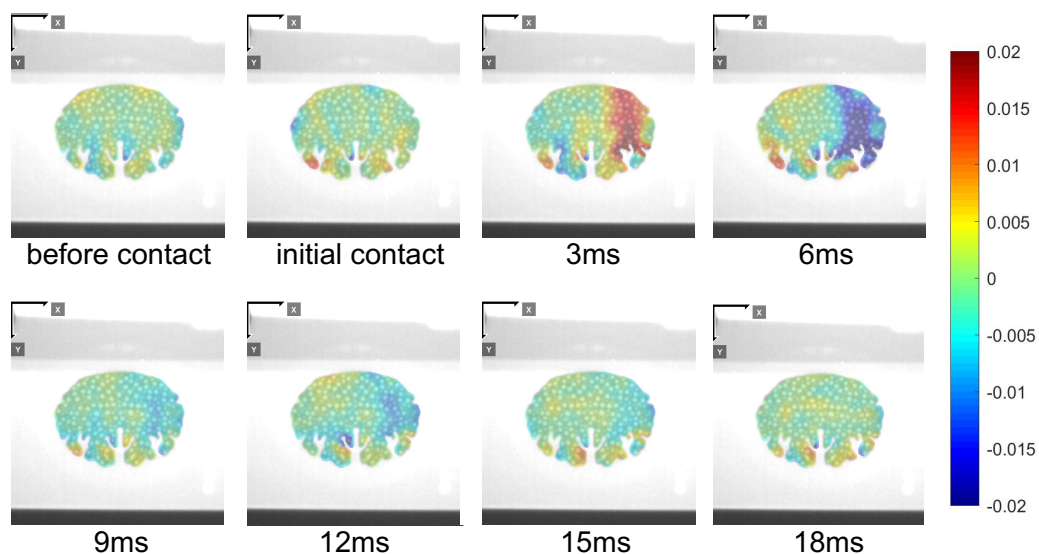


Figure C.4: A sequence of strain fields denoting ϵ_{xy} strains experienced by the complex surrogate when dropped in the downward orientation from 50 cm from one trial. The sequence includes frames before contact and initial contact with the anvil. The times labelled correspond to time after initial contact with the anvil.

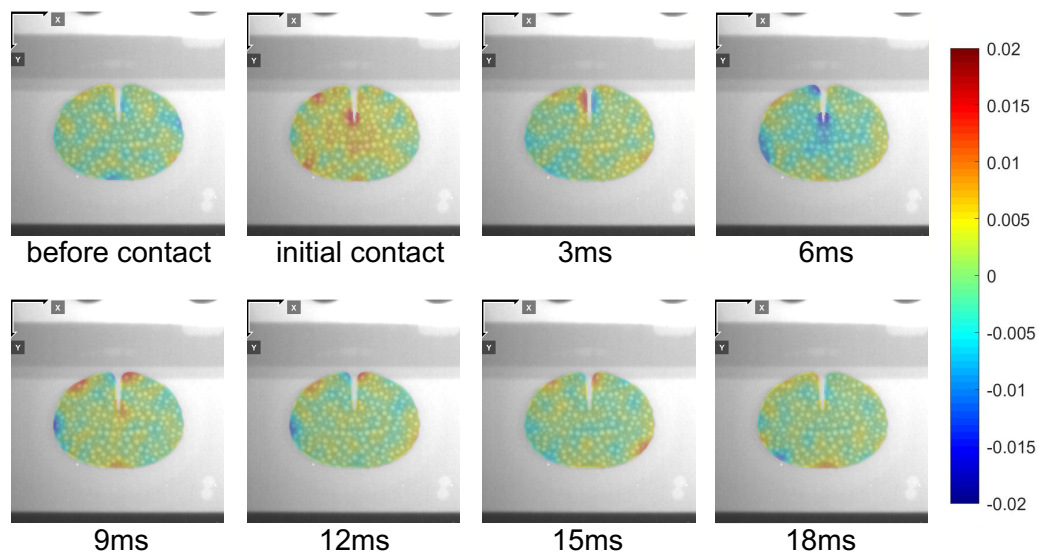


Figure C.5: A sequence of strain fields denoting ϵ_{xy} strains experienced by the smooth surrogate when dropped in the upward orientation from 50 cm from one trial. The sequence includes frames before contact and initial contact with the anvil. The times labelled correspond to time after initial contact with the anvil.

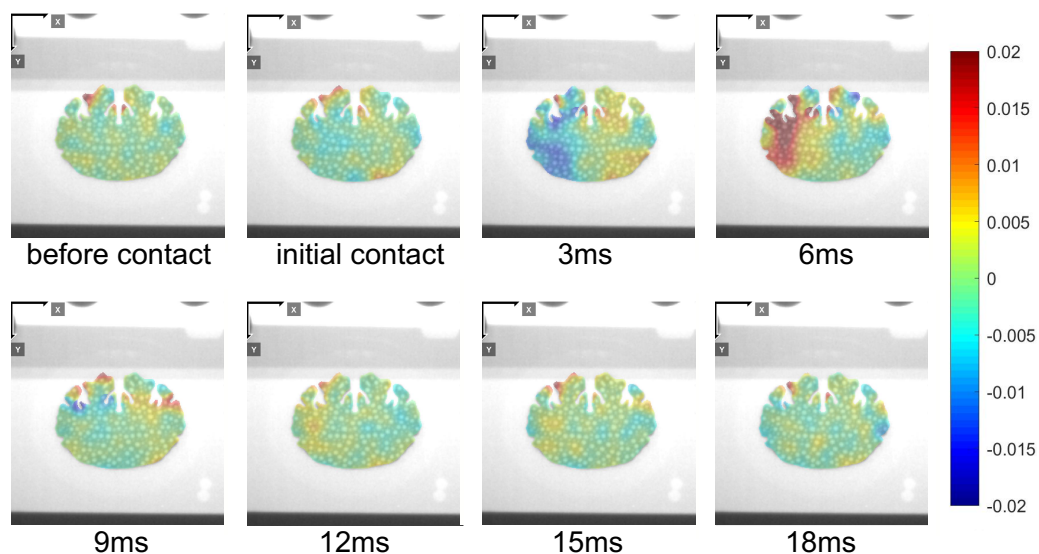


Figure C.6: A sequence of strain fields denoting ϵ_{xy} strains experienced by the complex surrogate when dropped in the upward orientation from 50 cm from one trial. The sequence includes frames before contact and initial contact with the anvil. The times labelled correspond to time after initial contact with the anvil.

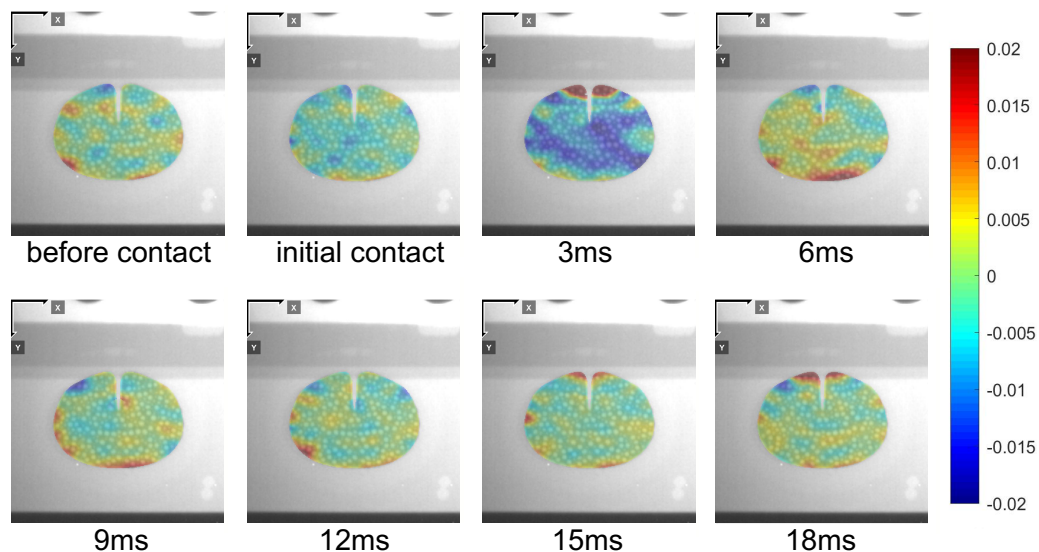


Figure C.7: A sequence of strain fields denoting ϵ_{yy} strains experienced by the smooth surrogate when dropped in the upward orientation from 50 cm from one trial. The sequence includes frames before contact and initial contact with the anvil. The times labelled correspond to time after initial contact with the anvil.

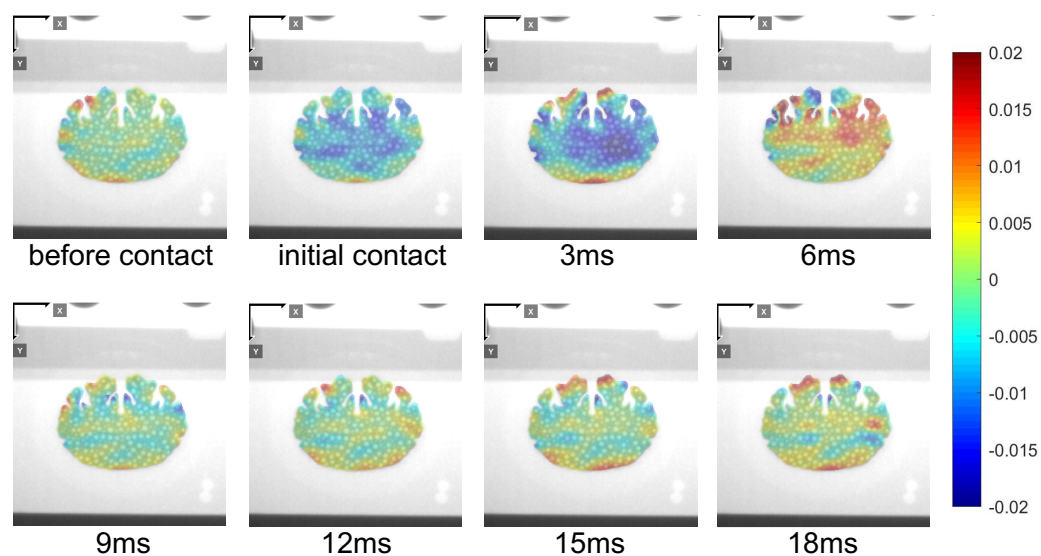


Figure C.8: A sequence of strain fields denoting ϵ_{yy} strains experienced by the complex surrogate when dropped in the upward orientation from 50 cm from one trial. The sequence includes frames before contact and initial contact with the anvil. The times labelled correspond to time after initial contact with the anvil.

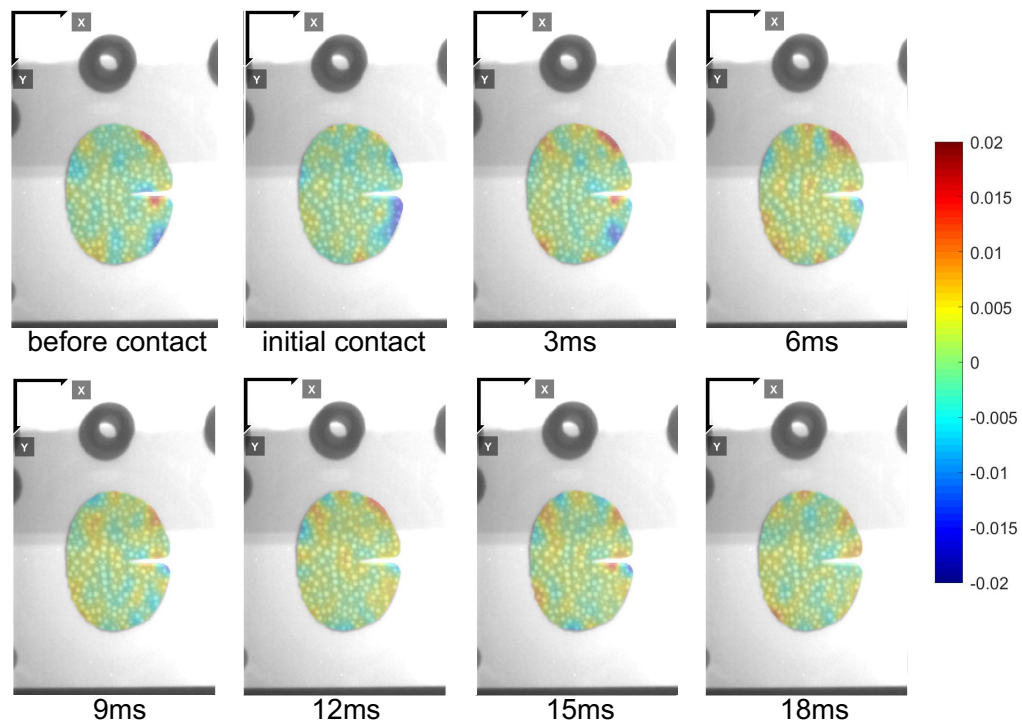


Figure C.9: A sequence of strain fields denoting ϵ_{xx} strains experienced by the smooth surrogate when dropped in the inward orientation from 50 cm from one trial. The sequence includes frames before contact and initial contact with the anvil. The times labelled correspond to time after initial contact with the anvil.

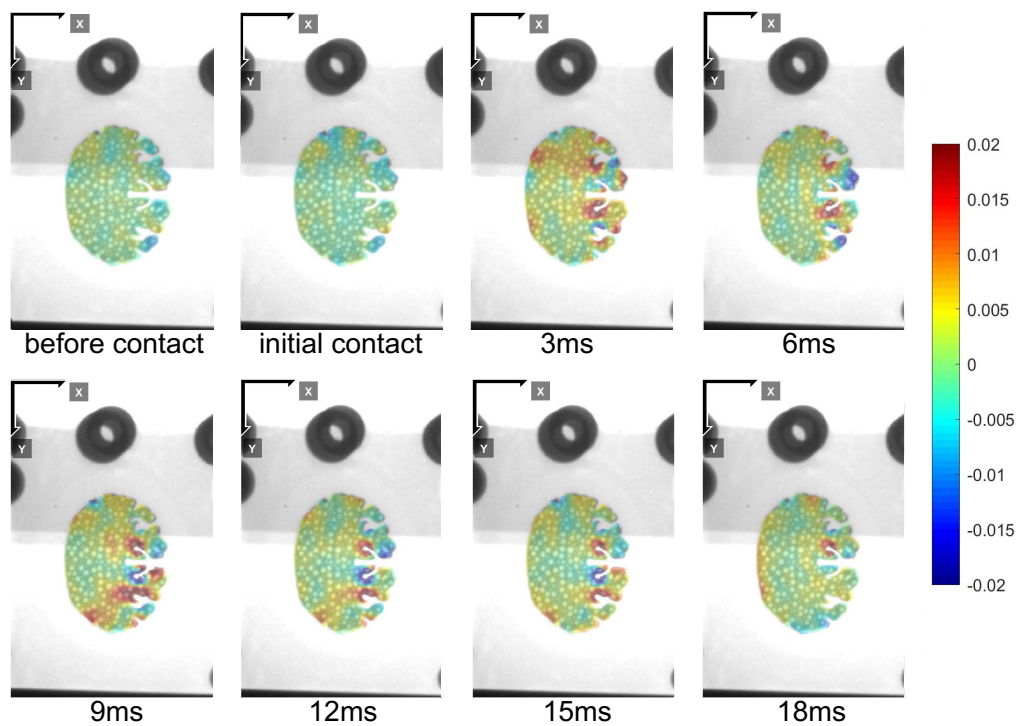


Figure C.10: A sequence of strain fields denoting ϵ_{xx} strains experienced by the complex surrogate when dropped in the inward orientation from 50 cm from one trial. The sequence includes frames before contact and initial contact with the anvil. The times labelled correspond to time after initial contact with the anvil.

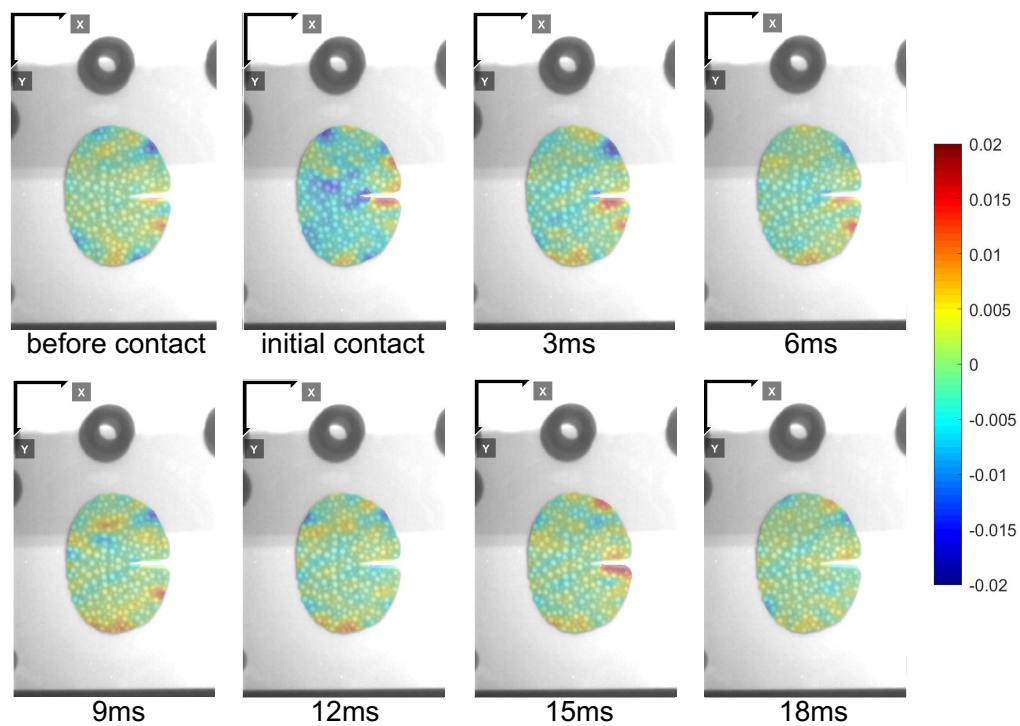


Figure C.11: A sequence of strain fields denoting ϵ_{yy} strains experienced by the smooth surrogate when dropped in the inward orientation from 50 cm from one trial. The sequence includes frames before contact and initial contact with the anvil. The times labelled correspond to time after initial contact with the anvil.

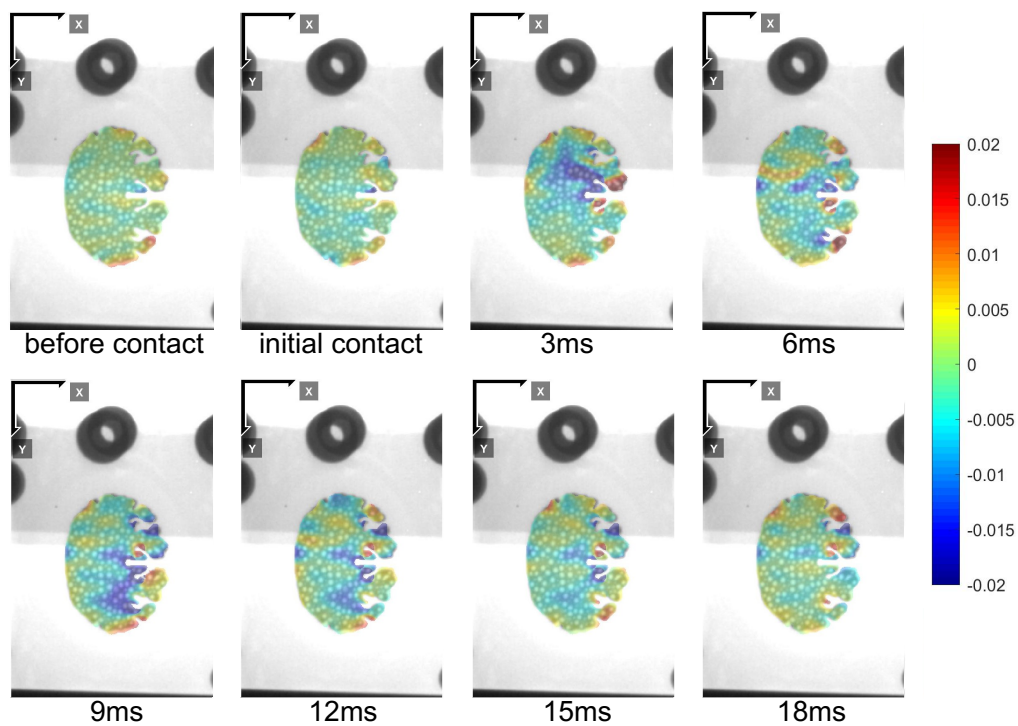


Figure C.12: A sequence of strain fields denoting ϵ_{yy} strains experienced by the complex surrogate when dropped in the inward orientation from 50 cm from one trial. The sequence includes frames before contact and initial contact with the anvil. The times labelled correspond to time after initial contact with the anvil.

Table C.3: Averaged peak volumetric strain between Markers 1 and 6 for both surrogates in all orientations analysed with DIC. As a note, strain values were only considered during the first 20 ms of the impact event.

Gyrification	Orientation	Height (cm)	Peak Volumetric Strain (%)	
			ϵ_v	ϵ_v
Smooth	Downward	30	-0.4	0.2
Complex			-0.5	0.4
Smooth		50	-0.5	0.2
Complex			-0.8	0.5
Smooth		70	-0.7	0.4
Complex			-1.2	0.6
Smooth		90	-0.9	0.7
Complex			-1.2	0.8
Smooth	Upward	30	-0.6	0.3
Complex			-1.0	0.2
Smooth		50	-0.8	0.7
Complex			-1.3	0.4
Smooth		70	-0.8	0.8
Complex			-1.4	0.4
Smooth		90	-0.8	0.7
Complex			-1.4	0.7
Smooth	Inward	50	-0.6	0.1
Complex			-0.5	0.1

Table C.4: Averaged peak volumetric strain between Markers 6 and 7 for both surrogates in all orientations analysed with DIC. As a note, strain values were only considered during the first 20 ms of the impact event.

Gyrification	Orientation	Height (cm)	Peak Volumetric Strain (%)	
			ϵ_v	ϵ_v
Smooth	Downward	30	-0.3	0.2
Complex			-0.9	0.3
Smooth		50	-0.3	0.3
Complex			-0.8	0.8
Smooth		70	-0.4	0.5
Complex			-0.8	0.8
Smooth		90	-0.4	0.4
Complex			-0.6	0.8
Smooth	Upward	30	-0.3	0.3
Complex			-1.3	0.6
Smooth		50	-0.3	0.2
Complex			-1.4	1.0
Smooth		70	-0.3	0.2
Complex			-1.7	1.2
Smooth		90	0.0	0.6
Complex			-1.5	1.0
Smooth	Inward	50	-0.4	0.2
Complex			-0.7	1.3

C.3 Particle Tracking: Brain Gyrfication Facing Downward

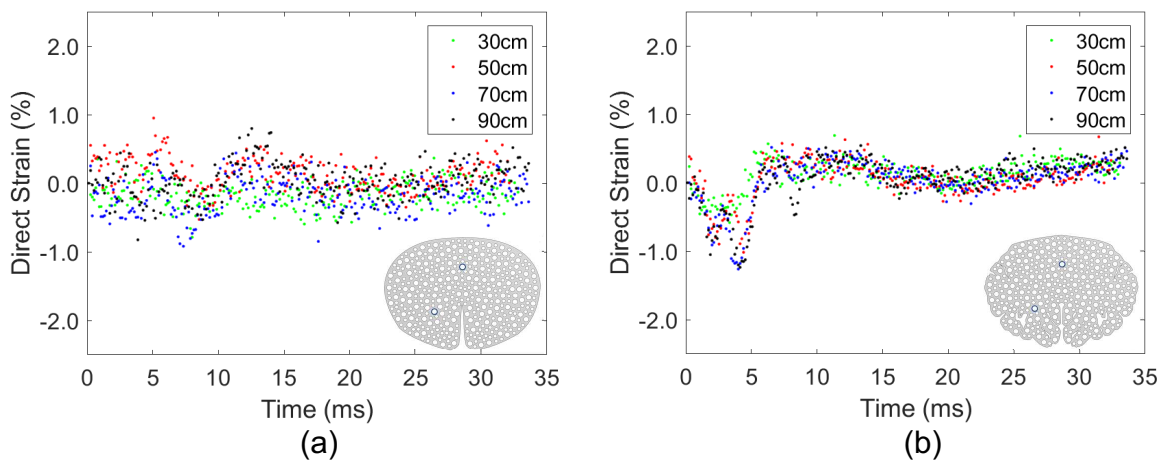


Figure C.13: Strain responses between Markers 1 and 4 of the smooth surrogate (a) and the complex surrogate (b) being dropped in the downward orientation. All four averaged responses from different drop heights are shown.

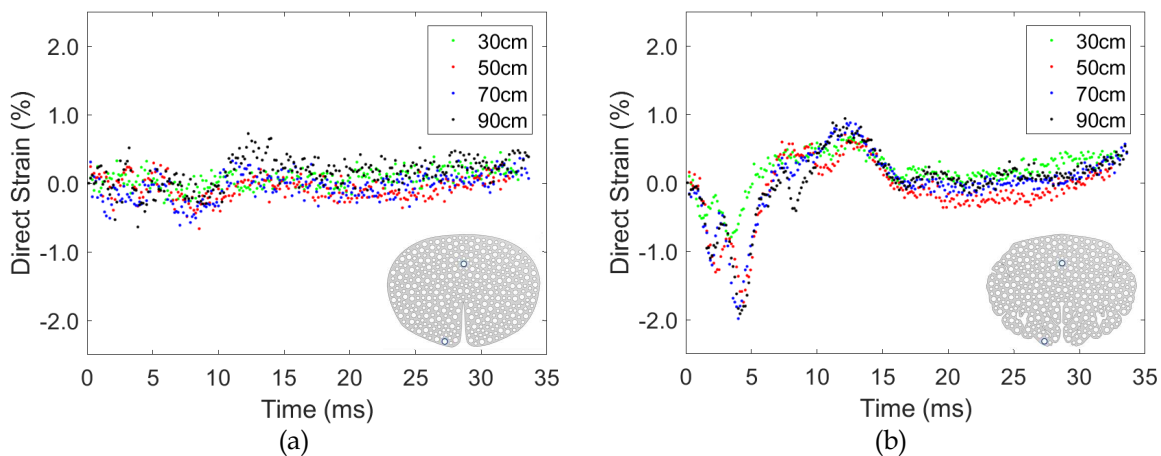


Figure C.14: Strain responses between Markers 1 and 5 of the smooth surrogate (a) and the complex surrogate (b) being dropped in the downward orientation. All four averaged responses from different drop heights are shown.

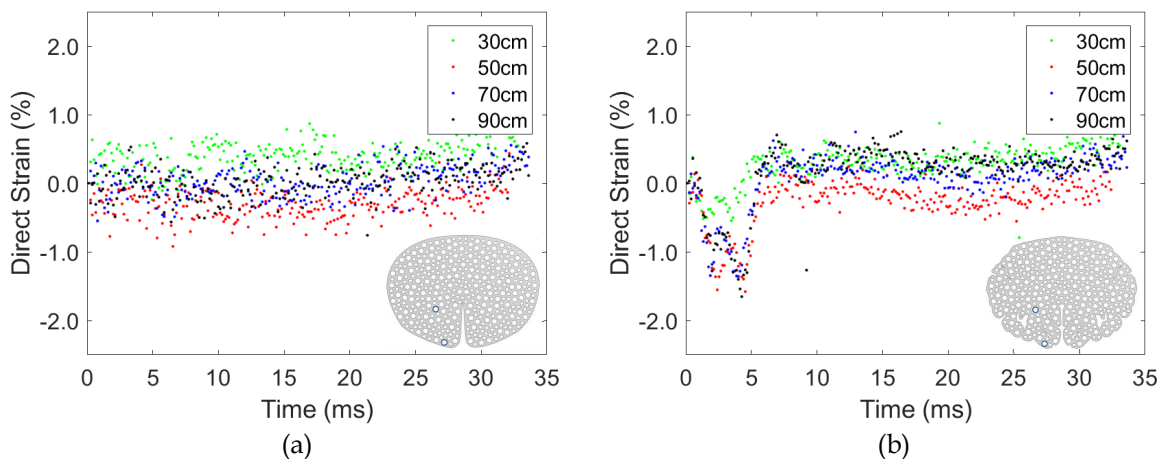


Figure C.15: Strain responses between Markers 4 and 5 of the smooth surrogate (a) and the complex surrogate (b) being dropped in the downward orientation. All four averaged responses from different drop heights are shown.

C.4 Particle Tracking: Brain Gyrfication Facing Upward

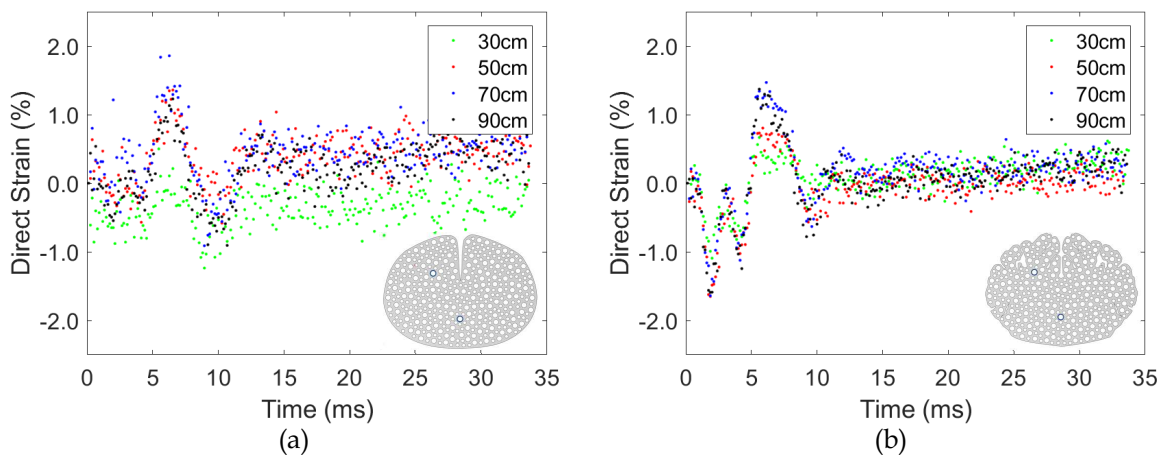


Figure C.16: Strain responses between Markers 1 and 4 of the smooth surrogate (a) and the complex surrogate (b) being dropped in the upward orientation. All four averaged responses from different drop heights are shown.

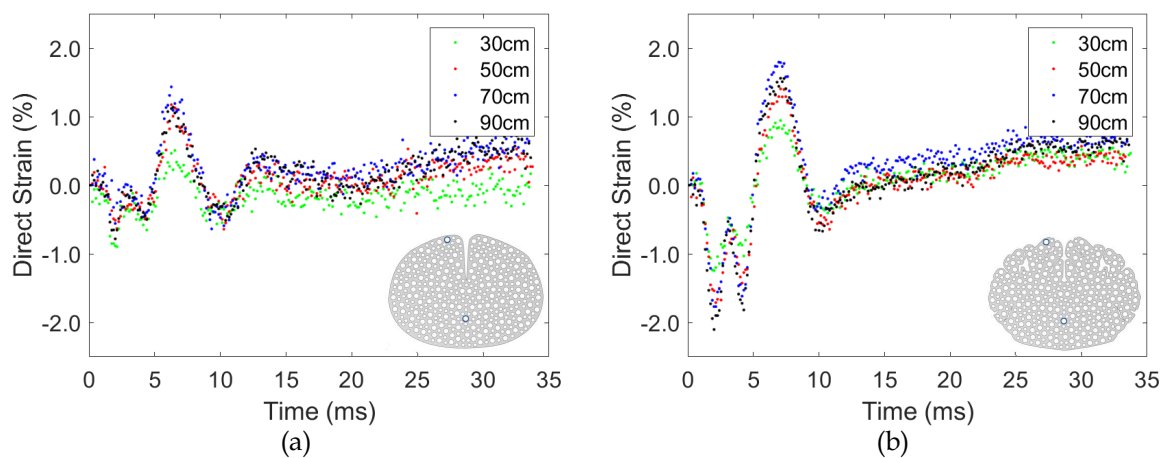


Figure C.17: Strain responses between Markers 1 and 5 of the smooth surrogate (a) and the complex surrogate (b) being dropped in the upward orientation. All four averaged responses from different drop heights are shown.

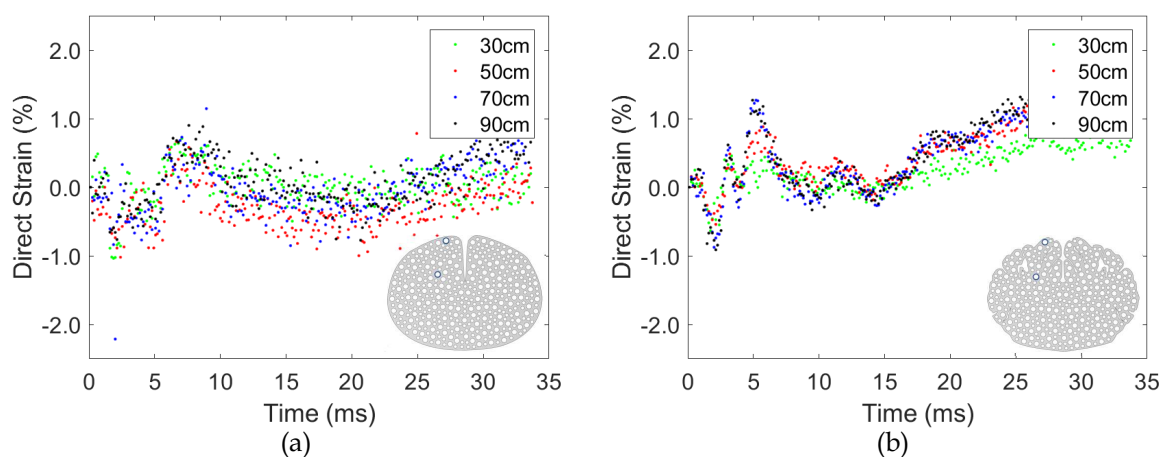


Figure C.18: Strain responses between Markers 4 and 5 of the smooth surrogate (a) and the complex surrogate (b) being dropped in the upward orientation. All four averaged responses from different drop heights are shown.

C.5 Particle Tracking: Brain Gyrfication Facing Inward

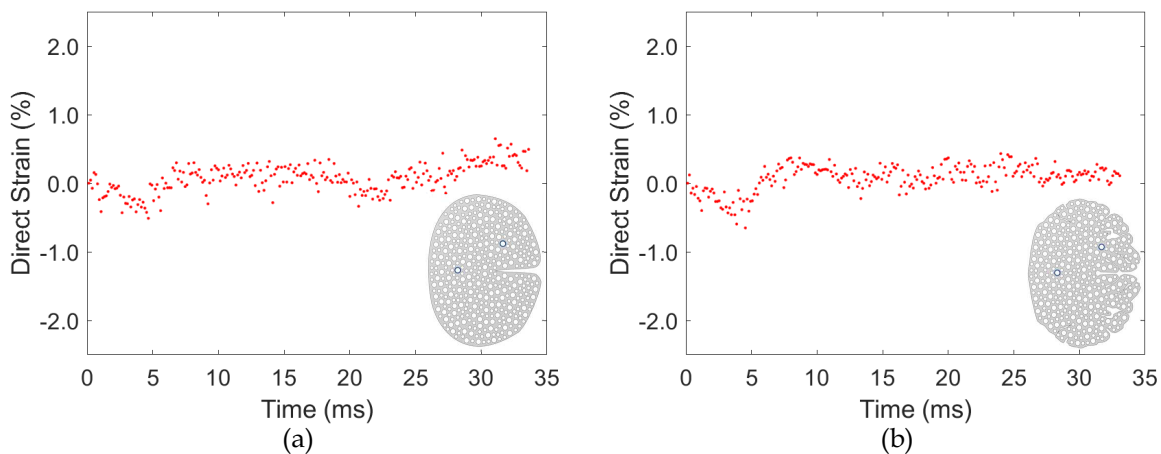


Figure C.19: The averaged strain responses between Markers 1 and 4 of the smooth surrogate (a) and the complex surrogate (b) being dropped in the inward orientation at 50 cm.

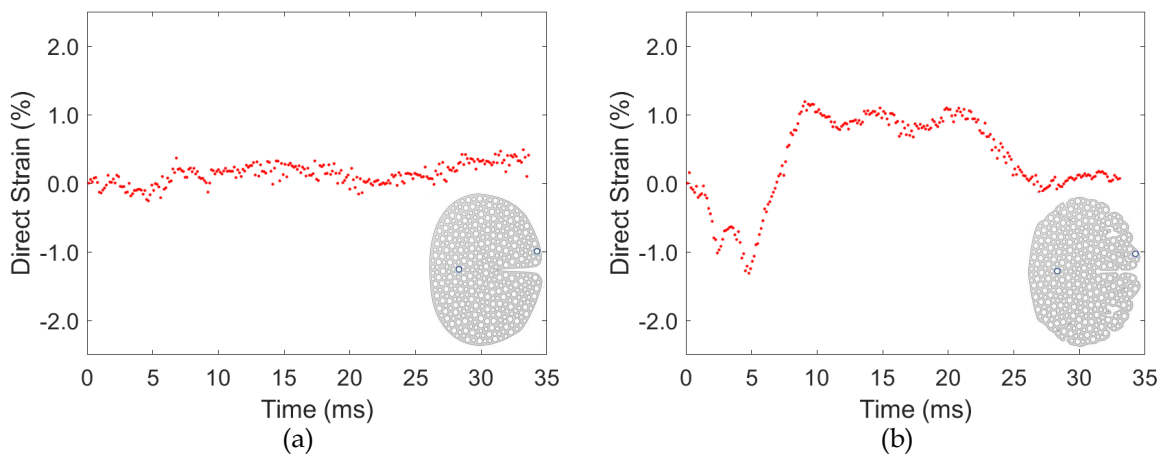


Figure C.20: The averaged strain responses between markers 1 and 5 of the smooth surrogate (a) and the complex surrogate (b) being dropped in the inward orientation at 50 cm.

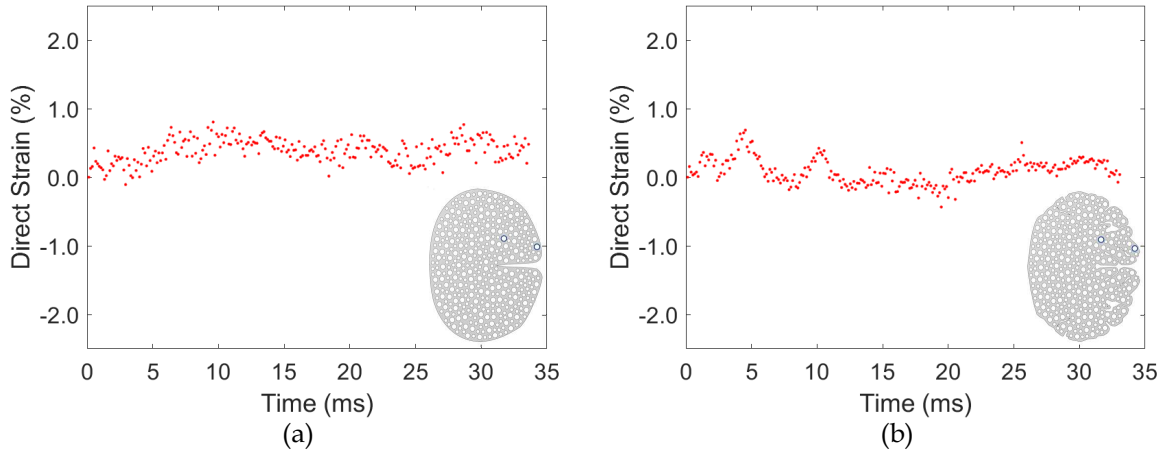


Figure C.21: The averaged strain responses between Markers 4 and 5 of the smooth surrogate (a) and the complex surrogate (b) being dropped in the inward orientation at 50 cm.

C.6 Particle Tracking: Supplementary Orientations

The surrogates were dropped in an additional four different orientations. The surrogates were placed with brain gyration facing outwards, as it was observed that motion was lesser closer to the 80/20 rails (Figure C.22a). As the surrogates were always dropped in the same position relative to one another, a series of drops were conducted to confirm that regardless of surrogate placement (on the left or right side of the drop system), the trends would remain the same (Figure C.22b). The inward orientation appeared to be more susceptible to positioning within the encasement, therefore to determine the effects of misalignment, a 5° surrogate tilt outwards and a 5° surrogate tilt inwards were examined (Figure C.22c and d).

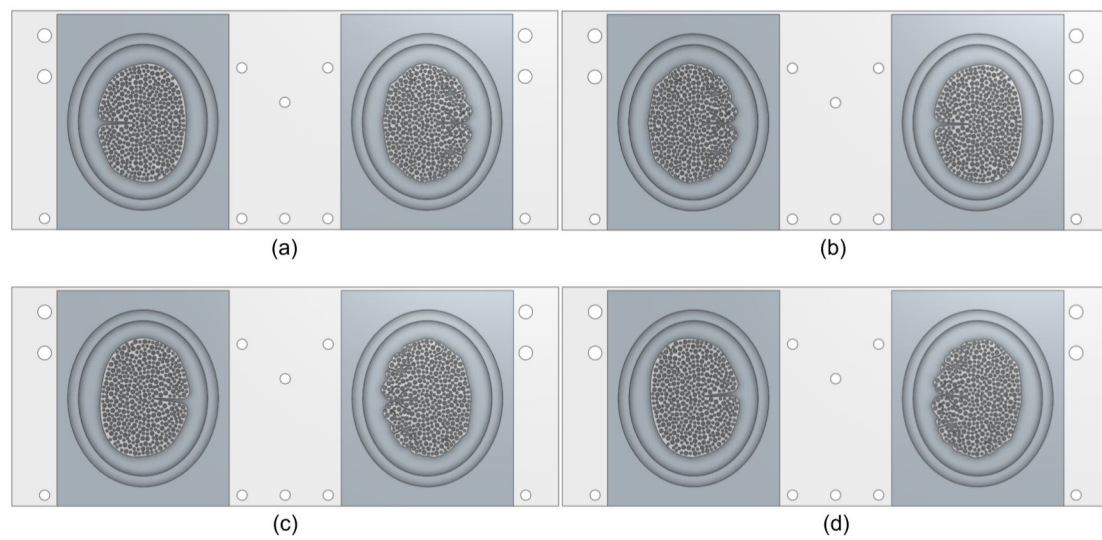


Figure C.22: Orientations of the surrogates with the surrogates (a) facing outwards, (b) in swapped positions, (c) with a 5° tilt inwards, and (d) with a 5° tilt outwards. In subfigures (a), (c), and (d) the smooth surrogate is to the left and the complex surrogate is to the right.

Outward Orientation

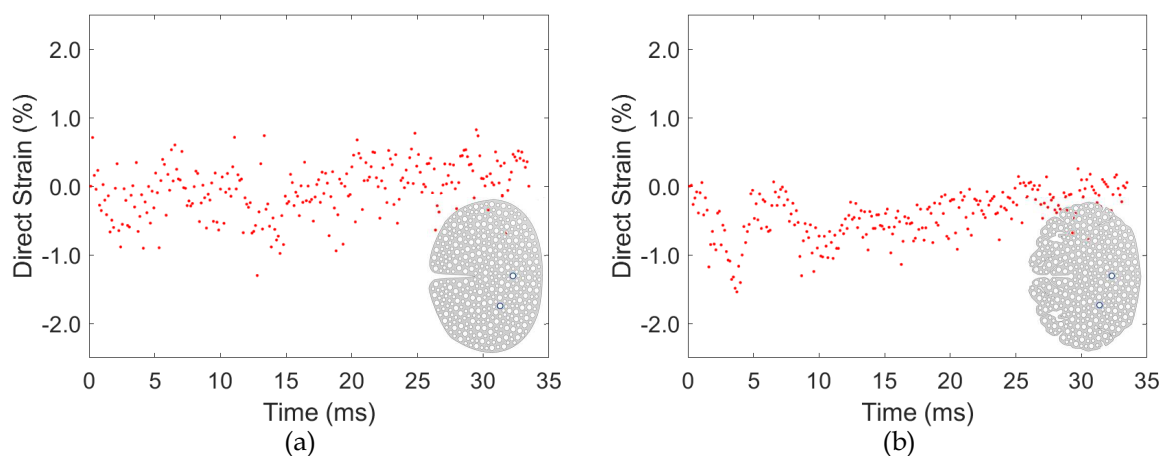


Figure C.23: The averaged strain responses between Markers 1 and 2 of the smooth surrogate (a) and the complex surrogate (b) being dropped in the outward orientation at 50 cm.

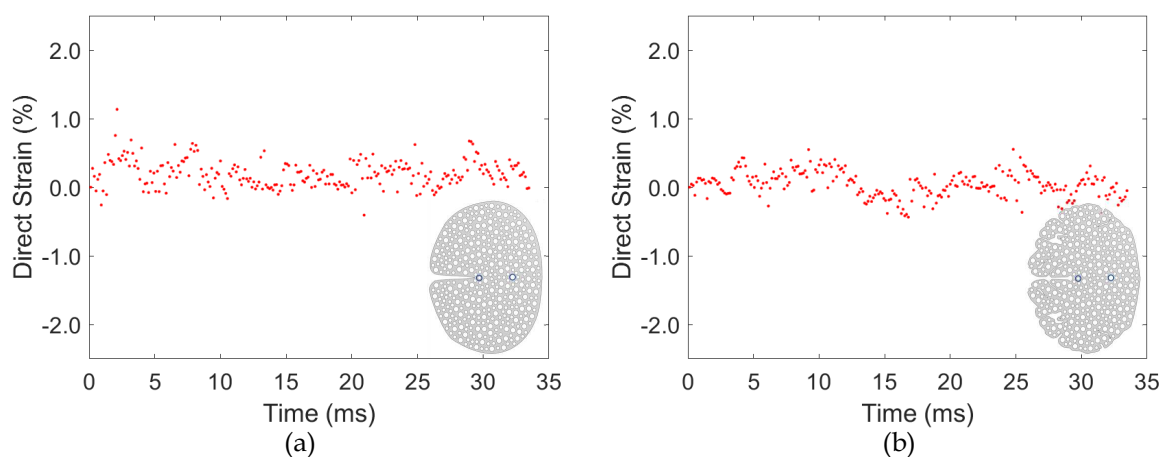


Figure C.24: The averaged strain responses between Markers 1 and 3 of the smooth surrogate (a) and the complex surrogate (b) being dropped in the outward orientation at 50 cm.

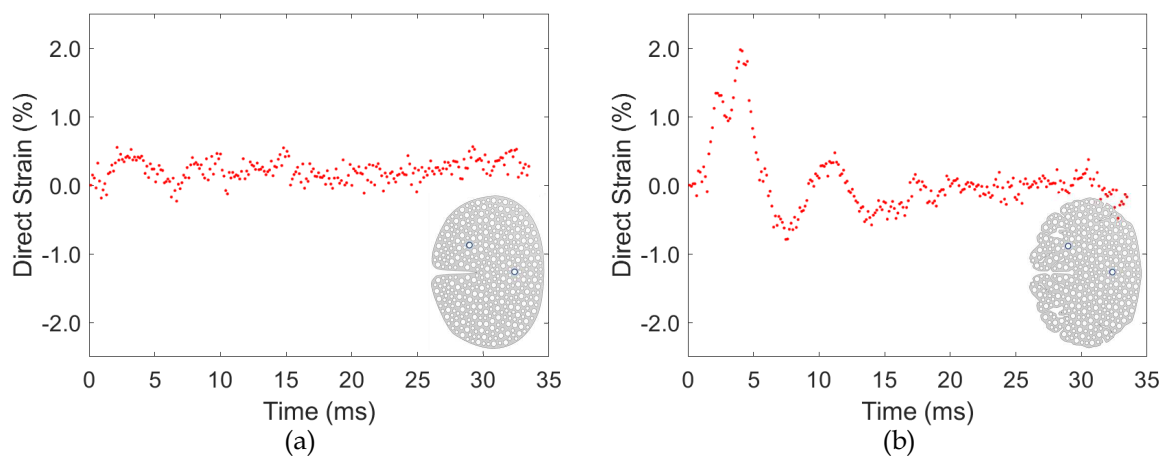


Figure C.25: The averaged strain responses between Markers 1 and 4 of the smooth surrogate (a) and the complex surrogate (b) being dropped in the outward orientation at 50 cm.

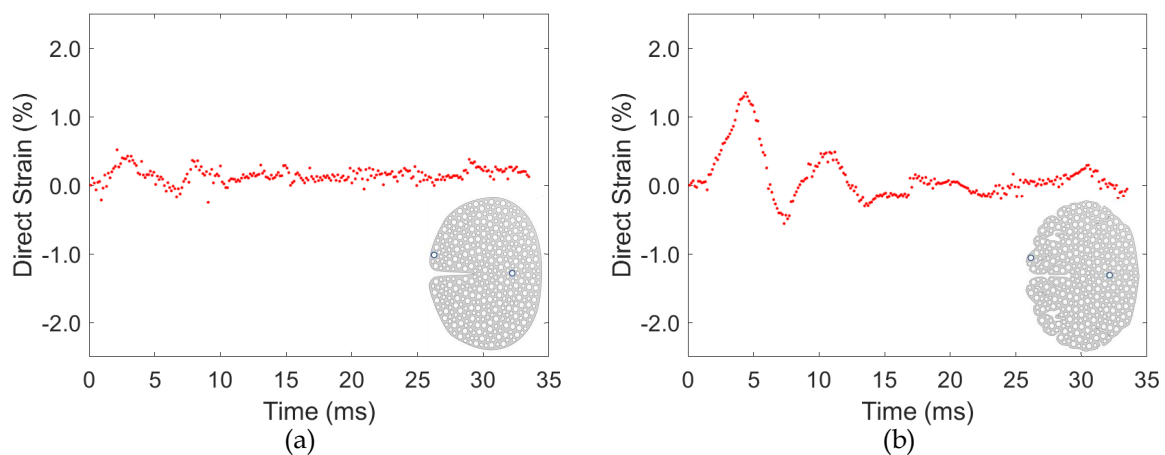


Figure C.26: The averaged strain responses between Markers 1 and 5 of the smooth surrogate (a) and the complex surrogate (b) being dropped in the outward orientation at 50 cm.

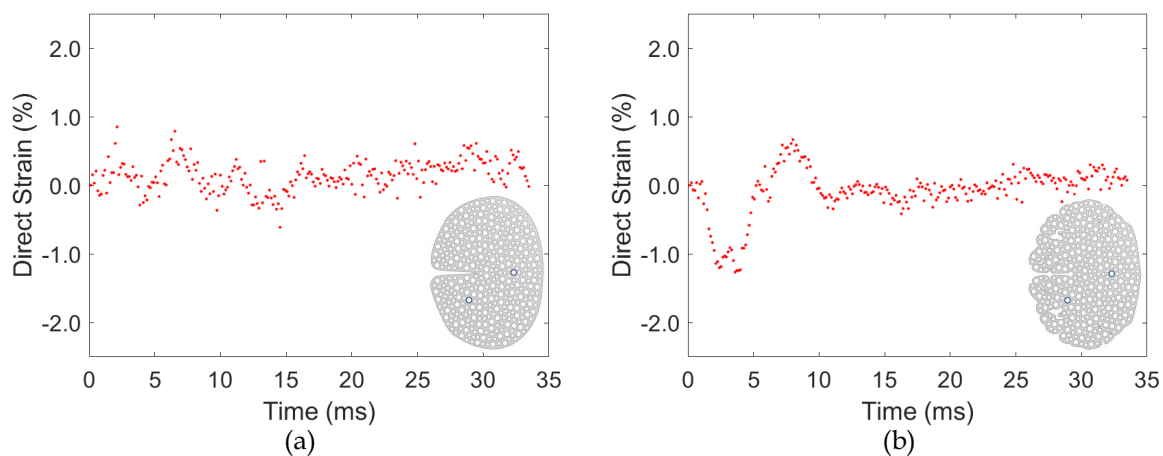


Figure C.27: The averaged strain responses between Markers 1 and 6 of the smooth surrogate (a) and the complex surrogate (b) being dropped in the outward orientation at 50 cm.

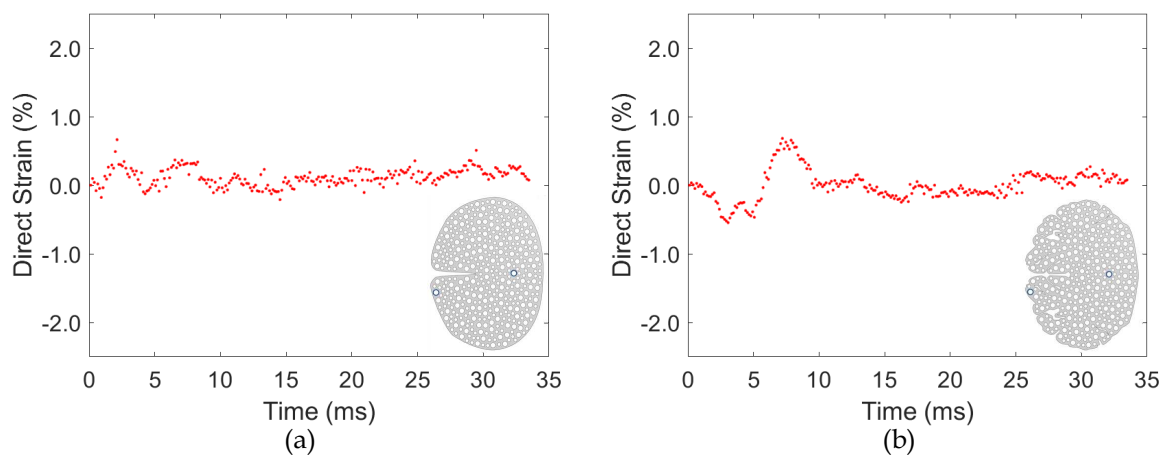


Figure C.28: The averaged strain responses between Markers 1 and 7 of the smooth surrogate (a) and the complex surrogate (b) being dropped in the outward orientation at 50 cm.

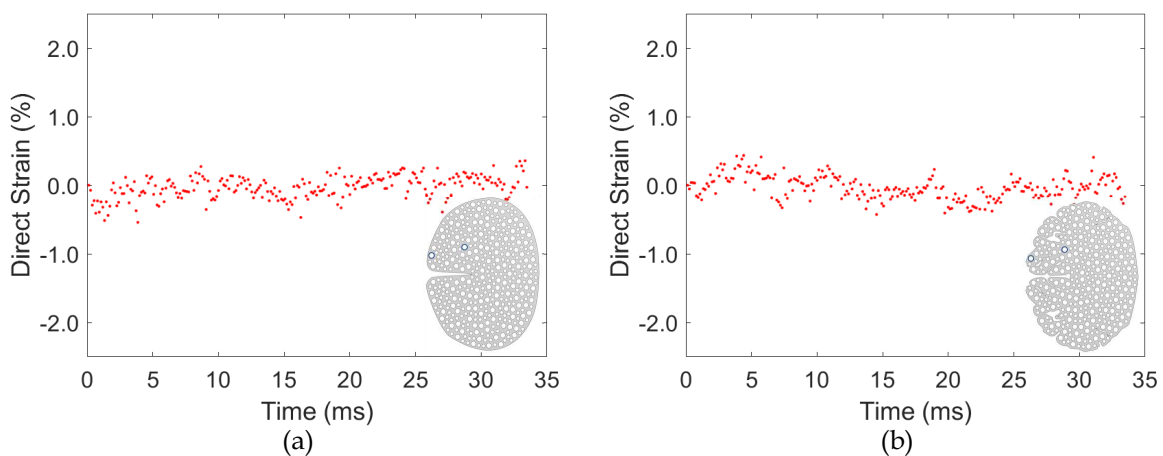


Figure C.29: The averaged strain responses between Markers 4 and 5 of the smooth surrogate (a) and the complex surrogate (b) being dropped in the outward orientation at 50 cm.

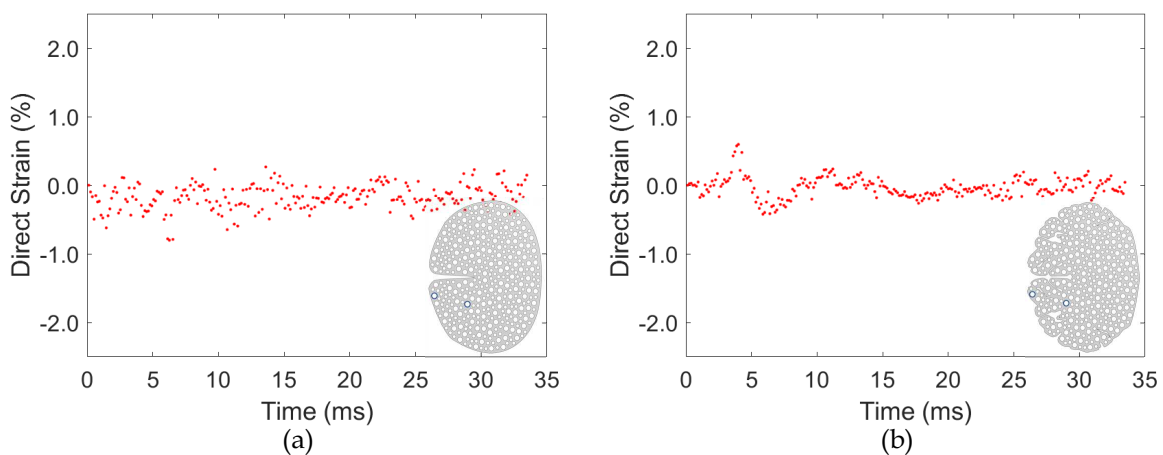


Figure C.30: The averaged strain responses between Markers 6 and 7 of the smooth surrogate (a) and the complex surrogate (b) being dropped in the outward orientation at 50 cm.

Swapped Orientation

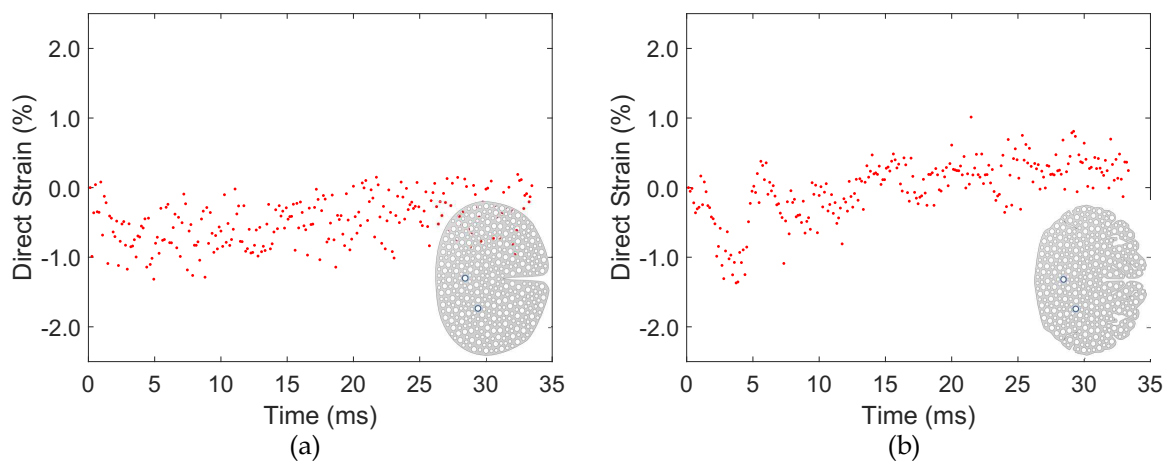


Figure C.31: The averaged strain responses between Markers 1 and 2 of the smooth surrogate (a) and the complex surrogate (b) being dropped in the inward orientation, but in swapped positions at 50 cm.

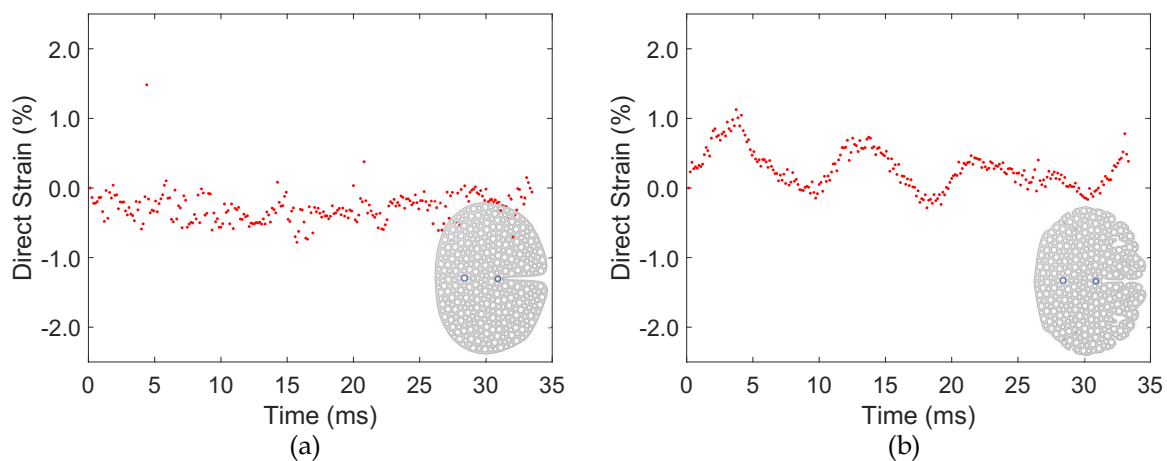


Figure C.32: The averaged strain responses between Markers 1 and 3 of the smooth surrogate (a) and the complex surrogate (b) being dropped in the inward orientation, but in swapped positions at 50 cm. Note, the complex surrogate had a jitter correction applied to the raw data.

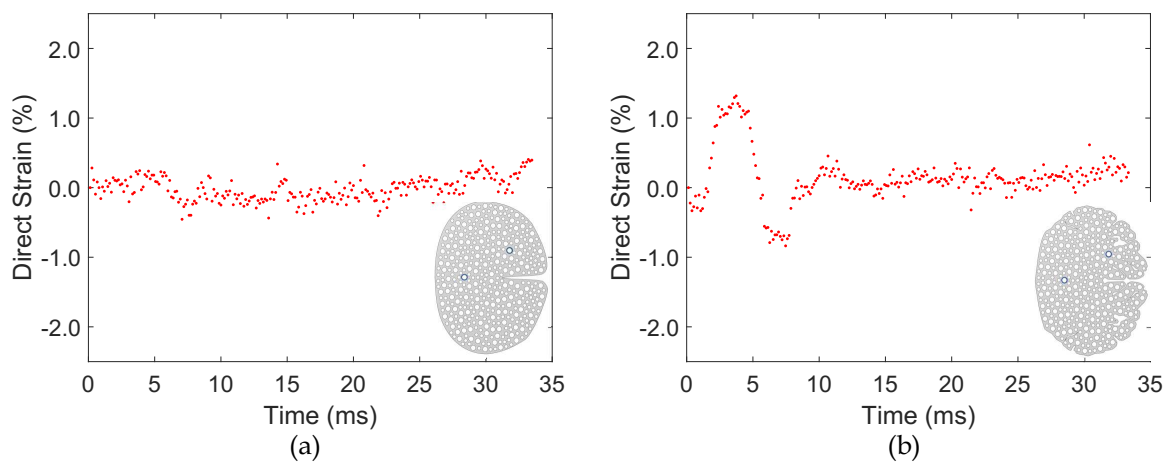


Figure C.33: The averaged strain responses between Markers 1 and 4 of the smooth surrogate (a) and the complex surrogate (b) being dropped in the inward orientation, but in swapped positions at 50 cm.

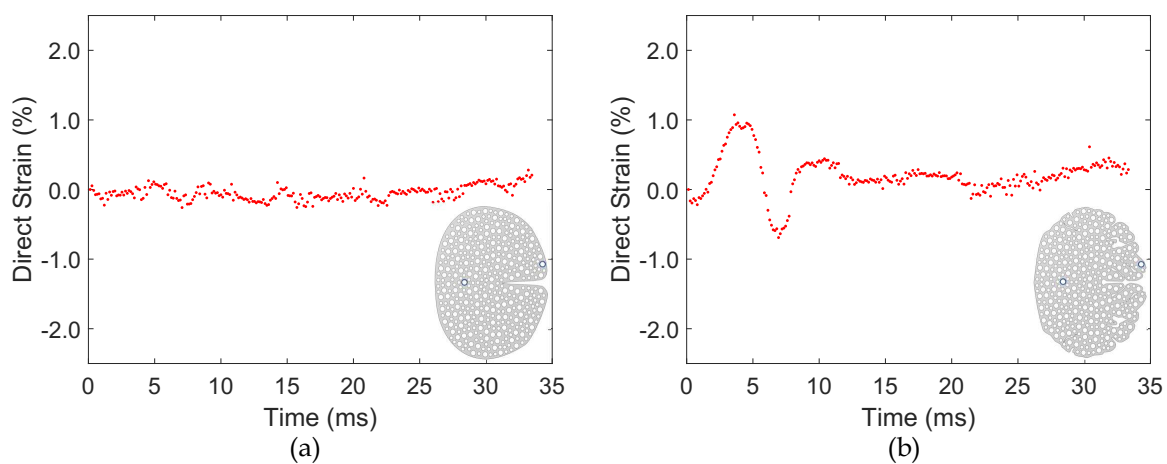


Figure C.34: The averaged strain responses between Markers 1 and 5 of the smooth surrogate (a) and the complex surrogate (b) being dropped in the inward orientation, but in swapped positions at 50 cm.

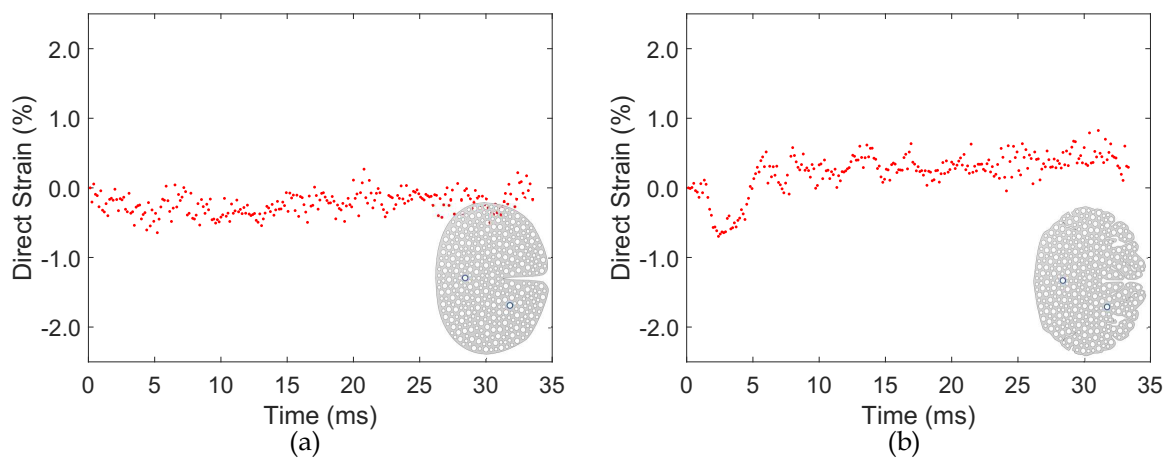


Figure C.35: The averaged strain responses between Markers 1 and 6 of the smooth surrogate (a) and the complex surrogate (b) being dropped in the inward orientation, but in swapped positions at 50 cm.

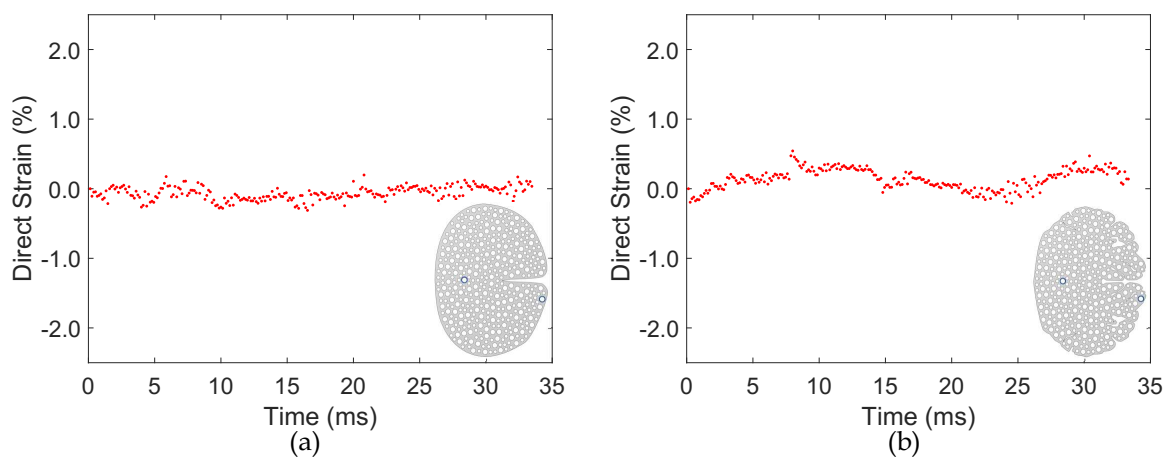


Figure C.36: The averaged strain responses between Markers 1 and 7 of the smooth surrogate (a) and the complex surrogate (b) being dropped in the inward orientation, but in swapped positions at 50 cm.

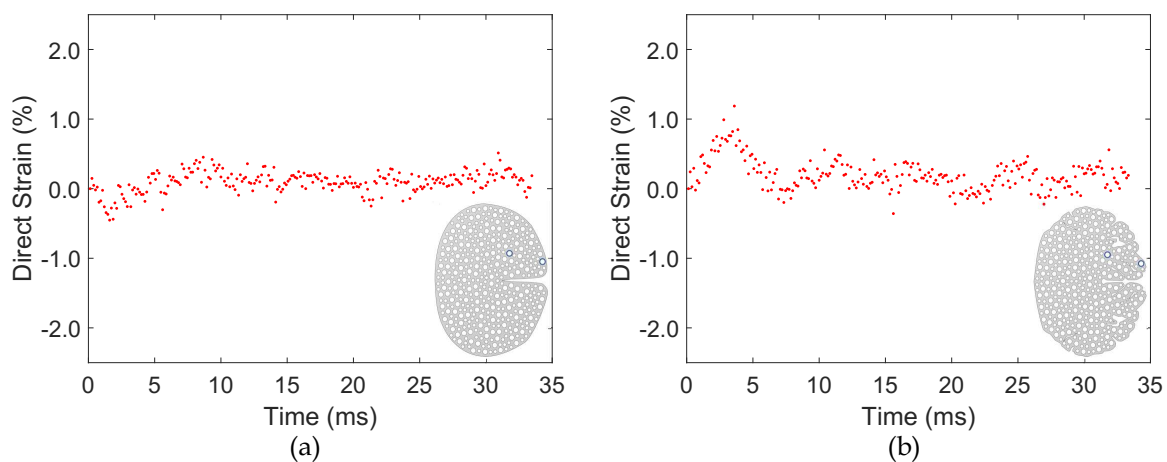


Figure C.37: The averaged strain responses between Markers 4 and 5 of the smooth surrogate (a) and the complex surrogate (b) being dropped in the inward orientation, but in swapped positions at 50 cm.

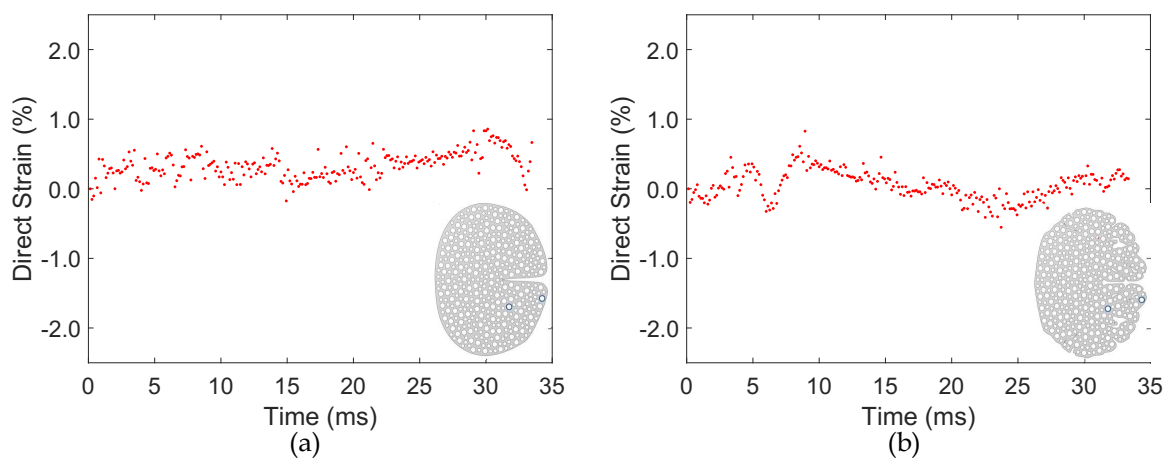


Figure C.38: The averaged strain responses between Markers 6 and 7 of the smooth surrogate (a) and the complex surrogate (b) being dropped in the inward orientation, but in swapped positions at 50 cm.

Five Degrees Inward

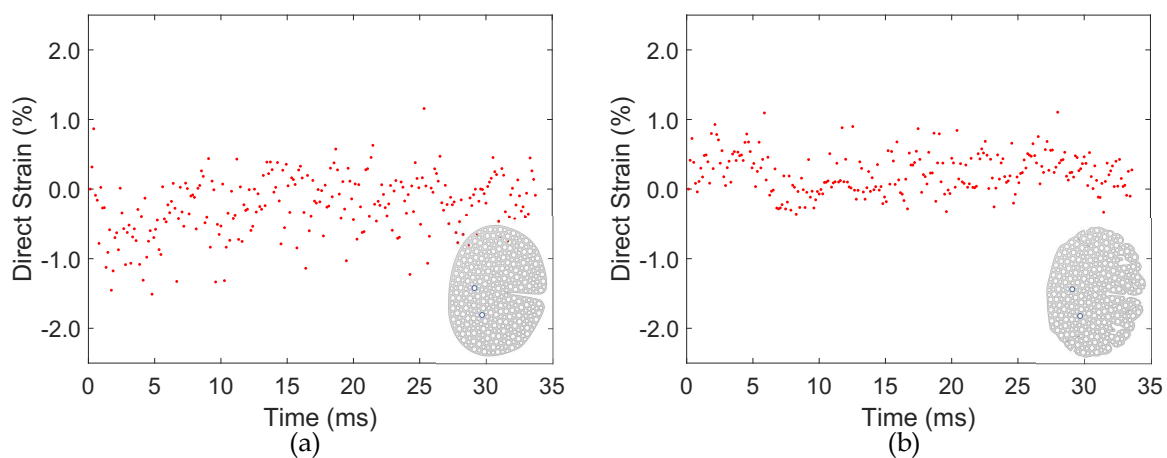


Figure C.39: The averaged strain responses between Markers 1 and 2 of the smooth surrogate (a) and the complex surrogate (b) being dropped in the inward orientation with a 5° inwards towards from the center at 50 cm.

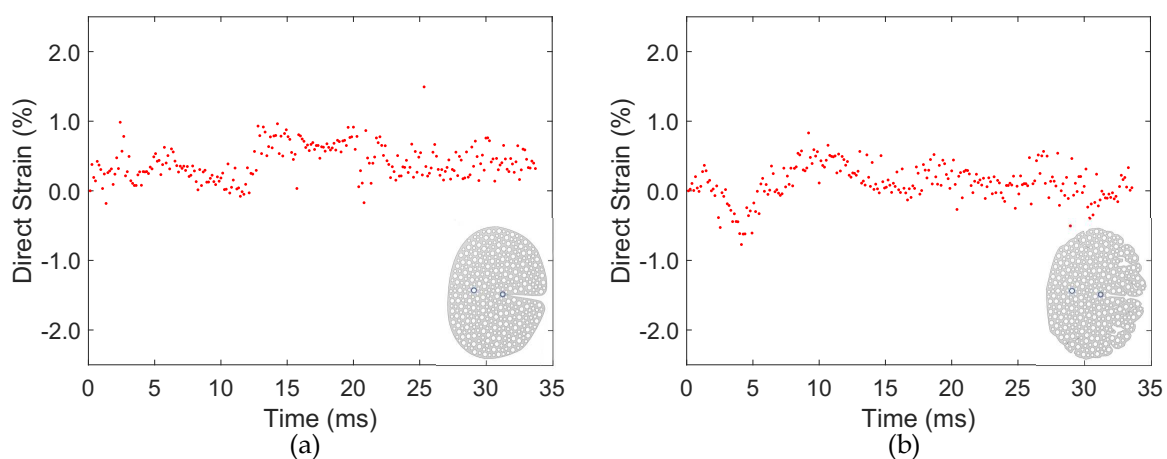


Figure C.40: The averaged strain responses between Markers 1 and 3 of the smooth surrogate (a) and the complex surrogate (b) being dropped in the inward orientation with a 5° inwards towards from the center at 50 cm.

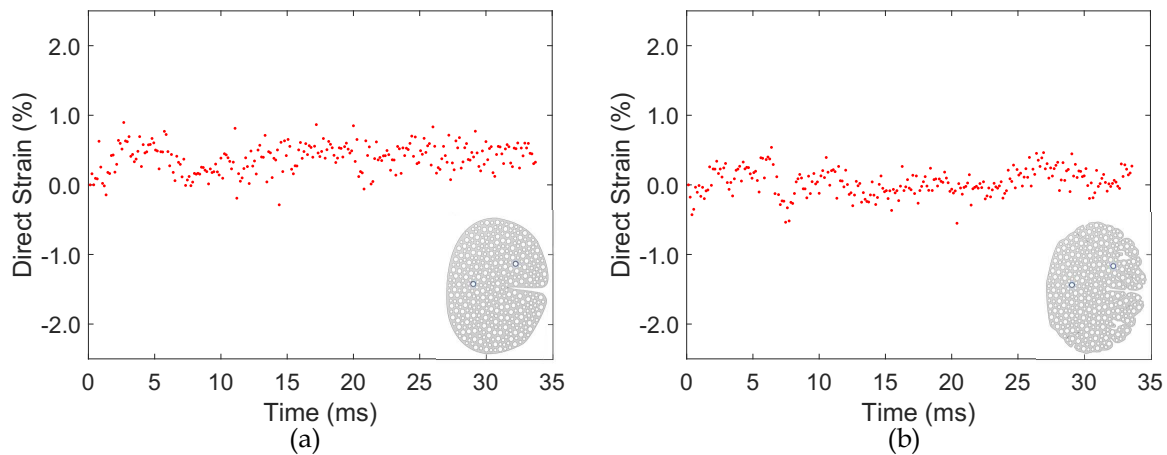


Figure C.41: The averaged strain responses between Markers 1 and 4 of the smooth surrogate (a) and the complex surrogate (b) being dropped in the inward orientation with a 5° tilt inwards towards the center at 50 cm.

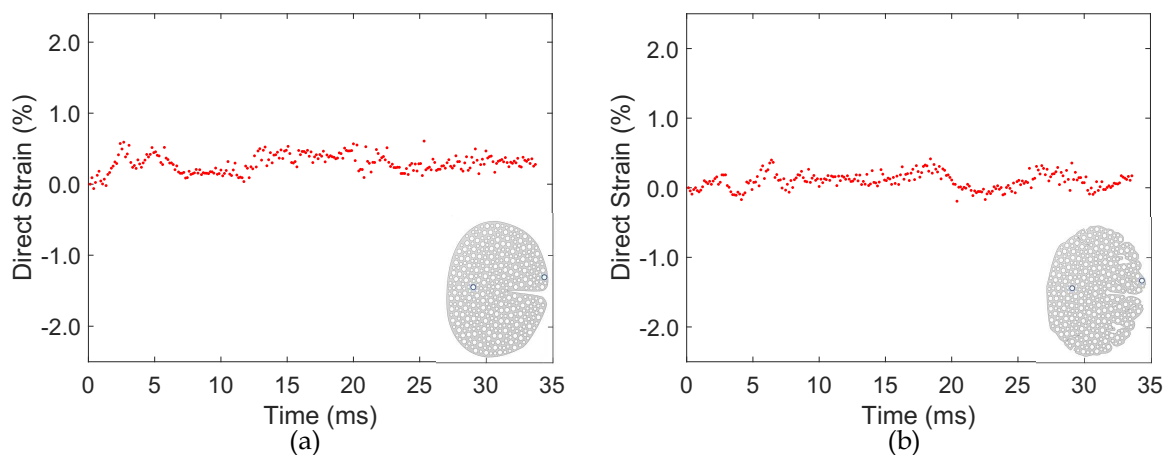


Figure C.42: The averaged strain responses between Markers 1 and 5 of the smooth surrogate (a) and the complex surrogate (b) being dropped in the inward orientation with a 5° tilt inwards towards the center at 50 cm.

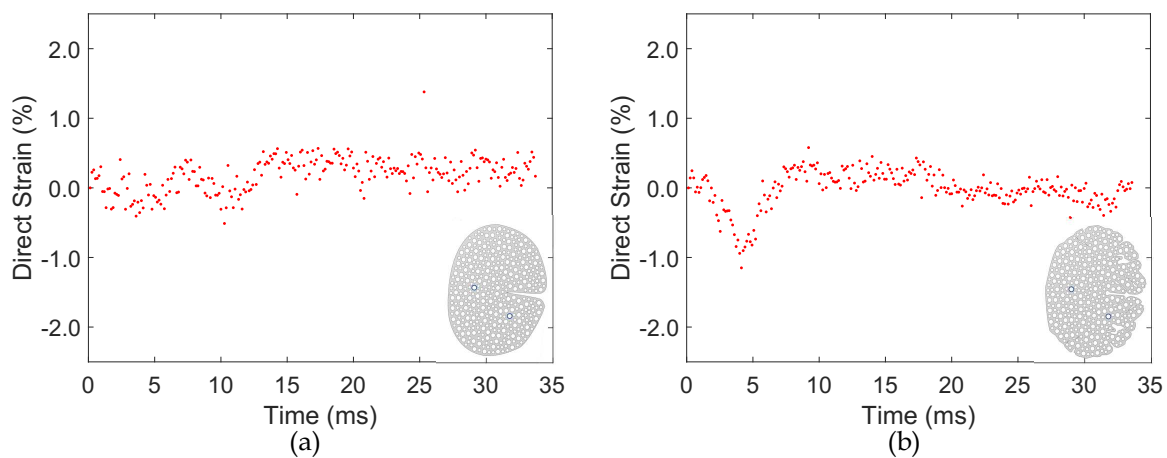


Figure C.43: The averaged strain responses between Markers 1 and 6 of the smooth surrogate (a) and the complex surrogate (b) being dropped in the inward orientation with a 5° inwards towards from the center at 50 cm.

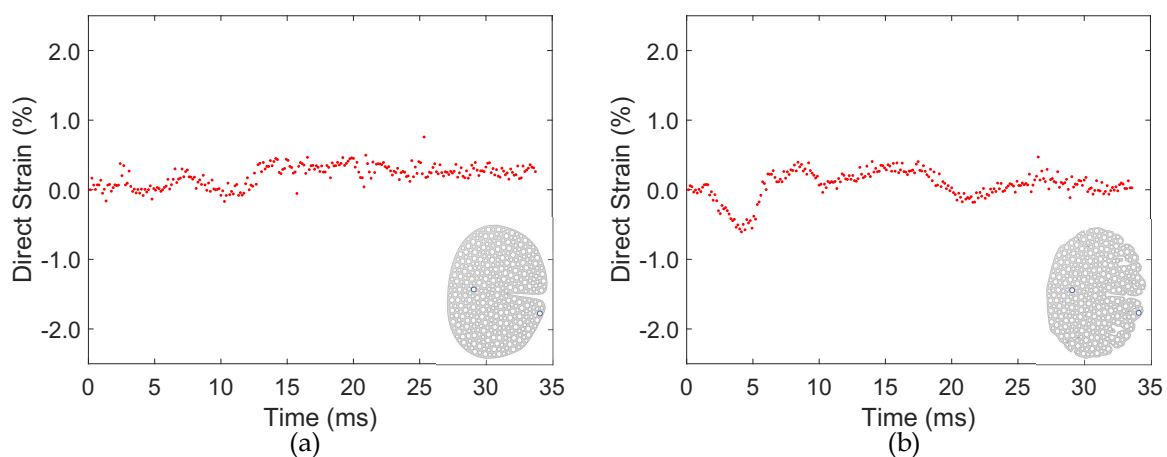


Figure C.44: The averaged strain responses between Markers 1 and 7 of the smooth surrogate (a) and the complex surrogate (b) being dropped in the inward orientation with a 5° tilt inwards towards the center at 50 cm.

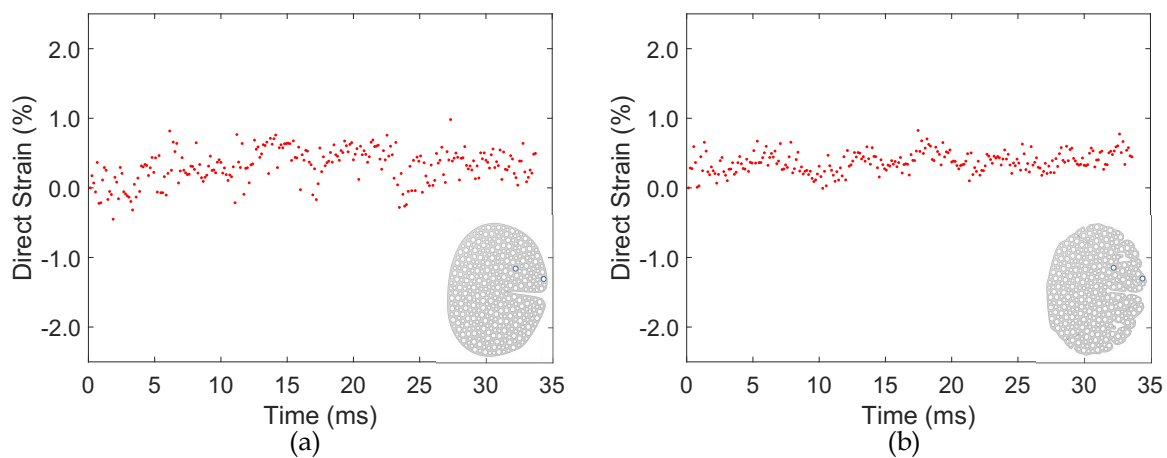


Figure C.45: The averaged strain responses between Markers 4 and 5 of the smooth surrogate (a) and the complex surrogate (b) being dropped in the inward orientation with a 5° tilt inwards towards the center at 50 cm.

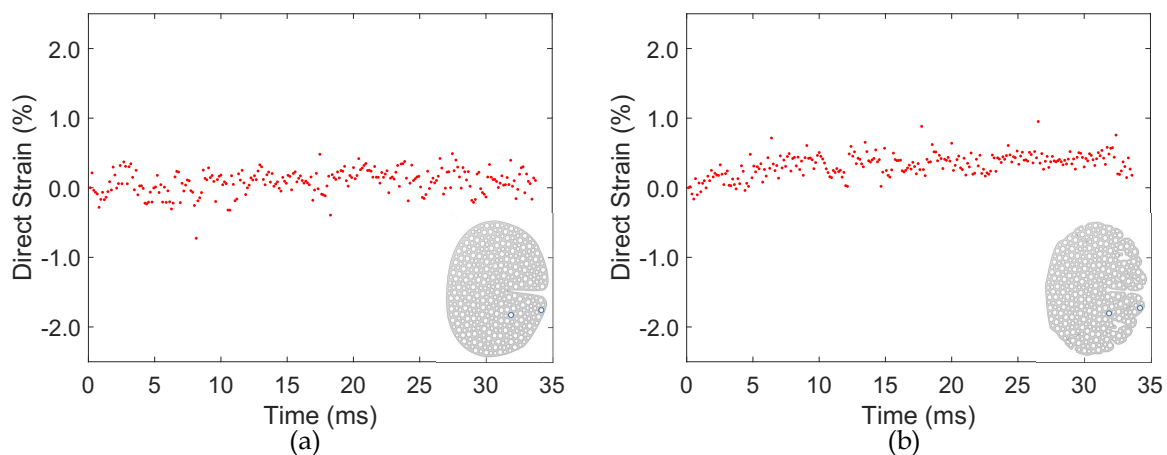


Figure C.46: The averaged strain responses between Markers 6 and 7 of the smooth surrogate (a) and the complex surrogate (b) being dropped in the inward orientation with a 5° tilt inwards towards the center at 50 cm.

Five Degrees Outward

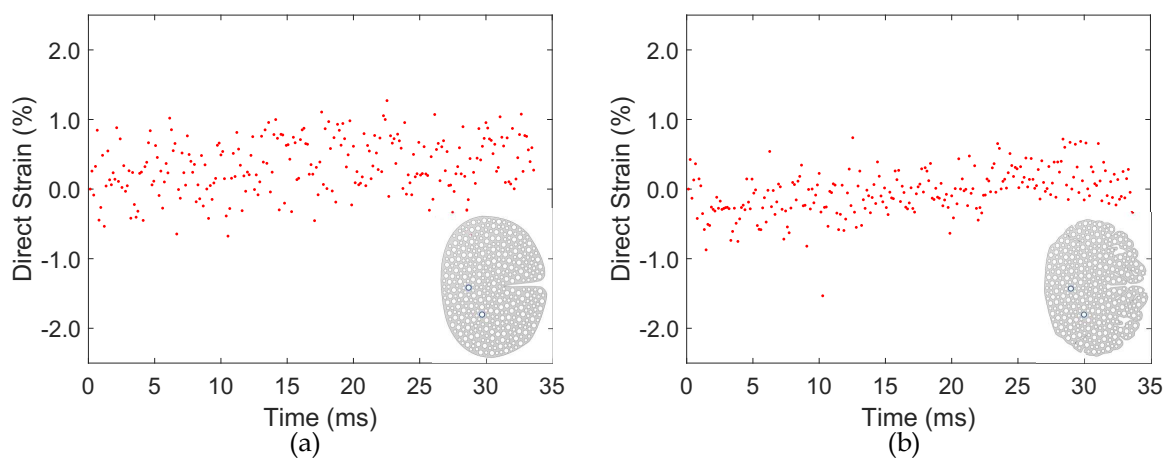


Figure C.47: The averaged strain responses between Markers 1 and 2 of the smooth surrogate (a) and the complex surrogate (b) being dropped in the inward orientation with a 5° tilt outward from the center at 50 cm.

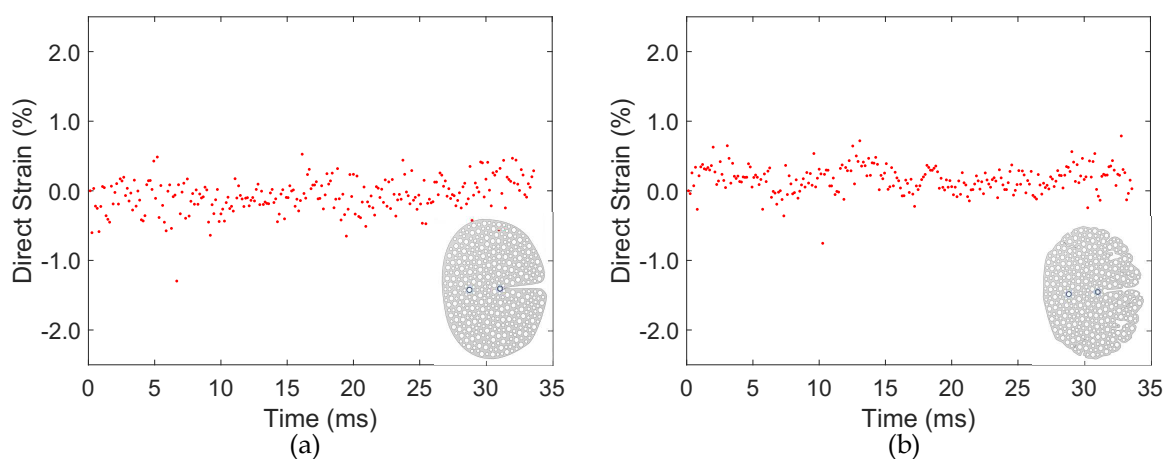


Figure C.48: The averaged strain responses between Markers 1 and 3 of the smooth surrogate (a) and the complex surrogate (b) being dropped in the inward orientation with a 5° tilt outward from the center at 50 cm.

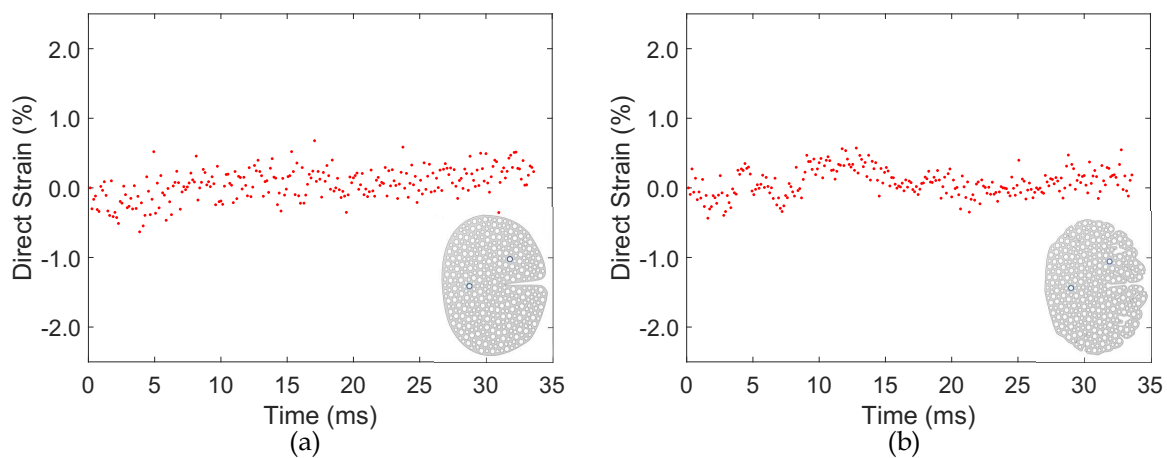


Figure C.49: The averaged strain responses between Markers 1 and 4 of the smooth surrogate (a) and the complex surrogate (b) being dropped in the inward orientation with a 5° tilt outward from the center at 50 cm.

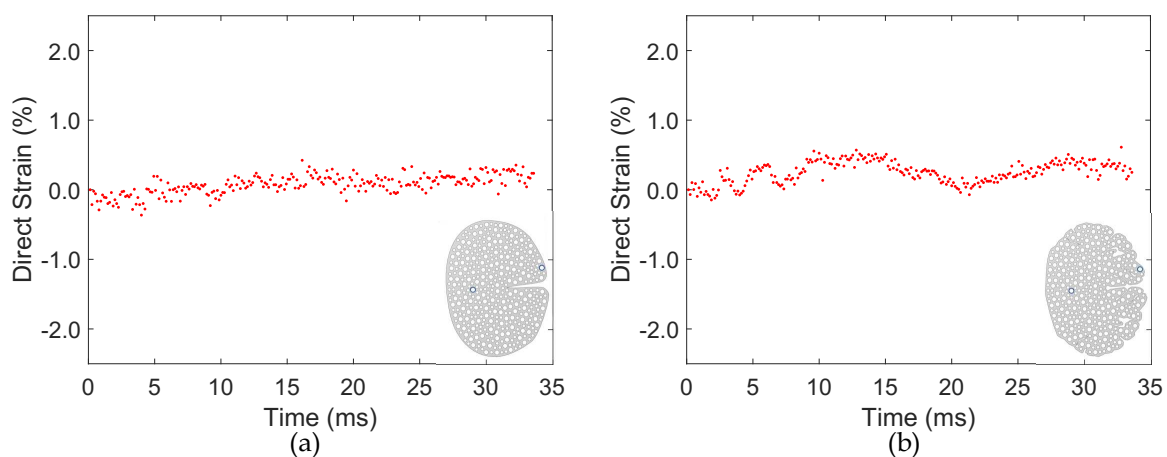


Figure C.50: The averaged strain responses between Markers 1 and 5 of the smooth surrogate (a) and the complex surrogate (b) being dropped in the inward orientation with a 5° tilt outward from the center at 50 cm.

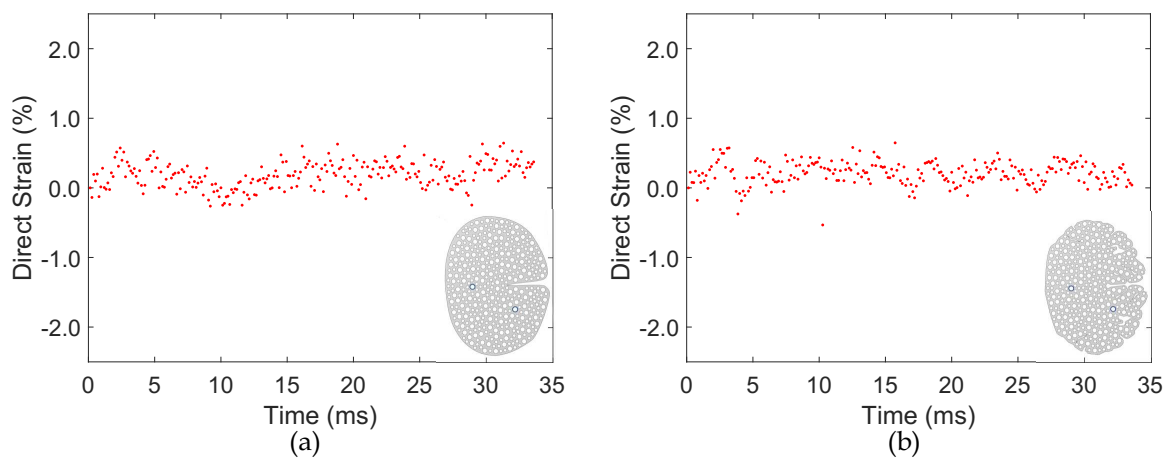


Figure C.51: The averaged strain responses between Markers 1 and 6 of the smooth surrogate (a) and the complex surrogate (b) being dropped in the inward orientation with a 5° tilt outward from the center at 50 cm.

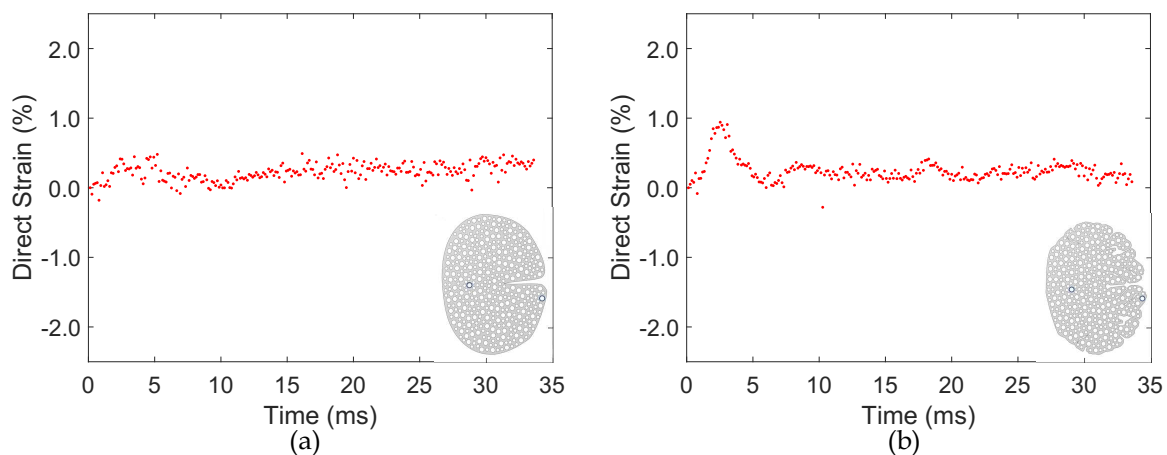


Figure C.52: The averaged strain responses between Markers 1 and 7 of the smooth surrogate (a) and the complex surrogate (b) being dropped in the inward orientation with a 5° tilt outward from the center at 50 cm.

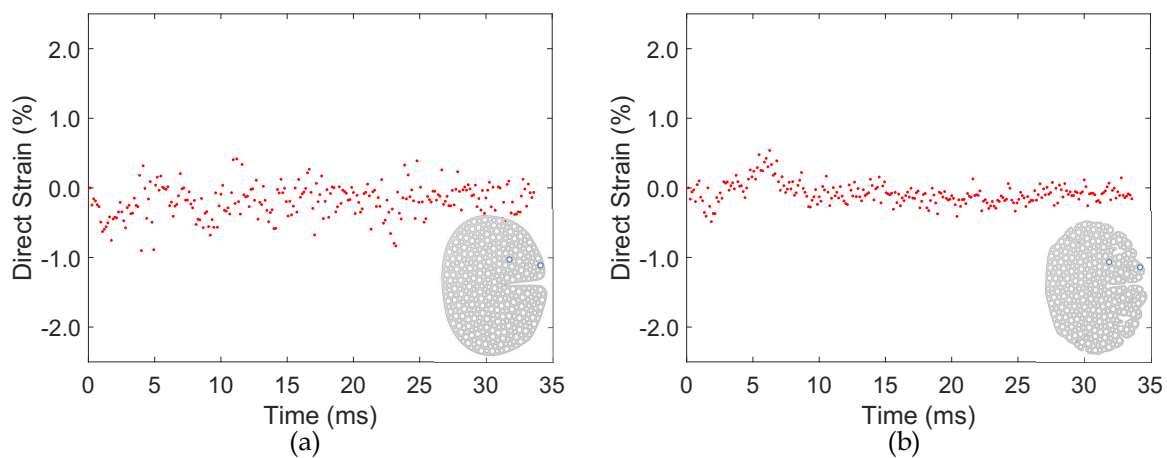


Figure C.53: The averaged strain responses between Markers 4 and 5 of the smooth surrogate (a) and the complex surrogate (b) being dropped in the inward orientation with a 5° tilt outward from the center at 50 cm.

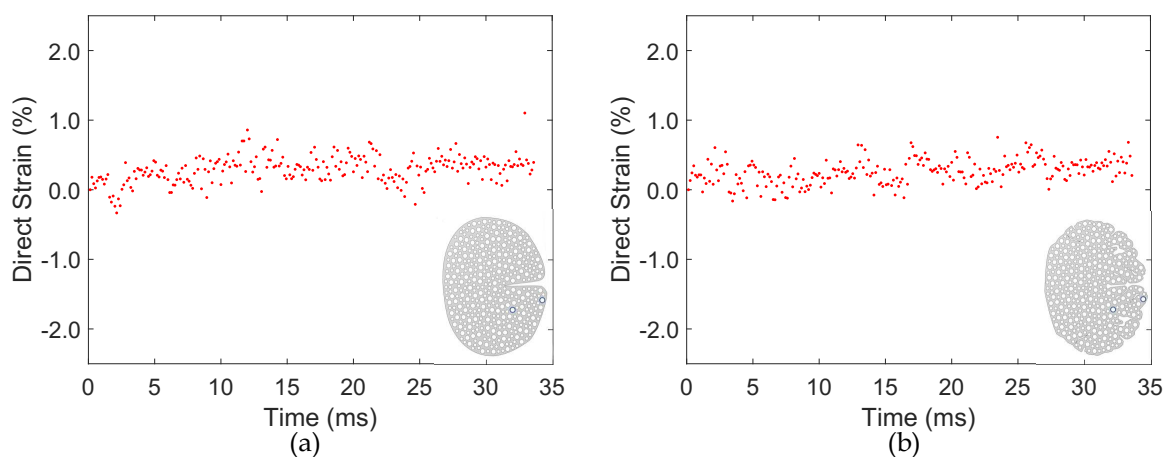


Figure C.54: The averaged strain responses between Markers 6 and 7 of the smooth surrogate (a) and the complex surrogate (b) being dropped in the inward orientation with a 5° tilt outward from the center at 50 cm.

Justification for Averaging Strain Responses

Below are figures showing the averaged strain response, along with the three trials used to justify averaging the strain data. The figures represent different orientations and markers.

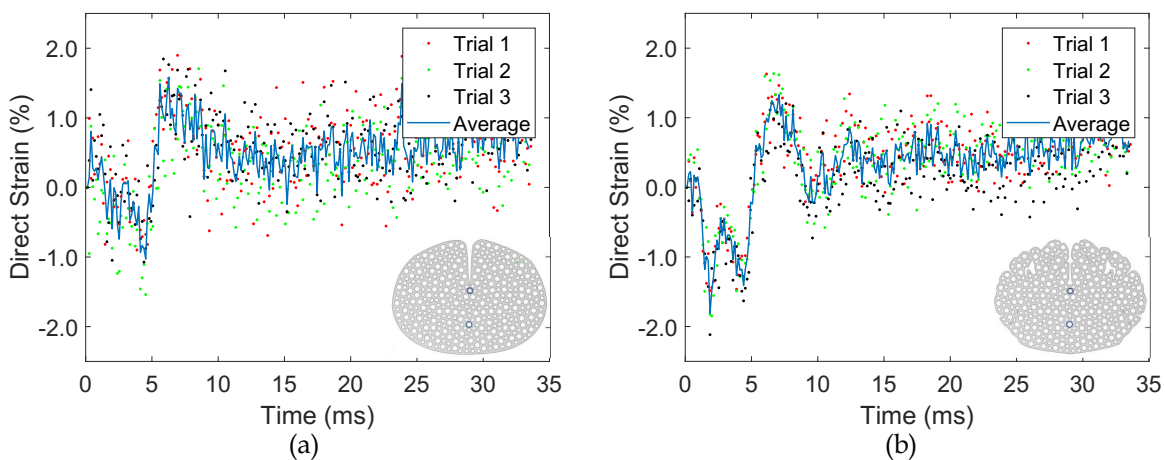


Figure C.55: The averaged strain response superimposed on the individual trials used to create the average between Markers 1 and 3 of the smooth sample (a) and the complex sample (b). The strain data is from a 70 cm drop with the surrogates being dropped in the upward orientation. The averaged and median strain responses follow near identical paths.

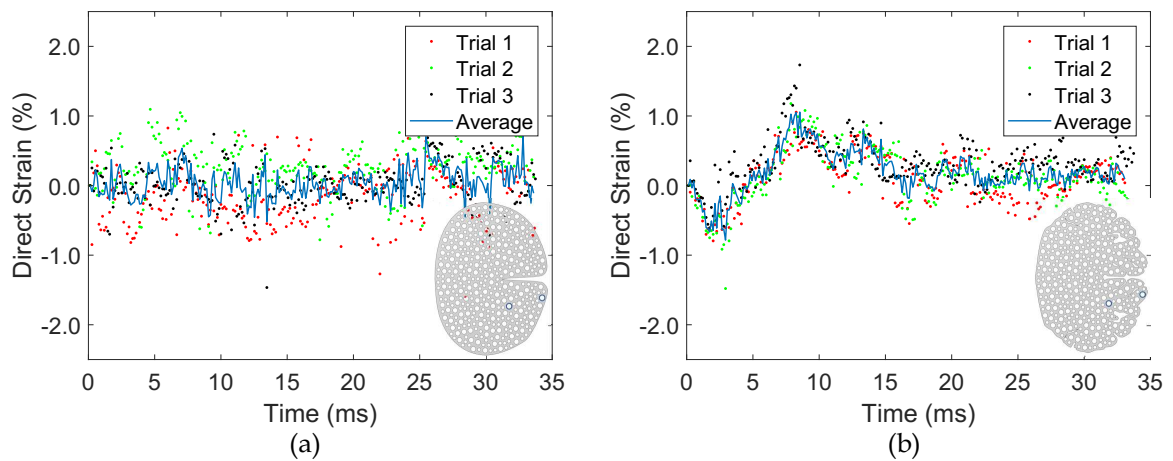


Figure C.56: The averaged strain response superimposed on the individual trials used to create the average between Markers 6 and 7 of the smooth surrogate (a) and the complex surrogate (b). The strain data is from a 50 cm drop with the surrogates being dropped in the inward orientation. The averaged and median strain responses follow similar paths.

Average and Standard Deviation for the Downward and Upward Orientations

Below are values of the average strain and standard deviation between trials at each height, orientation, and marker pairings 1 and 2, 1 and 6, and 6 and 7 for each surrogate.

Table C.5: Average peak compressive and tensile strains for each marker pair obtained from three trials at each height for the smooth surrogate when dropped in the downward orientation. Values in brackets represent the standard deviation.

Drop Height (cm)	Marker Pairing	Peak Compressive Strain (%)	Peak Tensile Strain (%)
30	1 and 2	-0.3 (0.7)	1.4 (0.2)
	1 and 6	-0.5 (0.4)	1.0 (0.2)
	6 and 7	-0.6 (0.6)	0.5 (0.4)
50	1 and 2	-1.0 (0.1)	0.5 (0.8)
	1 and 6	-0.9 (0.5)	0.4 (0.8)
	6 and 7	-0.6 (0.7)	0.5 (0.5)
70	1 and 2	-1.3 (0.3)	1.2 (0.8)
	1 and 6	-0.8 (0.4)	0.9 (0.1)
	6 and 7	-0.6 (0.5)	0.6 (0.5)
90	1 and 2	-0.7 (0.4)	1.4 (0.6)
	1 and 6	-1.2 (0.3)	1.0 (0.5)
	6 and 7	-1.0 (0.2)	0.2 (0.1)

Table C.6: Average peak compressive and tensile strains for each marker pair obtained from three trials at each height for the complex surrogate when dropped in the downward orientation. Values in brackets represent the standard deviation.

Drop Height (cm)	Marker Pairing	Peak Compressive Strain (%)	Peak Tensile Strain (%)
30	1 and 2	-1.0 (0.5)	1.3 (0.2)
	1 and 6	-0.8 (0.3)	0.6 (0.3)
	6 and 7	-0.7 (0.3)	0.6 (0.1)
50	1 and 2	-0.7 (0.5)	1.3 (0.2)
	1 and 6	-1.2 (0.3)	0.4 (0.0)
	6 and 7	-1.4 (0.3)	1.2 (0.3)
70	1 and 2	-1.3 (0.3)	1.2 (0.8)
	1 and 6	-1.9 (0.3)	0.2 (0.1)
	6 and 7	-1.0 (0.1)	1.3 (0.7)
90	1 and 2	-1.2 (0.3)	0.8 (0.1)
	1 and 6	-1.5 (0.0)	0.6 (0.2)
	6 and 7	-1.7 (0.2)	0.7 (0.4)

Table C.7: Average peak compressive and tensile strains for each marker pair obtained from three trials at each height for the smooth surrogate when dropped in the upward orientation. Values in brackets represent the standard deviation.

Drop Height (cm)	Marker Pairing	Peak Compressive Strain (%)	Peak Tensile Strain (%)
30	1 and 2	-0.7 (0.3)	0.9 (0.3)
	1 and 6	-1.3 (0.2)	0.7 (0.2)
	6 and 7	-0.6 (0.3)	1.1 (0.8)
50	1 and 2	-1.3 (0.3)	0.7 (1.0)
	1 and 6	-1.9 (0.2)	1.0 (0.4)
	6 and 7	-0.7 (0.2)	0.6 (0.3)
70	1 and 2	-1.1 (0.7)	1.3 (0.6)
	1 and 6	-2.1 (0.3)	1.5 (0.3)
	6 and 7	-0.8 (0.5)	0.4 (0.7)
90	1 and 2	-0.6 (0.3)	1.1 (0.3)
	1 and 6	-1.7 (0.3)	1.0 (0.3)
	6 and 7	-0.9 (0.2)	0.8 (0.2)

Table C.8: Average peak compressive and tensile strains for each marker pair obtained from three trials at each height for the complex surrogate when dropped in the upward orientation. Values in brackets represent the standard deviation.

Drop Height (cm)	Marker Pairing	Peak Compressive Strain (%)	Peak Tensile Strain (%)
30	1 and 2	-0.7 (0.2)	0.5 (0.2)
	1 and 6	-1.1 (0.1)	0.7 (0.1)
	6 and 7	-1.6 (0.3)	0.3 (0.2)
50	1 and 2	-0.6 (0.3)	1.0 (0.3)
	1 and 6	-1.6 (0.1)	1.0 (0.1)
	6 and 7	-1.3 (0.2)	1.4 (0.2)
70	1 and 2	-0.9 (0.5)	0.6 (0.2)
	1 and 6	-1.5 (0.3)	1.1 (0.3)
	6 and 7	-1.6 (0.2)	1.1 (0.3)
90	1 and 2	-1.4 (0.2)	0.5 (0.5)
	1 and 6	-2.1 (0.3)	0.8 (0.2)
	6 and 7	-1.8 (0.3)	1.2 (0.2)

Additional Comparisons Between DIC and Particle Tracking Data

Below are additional figures that compare the x- vs y- displacements obtained through DIC and particle tracking.

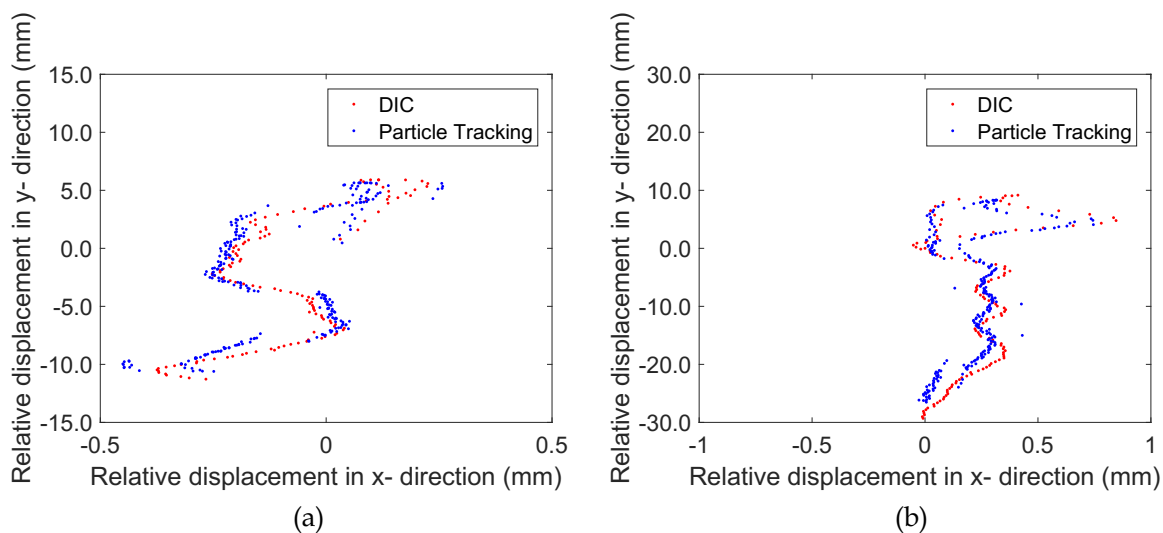


Figure C.57: The relative x- vs y- displacement plots obtained through DIC and particle tracking for Marker 1 for a) the smooth surrogate dropped in the inward orientation and b) the complex surrogate dropped in the upward orientation. Each displacement plot was obtained from the median trial for that specific surrogate and orientation.

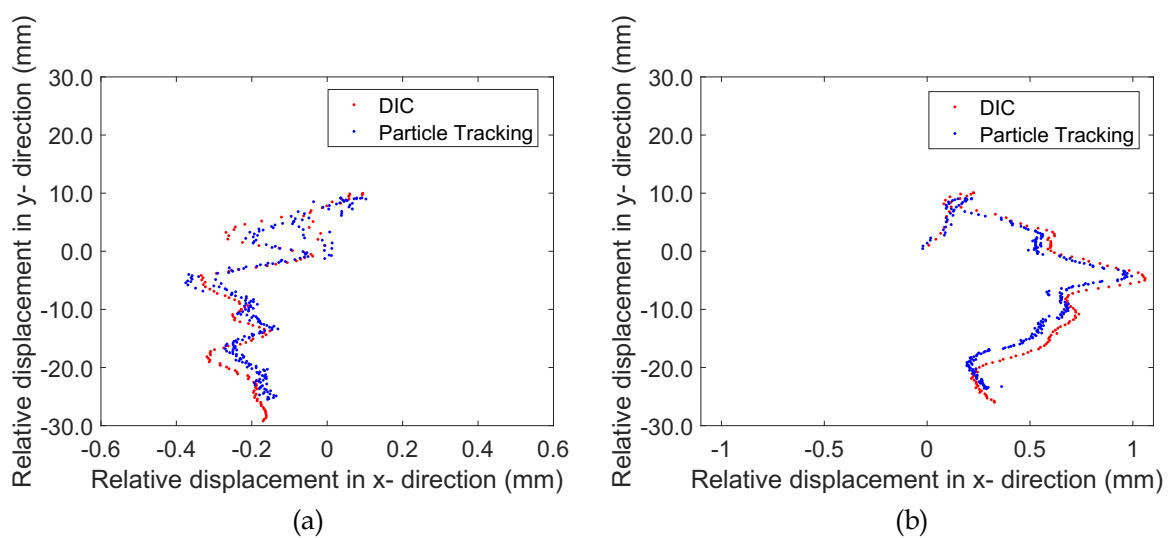


Figure C.58: The relative x- vs y- displacement plots obtained through DIC and particle tracking for Marker 6 for a) the smooth surrogate dropped in the upward orientation and b) the complex surrogate dropped in the downward orientation. Each displacement plot was obtained from the median trial for that specific surrogate and orientation.

Sub-pixel Jitter Analysis

Sub-pixel jitter resulting from the Mosaic ParticleTracker algorithm was evaluated. A single particle was tracked with a theoretically known x -displacement. Additionally, to evaluate the influences of sub-pixel jitter, corrections were made to the raw coordinates and the corrected strain responses were compared to the original strain responses. Each figure shows corrections made to markers within different regions.

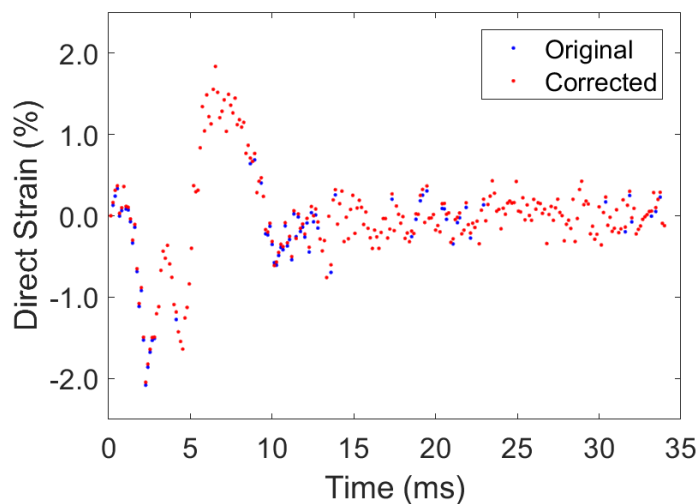


Figure C.59: The direct strain responses taken from the complex surrogate using Markers 6 and 7 at one trial from a height of 50 cm and dropped in the upward orientation. This was from the same trial as the displacement plots in Figure 60d. The influences of sub-pixel jitter are minimal when compared to the corrected strain response that removed jitter.

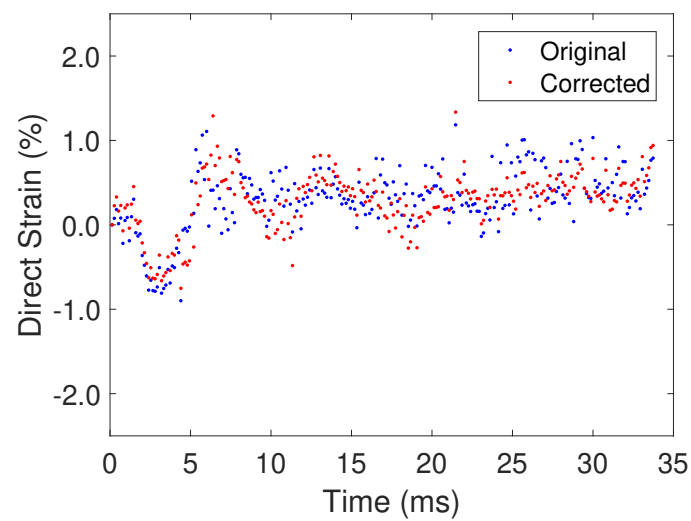


Figure C.60: The direct strain responses taken from the complex surrogate using Markers 1 and 6 at a height of 50 cm. The strain responses are from the same trial (2), when the surrogate was dropped in the swapped position. Both Markers 1 and 6 were corrected for jitter. The influences of sub-pixel jitter are minimal when compared to the corrected strain response, as trends and peak values remained the same.

Additional Viable *Ex Vivo* Porcine Brain Data

To supplement the figures in Chapter 5.2, a table of averaged peak tensile and compressive strain values from the surrounding areas is provided below.

Table C.9: Averaged peak tensile and compressive strains within the porcine brains measured in regions surrounding the highlighted Markers in each figure in Chapter 5.2. Values in brackets represent the standard deviation.

Specimen	Peak Compressive Strain (%)	Peak Tensile Strain (%)
May 16 Left Brain	-2.6 (1.2)	10.4 (1.8)
May 16 Right Brain	-9.3 (7.3)	7.8 (3.3)
June 6 Left Brain	-7.3 (3.1)	4.6 (1.1)
June 6 Right Brain	-8.0 (5.5)	6.7 (2.3)